



Programa de Doctorado “Matemáticas”

PHD DISSERTATION

---

Multilayer methods  
for geophysical flows:  
modelling and  
numerical approximation

---

*Author*

*José Garres Díaz*

*Supervisors*

Prof. Dr. *Enrique Domingo Fernández Nieto*

Prof. Dr. *Gladys Narbona Reina*

February 13, 2018



*A mis padres y hermana.  
A Marithania.*



# Agradecimientos

En primer lugar a mis directores, Enrique D. y Gladys, por haber confiado en mí para llevar a cabo este proyecto. Por vuestra dedicación e implicación, por tener siempre un hueco para mí, sin importar lo ocupados que estuviérais. Por trasmitirme no sólo conocimientos, sino también vuestra motivación y pasión por la investigación. Enrique, por todo lo que me has enseñado y por ser un modelo a seguir. Por cada discusión con la que he aprendido y disfrutado, llegando a poner a prueba tu infinita paciencia. Gladys, por tu ayuda resolviendo mis dudas de cualquier naturaleza, por tu confianza, por cada “¡ánimo!”, cada “¡eso lo haces tú en un rato!”, y por poner el punto de cordura en tantos momentos en los que algo requiere un poco más que “cuatro patás”.

Por cada consejo que me habéis dado, por los que me seguís dando, y por los que me daréis. Por el cariño con el que me tratasteis nada más llegar, y con el que me seguís tratando. Por el trato cercano, de compañeros, haciendo que la palabra “director” cobre nuevos significados. Por tenerme siempre presente. Porque no he podido tener mejores directores, y por todas esas cosas que olvido mencionar, gracias.

Anne, merci de m’avoir donné l’opportunité d’apprendre de toi pendant et après mon séjour à Paris. En travaillant avec toi, j’ai découvert le potentiel des Mathématiques Appliquées et les avantages des équipes interdisciplinaires: nos articles m’ont fait voir que si on travail ensemble, les géophysiciens et les mathématiciens tous gagnons.

Grazie Luca per avermi insegnato durante il mio soggiorno a Milano tutto ciò che so sugli schemi semi-impliciti. Per la tua disponibilità nel risolvere tutti i dubbi che sono sorti, sia dietro la tua scrivania durante il mio soggiorno o per e-mail a distanza, una volta tornato, e per il tuo coinvolgimento nel nostro lavoro. Grazie mille!

Me gustaría también agradecer a los miembros del grupo EDANYA de la Universidad de Málaga, con los que he coincidido en mis visitas a Málaga y en congresos. Especialmente a Manuel J. Castro, por su cercanía y predisposición a ayudarme.

Debo expresar mi gratitud a los profesores de la Facultad de Matemáticas de la Universidad de Murcia, donde me formé como matemático, y a los que forman parte del Máster en Ingeniería Matemática de las universidades gallegas, donde descubrí el área a la que quiero dedicar mi vida profesional.

A los miembros de mi grupo de investigación, “Modelado Matemático y Simulación de Sistemas Medioambientales”, por el cariño con el que me acogieron, por las comidas de Navidad post-navidadañas, y por lo cómodo que me han hecho sentir. A algunos miembros de los departamentos de Matemática Aplicada I y EDAN, en particular a los de Arquitectura, por el buen ambiente que se respira y del que he podido disfrutar durante estos años.

A mis compañeros del IMUS y la L2, con los que he tenido la suerte de compartir buenos momentos en comidas, cafés interminables, pastelitos, cenas y recenas. A Enrique, Javi, Cristian y agregados de los *Cafeses Bestias*, porque “sin nuestros ratos estos cuatro años no habrían sido lo mismo”, me alegra mucho haberlos disfrutado con vosotros. Enrique, por la *fase offline* de nuestras tesis compartiendo licor café en Santiago y por la *fase online* como compañeros de habitación en los congresos. A Asun, porque es un punto singular en Sevilla. A mis dos compañeros de piso: a Israel, por ser un apoyo constante en la primera etapa de esta tesis y por ser el primero al que llamé amigo en Sevilla; a Diego, con el que he compartido esta última fase, con mis derrotas al correr, victorias al pádel/tenis, y las que quedan...

Gracias también a mis amigos *de toda la vida* de Murcia. Nombro a Pedro V. por ser “el de toda la vida” y a Santiago, por su apoyo y por ser “mi caranclancas”, con todo lo que ello conlleva. A Antonio, por acogerme en su despacho y sacar siempre tiempo para vernos y compartir buenos ratos, alegrías y frustraciones de doctorandos, y a Isiah, por ayudarme a descubrir este camino y animarme a empezar un doctorado.

Marithania, eres la que ha soportado todos los vaivenes que realizar esta tesis ha supuesto. Por ser mi gran apoyo y a la vez mi primera y mayor crítica. Porque los esfuerzos y sacrificios contigo son más fáciles. No tengo palabras para agradecer todo lo que me das desde hace más de tres años. Por eso y porque cualquier futuro que imagino es a tu lado, te dedico esta tesis. A Marithania y Manolo, por vuestra generosidad, por cuidarme siempre que tenéis oportunidad y por acogerme en vuestra familia con el cariño con que lo habéis hecho.

Por último, el mayor de mis agradecimientos va para mi familia. Especialmente a mis padres y hermana, a quienes también dedico este trabajo. Porque en gran parte soy el resultado de vuestros esfuerzos. Ana Belén, siempre he sentido tu apoyo y cariño. Papá, por tu sensatez, por estar siempre ahí para aconsejarme y solventar cada dificultad que he encontrado (o decirme cómo hacerlo), y sobre todo por los abrazos que restan importancia a cualquier problema. Mamá, por tener más confianza en mí y en que al final las cosas salgan bien que yo mismo. Por ser la primera a la que llamo en un mal día y tener la capacidad de transformarlo con un “¿Me quieres? ¿Me echas de menos?”. Por hacerme sentir que soy lo primero en vuestras vidas, y apoyarme en cada decisión que he tomado sin importar las consecuencias que tuviera para vosotros. Porque sé que siempre estaréis a mi lado, incondicionalmente. Papá, mamá, Ana, quiero aprovechar esta frase, probablemente la última que entendáis de esta tesis, para deciros algo que no acostumbro: Os quiero.

A todos, gracias.

---

# Resumen

Esta tesis se enmarca en el ámbito de la Matemática Aplicada y la Mecánica de Fluidos Computacional. Concretamente, aborda el modelado matemático y la simulación numérica de flujos geofísicos mediante modelos multicapa. Las contribuciones principales se encuentran en los Capítulos 2, 3 y 4. En el Capítulo 1 se revisa brevemente la aproximación multicapa para las ecuaciones de Navier-Stokes con viscosidad constante, así como el procedimiento para obtener un modelo multicapa.

Las avalanchas granulares se han estudiado principalmente mediante modelos integrados. Sin embargo, esos modelos no reproducen variaciones en tiempo de los perfiles de velocidad. En el Capítulo 2 se presenta un modelo multicapa para avalanchas granulares secas considerando una viscosidad variable definida por la ley constitutiva  $\mu(I)$ . En este modelo no se prescribe el perfil normal de velocidad horizontal, lo que permite reproducir fuertes cambios en tiempo de estos perfiles.

En el Capítulo 3 se extiende el modelo multicapa anterior al caso de una masa granular confinada en un canal rectangular, para lo que se añade un nuevo término de fricción en las paredes laterales. Se presenta también un esquema numérico bien equilibrado para este modelo, con un tratamiento específico de los términos correspondientes a la fricción y la reología. Se muestra que el término de fricción lateral modifica significativamente la evolución de la avalancha. En particular, altera completamente el perfil vertical de velocidad, dando lugar a zonas donde el material queda estático bajo una capa superior que se mueve. Así mismo, se prueba que incluir el término de fricción lateral en modelos integrados de una capa puede dar lugar a soluciones carentes de sentido desde el punto de vista físico.

En el Capítulo 4 se presenta una discretización semi-implícita en tiempo para modelos multicapa, para los que se obtiene una condición CFL menos restrictiva en el caso de un flujo subcrítico, lo que permite reducir notablemente el coste computacional. La descripción multicapa propuesta es novedosa, ya que el número de capas verticales puede cambiar a lo largo del dominio computacional, sin una pérdida de precisión relevante. Estas técnicas se aplican a problemas de flujos oceánicos y de transporte de sedimento.





---

# Abstract

This thesis falls within the scopes of Applied Mathematics and Computational Fluid Dynamics. Namely, it addresses the mathematical modelling and numerical simulation of geophysical flows through multilayer shallow models. The main contributions are in Chapters 2, 3 and 4. In Chapter 1 we briefly review the multilayer approach for the Navier-Stokes equations with constant viscosity and the procedure for obtaining a multilayer model.

In the literature, granular flows have been mainly modelled by depth-averaged models. Nevertheless, those models cannot reproduce changes of velocity profiles. In Chapter 2 we present a multilayer shallow model for dry granular flows taking into account a variable viscosity coefficient given by the  $\mu(I)$  rheology constitutive law, where the normal profile of velocity is not prescribed. With this model we can reproduce strong changes in time of the normal profiles of horizontal velocity.

Chapter 3 focuses on the extension of the previous multilayer model to the case of a granular mass confined in a rectangular domain, by adding a new friction term at the lateral walls. We also present a well-balanced numerical discretization for this model, with an appropriate treatment of the friction and rheological terms. This lateral friction term modifies the granular mass evolution. In particular, it notably changes the normal profile of velocity, leading to areas of static grains below a moving layer of material. In addition, we prove that including the lateral friction term in depth-averaged models with a single layer can lead to solutions with no physical meaning.

In Chapter 4 we present a semi-implicit time discretization for multilayer systems. In the case of subcritical flows, we obtain a nonrestrictive CFL condition allowing to reduce the associated computational cost. This is an innovative multilayer discretization, since the number of vertical layers can be modified along the computational domain without a significant loss of accuracy. These discretizations are applied to coastal ocean flows and to sediment transport problems.



---

# Contents

<b>Abstract</b>	<b>ix</b>
<b>Introduction</b>	<b>1</b>
<b>1 Background on multilayer approach</b>	<b>13</b>
1.1 Introduction . . . . .	13
1.2 The initial system . . . . .	13
1.3 A multilayer approach . . . . .	16
1.3.1 Notation . . . . .	16
1.3.2 Weak solution with discontinuities . . . . .	17
1.3.3 Derivation of the final model: a particular weak solution . . . . .	20
1.4 Final multilayer model . . . . .	26
1.5 An alternative 3D multilayer model with energy balance . . . . .	28
<b>2 A <math>\mu(I)</math> rheology multilayer shallow model for dry granular flows</b>	<b>35</b>
2.1 Introduction . . . . .	35
2.2 Initial system with the $\mu(I)$ rheology . . . . .	36
2.3 The $\mu(I)$ rheology multilayer model . . . . .	39
2.3.1 Dimensional analysis . . . . .	39
2.3.2 A multilayer approach . . . . .	41
2.3.3 Derivation of the final model with $\mu(I)$ viscosity . . . . .	44
2.3.4 Final model . . . . .	47
2.4 Numerical tests . . . . .	48
2.4.1 Granular surface flows in a channel . . . . .	48
2.4.2 Granular collapse experiments . . . . .	54
<b>3 Well-balanced multilayer discretization and side walls friction</b>	<b>69</b>
3.1 Introduction . . . . .	69
3.2 A 2D-model including lateral walls friction . . . . .	70

3.2.1	A multilayer discretization . . . . .	76
3.3	Numerical approximation . . . . .	80
3.4	Numerical tests . . . . .	85
3.4.1	Uniform flow: influence of the channel width . . . . .	85
3.4.2	Well-Balanced test including dry areas: granular collapse over an arbitrary bottom . . . . .	89
3.4.3	Solutions at rest with lateral walls friction: multilayer vs monolayer	91
3.4.4	Laboratory experiments: dam break over rigid and erodible beds	95
<b>4</b>	<b>Semi-implicit time discretization with variable number of layers</b>	<b>105</b>
4.1	Introduction . . . . .	105
4.2	Multilayer shallow water models . . . . .	106
4.3	Spatial discretization with variable number of layers . . . . .	109
4.4	Semi-implicit time discretizations . . . . .	111
4.4.1	A $\theta$ -method time discretization . . . . .	113
4.4.2	A more accurate IMEX-ARK discretization . . . . .	118
4.5	Numerical results . . . . .	123
4.5.1	Free oscillations in a closed basin . . . . .	124
4.5.2	Steady subcritical flow over a peak with friction . . . . .	127
4.5.3	Tidal forcing over variable bathymetry . . . . .	129
4.5.4	An application to sediment transport problems . . . . .	133
	<b>Bibliography</b>	<b>139</b>

# List of Figures

I.1	<i>Sketch of a shallow domain</i> . . . . .	2
I.2	<i>Sketch of a multilayer domain</i> . . . . .	3
1.1	<i>Sketch of the domain and its multilayer division</i> . . . . .	16
2.1	<i>Test 1.1: Sketch of the analytical solution for a Bagnold flow</i> . . . . .	49
2.2	<i>Test 1.1: Analytical solution for a Bagnold flow: <math>u</math>, <math>p</math>, <math>\ D(u)\ </math>, <math>\tau</math>, <math>\mu(I)</math></i> . . . . .	51
2.3	<i>Test 1.1: Analytical solution for a Bagnold flow: computational times and errors</i> . . . . .	51
2.4	<i>Test 1.2: Analytical solution for a Bagnold flow with lateral walls friction</i> . . . . .	53
2.5	<i>Test 1.3: Laboratory experiments for a uniform flow: transient velocity profiles</i> . . . . .	54
2.6	<i>Test 2: Sketch of the initial and final state of the granular collapse</i> . . . . .	56
2.7	<i>Test 2: Laboratory experiments granular collapse: <math>\mu(I)</math>-MSM vs <math>\mu_s</math>-MSM</i> . . . . .	58
2.8	<i>Test 2: Laboratory experiments granular collapse, <math>\theta = 22^\circ</math>, <math>h_i = 1.82</math> mm: <math>\mu(I)</math> vs <math>\mu_s</math></i> . . . . .	59
2.9	<i>Test 2: Influence of the thickness <math>h_i</math> over <math>r_f</math> and <math>h_f</math>, <math>\theta = 22^\circ</math>: <math>\mu(I)</math>-MSM vs <math>\mu_s</math>-MSM</i> . . . . .	60
2.10	<i>Test 2: Influence of the thickness <math>h_i</math> over <math>r_f</math>: <math>\mu_s</math>-MSM vs <math>\mu_s</math>-monolayer</i> . . . . .	61
2.11	<i>Test 2: Influence of the thickness <math>h_i</math> over <math>r_f</math>: <math>\mu(I)</math>-MSM vs <math>\mu(I)</math>-monolayer</i> . . . . .	61
2.12	<i>Test 2: Influence of the thickness <math>h_i</math> over <math>t_f</math>: <math>\mu(I)</math>-MSM vs <math>\mu(I)</math>-monolayer</i> . . . . .	62
2.13	<i>Test 2: Time evolution of the free surface and the flow/non-flow interface, <math>\theta = 22^\circ</math>, <math>h_i = 1.82</math> mm: <math>\mu_s</math>-MSM vs <math>\mu_s</math>-monolayer</i> . . . . .	63
2.14	<i>Test 2: Time evolution of the free surface and the flow/non-flow interface, <math>\theta = 22^\circ</math>, <math>h_i = 1.82</math> mm: <math>\mu(I)</math>-MSM vs <math>\mu(I)</math>-monolayer</i> . . . . .	63
2.15	<i>Test 2: Laboratory experiments granular collapse: <math>\mu(I)</math>-MSM vs <math>\mu(I)</math>-C-MSM</i> . . . . .	64
2.16	<i>Test 2: Normal profiles of the downslope velocity, <math>\theta = 22^\circ</math>, <math>h_i = 1.82</math> mm</i> . . . . .	65
2.17	<i>Test 2: Normal profiles of the downslope velocity, <math>\theta = 0^\circ</math>, <math>h_i = 1.5</math> mm</i> . . . . .	66
2.18	<i>Test 2: Normal profiles of the normal velocity, <math>\theta = 22^\circ</math>, <math>h_i = 1.82</math> mm</i> . . . . .	66
3.1	<i>Sketch of a rectangular domain with width <math>W</math></i> . . . . .	71
3.2	<i>Sketch of the placing of the variables in the multilayer domain</i> . . . . .	78
3.3	<i>Test 1: Uniform flow: normal profiles of downslope velocity for different <math>W</math></i> . . . . .	86

3.4	<i>Test 1: Uniform flow: downslope velocity at the free surface for different <math>W</math></i>	87
3.5	<i>Test 1: Evolution of <math>W_c(\theta)</math>, <math>W_b(\theta)</math> and relative errors between the maximum and average velocities</i>	88
3.6	<i>Test 1: Normal profiles of downslope velocity: no-slip and friction condition</i>	88
3.7	<i>Test 2: Free surface evolution: influence of the hydrostatic reconstruction for the Coulomb friction term</i>	90
3.8	<i>Test 2: Free surface evolution: <math>\mu_w = 0</math> vs <math>\mu_w \neq 0</math></i>	90
3.9	<i>Test 2: Normal profiles of downslope velocity: <math>\mu(I)</math>-<math>\mu_w</math>-MSM vs [Jop et al. (2005)]</i>	91
3.10	<i>Test 3: Solution at rest with lateral walls friction: multilayer vs monolayer</i>	94
3.11	<i>Test 4: Time evolution of the free surface and the flow/no-flow interface, <math>\theta = 0^\circ, 16^\circ</math>: <math>\mu(I)</math> vs <math>\mu(I)</math>-<math>\mu_w</math></i>	96
3.12	<i>Test 4: Time evolution of the free surface and the flow/no-flow interface, <math>\theta = 19^\circ</math>: <math>\mu(I)</math> vs <math>\mu(I)</math>-<math>\mu_w</math></i>	97
3.13	<i>Test 4: Time evolution of the free surface and the flow/no-flow interface, <math>\theta = 22^\circ</math>, <math>h_i = 0, 4.6</math> mm: <math>\mu(I)</math> vs <math>\mu(I)</math>-<math>\mu_w</math></i>	98
3.14	<i>Test 4: Distribution of <math>u</math>, <math>w</math> and <math>\mu(I)</math>, <math>\theta = 0^\circ</math>, <math>t = 0.18</math> s: <math>\mu(I)</math> vs <math>\mu(I)</math>-<math>\mu_w</math></i>	99
3.15	<i>Test 4: Distribution of <math>u</math>, <math>w</math> and <math>\mu(I)</math>, <math>\theta = 16^\circ</math>, <math>t = 0.30</math> s: <math>\mu(I)</math> vs <math>\mu(I)</math>-<math>\mu_w</math></i>	100
3.16	<i>Test 4: Granular collapse over a rigid bed using <math>h_i = 0, 0.014, 0.14, 1.4, 4.6</math> mm</i>	101
3.17	<i>Test 4: Time evolution of the flow/no-flow interface for the granular collapse</i>	102
3.18	<i>Test 4: Time evolution of the flow/no-flow interface for a uniform flow</i>	103
4.1	<i>Sketch of the domain and its subdivision in a constant number of layers</i>	106
4.2	<i>Sketch of the domain subdivision in a variable number of layers</i>	111
4.3	<i>Free oscillations test: Sketch of the variable number of layers configuration</i>	125
4.4	<i>Free oscillations test: Free surface profiles</i>	126
4.5	<i>Free oscillations test: Errors with variable number of layers</i>	127
4.6	<i>Free oscillations test: Vertical profiles of velocity with variable number of layers</i>	127
4.7	<i>Steady subcritical flow test: Free surface profiles</i>	128
4.8	<i>Steady subcritical flow test: Error and vertical profiles of velocity with variable number of layers</i>	129
4.9	<i>Tidal forcing test: Sketch of the bottom topography</i>	130
4.10	<i>Tidal forcing test: Vector map of the whole velocity field</i>	130
4.11	<i>Tidal forcing test: Free surface profiles</i>	131
4.12	<i>Tidal forcing test: Errors with variable number of layers</i>	133
4.13	<i>Tidal forcing test: Vertical profiles of velocity with variable number of layers</i>	134
4.14	<i>Sediment transport test: Profile of the dune at different times</i>	136
4.15	<i>Sediment transport test: Free surface and bottom profiles</i>	136
4.16	<i>Sediment transport test: Sketch of the variable number of layers</i>	137
4.17	<i>Sediment transport test: Errors with variable number of layers</i>	138

---

## List of Tables

2.1	<i>Test 1.1: Convergence study for Bagnold flow test</i>	52
2.2	<i>Test 1.2: Convergence study for the Bagnold flow test with lateral walls friction</i>	53
2.3	<i>Test 2: Summary of notation of the different models and colors-symbols</i>	57
3.1	<i>Test 1: Values of the channel width: <math>W_c</math>, <math>W_b</math> and <math>W_0</math></i>	87
3.2	<i>Test 3: Convergence study with the monolayer model</i>	93
4.1	<i>Butcher tableaux of the explicit ARK2 method</i>	119
4.2	<i>Butcher tableaux of the implicit ARK2 method</i>	120
4.3	<i>Free oscillations test: Relative errors and Courant numbers achieved</i>	125
4.4	<i>Steady subcritical flow test: Relative errors and Courant numbers achieved</i>	128
4.5	<i>Tidal forcing test: Relative errors and Courant numbers achieved</i>	132
4.6	<i>Tidal forcing test: Computational times and speed-up</i>	132
4.7	<i>Sediment transport test: Relative errors and Courant numbers achieved</i>	136
4.8	<i>Sediment transport test: Computational times and speed-up</i>	137





---

# Introduction

Mathematical modelling of geophysical flows remains one of the most challenging scientific problems in our days since it is a powerful tool for understanding the dynamics of the environmental agents (rivers, oceans, atmosphere, etc.) and their associated transformations. In fact, it provides a unique tool for hazard assessment due to natural disasters, as tsunamis propagations and inundations, dam and levee failures, flooding, avalanches, eruptions of volcanoes, toxic spills, etc. In particular, this thesis is focused on the geophysical phenomena where granular flows are involved, which can be classified as short timescale (avalanches, debris or rock avalanches, landslides, granular collapses, gravity currents, etc) and long timescale processes (coastal ocean processes, river dynamics, sediment transport and erosion/deposition processes).

From the mathematical point of view, the motion of fluids is described by the Navier-Stokes equations. These equations are derived from the conservation laws of mass and momentum, coming from two basic principles: (i) mass is neither created nor destroyed; (ii) the rate of change of momentum of a portion of the fluid equals the force applied to it (Newton's second law). The Navier-Stokes equations describe exactly the flow dynamics. However, its numerical resolution is extremely hard in terms of the computational cost, even for the simplest configurations.

In order to avoid solving these equations, the classic Saint-Venant model [103], which is obtained by integrating the Navier-Stokes equations along the thickness of the flow, was introduced. This model assumes that the thickness of the flow is small when compared with the horizontal dimension, and therefore the variations along the vertical direction are neglected and depth-averaged variables are considered (see figure I.1). This is the so-called shallow water (or thin-layer) hypothesis. Models assuming it are known as shallow or depth-averaged models, and they have been usually used in the framework of gravity-driven, shallow and free surface flows.

A rigorous derivation of this model was presented by Gerbeau & Perthame [61] from a dimensional analysis of the full Navier-Stokes system. They also introduced the viscous Saint-Venant system. The shallow water approximation has been widely validated for

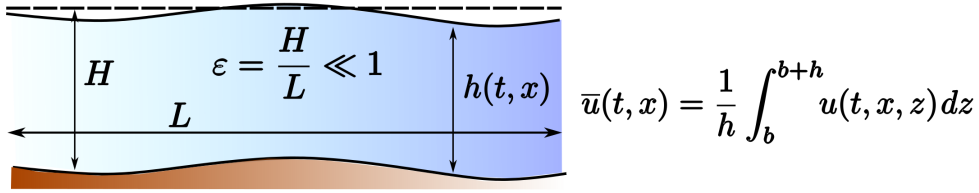


Figure I.1: Sketch of a shallow domain with characteristic length  $L$  and height  $H$ .  $u$  represents the velocity of the fluid, whose thickness is  $h$  and  $b$  the bottom, then  $\bar{u}$  is the depth-averaged velocity.

applications to the dynamics of rivers, coastal areas, etc., but also for complex flows like dry avalanches, debris flows, etc. when appropriate terms are included (see e.g. [105, 73, 71, 28, 89, 29, 97, 88, 53, 26]).

The main advantage of depth-averaged models is the fact that they are very efficient in contrast with 3D Navier-Stokes equations, which have a high associated computational cost. The case of depth-averaged simulations is much more efficient. However, there is an important loss of physical information (e.g. 3D behaviour of the flow) due to the fact that the horizontal velocity does not depend on the vertical coordinate. In particular, it makes impossible to obtain changes in time of velocity profiles and even the correct averaged horizontal velocity in most cases.

Multilayer models appear as an interesting intermediate step between the full Navier-Stokes equations and the classic Saint-Venant type models. In a few words, these models are deduced by subdividing the computational domain in shallow vertical layers, and the classic shallow water hypothesis is applied in each of those vertical layers (see figure I.2). Thus, the averaged horizontal velocity  $\bar{u}_\alpha$  is constant in that layer, but may be different from the velocities  $\bar{u}_\beta$  with  $\beta \neq \alpha$ . The main advantages of multilayer models are: (i) they allow us to partially recover the vertical structure of the flow, which is specially important in the presence of viscous terms; (ii) they keep the low cost associated to the numerical treatment of the free surface; (iii) the mass is exactly preserved (see e.g. [7, 9, 56, 104]).

Multilayer models were introduced by Audusse [3] (and later extended in [8]) in order to take into account the vertical structure in the simulation of geophysical flows, making it possible in particular to resolve the shape of velocity profiles. Next, a different multilayer model, which takes into account the exchange of mass and momentum between the layers, was derived by Audusse *et al.* [7, 9], and Sainte-Marie [104]. In particular, this multilayer model was applied to study movable beds by adding an Exner equation by Audusse *et al.* [4].

A different formulation was proposed by Fernández-Nieto *et al.* [56], which has several differences with respect to previous multilayer models. The model proposed in [56] is derived by assuming a discontinuous profile of the velocity, and the solution is obtained as a particular weak solution of the full Navier-Stokes system. Moreover, the mass and momentum transfer terms at the interfaces of the normal partition are

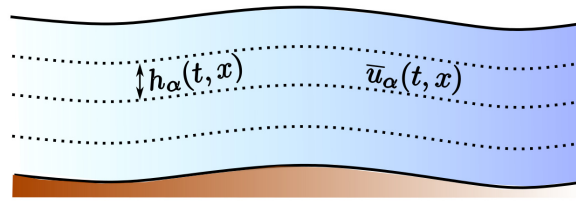


Figure I.2: Sketch of a multilayer domain.  $h_\alpha$ ,  $\bar{u}_\alpha$  are the thickness and the depth-averaged velocity in the layer  $\alpha$ , respectively.

deduced from the jump conditions satisfied by the weak solutions of the Navier-Stokes system. In addition, the vertical velocity is computed in a postprocessing step based on the incompressibility condition, but accounting also for the mass transfer terms between the internal layers.

In the scope of the fluid mechanics, PDEs systems are usually solved numerically by using finite element methods, finite difference methods or finite volume methods. In particular, we focus on finite volume methods (see e.g. LeVeque [81]). These methods allow us to discretize hyperbolic systems of conservation laws, which take the form

$$\partial_t w + \partial_x F(w) = 0,$$

where  $(t, x)$  denote the temporal and spatial variables,  $w$  is the vector of conservative variables and  $F(w)$  is the vector of flux functions. The system is said to be hyperbolic if the jacobian matrix  $\partial F(w)/\partial w \in \mathcal{M}_{n \times n}$  has  $n$  real eigenvalues and the eigenvectors are linearly independent.

Finite volume methods are based on subdividing the spatial domain into *control* or *finite volumes*, and considering the approximation of the integral of the conservative variables ( $w$ ) over each control volume. Then, these values are updated in each time step by using the approximations of the flux through the boundaries of the control volumes.

Nevertheless, when trying to approach to more realistic applications, this system appears together with sources terms  $S(w)$  (e.g. variations of the topography) and non conservative products  $B(w)\partial_x w$  (e.g. interactions between the conservative variables). Thus, the PDE system is written as

$$\partial_t w + \partial_x F(w) = S(w) + B(w)\partial_x w.$$

These source and non conservative terms entail new difficulties, such as defining well-balanced schemes (those which preserve steady solutions, in particular water at rest) and dealing with wet/dry transition (an empty control volume at time  $t^n$  that is filled at time  $t^{n+1}$ , and vice versa). Many efforts have been devoted to the development of numerical schemes for depth-averaged models solving those problems. For example, the hydrostatic reconstruction method is a technique allowing to recover the well-balanced property for depth-averaged models of avalanches, which also include wet/dry

fronts (see e.g. [6, 25, 37]). Another numerical treatment to deal with dry areas was introduced by Castro *et al.* [33], and improved in Castro *et al.* [34]. Parés & Castro [95] investigated the well-balancing of the Roe's method for non-conservative hyperbolic systems. Furthermore, those numerical schemes must be able to deal with the possible discontinuity of the solutions in the presence of non conservative products (see e.g. the family of *path-conservative* schemes introduced by Parés [94]).

Finally, models containing viscous terms are also typical in physical applications. Those terms entail a very restrictive condition in the time step when discretized explicitly. For this reason, it is frequent to use an splitting procedure, where firstly the hyperbolic part of the system is solved, and secondly the viscous terms are considered and usually discretized with semi-implicit schemes.

An important part of this thesis is devoted to the study of granular flows through multilayer models, namely dry granular flows. These flows have a noticeable vertical structure. Actually, the velocity is higher close to the free surface than near to the bottom. It is a fact that depth-averaged models are not able to take into account this structure, whereas multilayer models do. In particular, they improve the approximation of the viscosity coefficient, which is essential to properly reproduce the evolution of viscoplastic flows. The last part of this thesis is focused on reducing the computational cost of large timescale simulations for multilayer models. To this aim, we investigate semi-implicit time discretizations for multilayer systems.

Due to the high computational cost of solving the full 3D Navier-Stokes equations, in particular in the geophysical context, granular flows have often been simulated using depth-averaged models (e.g. [105, 73, 89, 88, 86]), in particular for application on natural geophysical flows on Earth and on other planets (e.g. [92, 82, 96, 52, 90, 83]).

The use of depth-averaged models for dry granular flows was pioneered by Savage & Hutter [105]. This model has been deeply investigated, even for submarine avalanches, debris flows, etc. It assumes a Coulomb friction law where the shear stress at the bottom is proportional to the normal stress, with a constant friction coefficient  $\mu$ . Nevertheless, the use of depth-averaged models for complex flows presents important shortcomings, specially related to the description of the stress tensor.

The behaviour of real geophysical flows is very complex due to topography effects, the heterogeneity of the material involved, the presence of fluid/gas phases, fragmentation, etc. ([47]). One of the major issues is to quantify erosion/deposition processes that play a key role in geophysical flow dynamics but are very difficult to measure in the field (see e.g. [44, 72, 14]).

Laboratory experiments on granular flows are very useful to test flow models on simple configurations where detailed measurements can be performed, even if some physical processes may differ between the large and small scale. These experiments may help in defining appropriate rheological laws to describe the behaviour of granular materials. Recent experiments by Mangeney *et al.* [87] and Farin *et al.* [51] on granular

column collapse have quantified how the dynamics and deposits of dry granular flows change in the presence of an erodible bed. They showed a significant increase of the runout distance (i.e. maximum distance reached by the deposit) and flow duration with increasing thickness of the erodible bed. This strong effect of bed entrainment was observed only for flows on slopes higher than a critical angle of approximately  $16^\circ$  for glass beads. The Savage & Hutter model does not reproduce this increase in runout distance observed. Actually, the analytical solution deduced by Faccanoni & Mangeney [50] proves that this model leads to the opposite effect. It is an open question whether this behaviour can be reproduced by granular flow models. Moreover, a key issue is whether this opposite behaviour between the experiments and simulations is due to the thin-layer approximation and/or depth-averaging process or to the rheological law implemented in the model (i.e. constant friction coefficient). Multilayer models can be a promising alternative to depth-averaged models in order to shed light on these questions, since an appropriate approximation of the normal effects seems to be a requirement to reproduce the dynamics of these flows properly.

Granular flows can behave either as a fluid or a rigid solid depending on the forces applied to them. In order to describe the non-Newtonian nature of those flows, we must consider the rheology, which is the branch of physics that deals with the deformation and flow of matter. Defining an appropriate rheological law to describe and understand the behaviour of granular material is still a major challenge. In particular, a key issue is to describe the transition between flow (fluid-like) and no-flow (solid-like) behaviour. Granular flows have been described by viscoplastic laws and especially by the so-called  $\mu(I)$  rheology, introduced by Jop *et al.* [76]. It specifies that the friction coefficient  $\mu$  is variable and depends on the inertial number  $I$ . This nondimensional number can be understood as the ratio between two timescales, the microscopic timescale associated to the local rearrangement of the particles and the macroscopic timescale reflecting the mean shear deformation. The  $\mu(I)$  rheology includes a Drucker-Prager yield criterion, i.e., the material flows if the stress tensor is over a threshold, otherwise the medium behaves as a rigid solid. In addition, the  $\mu(I)$  rheology is ill-posed (i.e. uncontrollable growth of small perturbations) for low and high values of  $I$ , even for steady-uniform flows where  $I$  ranges from zero to infinity when the slope varies between the limit angles of the  $\mu(I)$  rheology. Nevertheless, recently the well-posedness of the full  $\mu(I)$  rheology is proved by Barker *et al.* [12] for a large intermediate range of values of the inertial number  $I$ .

Lagrée *et al.* [79] implemented the  $\mu(I)$  rheology in a full Navier-Stokes solver (Gerris) by defining a viscosity from the  $\mu(I)$  rheology. They validated the model with 2D analytical solutions and compared it to 2D discrete element simulations of granular collapses over horizontal rigid beds and with other rheologies. Using an augmented Lagrangian method combined with finite element discretization to solve the 2D full Navier-Stokes equations, Martin *et al.* [91] and Ionescu *et al.* [70] showed that the  $\mu(I)$  rheology quantitatively reproduces laboratory experiments of granular collapses over

horizontal and inclined planes. They interpret the  $\mu(I)$  rheology as a viscoplastic flow with a Drucker-Prager yield stress criterion and a viscosity depending on the pressure and strain rate. They showed that the mean value of this viscosity has a key impact on the simulated front dynamics and on the deposit of granular column collapses.

Lusso *et al.* [85] used an Arbitrary Lagrangian Eulerian (ALE) formulation for the displacement of the domain to simulate a 2D viscoplastic flow considering a Drucker-Prager yield stress criterion and a constant viscosity. They obtained similar results taking into account either a regularization method or the augmented Lagrangian algorithm to avoid the singularity when the strain rate tensor vanishes, in the case of the collapse and spreading of a granular column. These studies showed the difficulty of the ALE method to deal with detailed description of the front propagation due to the deformation of the mesh and possible overturning of the elements at the front, in particular when trying to simulate granular flows over an initial layer of material lying on the bed. On the contrary, the multilayer description of the front could be very precise because the number of layers in the normal direction to the slope does not depend on the thickness of the flow. However, due to the eulerian description of the flow, multilayer models cannot describe the overturning of the front that may arise. Finally, multilayer approach is well adapted to describe erosion processes in a thin layer of erodible material because, again, the vertical discretization does not depend on the material thickness and the numerical cost is quite low.

Furthermore, by comparing the simulated normal velocity profiles and the time change of the position of the flow/no-flow interface (i.e. a moving layer over a static layer of material) with laboratory experiments by Farin *et al.* [51], they concluded that a pressure and rate-dependent viscosity can be important to study flows over an erodible bed. A similar conclusion is presented by Lusso *et al.* [84] after comparing the normal velocity profiles and the position of the flow/no-flow interface during the stopping phase of granular flows over erodible beds calculated with a simplified thin-layer but not depth-averaged viscoplastic model (Bouchut *et al.* [27]) with those measured in laboratory experiments. Moreover, by using analytical solutions, interestingly they showed that the flow/no-flow interface evolution is related to the normal gradient of the velocity at this interface. As a result, describing erosion/deposition processes related to static/flowing transition requires a model that is able to recover the time and space variation of the velocity profile. However, the proposed model (see [84]) is restricted to uniform flows in the downslope direction. Once more, multilayer models can be an encouraging alternative since the vertical effects seem to be essential to properly define the viscosity coefficient and reproduce the dynamics of these flows, namely those flows over an erodible bed. In addition, the approximation of the flow/no-flow (i.e. flowing/static) interface by using multilayer models is inherited from the fact of having more than a single layer.

On the other hand, Capart *et al.* [32] recently proposed a depth-integrated model taking into account a linearization of the  $\mu(I)$  rheology. They prescribed an S-shaped velocity profile corresponding to equilibrium debris flows and typical of granular flows

over erodible beds. Their velocity profiles were reconstructed using the computed averaged velocity making it possible to compare their results with velocity profiles measured in laboratory experiments. Gray & Edwards [64] introduced the  $\mu(I)$  rheology in a depth-averaged model by adding a viscous term and prescribing the well known Bagnold velocity profile, typical of granular flows over rigid beds. Edwards & Gray [49] showed the ability of this model to capture roll-waves and erosion-deposition waves, if it is combined with the basal friction law introduced in Pouliquen & Forterre [100].

At small scale (laboratory scale), Taberlet *et al.* [108] and Jop *et al.* [75] showed the importance of side walls friction for uniform flows over inclined channels. They proposed to model this effect by adding an extra term to the definition of  $\mu(I)$  for the case of uniform flows. This sidewalls friction term could change the granular mass evolution. In particular, its influence on the normal profile of velocity is evident, since it increases the effective friction when going from the free surface to the bottom. Moreover, this term leads to areas of static grains below a moving layer of material. Jop *et al.* [77] used this additional term to simulate the transient normal profiles of velocity in narrow channels and compared their simulations with laboratory experiments. Recently, Baker *et al.* [10] extended the depth-averaged model introduced in Gray & Edwards [64] to the two horizontal dimensions case for steady uniform flows between parallel plates. They included a new viscous term for the side walls friction and studied the normal profiles of velocity in narrow and wide channels. They compared the full and the depth-averaged  $\mu(I)$  rheology and concluded that they cannot reproduce the different profiles of the velocity observed in transient flows because of the prescribed vertical profile, in particular close to the lateral walls of narrow channels.

On the contrary, Capart *et al.* [32] prescribed a typical S-shaped profile for the downslope velocity, so that they were able to reproduce velocity profiles when flow was decelerating but not the Bagnold profile observed in other regimes. Actually, as observed in highly transient flows such as in granular collapses, the velocity profiles change from Bagnold-like near the front to S-shaped upstream where upper grains flow above static grains (see [70]). Moreover, granular collapse experiments and simulations have shown that during the stopping phase and when erosion/deposition processes occur, static zones may develop near the bottom and propagate upwards. As mentioned before, only the mean velocity over the whole thickness of the flow is calculated in depth-averaged models (i.e., the whole granular column is either flowing or at rest, except for the model proposed by Capart *et al.* [32]). Therefore, the existence of the flow/no-flow interface makes inappropriate the use of depth-averaged models to study those flows. Furthermore, the resulting normal gradient of the downslope velocity, which changes in time, is a significant term in the strain rate and therefore strongly influences the  $\mu(I)$  coefficient. Thus, multilayer models can be a powerful alternative to standard depth-averaged models due to the fact that both profiles, S-shaped and Bagnold-like, could be reproduced a priori since the normal profile of velocity is not prescribed.

We now detail the contributions of this work to this issue:

- In Chapter 1 we review the multilayer approach for a model with a constant viscosity coefficient. Moreover, we present a detailed exposition of the procedure to obtain a multilayer model. This model satisfies an energy balance for the 2D case. Nevertheless, it is not proved for the 3D case. We also propose an alternative 3D multilayer model. It exactly satisfies a dissipative energy balance and matches the previous multilayer model in [56] for the 2D case.
- In Chapter 2 we derive a multilayer shallow model with the  $\mu(I)$  rheology for dry granular flows, making it possible to compute 2D profiles of the velocity in the directions along and normal to a reference plane with constant slope, without prescribing a typical vertical profile (e.g. Bagnold or S-shaped profile). We validate this model using the 2D analytical solution of a Bagnold flow and a flow in a narrow channel with strong effect of the lateral wall friction. In addition, we compare this model with granular flow experiments on erodible beds ([77, 87, 51]). In particular, we show that the multilayer model together with the  $\mu(I)$  rheology reproduces the observed increase of the runout distance, when increasing the thickness of the erodible bed. An important result is the fact that the model is able to reproduce strong changes in velocity profiles of the downslope velocity during highly transient flows, from Bagnold-like to S-shaped profiles and vice versa.
- In Chapter 3 we present an extension of the model introduced in Chapter 2 that describes dry granular flows in a rectangular channel by including a Coulomb friction term at the lateral walls. This model is obtained through an asymptotic analysis and the hypothesis of a one-dimensional flow. We also present a well-balanced numerical discretization of the proposed multilayer shallow model with the  $\mu(I)$  rheology and lateral Coulomb friction, including the treatment of dry areas. We show that both, Bagnold and S-shaped vertical profiles of velocity can be automatically recovered. We also show that approximating side walls friction using single-layer models may lead to strong errors, they can even reproduce solutions with no physical meaning. Finally, we compare with laboratory experiments, showing the capability of the model to reproduce the time evolution of the flow/no-flow interface, as well as the erosion processes that arise in the presence of an erodible bed.

Most results of chapters 2 and 3 have been published in [54] and [55], in collaboration with the supervisors of this thesis, and with Prof. Anne Mangeney during and after a research stay in the “Institut de Physique du Globe de Paris” (Université Paris Diderot, Paris, France).



From now on, we focus on large scale geophysical flows, i.e. those flows which require huge computational efforts due to the large time and/or horizontal scale. On this scope, multilayer shallow water models can be seen as an alternative to more standard approaches for vertical discretizations, such as natural height coordinates (also known as  $z$ -coordinates in the literature on numerical modelling of atmospheric and oceanic flows), employed e.g. in [19, 31, 40], terrain following coordinates (also known as  $\sigma$ -coordinates in the literature), see e.g. [67], and isopycnal coordinates, see e.g. [17, 39]. Each technique has its own advantages and shortcomings, as highlighted in the discussions and reviews in [1, 19, 21, 68]. Multilayer approaches are appealing, because they share some of the advantages of  $z$ -coordinates, such as the absence of metric terms in the model equations, while not requiring special treatment of the lower boundary. On the other hand, multilayer approaches share one of the main disadvantages of  $\sigma$ -coordinates, since they require, at least in the formulations employed so far, to use the same number of layers independently of the fluid depth. Furthermore, an implicit regularity assumption on the bottom and free surface boundaries is required, in order to avoid that too steeply inclined layers arise, which would contradict the fundamental hydrostatic assumption underlying the model.

In order to reduce the computational cost of large simulation in subcritical flows, we consider semi-implicit time discretizations as a powerful alternative. In particular, the semi-implicit finite differences method introduced by Casulli & Cheng [41] and Casulli & Cattani [40], which allows us to obtain a less restrictive CFL condition in subcritical regimes, and therefore to use larger time steps in the computations. Actually, with this method, the CFL condition depends on the flow velocity, but not on the free surface gradient.

Different time discretizations can be employed a priori. The well-known  $\theta$ -method has been used successfully in coastal and atmospheric models (see e.g. Casulli & Cattani [40], Davies *et al.* [45]), with parameter  $\theta > 1/2$ . This choice of the parameter leads to a L-stable method, since it adds damping, which is essential for applications in low Mach/Froude number regimes. The time linearization in the free surface gradient term is also frequent, leading to a major reduction of the computational cost in computationally intensive applications, since it avoids to solve a global nonlinear problem. This approach has been widely used in environmental fluid dynamics (see e.g. Rosatti *et al.* [102])

A more accurate IMEX-ARK2 method was proposed in Giraldo *et al.* [62]. In this approach, stiff (implicitly discretized) and non stiff (explicitly discretized) terms must be clearly identified depending on the application regime. For shallow water-like applications in the subcritical, hydrostatic regime, the free surface gradients and divergence terms are the terms that cause the greatest stability restrictions, as shown in Robert [101] and Casulli [38]. Vertical turbulent viscosity and friction come next in the stiffness scale, both because the vertical spacing can be small and because vertical shear can be large, thus inducing significant turbulent stresses that are parameterized by large turbulent viscosity coefficients. Horizontal advection is definitely not stiff in the

low Froude number regime. Finally, vertical advection lies somehow in the middle, i.e., it is usually non stiff, although it can turn out to be stiff depending on the application.

A straightforward application of this method is the study of sediment transport processes, since a determining feature of problems is the fact that the characteristic time is very long, and therefore a huge computational time is required to obtain results. The particular case of bed load sediment transport problem can be studied through Saint-Venant-Exner-type models (see e.g. [57, 36]), which add a continuity equation for the sediment layer (Exner equation) to the Saint-Venant system. This additional equation can be coupled or not to the hydrodynamical model. When the coupled case is considered, the whole system is solved at the same time, whereas it is solved in two steps in the non-coupled case: firstly the hydrodynamical variables are calculated, and secondly the Exner equation is used to update the thickness of the sediment layer, using the computed hydrodynamical variables. In this work we consider the second case.

The contributions of this work to this issue are in Chapter 4. We propose an extension of the discretization approaches for multilayer shallow water models, aimed at making them more flexible and efficient for realistic applications to coastal flows. We propose two strategies, which can act simultaneously:

- Efficient semi-implicit discretizations have been applied for the first time to multilayer systems following [41, 40], allowing to achieve significant computational gains in subcritical regimes. Firstly, a time discretization based on the off-centered trapezoidal rule (or  $\theta$ -method). Secondly, a more accurate Implicit-Explicit Additive Runge Kutta method (IMEX-ARK2).
- A novel multilayer discretization, in which the number of vertical layers can vary over the computational domain. This removes one disadvantages of previous multilayer systems and the main disadvantage of  $\sigma$ -coordinates where it is mandatory to use the same number of layers independently of the fluid depth. The motivation is twofold: firstly, we want to adapt the vertical discretization to the features of the bathymetry, e.g. when the computational domain contains both, shallow and deep areas. Secondly, we want to get a finer vertical profile of velocity in a specific region of the domain, but not somewhere else. One could use a refined multilayer discretization in that region, simplifying it in the rest of the domain.

We show that, in the typical regimes in which the application of multilayer shallow water models is justified, the resulting discretization does not introduce significant errors and allows us to reduce substantially the computational cost in areas with complex bathymetry. In particular, we present an application to a sediment transport problem, showing a remarkable improvement with respect to standard discretization approaches.

---

The results of Chapter 4 has been published in [23], in collaboration with the supervisors of this thesis, and with Prof. Luca Bonaventura during and after a research stay in the “Laboratorio di Modellistica e Calcolo Scientifico (MOX)” (Politecnico di Milano, Milan, Italy).



# Background on multilayer approach

## 1.1 Introduction

Following Fernández-Nieto *et al.* [56], in this chapter we describe the procedure to obtain a multilayer system in the simple case of constant kinematic viscosity. We review its general derivation in the three-dimensional case. This multilayer approach constitutes the starting point for the different multilayer extensions to specific applications presented in the following chapters. On the other hand, proving that this 3D model satisfies an energy balance is still an open problem. Nevertheless, it can be demonstrated for the 2D case. Here, we propose an alternative 3D multilayer system satisfying a dissipative energy inequality.

The plan of this chapter is as follows. In Section 1.2 we present the initial system consisting of the 3D Navier-Stokes equations and the appropriate boundary conditions. We also give the local coordinates system that we consider for the derivation. In Section 1.3 we present the multilayer approach following [56], and we give a detailed account of the derivation of the 3D multilayer model. The final multilayer model is presented in Section 1.4. Finally, in Section 1.5 a different 3D multilayer model is proposed. This model satisfies a dissipative energy balance, which is an important property for a geophysical model to be physically relevant.

## 1.2 The initial system

The governing equations are established by the 3D incompressible Navier-Stokes equations. Start by considering a flow with velocity  $\mathbf{u} \in \mathbb{R}^3$  and constant density  $\rho \in \mathbb{R}$ . Then, the dynamics of the system is described by the following equations given by the conservation of momentum together with the incompressibility assumption:

$$\begin{cases} \nabla \cdot \mathbf{u} = 0, \\ \rho \partial_t \mathbf{u} + \rho \nabla \cdot (\mathbf{u} \otimes \mathbf{u}) - \nabla \cdot \boldsymbol{\sigma} = \rho \mathbf{g}, \end{cases} \quad (1.1)$$

where  $\mathbf{g}$  is acceleration due to the gravity. The total stress tensor is

$$\boldsymbol{\sigma} = -p\mathcal{I} + \boldsymbol{\tau}, \quad (1.2)$$

with  $p \in \mathbb{R}$  the pressure and  $\mathcal{I}$  is the 3D identity tensor.  $\boldsymbol{\tau}$  is the deviatoric stress tensor given by

$$\boldsymbol{\tau} = \eta D(\mathbf{u}),$$

with  $\eta = 2\eta_0$ , where  $\eta_0 \in \mathbb{R}$  (constant) denotes the kinematic viscosity and  $D(\mathbf{u})$  the strain rate tensor

$$D(\mathbf{u}) = \frac{1}{2}(\nabla \mathbf{u} + (\nabla \mathbf{u})').$$

where  $(\cdot)'$  denotes the transpose operator.

In order to conclude the govern system, we must set the boundary conditions. To do this, we consider the usual geometric setting, that is, the flow fills a spatial domain limited by a fixed topography at the bottom and by the free surface at the top. Since the domain is moved with the velocity of the material, we set the kinematic condition

$$N_t + \mathbf{u} \cdot \mathbf{n}^h = 0, \text{ at the free surface,} \quad (1.3)$$

with  $(N_t, \mathbf{n}^h)$  the time-space normal vector to the free surface. We also assume a free total stress condition

$$\boldsymbol{\sigma} \mathbf{n}^h = \mathbf{0}; \quad p = 0, \text{ at the free surface.} \quad (1.4)$$

At the bottom we consider the no-penetration condition

$$\mathbf{u} \cdot \mathbf{n}^b = 0, \text{ at the bottom,} \quad (1.5)$$

where  $\mathbf{n}^b$  is the downward unit normal vector to the bottom. We must also consider an appropriate boundary condition depending on the particular problem which we are interested in, giving a value for the tangential component of the tensor

$$\boldsymbol{\sigma} \mathbf{n} - ((\boldsymbol{\sigma} \mathbf{n}) \cdot \mathbf{n}) \mathbf{n}, \quad (1.6)$$

at the bottom and the free surface, for  $\mathbf{n} = \mathbf{n}^b, \mathbf{n}^h$  respectively.

## Local coordinates

Let us consider tilted coordinates, which are commonly used in the literature for ocean models and granular flows (see [28, 29, 53, 96, 64, 26, 27],...). Let  $\tilde{b}(x)$  be an inclined fixed plane of constant angle  $\theta$  with respect to the horizontal axis, we define the coordinates  $(\mathbf{x}, z) \in \Omega \times \mathbb{R}^+ \subset \mathbb{R}^3$ , where  $\mathbf{x} = (x, y) \in \Omega \subset \mathbb{R}^2$ . The  $\mathbf{x}$  and  $z$  axis are measured

along the inclined plane and along the normal direction respectively (see figure 1.1). In this reference frame the gravitational force is written as

$$\mathbf{g} = (-g \sin \theta, 0, -g \cos \theta)'$$

In addition, we set  $h(t, \mathbf{x})$  the thickness of the flow over an arbitrary bottom topography  $b(\mathbf{x})$ . Both are measured in the normal direction to the inclined plane  $\tilde{b}(\mathbf{x})$ . We consider the velocity  $\mathbf{u} \in \mathbb{R}^3$  with horizontal (downslope direction) and vertical (normal direction) components  $(\mathbf{u}^x, w)$ , with  $\mathbf{u}^x = (u, v)$ . We set  $\nabla = (\nabla_x, \partial_z)$  and  $\nabla_x = (\partial_x, \partial_y)$ , the usual differential operators in the space variables.

With these definitions we write:

$$\boldsymbol{\tau} = \begin{pmatrix} \tau^{xx} & \tau^{xz} \\ \tau^{xz} & \tau^{zz} \end{pmatrix} \quad \text{and} \quad D(\mathbf{u}) = \frac{1}{2} \begin{pmatrix} 2D^x(\mathbf{u}^x) & \partial_z \mathbf{u}^x + (\nabla_x w)' \\ (\partial_z \mathbf{u}^x)' + \nabla_x w & 2\partial_z w \end{pmatrix},$$

where  $D^x(\mathbf{u}^x) = \frac{\nabla_x \mathbf{u}^x + (\nabla_x \mathbf{u}^x)'}{2}$ . In this reference frame, system (1.1) can be developed as

$$\begin{cases} \nabla_x \mathbf{u}^x + \partial_z w = 0, \\ \rho(\partial_t \mathbf{u}^x + \mathbf{u}^x \nabla_x \mathbf{u}^x + w \partial_z \mathbf{u}^x) + \nabla_x p = -\rho \mathbf{g}_x \sin \theta + \nabla_x \cdot \boldsymbol{\tau}^{xx} + \partial_z \tau^{xz}, \\ \rho(\partial_t w + \mathbf{u}^x \cdot \nabla_x w + w \partial_z w) + \partial_z p = -\rho g \cos \theta + \nabla_x \cdot \boldsymbol{\tau}^{xz} + \partial_z \tau^{zz}, \end{cases} \quad (1.7)$$

where  $\mathbf{g}_x = (-g, 0)'$ . For the boundary conditions (1.3)-(1.6) we just take into account the definitions of the normal vectors. In particular, the time and space normal vectors to the free surface are respectively

$$N_t = \partial_t h; \quad \mathbf{n}^h = \frac{(\nabla_x(b+h), -1)}{\sqrt{1 + \|\nabla_x(b+h)\|^2}},$$

and the normal vector to the bottom reads:

$$\mathbf{n}^b = \frac{(\nabla_x b, -1)}{\sqrt{1 + \|\nabla_x b\|^2}}.$$

This system (1.1)-(1.7) is the starting point for the multilayer approach introduced in [56], which we apply in the next section.

## 1.3 A multilayer approach

In a few words, this method consists of subdividing the domain along the vertical direction in shallow layers, and applying the classic shallow water hypothesis (see e.g. [103, 61]) inside of each layer. Then, the downslope velocity is approximated by a piecewise constant function, i.e., it is constant in each layer, however these velocities can be different ones from others. In the next lines we introduce the required notation and describe in detail the derivation of the multilayer model.

### 1.3.1 Notation

We denote the domain  $\Omega_F(t)$  and its projection  $I_F(t)$  on the reference plane, for a positive  $t \in [0, T]$ , i.e.

$$I_F(t) = \left\{ \mathbf{x} \in \mathbb{R}^2; (\mathbf{x}, z) \in \Omega_F(t) \right\}.$$

The multilayer approach considers a vertical partition of the domain in  $N \in \mathbb{N}^*$  layers with preset thicknesses  $h_\alpha(t, \mathbf{x})$  for  $\alpha = 1, \dots, N$ , (see figure 1.1). Note that  $\sum_{\alpha=1}^N h_\alpha = h$ . In practice, we set a vertical partition of the domain as follows: we introduce the positive coefficients  $l_\alpha$  such that

$$h_\alpha = l_\alpha h \quad \text{for } \alpha = 1, \dots, N; \quad \sum_{\alpha=1}^N l_\alpha = 1.$$

Note that the thickness of each layer is automatically adapted to the movement of the free surface, since it depends on the total thickness of the mass flow. These layers are separated by  $N + 1$  interfaces  $\Gamma_{\alpha+1/2}(t)$ , which are described by the equations  $z = z_{\alpha+1/2}(t, \mathbf{x})$  for  $\alpha = 0, 1, \dots, N$ ,  $\mathbf{x} \in I_F(t)$ . We assume that these interfaces are smooth

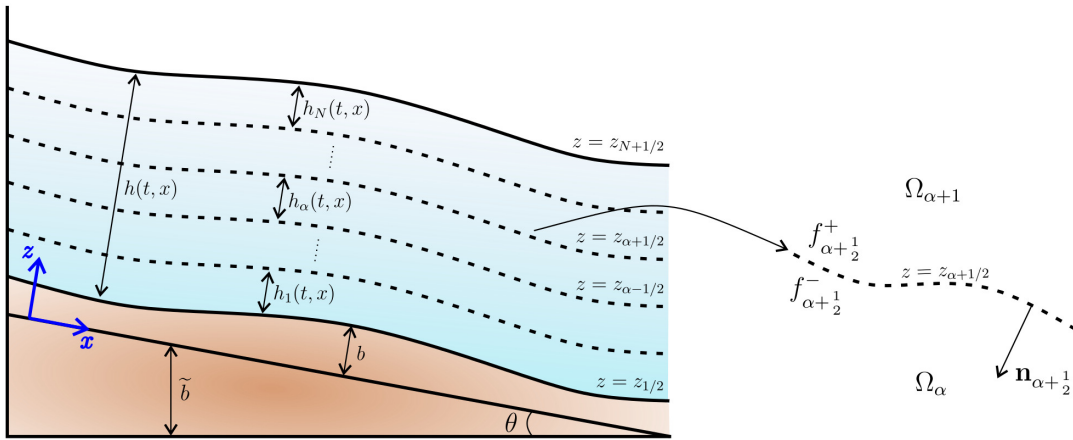


Figure 1.1: Sketch of the domain and its multilayer division.



enough. Observe that the fixed bottom and the free surface are respectively  $b = z_{\frac{1}{2}}$  and  $b + h = z_{N+\frac{1}{2}}$ , corresponding to the interfaces at the bottom  $\Gamma_{\frac{1}{2}}$  and at the free surface  $\Gamma_{N+\frac{1}{2}}$  respectively. Note that  $z_{\alpha+\frac{1}{2}} = b + \sum_{\beta=1}^{\alpha} h_{\beta}$  and  $h_{\alpha} = z_{\alpha+\frac{1}{2}} - z_{\alpha-\frac{1}{2}}$ , for  $\alpha = 1, \dots, N$ . The subdomain between  $\Gamma_{\alpha-\frac{1}{2}}$  and  $\Gamma_{\alpha+\frac{1}{2}}$  is denoted by  $\Omega_{\alpha}(t)$ , for a positive  $t \in [0, T]$ ,

$$\Omega_{\alpha}(t) = \left\{ (\mathbf{x}, z); \mathbf{x} \in I_F(t) \text{ and } z_{\alpha-\frac{1}{2}} < z < z_{\alpha+\frac{1}{2}} \right\}.$$

We need to introduce a specific notation about the approximations of the variables on the interfaces (see figure 1.1). For a function  $f$  and for  $\alpha = 0, 1, \dots, N$ , we set

$$f_{\alpha+\frac{1}{2}}^{-} := (f|_{\Omega_{\alpha}(t)})|_{\Gamma_{\alpha+\frac{1}{2}}(t)} \quad \text{and} \quad f_{\alpha+\frac{1}{2}}^{+} := (f|_{\Omega_{\alpha+1}(t)})|_{\Gamma_{\alpha+\frac{1}{2}}(t)}. \quad (1.8)$$

Note that if the function  $f$  is continuous,

$$f_{\alpha+\frac{1}{2}} := f|_{\Gamma_{\alpha+\frac{1}{2}}(t)} = f_{\alpha+\frac{1}{2}}^{+} = f_{\alpha+\frac{1}{2}}^{-}.$$

In addition, for a given time  $t$ , we denote

$$\mathbf{n}_{t, \alpha+\frac{1}{2}} = \frac{\left( \partial_t z_{\alpha+\frac{1}{2}}, \nabla_{\mathbf{x}} z_{\alpha+\frac{1}{2}}, -1 \right)'}{\sqrt{1 + \|\nabla_{\mathbf{x}} z_{\alpha+\frac{1}{2}}\|^2 + \left( \partial_t z_{\alpha+\frac{1}{2}} \right)^2}} \quad \text{and} \quad \mathbf{n}_{\alpha+\frac{1}{2}} = \frac{\left( \nabla_{\mathbf{x}} z_{\alpha+\frac{1}{2}}, -1 \right)'}{\sqrt{1 + \|\nabla_{\mathbf{x}} z_{\alpha+\frac{1}{2}}\|^2}},$$

the space-time unit normal vector and the space unit normal vector to the interface  $\Gamma_{\alpha+\frac{1}{2}}(t)$  outward to the layer  $\Omega_{\alpha+1}(t)$  for  $\alpha = 0, \dots, N$ .

### 1.3.2 Weak solution with discontinuities

We are looking for a particular weak solution  $(\mathbf{u}, p, \rho)$  of (1.1). This solution must meet the following conditions:

- (i)  $(\mathbf{u}, p, \rho)$  is a standard weak solution of (1.1) in each layer  $\Omega_{\alpha}(t)$ ,
- (ii)  $(\mathbf{u}, p, \rho)$  satisfies the normal flux jump condition for mass and momentum at the interfaces  $\Gamma_{\alpha+\frac{1}{2}}(t)$ , namely:

$$[(\rho; \rho \mathbf{u})]_{\alpha+\frac{1}{2}} \mathbf{n}_{t, \alpha+\frac{1}{2}} = 0; \quad (1.9)$$

$$[(\rho \mathbf{u}; \rho \mathbf{u} \otimes \mathbf{u} - \boldsymbol{\sigma})]_{\alpha+\frac{1}{2}} \mathbf{n}_{t, \alpha+\frac{1}{2}} = 0, \quad (1.10)$$

where  $[(a; b)]_{\alpha+\frac{1}{2}}$  denotes the jump of  $(a; b)$  across the interface  $\Gamma_{\alpha+\frac{1}{2}}(t)$ .

Some assumptions are made on the solution  $(\mathbf{u}, p, \rho)$  for each layer in the spirit of the multilayer approach. Firstly, a particular family of velocity functions is considered, by assuming that the thickness of each layer is small enough to make the horizontal

velocities independent of the vertical variable  $z$  (usual shallow water domain hypothesis). As a consequence, thanks to the incompressibility condition in each layer, we obtain that the vertical velocities are linear in  $z$  and may be discontinuous. We denote the velocity in each layer as

$$\mathbf{u}|_{\Omega_\alpha(t)} := \mathbf{u}_\alpha := (\mathbf{u}_\alpha^x, w_\alpha)', \quad (1.11)$$

where  $\mathbf{u}_\alpha^x$  and  $w_\alpha$  are the horizontal and vertical velocities, respectively. Furthermore,  $\mathbf{u}_\alpha^x$  is the averaged velocity on layer  $\alpha$

$$\mathbf{u}_\alpha^x(\mathbf{x}) := \frac{1}{h_\alpha} \int_{z_{\alpha-\frac{1}{2}}}^{z_{\alpha+\frac{1}{2}}} \mathbf{u}_\alpha(\mathbf{x}, z) dz. \quad (1.12)$$

Therefore,

$$\partial_z \mathbf{u}_\alpha^x = 0; \quad \partial_z w_\alpha = d_\alpha(t, \mathbf{x}) \quad (1.13)$$

for some smooth function  $d_\alpha(t, \mathbf{x})$ .

Secondly, a hydrostatic pressure is assumed as in [56]. This hypothesis leads to

$$\partial_z p_\alpha = -\rho g \cos \theta,$$

and by the continuity of the dynamic pressure we deduce that

$$p_\alpha(z) = \rho g \cos \theta (b + h - z). \quad (1.14)$$

### Mass conservation across the interfaces and normal velocity

The mass conservation jump condition (1.9) gives us the definition of the normal mass flux at the interface  $\Gamma_{\alpha+\frac{1}{2}}(t)$ , denoted by  $G_{\alpha+\frac{1}{2}} := G_{\alpha+\frac{1}{2}}^+ = G_{\alpha+\frac{1}{2}}^-$  for:

$$G_{\alpha+\frac{1}{2}}^\pm = \partial_t z_{\alpha+\frac{1}{2}} + \mathbf{u}_{\alpha+\frac{1}{2}}^{x,\pm} \cdot \nabla_{\mathbf{x}} z_{\alpha+\frac{1}{2}} - w_{\alpha+\frac{1}{2}}^\pm, \quad (1.15)$$

where  $\mathbf{u}_{\alpha+\frac{1}{2}}^{x,\pm}$  is defined using (1.8) and (1.13) as

$$\mathbf{u}_{\alpha+\frac{1}{2}}^{x,-} = \mathbf{u}_{\alpha-\frac{1}{2}}^{x,+} = \mathbf{u}_\alpha^x.$$

By integrating the incompressibility equation and using this mass conservation condition, we get the definition of the vertical velocity  $w_\alpha$  for  $\mathbf{u}_\alpha^x$  a solution of (1.1) (see [56] for details). Thus, if we consider that there is no mass transference with the bottom (i.e.  $G_{1/2} = 0$ ), we obtain

$$w_{\frac{1}{2}}^+ = \mathbf{u}_1^x \cdot \nabla_{\mathbf{x}} b + \partial_t b,$$

and for  $\alpha = 1, \dots, N$  and  $z \in (z_{\alpha-\frac{1}{2}}, z_{\alpha+\frac{1}{2}})$ ,

$$\left\{ \begin{array}{l} w_\alpha(t, \mathbf{x}, z) = w_{\alpha-\frac{1}{2}}^+(t, \mathbf{x}) - (z - z_{\alpha-\frac{1}{2}}) \nabla_{\mathbf{x}} \cdot \mathbf{u}_\alpha^x(t, \mathbf{x}), \\ w_{\alpha+\frac{1}{2}}^+ = (\mathbf{u}_{\alpha+1}^x - \mathbf{u}_\alpha^x) \cdot \nabla_{\mathbf{x}} z_{\alpha+\frac{1}{2}} + w_{\alpha+\frac{1}{2}}^-; \end{array} \right. \quad (1.16)$$

where

$$w_{\alpha+\frac{1}{2}}^- = w_{\alpha-\frac{1}{2}}^+ - h_\alpha \nabla_{\mathbf{x}} \cdot \mathbf{u}_\alpha. \quad (1.17)$$

### Momentum conservation across the interfaces

The momentum conservation jump conditions (1.10) can be easily written as

$$[\boldsymbol{\sigma}]_{\alpha+\frac{1}{2}} \left( \nabla_{\mathbf{x}} z_{\alpha+\frac{1}{2}}, -1 \right) = [(\rho \mathbf{u}; \rho \mathbf{u} \otimes \mathbf{u})]_{\alpha+\frac{1}{2}} \left( \partial_t z_{\alpha+\frac{1}{2}}, \nabla_{\mathbf{x}} z_{\alpha+\frac{1}{2}}, -1 \right), \quad (1.18)$$

and using the definition of the normal mass flux  $G_{\alpha+\frac{1}{2}}$ , it follows that

$$[(\rho \mathbf{u}; \rho \mathbf{u} \otimes \mathbf{u})]_{\alpha+\frac{1}{2}} \left( \partial_t z_{\alpha+\frac{1}{2}}, \nabla_{\mathbf{x}} z_{\alpha+\frac{1}{2}}, -1 \right) = \rho G_{\alpha+\frac{1}{2}} [\mathbf{u}]_{\alpha+\frac{1}{2}}.$$

Therefore, the momentum jump conditions become:

$$[\boldsymbol{\sigma}]_{\alpha+\frac{1}{2}} \mathbf{n}_{\alpha+\frac{1}{2}} = \frac{\rho G_{\alpha+\frac{1}{2}}}{\sqrt{1 + \|\nabla_{\mathbf{x}} z_{\alpha+\frac{1}{2}}\|^2}} [\mathbf{u}]_{\alpha+\frac{1}{2}},$$

where, for  $\alpha = 1, \dots, N-1$ , the total stress tensor is

$$\boldsymbol{\sigma}_{\alpha+\frac{1}{2}}^\pm = -p_{\alpha+\frac{1}{2}} \mathcal{I} + \boldsymbol{\tau}_{\varepsilon, \alpha+\frac{1}{2}}^\pm,$$

with  $p_{\alpha+\frac{1}{2}} = p_{\alpha+\frac{1}{2}}^+ = p_{\alpha+\frac{1}{2}}^-$  and  $\boldsymbol{\tau}_{\alpha+\frac{1}{2}}^\pm$  approximations of  $p_\alpha$  and  $\boldsymbol{\tau}_\alpha$  at  $\Gamma_{\alpha+\frac{1}{2}}$ . The jump on the total stress tensor  $\boldsymbol{\sigma}$  is reduced to the jump in the deviatoric stress tensor  $\boldsymbol{\tau}$  thanks to the continuity of the pressure at the interface  $\Gamma_{\alpha+\frac{1}{2}}$ . Then we obtain that

$$\left( \boldsymbol{\tau}_{\alpha+\frac{1}{2}}^+ - \boldsymbol{\tau}_{\alpha+\frac{1}{2}}^- \right) \mathbf{n}_{\alpha+\frac{1}{2}} = \frac{\rho G_{\alpha+\frac{1}{2}}}{\sqrt{1 + \|\nabla_{\mathbf{x}} z_{\alpha+\frac{1}{2}}\|^2}} [\mathbf{u}]_{\alpha+\frac{1}{2}}.$$

Finally, by introducing the consistency condition

$$\tilde{\boldsymbol{\tau}}_{\alpha+\frac{1}{2}} = \frac{1}{2} \left( \boldsymbol{\tau}_{\alpha+\frac{1}{2}}^+ + \boldsymbol{\tau}_{\alpha+\frac{1}{2}}^- \right),$$

the momentum jump condition gives

$$\boldsymbol{\tau}_{\alpha+\frac{1}{2}}^\pm \mathbf{n}_{\alpha+\frac{1}{2}} = \tilde{\boldsymbol{\tau}}_{\alpha+\frac{1}{2}} \mathbf{n}_{\alpha+\frac{1}{2}} \pm \frac{1}{2} \frac{\rho G_{\alpha+\frac{1}{2}}}{\sqrt{1 + \|\nabla_{\mathbf{x}} z_{\alpha+\frac{1}{2}}\|^2}} [\mathbf{u}]_{\alpha+\frac{1}{2}}, \quad (1.19)$$

where  $\tilde{\boldsymbol{\tau}}_{\alpha+\frac{1}{2}}$  is an approximation of  $2\eta_0 D(\mathbf{u}_\alpha)_{\alpha+\frac{1}{2}}$ , defined by

$$\tilde{D}_{\alpha+\frac{1}{2}} = \frac{1}{2} \begin{pmatrix} 2D_{\mathbf{x}} \left( \frac{\mathbf{u}_{\alpha+\frac{1}{2}}^{x,+} + \mathbf{u}_{\alpha+\frac{1}{2}}^{x,-}}{2} \right) & \tilde{D}_{\alpha+\frac{1}{2}, \mathbf{x}z} \\ \left( \tilde{D}_{\alpha+\frac{1}{2}, \mathbf{x}z} \right)' & 2\mathcal{U}_{\mathcal{Z}, \alpha+\frac{1}{2}}^V \end{pmatrix}. \quad (1.20)$$

In this equation,

$$\tilde{D}_{\alpha+\frac{1}{2},xz} = \nabla_x \left( \frac{w_{\alpha+\frac{1}{2}}^+ + w_{\alpha+\frac{1}{2}}^-}{2} \right)' + \mathcal{U}_{\mathcal{Z},\alpha+\frac{1}{2}}^H,$$

and  $(\mathcal{U}_{\mathcal{Z},\alpha+\frac{1}{2}}^H, \mathcal{U}_{\mathcal{Z},\alpha+\frac{1}{2}}^V)$  is defined to approximate the derivatives in  $z$ . We use a mixed formulation because of the possible vertical discontinuous profile. Thus, the auxiliary unknown  $\mathcal{U}_{\mathcal{Z}}$  satisfies

$$\mathcal{U}_{\mathcal{Z}} - \partial_z \mathbf{u} = 0, \quad \text{with } \mathcal{U}_{\mathcal{Z}} = (\mathcal{U}_{\mathcal{Z}}^H, \mathcal{U}_{\mathcal{Z}}^V). \quad (1.21)$$

In order to approximate  $\mathcal{U}_{\mathcal{Z}}$ , we approximate  $\mathbf{u}$  by  $\tilde{\mathbf{u}}$ , a  $\mathbb{P}_1(z)$  interpolation such that  $\tilde{\mathbf{u}}|_{z=\frac{1}{2}(z_{\alpha-\frac{1}{2}}+z_{\alpha+\frac{1}{2}})} = \mathbf{u}_\alpha$ . Then  $\mathcal{U}_{\mathcal{Z},\alpha+\frac{1}{2}} = (\mathcal{U}_{\mathcal{Z},\alpha+\frac{1}{2}}^H, \mathcal{U}_{\mathcal{Z},\alpha+\frac{1}{2}}^V)$  is an approximation of  $\mathcal{U}_{\mathcal{Z}}(\tilde{\mathbf{u}})$  at  $\Gamma_{\alpha+\frac{1}{2}}$ . In order to define  $\mathcal{U}_{\mathcal{Z},\alpha+\frac{1}{2}}^H$ , we focus on the definition of the normal derivative on the interface  $\Gamma_{\alpha+\frac{1}{2}}$ , that is,

$$\partial_{(-n_{\alpha+\frac{1}{2}})} \mathbf{u} = -\nabla \mathbf{u} \mathbf{n}_{\alpha+\frac{1}{2}} = \frac{-1}{\sqrt{1 + \|\nabla_x z_{\alpha+\frac{1}{2}}\|^2}} \left( \nabla_x \mathbf{u}_{\alpha+\frac{1}{2}}^x \nabla_x z_{\alpha+\frac{1}{2}} - \mathcal{U}_{\mathcal{Z},\alpha+\frac{1}{2}}^H \right),$$

where the sign minus is taken because we need the normal vector to the interface  $\Gamma_{\alpha+\frac{1}{2}}(t)$  outward to the layer  $\Omega_\alpha(t)$ . We propose the approximation

$$\partial_{(-n_{\alpha+\frac{1}{2}})} \mathbf{u} = \frac{\mathbf{u}_{\alpha+1}^x - \mathbf{u}_\alpha^x}{h_{\alpha+\frac{1}{2}}}, \quad \text{for } \alpha = 1, \dots, N-1,$$

with  $h_{\alpha+\frac{1}{2}}$  being the distance between the midpoints of layers  $\alpha$  and  $\alpha+1$ . Then, we obtain the approximation

$$\mathcal{U}_{\mathcal{Z},\alpha+\frac{1}{2}}^H = \frac{\mathbf{u}_{\alpha+1}^x - \mathbf{u}_\alpha^x}{h_{\alpha+\frac{1}{2}}} \sqrt{1 + \|\nabla_x z_{\alpha+\frac{1}{2}}\|^2} + \nabla_x \left( \frac{\mathbf{u}_\alpha^x + \mathbf{u}_{\alpha+1}^x}{2} \right) \nabla_x z_{\alpha+\frac{1}{2}}, \quad (1.22)$$

for  $\alpha = 1, \dots, N-1$ , where we have considered  $\mathbf{u}_{\alpha+\frac{1}{2}}^x = \frac{\mathbf{u}_\alpha^x + \mathbf{u}_{\alpha+1}^x}{2}$ . For the particular case of the bottom and the free surface,  $\mathcal{U}_{\mathcal{Z},\frac{1}{2}}^H$  and  $\mathcal{U}_{\mathcal{Z},N+\frac{1}{2}}^H$  must be defined by the boundary condition (1.6).

### 1.3.3 Derivation of the final model: a particular weak solution

In this subsection, we review the derivation of the final multilayer model obtained in [56] by looking for a particular weak solution of the system (1.1). Firstly, these equations are multiplied by particular test functions and secondly we integrate this system in the domain  $\Omega_\alpha(t)$ .

Let us consider the weak formulation of (1.1) in  $\Omega_\alpha(t)$  for  $\alpha = 1, \dots, N$ . We assume that the velocity  $\mathbf{u}$ , the pressure  $p$  and the density  $\rho$  are smooth in each  $\Omega_\alpha(t)$  but may be discontinuous across the interfaces  $\Gamma_{\alpha+1/2}$  for  $\alpha = 1, \dots, N-1$ , as stated previously.

Assuming that  $\mathbf{u}_\alpha \in L^2(0, T; H^1(\Omega_\alpha(t))^3)$ ,  $\partial_t \mathbf{u}_\alpha \in L^2(0, T; L^2(\Omega_\alpha(t))^3)$  and  $p_\alpha \in L^2(0, T; L^2(\Omega_\alpha(t)))$ , then a weak solution in  $\Omega_\alpha(t)$  should satisfy

$$\left\{ \begin{array}{l} 0 = \int_{\Omega_\alpha(t)} (\nabla \cdot \mathbf{u}_\alpha) \varphi \, d\Omega, \\ \int_{\Omega_\alpha(t)} \rho \mathbf{g} \cdot \mathbf{v} \, d\Omega = \int_{\Omega_\alpha(t)} \rho \partial_t \mathbf{u}_\alpha \cdot \mathbf{v} \, d\Omega + \int_{\Omega_\alpha(t)} \rho (\mathbf{u}_\alpha \cdot \nabla \mathbf{u}_\alpha) \cdot \mathbf{v} \, d\Omega + \\ + \int_{\Omega_\alpha(t)} (\nabla \cdot (p_\alpha \mathcal{I})) \cdot \mathbf{v} \, d\Omega - \int_{\Omega_\alpha(t)} (\nabla \cdot \boldsymbol{\tau}_\alpha) \cdot \mathbf{v} \, d\Omega, \end{array} \right. \quad (1.23)$$

for all  $\varphi \in L^2(\Omega_\alpha(t))$  and for all  $\mathbf{v} \in H^1(\Omega_\alpha(t))^3$ .

We consider unknowns, velocities and pressures, that satisfy (1.13)-(1.14) and the system (1.23) for test functions such that

$$\partial_z \varphi = 0,$$

and

$$\mathbf{v}(t, \mathbf{x}, z) = \left( \mathbf{v}^x(t, \mathbf{x}), (z - b) \mathbf{V}(t, \mathbf{x}) \right)', \quad \mathbf{v}|_{\partial I_F(t)} = 0, \quad (1.24)$$

where  $\mathbf{v}^x(t, \mathbf{x})$  and  $\mathbf{V}(t, \mathbf{x})$  are smooth functions that do not depend on  $z$ .

We will now develop (1.23) in order to obtain the mass and momentum conservation equations that satisfy the weak solution for this family of test functions for each layer.

### Mass conservation

Focusing on the mass equation, we use the definition of  $\mathbf{u}_\alpha^x$  (1.12) together with the Leibnitz's rule to rewrite it as

$$\int_{I_F(t)} \varphi(t, \mathbf{x}) \left( \nabla_{\mathbf{x}} \cdot (h_\alpha \mathbf{u}_\alpha^x) - \mathbf{u}_\alpha^x \cdot \nabla_{\mathbf{x}} z_{\alpha+\frac{1}{2}} + w_{\alpha+\frac{1}{2}}^- + \mathbf{u}_\alpha^x \cdot \nabla_{\mathbf{x}} z_{\alpha-\frac{1}{2}} - w_{\alpha-\frac{1}{2}}^+ \right) d\mathbf{x} = 0.$$

Taking into account the normal mass flux (1.15) we get

$$\int_{I_F(t)} \varphi(t, \mathbf{x}) \left( \partial_t h_\alpha + \nabla_{\mathbf{x}} \cdot (h_\alpha \mathbf{u}_\alpha^x) - G_{\alpha+\frac{1}{2}} + G_{\alpha-\frac{1}{2}} \right) d\mathbf{x} = 0,$$

for all  $\varphi(t, \cdot) \in L^2(I_F(t))$ . Therefore, the mass conservation law for each layer is

$$\partial_t h_\alpha + \nabla_{\mathbf{x}} \cdot (h_\alpha \mathbf{u}_\alpha^x) = G_{\alpha+\frac{1}{2}} - G_{\alpha-\frac{1}{2}}, \quad \alpha = 1, \dots, N, \quad (1.25)$$

where  $G_{N+1/2}$  and  $G_{1/2}$  stand for the mass exchange at the free surface and the bottom level respectively and both should be given data.

### Momentum conservation

Let  $\mathbf{v} \in H^1(\Omega_\alpha)^3$  be a test function satisfying (1.24). We develop the momentum equation in (1.23) by integrating with respect to the variable  $z$  and by identifying the horizontal and vertical components of the vector test function  $\mathbf{v}$ . In addition, taking into account the hydrostatic pressure framework, we can leave out the equation corresponding to the vertical component. This is equivalent to considering the vector test function where the vertical component vanishes, i.e.  $\mathbf{v} = (\mathbf{v}^x(t, \mathbf{x}), 0)$ .

Let us remind the reader two identities which are used to rewrite the momentum equations:

$$\begin{aligned} \int_{\Omega_\alpha(t)} \nabla \cdot (p_\alpha \mathcal{I}) \cdot \mathbf{v} \, d\Omega &= - \int_{\Omega_\alpha(t)} (p_\alpha \mathcal{I}) : \nabla \mathbf{v} \, d\Omega - \\ &- \int_{\Gamma_{\alpha+\frac{1}{2}}(t)} \left( p_{\alpha+\frac{1}{2}} \mathcal{I} \mathbf{v} \right) \cdot \mathbf{n}_{\alpha+\frac{1}{2}} \, d\Gamma + \int_{\Gamma_{\alpha-\frac{1}{2}}(t)} \left( p_{\alpha-\frac{1}{2}} \mathcal{I} \mathbf{v} \right) \cdot \mathbf{n}_{\alpha-\frac{1}{2}} \, d\Gamma ; \end{aligned}$$

and

$$\begin{aligned} \int_{\Omega_\alpha(t)} (\nabla \cdot \boldsymbol{\tau}_\alpha) \cdot \mathbf{v} \, d\Omega &= - \int_{\Omega_\alpha(t)} \boldsymbol{\tau}_\alpha : \nabla \mathbf{v} \, d\Omega - \\ &- \int_{\Gamma_{\alpha+\frac{1}{2}}(t)} \left( \boldsymbol{\tau}_{\alpha+\frac{1}{2}}^- \mathbf{v} \right) \cdot \mathbf{n}_{\alpha+\frac{1}{2}} \, d\Gamma + \int_{\Gamma_{\alpha-\frac{1}{2}}(t)} \left( \boldsymbol{\tau}_{\alpha-\frac{1}{2}}^+ \mathbf{v} \right) \cdot \mathbf{n}_{\alpha-\frac{1}{2}} \, d\Gamma . \end{aligned}$$

Therefore, the horizontal momentum equation reads, for a weak solution  $\mathbf{u}$ , test functions  $\mathbf{v} = (\mathbf{v}^x(t, \mathbf{x}), 0)$ , and for all  $\alpha = 1, \dots, N$ :

$$\begin{aligned} \int_{\Omega_\alpha(t)} \rho \mathbf{g} \cdot (\mathbf{v}^x, 0) \, d\Omega &= \int_{\Omega_\alpha(t)} \rho \partial_t (\mathbf{u}_\alpha^x, w_\alpha) \cdot (\mathbf{v}^x, 0) \, d\Omega + \\ &+ \int_{\Omega_\alpha(t)} \rho \left( (\mathbf{u}_\alpha^x, w_\alpha) \cdot \nabla (\mathbf{u}_\alpha^x, w_\alpha) \right) \cdot (\mathbf{v}^x, 0) \, d\Omega - \\ &- \int_{\Omega_\alpha(t)} p_\alpha : \nabla (\mathbf{v}^x, 0) \, d\Omega + \int_{\Omega_\alpha(t)} \boldsymbol{\tau}_\alpha : \nabla (\mathbf{v}^x, 0) \, d\Omega + \\ &+ \int_{\Gamma_{\alpha+\frac{1}{2}}(t)} \left( \left( -p_{\alpha+\frac{1}{2}} \mathcal{I} + \boldsymbol{\tau}_{\alpha+\frac{1}{2}}^- \right) \mathbf{n}_{\alpha+\frac{1}{2}} \right) \cdot (\mathbf{v}^x, 0) \, d\Gamma - \\ &- \int_{\Gamma_{\alpha-\frac{1}{2}}(t)} \left( \left( -p_{\alpha-\frac{1}{2}} \mathcal{I} + \boldsymbol{\tau}_{\alpha-\frac{1}{2}}^+ \right) \mathbf{n}_{\alpha-\frac{1}{2}} \right) \cdot (\mathbf{v}^x, 0) \, d\Gamma . \end{aligned} \tag{1.26}$$

Each term in previous equation must be developed, taking into account that

$$\partial_z \mathbf{u}_\alpha^x = \partial_z \mathbf{v}^x = \mathbf{v}|_{\partial I_F(t)} = \mathbf{0}.$$

We develop only those terms that are not trivial in (1.26). This is the case of the pressure term, which we write as

$$\begin{aligned} - \int_{\Omega_\alpha(t)} p_\alpha \nabla_{\mathbf{x}} \cdot \mathbf{v}^{\mathbf{x}} d\Omega &= - \int_{I_F(t)} \left( \int_{z_{\alpha-1/2}}^{z_{\alpha+1/2}} p_\alpha dz \right) \nabla_{\mathbf{x}} \cdot \mathbf{v}^{\mathbf{x}} d\mathbf{x} = \\ &= \int_{I_F(t)} \nabla_{\mathbf{x}} \left( \int_{z_{\alpha-1/2}}^{z_{\alpha+1/2}} p_\alpha dz \right) \cdot \mathbf{v}^{\mathbf{x}} d\mathbf{x} - \int_{\partial I_F(t)} \left( \int_{z_{\alpha-1/2}}^{z_{\alpha+1/2}} p_\alpha dz \right) \mathbf{v}^{\mathbf{x}} \cdot \mathbf{n} d\Gamma. \end{aligned}$$

Moreover, thanks to the Leibniz's rule and using that  $\mathbf{v}$  vanishes over the boundary of  $I_F(t)$ , this leads to

$$- \int_{\Omega_\alpha(t)} p_\alpha \nabla_{\mathbf{x}} \cdot \mathbf{v}^{\mathbf{x}} d\Omega = \int_{I_F(t)} \left( \int_{z_{\alpha-1/2}}^{z_{\alpha+1/2}} \nabla_{\mathbf{x}} p_\alpha dz + p_\alpha \frac{dz}{d\mathbf{x}} \Big|_{z_{\alpha-1/2}}^{z_{\alpha+1/2}} \right) \cdot \mathbf{v}^{\mathbf{x}} d\mathbf{x}.$$

We now write the definition of the pressure (1.14), and previous integral does not depend on  $z$ , then it is rewritten as

$$\begin{aligned} &\int_{I_F(t)} \left( \rho g \cos \theta h_\alpha \nabla_{\mathbf{x}} (b+h) + p_{\alpha+1/2} \nabla_{\mathbf{x}} z_{\alpha+1/2} - p_{\alpha-1/2} \nabla_{\mathbf{x}} z_{\alpha-1/2} \right) \cdot \mathbf{v}^{\mathbf{x}} d\mathbf{x} = \\ &= \int_{I_F(t)} \rho g \cos \theta h_\alpha \nabla_{\mathbf{x}} (b+h) \cdot \mathbf{v}^{\mathbf{x}} d\mathbf{x} + \\ &\quad + \int_{I_F(t)} p_{\alpha+1/2} \mathbf{n}_{\alpha+1/2} \cdot (\mathbf{v}^{\mathbf{x}}, 0) \sqrt{1 + |\nabla_{\mathbf{x}} z_{\alpha+1/2}|^2} d\mathbf{x} - \\ &\quad - \int_{I_F(t)} p_{\alpha-1/2} \mathbf{n}_{\alpha-1/2} \cdot (\mathbf{v}^{\mathbf{x}}, 0) \sqrt{1 + |\nabla_{\mathbf{x}} z_{\alpha-1/2}|^2} d\mathbf{x}. \end{aligned}$$

For the horizontal diffusion term, we have

$$\begin{aligned} \int_{\Omega_\alpha(t)} \boldsymbol{\tau}_\alpha^{\mathbf{x}\mathbf{x}} : \nabla_{\mathbf{x}} \mathbf{v}^{\mathbf{x}} d\Omega &= \int_{I_F(t)} \left( \int_{z_{\alpha-1/2}}^{z_{\alpha+1/2}} \boldsymbol{\tau}_\alpha^{\mathbf{x}\mathbf{x}} dz \right) : \nabla_{\mathbf{x}} \mathbf{v}^{\mathbf{x}} d\mathbf{x} = \\ &= - \int_{I_F(t)} \nabla_{\mathbf{x}} \cdot \left( \int_{z_{\alpha-1/2}}^{z_{\alpha+1/2}} \boldsymbol{\tau}_\alpha^{\mathbf{x}\mathbf{x}} dz \right) \cdot \mathbf{v}^{\mathbf{x}} d\mathbf{x} + \int_{\partial I_F(t)} \left( \int_{z_{\alpha-1/2}}^{z_{\alpha+1/2}} \boldsymbol{\tau}_\alpha^{\mathbf{x}\mathbf{x}} dz \right) \mathbf{v}^{\mathbf{x}} \cdot \mathbf{n} d\Gamma. \end{aligned}$$

Once more, the term over the boundary of  $I_F(t)$  vanishes since  $\mathbf{v}|_{\partial I_F(t)} = \mathbf{0}$ . Then we get

$$\int_{\Omega_\alpha(t)} \boldsymbol{\tau}_\alpha^{\mathbf{x}\mathbf{x}} : \nabla_{\mathbf{x}} \mathbf{v}^{\mathbf{x}} d\Omega = - \int_{I_F(t)} \nabla_{\mathbf{x}} \cdot \left( \eta_0 h_\alpha (\nabla_{\mathbf{x}} \mathbf{u}_\alpha^{\mathbf{x}} + (\nabla_{\mathbf{x}} \mathbf{u}_\alpha^{\mathbf{x}})') \right) \cdot \mathbf{v}^{\mathbf{x}} d\mathbf{x}.$$

On the other hand, the term that appears on the interfaces is written

$$\begin{aligned} & \int_{\Gamma_{\alpha+\frac{1}{2}}(t)} \left( \left( -p_{\alpha+\frac{1}{2}} \mathcal{I} + \boldsymbol{\tau}_{\alpha+\frac{1}{2}}^- \right) \mathbf{n}_{\alpha+\frac{1}{2}} \right) \cdot (\mathbf{v}^x, 0) \, d\Gamma = \\ & = \int_{I_F(t)} \left( \left( -p_{\alpha+\frac{1}{2}} \mathcal{I} + \boldsymbol{\tau}_{\alpha+\frac{1}{2}}^- \right) \mathbf{n}_{\alpha+\frac{1}{2}} \right) \cdot (\mathbf{v}^x, 0) \sqrt{1 + \left| \nabla_{\mathbf{x}} z_{\alpha+\frac{1}{2}} \right|^2} \, d\mathbf{x}. \end{aligned}$$

Moreover,

$$\left( \boldsymbol{\tau}_{\alpha+\frac{1}{2}}^- \mathbf{n}_{\alpha+\frac{1}{2}} \right) \cdot (\mathbf{v}^x, 0) \sqrt{1 + \left| \nabla_{\mathbf{x}} z_{\alpha+\frac{1}{2}} \right|^2} = \left( \boldsymbol{\tau}_{\alpha+\frac{1}{2}}^{xx,-} \nabla_{\mathbf{x}} z_{\alpha+\frac{1}{2}} - \boldsymbol{\tau}_{\alpha+\frac{1}{2}}^{xz,-} \right) \cdot \mathbf{v}^x.$$

Introducing these calculations into (1.26) and noticing that  $\mathbf{g} = (-g \sin \theta, 0, -g \cos \theta)'$ , we obtain for all  $\mathbf{v}^x \in H^1(\Omega(t))^2$

$$\begin{aligned} & \int_{I_F(t)} \left[ \rho h_{\alpha} \partial_t \mathbf{u}_{\alpha}^x + \rho h_{\alpha} \mathbf{u}_{\alpha}^x \cdot \nabla_{\mathbf{x}} \mathbf{u}_{\alpha}^x + \rho g \cos \theta h_{\alpha} \nabla_{\mathbf{x}} (b + h) + \right. \\ & \quad \left. + \rho g \cos \theta h_{\alpha} \tan \theta - \nabla_{\mathbf{x}} \cdot \left( \eta_0 h_{\alpha} (\nabla_{\mathbf{x}} \mathbf{u}_{\alpha}^x + (\nabla_{\mathbf{x}} \mathbf{u}_{\alpha}^x)') \right) + \right. \\ & \quad \left. + \left( \boldsymbol{\tau}_{\alpha+\frac{1}{2}}^{xx,-} \nabla_{\mathbf{x}} z_{\alpha+\frac{1}{2}} - \boldsymbol{\tau}_{\alpha+\frac{1}{2}}^{xz,-} \right) - \left( \boldsymbol{\tau}_{\alpha-\frac{1}{2}}^{xx,+} \nabla_{\mathbf{x}} z_{\alpha-\frac{1}{2}} - \boldsymbol{\tau}_{\alpha-\frac{1}{2}}^{xz,+} \right) \right] \cdot \mathbf{v}^x \, dx = 0. \end{aligned}$$

As result, this leads, for each layer  $\alpha = 1, \dots, N$ , to the momentum equation

$$\begin{aligned} & \rho h_{\alpha} \partial_t \mathbf{u}_{\alpha}^x + \rho h_{\alpha} \mathbf{u}_{\alpha}^x \cdot \nabla_{\mathbf{x}} \mathbf{u}_{\alpha}^x + \rho g \cos \theta h_{\alpha} \nabla_{\mathbf{x}} (\tilde{b} + b + h) - \\ & \quad - \nabla_{\mathbf{x}} \cdot \left( \eta_0 h_{\alpha} (\nabla_{\mathbf{x}} \mathbf{u}_{\alpha}^x + (\nabla_{\mathbf{x}} \mathbf{u}_{\alpha}^x)') \right) + \\ & \quad + \left( \boldsymbol{\tau}_{\alpha+\frac{1}{2}}^{xx,-} \nabla_{\mathbf{x}} z_{\alpha+\frac{1}{2}} - \boldsymbol{\tau}_{\alpha+\frac{1}{2}}^{xz,-} \right) - \left( \boldsymbol{\tau}_{\alpha-\frac{1}{2}}^{xx,+} \nabla_{\mathbf{x}} z_{\alpha-\frac{1}{2}} - \boldsymbol{\tau}_{\alpha-\frac{1}{2}}^{xz,+} \right) = 0. \end{aligned}$$

Observe that

$$\boldsymbol{\tau}_{\alpha+\frac{1}{2}}^{xx,-} \nabla_{\mathbf{x}} z_{\alpha+\frac{1}{2}} - \boldsymbol{\tau}_{\alpha+\frac{1}{2}}^{xz,-} = \left[ \boldsymbol{\tau}_{\alpha+\frac{1}{2}}^- \mathbf{n}_{\alpha+\frac{1}{2}} \sqrt{1 + \left| \nabla_{\mathbf{x}} z_{\alpha+\frac{1}{2}} \right|^2} \right]_H,$$

where  $[\cdot]_H$  denotes the horizontal components. Now by (1.19) we obtain

$$\begin{aligned} & \left[ \boldsymbol{\tau}_{\alpha+\frac{1}{2}}^- \mathbf{n}_{\alpha+\frac{1}{2}} \sqrt{1 + \left| \nabla_{\mathbf{x}} z_{\alpha+\frac{1}{2}} \right|^2} \right]_H = \left[ \tilde{\boldsymbol{\tau}}_{\alpha+\frac{1}{2}} \mathbf{n}_{\alpha+\frac{1}{2}} \sqrt{1 + \left| \nabla_{\mathbf{x}} z_{\alpha+\frac{1}{2}} \right|^2} - \frac{1}{2} \rho G_{\alpha+\frac{1}{2}} [\mathbf{u}]_{\alpha+\frac{1}{2}} \right]_H = \\ & = \tilde{\boldsymbol{\tau}}_{\alpha+\frac{1}{2}}^{xx} \nabla_{\mathbf{x}} z_{\alpha+\frac{1}{2}} - \tilde{\boldsymbol{\tau}}_{\alpha+\frac{1}{2}}^{xz} - \frac{1}{2} \rho G_{\alpha+\frac{1}{2}} (\mathbf{u}_{\alpha+1}^x - \mathbf{u}_{\alpha}^x), \end{aligned}$$



and analogously

$$\left[ \tau_{\alpha-\frac{1}{2}}^+ \mathbf{n}_{\alpha-\frac{1}{2}} \sqrt{1 + |\nabla_{\mathbf{x}} z_{\alpha+\frac{1}{2}}|^2} \right]_H = \tilde{\tau}_{\alpha-\frac{1}{2}}^{xx} \nabla_{\mathbf{x}} z_{\alpha-\frac{1}{2}} - \tilde{\tau}_{\alpha-\frac{1}{2}}^{xz} + \frac{1}{2} \rho G_{\alpha-\frac{1}{2}} (\mathbf{u}_{\alpha}^x - \mathbf{u}_{\alpha-1}^x).$$

This allows us to rewrite the momentum equation as

$$\begin{aligned} & \rho h_{\alpha} \partial_t \mathbf{u}_{\alpha}^x + \rho h_{\alpha} \mathbf{u}_{\alpha}^x \cdot \nabla_{\mathbf{x}} \mathbf{u}_{\alpha}^x + \rho g \cos \theta h_{\alpha} \nabla_{\mathbf{x}} (\tilde{b} + b + h) - \\ & - \nabla_{\mathbf{x}} \cdot \left( \eta_0 h_{\alpha} (\nabla_{\mathbf{x}} \mathbf{u}_{\alpha}^x + (\nabla_{\mathbf{x}} \mathbf{u}_{\alpha}^x)') \right) + \\ & + \left( \tilde{\tau}_{\alpha+\frac{1}{2}}^{xx} \nabla_{\mathbf{x}} z_{\alpha+\frac{1}{2}} - \tilde{\tau}_{\alpha+\frac{1}{2}}^{xz} \right) - \left( \tilde{\tau}_{\alpha-\frac{1}{2}}^{xx} \nabla_{\mathbf{x}} z_{\alpha-\frac{1}{2}} - \tilde{\tau}_{\alpha-\frac{1}{2}}^{xz} \right) = \\ & = \frac{1}{2} \rho G_{\alpha+\frac{1}{2}} (\mathbf{u}_{\alpha+1}^x - \mathbf{u}_{\alpha}^x) + \frac{1}{2} \rho G_{\alpha-\frac{1}{2}} (\mathbf{u}_{\alpha}^x - \mathbf{u}_{\alpha-1}^x). \end{aligned}$$

We now introduce the following definition for the viscous terms:

$$\begin{aligned} \mathbf{K}_{\alpha+\frac{1}{2}} &= \left( \tilde{\tau}_{\alpha+\frac{1}{2}}^{xx} \nabla_{\mathbf{x}} z_{\alpha+\frac{1}{2}} - \tilde{\tau}_{\alpha+\frac{1}{2}}^{xz} \right) = \left[ \tilde{\tau}_{\alpha+\frac{1}{2}} \mathbf{n}_{\alpha+\frac{1}{2}} \sqrt{1 + |\nabla_{\mathbf{x}} z_{\alpha+\frac{1}{2}}|^2} \right]_H = \\ &= 2 \eta_0 \left[ \tilde{D}_{\alpha+\frac{1}{2}} \mathbf{n}_{\alpha+\frac{1}{2}} \right]_H \sqrt{1 + |\nabla_{\mathbf{x}} z_{\alpha+\frac{1}{2}}|^2} = 2 \eta_0 D_{\mathbf{x}} \left( \frac{\mathbf{u}_{\alpha+\frac{1}{2}}^{x,+} + \mathbf{u}_{\alpha+\frac{1}{2}}^{x,-}}{2} \right) \nabla_{\mathbf{x}} z_{\alpha+\frac{1}{2}} - \quad (1.27) \\ &- \eta_0 \nabla_{\mathbf{x}} \left( \frac{w_{\alpha+\frac{1}{2}}^+ + w_{\alpha+\frac{1}{2}}^-}{2} \right)' - \eta_0 \mathbf{u}_{\mathbf{z},\alpha+\frac{1}{2}}^H, \end{aligned}$$

for  $\alpha = 1, \dots, N-1$ , and  $K_{\frac{1}{2}}$  and  $K_{N+\frac{1}{2}}$  must be defined accordingly with the boundary condition at the bottom and free surface (1.6). Finally, by combining the previous equation with (1.25) we get the momentum equation:

$$\begin{aligned} & \rho \partial_t (h_{\alpha} \mathbf{u}_{\alpha}^x) + \rho \nabla_{\mathbf{x}} \cdot (h_{\alpha} \mathbf{u}_{\alpha}^x \otimes \mathbf{u}_{\alpha}^x) + \rho g \cos \theta h_{\alpha} \nabla_{\mathbf{x}} (\tilde{b} + b + h) - \\ & - \nabla_{\mathbf{x}} \cdot \left( \eta_0 h_{\alpha} (\nabla_{\mathbf{x}} \mathbf{u}_{\alpha}^x + (\nabla_{\mathbf{x}} \mathbf{u}_{\alpha}^x)') \right) + \\ & = \mathbf{K}_{\alpha-\frac{1}{2}} - \mathbf{K}_{\alpha+\frac{1}{2}} + \frac{1}{2} \rho G_{\alpha+\frac{1}{2}} (\mathbf{u}_{\alpha+1}^x + \mathbf{u}_{\alpha}^x) - \frac{1}{2} \rho G_{\alpha-\frac{1}{2}} (\mathbf{u}_{\alpha}^x + \mathbf{u}_{\alpha-1}^x), \end{aligned}$$

for  $\alpha = 1, \dots, N$ .

## 1.4 Final multilayer model

The final multilayer model reads, for  $\alpha = 1, \dots, N$ ,

$$\left\{ \begin{array}{l} l_\alpha \left( \partial_t h + \nabla_{\mathbf{x}} \cdot (h \mathbf{u}_\alpha^x) \right) = G_{\alpha+\frac{1}{2}} - G_{\alpha-\frac{1}{2}}, \\ l_\alpha \left( \rho \partial_t (h \mathbf{u}_\alpha^x) + \rho \nabla_{\mathbf{x}} \cdot (h \mathbf{u}_\alpha^x \otimes \mathbf{u}_\alpha^x) + \rho g \cos \theta h \nabla_{\mathbf{x}} (\tilde{b} + b + h) - \right. \\ \left. - \nabla_{\mathbf{x}} \cdot \left( \eta_0 h \left( \nabla_{\mathbf{x}} \mathbf{u}_\alpha^x + (\nabla_{\mathbf{x}} \mathbf{u}_\alpha^x)' \right) \right) \right) + \\ = \mathbf{K}_{\alpha-\frac{1}{2}} - \mathbf{K}_{\alpha+\frac{1}{2}} + \frac{1}{2} \rho G_{\alpha+\frac{1}{2}} (\mathbf{u}_{\alpha+1}^x + \mathbf{u}_\alpha^x) - \frac{1}{2} \rho G_{\alpha-\frac{1}{2}} (\mathbf{u}_\alpha^x + \mathbf{u}_{\alpha-1}^x), \end{array} \right. \quad (1.28)$$

where  $G_{\alpha+\frac{1}{2}}$  and  $K_{\alpha+\frac{1}{2}}$  are given in (1.15) and (1.27).

Once the vertical mesh is fixed through the positive coefficients  $l_\alpha$ , the model (1.28) has  $2N$  equations and unknowns:

$$h, \{\mathbf{u}_\alpha^x\}_{\alpha=1, \dots, N}, \quad \{G_{\alpha+\frac{1}{2}}\}_{\alpha=1, \dots, N-1}.$$

However, thanks to (1.15), the mass transfer terms can be rewritten as

$$G_{\alpha+\frac{1}{2}} = \partial_t z_{\alpha+\frac{1}{2}} + \frac{\mathbf{u}_\alpha^x + \mathbf{u}_{\alpha+1}^x}{2} \nabla_{\mathbf{x}} z_{\alpha+\frac{1}{2}} - w_{\alpha+\frac{1}{2}}, \quad \text{where} \quad w_{\alpha+\frac{1}{2}} = \frac{w_{\alpha+\frac{1}{2}}^+ + w_{\alpha+\frac{1}{2}}^-}{2}.$$

As a consequence, the system has  $2N$  unknowns, now corresponding to the total height  $h$ , the horizontal velocity  $\{u_\alpha\}_{\alpha=1, \dots, N}$  in each layer and the averaged vertical velocity at each internal interface  $\{w_{\alpha+\frac{1}{2}}\}_{\alpha=1, \dots, N-1}$ .

Nevertheless, the system can be rewritten with  $N + 1$  equations and unknowns as we explain in the following. By summing the continuity equations from 1 to  $\alpha$ ,  $G_{\alpha+\frac{1}{2}}$  can be written as

$$G_{\alpha+\frac{1}{2}} = G_{\frac{1}{2}} + \sum_{\beta=1}^{\alpha} \left( \partial_t h_\beta + \nabla_{\mathbf{x}} \cdot (h_\beta \mathbf{u}_\beta^x) \right). \quad (1.29)$$

Moreover, we assume that  $G_{1/2} = G_{N+1/2} = 0$ , as boundary conditions at the bottom and the free surface, respectively. This represents the fact that there is no transference of mass at the bottom nor the free surface level. Then, for the special case  $\alpha = N$ , the above equation leads to

$$\partial_t h + \nabla_{\mathbf{x}} \cdot \left( h \sum_{\beta=1}^N l_\beta \mathbf{u}_\beta^x \right) = 0.$$

Making use of the above equation in (1.29), we obtain

$$G_{\alpha+\frac{1}{2}} = \sum_{\beta=1}^{\alpha} \left( \nabla_{\mathbf{x}} \cdot (l_{\beta} h \mathbf{u}_{\beta}^{\mathbf{x}}) - l_{\beta} \sum_{\zeta=1}^N \nabla_{\mathbf{x}} \cdot (l_{\zeta} h \mathbf{u}_{\zeta}^{\mathbf{x}}) \right). \quad (1.30)$$

As conclusion,  $G_{\alpha+\frac{1}{2}}$  is written in terms of the the total height ( $h$ ) and the discharge of each layer

$$\mathbf{q}_{\alpha} = h \mathbf{u}_{\alpha}^{\mathbf{x}}, \quad \text{for } \alpha = 1, \dots, N,$$

then the system is rewritten with  $N + 1$  equations and unknowns  $h, \{\mathbf{q}_{\alpha}\}_{\alpha=1, \dots, N}$ . Finally, by introducing the coefficients

$$\xi_{\alpha, \zeta} = \begin{cases} (1 - (l_1 + \dots + l_{\alpha})) l_{\zeta}, & \text{if } \zeta \leq \alpha, \\ -(l_1 + \dots + l_{\alpha}) l_{\zeta}, & \text{otherwise,} \end{cases} \quad (1.31)$$

for  $\alpha, \zeta \in \{1, \dots, N\}$ , the system (1.27)-(1.28) is rewritten as

$$\left\{ \begin{array}{l} \partial_t h + \nabla_{\mathbf{x}} \cdot \left( \sum_{\beta=1}^N l_{\beta} \mathbf{q}_{\beta} \right) = 0, \\ \partial_t \mathbf{q}_{\alpha} + \nabla_{\mathbf{x}} \cdot \left( \frac{\mathbf{q}_{\alpha} \otimes \mathbf{q}_{\alpha}}{h} \right) + g \cos \theta h \nabla_{\mathbf{x}} (z_b + h) - \\ - \nu_0 \nabla_{\mathbf{x}} \cdot \left( \nabla_{\mathbf{x}} \mathbf{q}_{\alpha} + (\nabla_{\mathbf{x}} \mathbf{q}_{\alpha})' - 2 \frac{\mathbf{q}_{\alpha}}{h} \partial_x h \right) + \\ + \sum_{\zeta=1}^N \frac{1}{2 l_{\alpha} h} \left( (\mathbf{q}_{\alpha} + \mathbf{q}_{\alpha-1}) \xi_{\alpha-1, \zeta} - (\mathbf{q}_{\alpha+1} + \mathbf{q}_{\alpha}) \xi_{\alpha, \zeta} \right) \nabla_{\mathbf{x}} \cdot \mathbf{q}_{\zeta} = \\ = \frac{1}{\rho l_{\alpha}} \left( \mathbf{K}_{\alpha-\frac{1}{2}} - \mathbf{K}_{\alpha+\frac{1}{2}} \right), \quad \text{for } \alpha = 1, \dots, N, \end{array} \right. \quad (1.32)$$

where  $\nu_0 = \eta_0 / \rho$  and  $z_b = \tilde{b} + b$  have been introduced for simplicity.

The previous model in the 2D case satisfies a dissipative energy balance, whereas it has not been proved for the 3D case yet. In the following section, we propose an alternative 3D multilayer model with an associate energy balance. Furthermore, it matches model (1.28) in the 2D case. Bristeau *et al.* [30] proved a energy balance for the two-dimensional hydrostatic Navier-Stokes equations with a general tensor  $\tau$ , i.e., constant or variable viscosity coefficient. Nevertheless, in [30] the hydrostatic assumption is applied in a particular way. They neglected the convective terms in the vertical momentum equation (vertical acceleration) but keep the viscous terms. Actually, those viscous terms are essential to prove the energy balance.

## 1.5 An alternative 3D multilayer model with energy balance

Here we comment an interesting alternative to prove a dissipative energy inequality for the model with constant viscosity. A similar multilayer model is obtained using the following identity

$$\nabla_x \cdot \left( (\nabla_x \mathbf{u}^x)' \right) = \nabla_x \cdot \left( Tr(\nabla_x \mathbf{u}^x) \mathcal{I}_2 \right),$$

where  $Tr(\cdot)$  is the trace operator and  $\mathcal{I}_2$  is the 2D identity tensor. Thanks to previous equation, it is easy to verify that

$$\nabla \cdot \boldsymbol{\tau} = \nabla \cdot (\eta_0 D(\mathbf{u})) = \nabla \cdot (\eta_0 \widehat{D}(\mathbf{u})) = \nabla \cdot \widehat{\boldsymbol{\tau}},$$

with

$$\widehat{D}(\mathbf{u}) = \frac{1}{2} \begin{pmatrix} 2\widehat{D}^x(\mathbf{u}^x) & \partial_z \mathbf{u}^x + (\nabla_x w)' \\ (\partial_z \mathbf{u}^x)' + \nabla_x w & 2\partial_z w \end{pmatrix} \text{ and } \widehat{D}^x(\mathbf{u}^x) = \frac{\nabla_x \mathbf{u}^x + Tr(\nabla_x \mathbf{u}^x) \mathcal{I}_2}{2}.$$

By considering that definition of  $\widehat{D}(\mathbf{u})$ , a multilayer model can be analogously derived. Note that this can be seen as a redefinition of the tensor  $\boldsymbol{\tau}$ , where we change  $(\nabla_x \mathbf{u}^x)'$  by  $Tr(\nabla_x \mathbf{u}^x) \mathcal{I}_2$  in the definition of  $D^x(\mathbf{u}^x)$ . The resulting model reads, for  $\alpha = 1, \dots, N$ ,

$$\left\{ \begin{array}{l} \partial_t h_\alpha + \nabla_x \cdot (h_\alpha \mathbf{u}_\alpha^x) = G_{\alpha+\frac{1}{2}} - G_{\alpha-\frac{1}{2}}, \\ \partial_t (h_\alpha \mathbf{u}_\alpha^x) + \nabla_x \cdot (h_\alpha \mathbf{u}_\alpha^x \otimes \mathbf{u}_\alpha^x) + g \cos \theta h_\alpha \nabla_x (z_b + h) - \\ - \nabla_x \cdot \left( \nu_0 h_\alpha (\nabla_x \mathbf{u}_\alpha^x + Tr(\nabla_x \mathbf{u}_\alpha^x) \mathcal{I}_2) \right) + \\ = \frac{1}{\rho} \left( \mathbf{K}_{\alpha-\frac{1}{2}} - \mathbf{K}_{\alpha+\frac{1}{2}} \right) + \frac{1}{2} G_{\alpha+\frac{1}{2}} (\mathbf{u}_{\alpha+1}^x + \mathbf{u}_\alpha^x) - \frac{1}{2} G_{\alpha-\frac{1}{2}} (\mathbf{u}_\alpha^x + \mathbf{u}_{\alpha-1}^x), \end{array} \right. \quad (1.33)$$

where

$$\mathbf{K}_{\alpha+\frac{1}{2}} = \eta_0 \left( \nabla_x \mathbf{u}_{\alpha+\frac{1}{2}}^x + Tr(\nabla_x \mathbf{u}_{\alpha+\frac{1}{2}}^x) \mathcal{I}_2 \right) \nabla_x z_{\alpha+\frac{1}{2}} - \eta_0 \left( \nabla_x w_{\alpha+\frac{1}{2}} \right)' - \eta_0 \mathcal{U}_{\mathcal{Z}, \alpha+\frac{1}{2}}^H, \quad (1.34)$$

with  $\mathcal{U}_{\mathcal{Z}, \alpha+\frac{1}{2}}^H$  defined by (1.22) and

$$\mathbf{u}_{\alpha+\frac{1}{2}}^x = \frac{\mathbf{u}_{\alpha+1}^x + \mathbf{u}_\alpha^x}{2}; \quad w_{\alpha+\frac{1}{2}} = \frac{w_{\alpha+\frac{1}{2}}^+ + w_{\alpha+\frac{1}{2}}^-}{2}.$$

**Proposition 1.** Denoting the energy of the layer  $\alpha = 1, \dots, N$  for the system (1.33)-(1.34) by

$$E_\alpha = h_\alpha \left( \frac{|\mathbf{u}_\alpha^x|^2}{2} + g \cos \theta \left( z_b + \frac{h}{2} \right) \right),$$

the following dissipative energy inequality is satisfied:

$$\begin{aligned} & \partial_t \left( \sum_{\alpha=1}^N E_\alpha \right) + \partial_x \left[ \sum_{\alpha=1}^N \left( E_\alpha + g \cos \theta h_\alpha \frac{h}{2} \right) \mathbf{u}_\alpha^x \right. \\ & - \nu_0 \sum_{\alpha=1}^N \left( h_\alpha \left( (\nabla_x \mathbf{u}_\alpha^x)' + \text{Tr}(\nabla_x \mathbf{u}_\alpha^x) \mathcal{I}_2 \right) \mathbf{u}_\alpha^x - h_\alpha \mathbf{u}_\alpha^x \nabla_x \cdot \mathbf{u}_\alpha^x \right) - \\ & \left. - \frac{1}{2} \nu_0 \sum_{\alpha=1}^{N-1} \left( \mathbf{u}_{\alpha+1}^x - \mathbf{u}_\alpha^x \right) \otimes \left( \mathbf{u}_{\alpha+1}^x + \mathbf{u}_\alpha^x \right) \cdot \nabla_x z_{\alpha+\frac{1}{2}} \right] \leq g \cos \theta h \partial_t z_b - \\ & - \nu_0 \sum_{\alpha=1}^N h_\alpha |\nabla_x \mathbf{u}_\alpha^x|^2 - \nu_0 \sum_{\alpha=1}^{N-1} \frac{(\mathbf{u}_{\alpha+1}^x - \mathbf{u}_\alpha^x)^2}{h_{\alpha+\frac{1}{2}}} \sqrt{1 + |\nabla_x z_{\alpha+\frac{1}{2}}|^2} + \\ & - \frac{1}{\rho} \left( \mathbf{u}_N^x \mathbf{K}_{N+\frac{1}{2}} - \mathbf{u}_1^x \mathbf{K}_{\frac{1}{2}} \right). \end{aligned}$$

*Proof.* Firstly, we write the momentum equation in terms of the horizontal velocity and it is multiplied by  $\mathbf{u}_\alpha^x$ . Next, the mass equation is multiplied by

$$\left( \frac{|\mathbf{u}_\alpha^x|}{2} + g \cos \theta (z_b + h) \right). \quad (1.35)$$

Then, both equations are combined and summed up from  $\alpha = 1$  to  $\alpha = N$ . Thus, we obtain that the global system satisfy a dissipative energy balance.

Let us start writing the momentum equation in term of the velocity, where the mass equation is used to simplify the convective terms:

$$\begin{aligned} & h_\alpha \partial_t \mathbf{u}_\alpha^x + h_\alpha \mathbf{u}_\alpha^x \cdot \nabla_x \mathbf{u}_\alpha^x + g \cos \theta h_\alpha \nabla_x (z_b + h) - \\ & - \nabla_x \cdot \left( \nu_0 h_\alpha \left( \nabla_x \mathbf{u}_\alpha^x + \text{Tr}(\nabla_x \mathbf{u}_\alpha^x) \mathcal{I}_2 \right) \right) = \frac{1}{\rho} \left( \mathbf{K}_{\alpha-\frac{1}{2}} - \mathbf{K}_{\alpha+\frac{1}{2}} \right) + \\ & + \frac{1}{2} G_{\alpha+\frac{1}{2}} (\mathbf{u}_{\alpha+1}^x - \mathbf{u}_\alpha^x) + \frac{1}{2} G_{\alpha-\frac{1}{2}} (\mathbf{u}_\alpha^x - \mathbf{u}_{\alpha-1}^x). \end{aligned} \quad (1.36)$$

By multiplying the previous equation by  $\mathbf{u}_\alpha^x$ , we obtain

$$\begin{aligned}
& h_\alpha \partial_t \frac{|\mathbf{u}_\alpha^x|^2}{2} + h_\alpha \nabla_x \cdot \left( \frac{|\mathbf{u}_\alpha^x|^2}{2} \mathbf{u}_\alpha^x \right) - h_\alpha \frac{|\mathbf{u}_\alpha^x|^2}{2} \nabla_x \cdot \mathbf{u}_\alpha^x + \mathbf{u}_\alpha^x \cdot g \cos \theta h_\alpha \nabla_x (z_b + h) - \\
& - \mathbf{u}_\alpha^x \cdot \nabla_x \cdot \left( \nu_0 h_\alpha \left( \nabla_x \mathbf{u}_\alpha^x + \text{Tr}(\nabla_x \mathbf{u}_\alpha^x) \mathcal{I}_2 \right) \right) = \frac{1}{\rho} \mathbf{u}_\alpha^x \cdot \left( \mathbf{K}_{\alpha-\frac{1}{2}} - \mathbf{K}_{\alpha+\frac{1}{2}} \right) + \\
& + \frac{1}{2} G_{\alpha+\frac{1}{2}} (\mathbf{u}_{\alpha+1}^x \cdot \mathbf{u}_\alpha^x - |\mathbf{u}_\alpha^x|^2) + \frac{1}{2} G_{\alpha-\frac{1}{2}} (|\mathbf{u}_\alpha^x|^2 - \mathbf{u}_\alpha^x \cdot \mathbf{u}_{\alpha-1}^x),
\end{aligned} \tag{1.37}$$

where we have used the identities

$$\mathbf{u} \cdot (\mathbf{u} \cdot \nabla \mathbf{u}) = \nabla \cdot \left( \frac{|\mathbf{u}|^2}{2} \mathbf{u} \right) - \frac{|\mathbf{u}|^2}{2} \nabla \cdot \mathbf{u}; \quad \text{and} \quad \mathbf{u} \cdot \partial_t \mathbf{u} = \partial_t \frac{|\mathbf{u}|^2}{2}.$$

Let us consider the mass conservation equation multiplied by (1.35),

$$\begin{aligned}
& \frac{|\mathbf{u}_\alpha^x|^2}{2} \partial_t h_\alpha + \frac{|\mathbf{u}_\alpha^x|^2}{2} \nabla_x \cdot (h_\alpha \mathbf{u}_\alpha^x) + g \cos \theta (z_b + h) \partial_t h_\alpha + \\
& + g \cos \theta (z_b + h) \nabla_x \cdot (h_\alpha \mathbf{u}_\alpha^x) = \left( \frac{|\mathbf{u}_\alpha^x|^2}{2} + \rho g (z_b + h) \right) (G_{\alpha+\frac{1}{2}} - G_{\alpha-\frac{1}{2}}).
\end{aligned} \tag{1.38}$$

Noticing that

$$h_\alpha \nabla_x \cdot \left( \frac{|\mathbf{u}_\alpha^x|^2}{2} \mathbf{u}_\alpha^x \right) - h_\alpha \frac{|\mathbf{u}_\alpha^x|^2}{2} \nabla_x \cdot \mathbf{u}_\alpha^x + \frac{|\mathbf{u}_\alpha^x|^2}{2} \nabla_x \cdot (h_\alpha \mathbf{u}_\alpha^x) = \nabla_x \cdot \left( h_\alpha \mathbf{u}_\alpha^x \frac{|\mathbf{u}_\alpha^x|^2}{2} \right),$$

and

$$g \cos \theta h \partial_t h_\alpha = \partial_t \left( g \cos \theta h_\alpha h - g \cos \theta \frac{h_\alpha h}{2} \right) - \frac{g \cos \theta}{2} (h_\alpha \partial_t h - h \partial_t h_\alpha),$$

we sum (1.37) and (1.38) and we obtain the equation

$$\begin{aligned}
& \partial_t \left( h_\alpha \frac{|\mathbf{u}_\alpha^x|^2}{2} + h_\alpha g \cos \theta \left( z_b + \frac{h}{2} \right) \right) + \nabla_x \cdot \left( h_\alpha \left( \frac{|\mathbf{u}_\alpha^x|^2}{2} + g \cos \theta (z_b + h) \right) \mathbf{u}_\alpha^x \right) - \\
& - \mathbf{u}_\alpha^x \cdot \nabla_x \cdot \left( \nu_0 h_\alpha \left( \nabla_x \mathbf{u}_\alpha^x + \text{Tr}(\nabla_x \mathbf{u}_\alpha^x) \mathcal{I}_2 \right) \right) + \frac{1}{\rho} \mathbf{u}_\alpha^x \cdot \left( \mathbf{K}_{\alpha+\frac{1}{2}} - \mathbf{K}_{\alpha-\frac{1}{2}} \right) = \\
& = g \cos \theta h_\alpha \partial_t z_b + \frac{g \cos \theta}{2} (h_\alpha \partial_t h - h \partial_t h_\alpha) + \\
& + G_{\alpha+\frac{1}{2}} \left( \frac{\mathbf{u}_{\alpha+1}^x \cdot \mathbf{u}_\alpha^x}{2} + g \cos \theta (z_b + h) \right) - G_{\alpha-\frac{1}{2}} \left( \frac{\mathbf{u}_\alpha^x \cdot \mathbf{u}_{\alpha-1}^x}{2} + g \cos \theta (z_b + h) \right).
\end{aligned}$$

Regarding to the horizontal diffusion term, it is easy to verify that the following identities hold:

$$\begin{aligned} & \mathbf{u} \cdot \nabla \cdot \left( \nu_0 h_\alpha \left( \nabla \mathbf{u} + \text{Tr}(\nabla \mathbf{u}) \mathcal{I}_2 \right) \right) = \\ & = \nabla \cdot \left( \nu_0 h_\alpha \left( (\nabla \mathbf{u})' + \text{Tr}(\nabla \mathbf{u}) \mathcal{I}_2 \right) \mathbf{u} \right) - \nu_0 h_\alpha \left( \nabla \mathbf{u} + \text{Tr}(\nabla \mathbf{u}) \mathcal{I}_2 \right) : \nabla \mathbf{u}, \end{aligned}$$

and

$$\nu_0 h_\alpha \left( \nabla \mathbf{u} + \text{Tr}(\nabla \mathbf{u}) \mathcal{I}_2 \right) : \nabla \mathbf{u} = \nu_0 h_\alpha \left( (\text{Tr}(\nabla \mathbf{u}))^2 + |\nabla \mathbf{u}|^2 \right).$$

The second term appears with a negative contribution to the right hand side of the inequality, thus it is a dissipative term. Therefore, denoting

$$E_\alpha = h_\alpha \left( \frac{|\mathbf{u}_\alpha^x|^2}{2} + g \cos \theta \left( z_b + \frac{h}{2} \right) \right),$$

and noticing that  $\text{Tr}(\nabla \mathbf{u}) = \nabla \cdot \mathbf{u}$ , we have for  $\alpha = 1, \dots, N$  the following energy equality

$$\begin{aligned} & \partial_t E_\alpha + \nabla_x \cdot \left[ \left( E_\alpha + g \cos \theta h_\alpha \frac{h}{2} \right) \mathbf{u}_\alpha^x - \nu_0 h_\alpha \left( (\nabla_x \mathbf{u}_\alpha^x)' + \text{Tr}(\nabla_x \mathbf{u}_\alpha^x) \mathcal{I}_2 \right) \mathbf{u}_\alpha^x \right] + \\ & + \frac{1}{\rho} \underbrace{\mathbf{u}_\alpha^x \cdot \left( \mathbf{K}_{\alpha+\frac{1}{2}} - \mathbf{K}_{\alpha-\frac{1}{2}} \right)}_{(a)} = -\nu_0 h_\alpha \left( (\nabla_x \cdot \mathbf{u}_\alpha^x)^2 + |\nabla_x \mathbf{u}_\alpha^x|^2 \right) + \\ & + g \cos \theta h_\alpha \partial_t z_b + \underbrace{\frac{g \cos \theta}{2} (h_\alpha \partial_t h - h \partial_t h_\alpha)}_{(b)_\alpha} + \\ & + \underbrace{G_{\alpha+\frac{1}{2}} \left( \frac{\mathbf{u}_{\alpha+1}^x \cdot \mathbf{u}_\alpha^x}{2} + g \cos \theta (z_b + h) \right) - G_{\alpha-\frac{1}{2}} \left( \frac{\mathbf{u}_\alpha^x \cdot \mathbf{u}_{\alpha-1}^x}{2} + g \cos \theta (z_b + h) \right)}_{(c)_\alpha}. \end{aligned} \tag{1.39}$$

We now sum up (1.39) from  $\alpha = 1$  to  $\alpha = N$ , and focus on the term (a). Looking at the

definition of  $\mathbf{K}_{\alpha+\frac{1}{2}}$  (1.34), and  $\mathbf{U}_{\mathcal{Z},\alpha+\frac{1}{2}}^H$  (1.22), we write

$$\begin{aligned} \frac{1}{\eta_0} \left( \mathbf{K}_{\alpha+\frac{1}{2}} - \mathbf{K}_{\alpha-\frac{1}{2}} \right) &= \underbrace{Tr \left( \nabla_{\mathbf{x}} \mathbf{u}_{\alpha+\frac{1}{2}}^x \right) \mathcal{I}_2 \nabla_{\mathbf{x}} z_{\alpha+\frac{1}{2}}}_{(a.1)_{\alpha+1/2}} - \underbrace{Tr \left( \nabla_{\mathbf{x}} \mathbf{u}_{\alpha-\frac{1}{2}}^x \right) \mathcal{I}_2 \nabla_{\mathbf{x}} z_{\alpha-\frac{1}{2}}}_{(a.1)_{\alpha-1/2}} - \\ &- \frac{1}{2} \nabla_{\mathbf{x}} \left( w_{\alpha+\frac{1}{2}}^+ + w_{\alpha+\frac{1}{2}}^- - \left( w_{\alpha-\frac{1}{2}}^+ + w_{\alpha-\frac{1}{2}}^- \right) \right)' - \\ &- \left( \underbrace{\left( \frac{\mathbf{u}_{\alpha+1}^x - \mathbf{u}_{\alpha}^x}{h_{\alpha+\frac{1}{2}}} \sqrt{1 + \left| \nabla_{\mathbf{x}} z_{\alpha+\frac{1}{2}} \right|^2} \right)}_{(a.3)_{\alpha+1/2}} - \underbrace{\left( \frac{\mathbf{u}_{\alpha}^x - \mathbf{u}_{\alpha-1}^x}{h_{\alpha-\frac{1}{2}}} \sqrt{1 + \left| \nabla_{\mathbf{x}} z_{\alpha-\frac{1}{2}} \right|^2} \right)}_{(a.3)_{\alpha-1/2}} \right) \end{aligned}$$

We use the definition of the vertical velocity (1.16)-(1.17) to rewrite the middle term in previous equation as

$$\begin{aligned} w_{\alpha+\frac{1}{2}}^+ + w_{\alpha+\frac{1}{2}}^- - \left( w_{\alpha-\frac{1}{2}}^+ + w_{\alpha-\frac{1}{2}}^- \right) &= w_{\alpha+\frac{1}{2}}^+ - w_{\alpha+\frac{1}{2}}^- + 2w_{\alpha+\frac{1}{2}}^- + w_{\alpha-\frac{1}{2}}^+ - w_{\alpha-\frac{1}{2}}^- - 2w_{\alpha-\frac{1}{2}}^+ = \\ &= \underbrace{\left( \mathbf{u}_{\alpha+1}^x - \mathbf{u}_{\alpha}^x \right) \cdot \nabla_{\mathbf{x}} z_{\alpha+\frac{1}{2}}}_{(a.2)_{\alpha+1/2}} + \underbrace{\left( \mathbf{u}_{\alpha}^x - \mathbf{u}_{\alpha-1}^x \right) \cdot \nabla_{\mathbf{x}} z_{\alpha-\frac{1}{2}}}_{(a.2)_{\alpha+1/2}} - \underbrace{2h_{\alpha} \nabla_{\mathbf{x}} \cdot \mathbf{u}_{\alpha}^x}_{(a.2)_{\alpha}}. \end{aligned}$$

With this notation we can write

$$\begin{aligned} \frac{1}{\eta_0} \left( \mathbf{K}_{\alpha+\frac{1}{2}} - \mathbf{K}_{\alpha-\frac{1}{2}} \right) &= (a.1)_{\alpha+1/2} - (a.1)_{\alpha-1/2} - \\ &- \frac{1}{2} \nabla_{\mathbf{x}} \left( (a.2)_{\alpha+1/2} + (a.1)_{\alpha-1/2} + (a.2)_{\alpha} \right)' \\ &- \left( (a.3)_{\alpha+1/2} - (a.3)_{\alpha-1/2} \right). \end{aligned}$$

We consider the terms involving the interface  $\Gamma_{\alpha+\frac{1}{2}}$  in equation  $\alpha$  and  $\alpha+1$ . From terms (a.1) and (a.2), we have

$$\begin{aligned} (a.1)_{\alpha+1/2} \cdot \mathbf{u}_{\alpha}^x - (a.1)_{\alpha+1/2} \cdot \mathbf{u}_{\alpha+1}^x &= \\ &= \frac{1}{2} Tr \left( \nabla_{\mathbf{x}} \left( \mathbf{u}_{\alpha+1}^x + \mathbf{u}_{\alpha}^x \right) \right) \mathcal{I}_2 \nabla_{\mathbf{x}} z_{\alpha+\frac{1}{2}} \cdot \left( \mathbf{u}_{\alpha}^x - \mathbf{u}_{\alpha+1}^x \right); \end{aligned} \tag{1.40}$$

$$\begin{aligned} -\frac{1}{2} \nabla_{\mathbf{x}} \left( (a.2)_{\alpha+1/2} \cdot \mathbf{u}_{\alpha}^x + (a.2)_{\alpha+1/2} \cdot \mathbf{u}_{\alpha+1}^x \right)' &= \\ &= -\frac{1}{2} \nabla_{\mathbf{x}} \left( \left( \mathbf{u}_{\alpha+1}^x - \mathbf{u}_{\alpha}^x \right) \cdot \nabla_{\mathbf{x}} z_{\alpha+\frac{1}{2}} \right)' \cdot \left( \mathbf{u}_{\alpha}^x + \mathbf{u}_{\alpha+1}^x \right), \end{aligned} \tag{1.41}$$

and the sum of equations (1.40) and (1.41) gives

$$-\frac{1}{2} \nabla_{\mathbf{x}} \cdot \left( \left( \mathbf{u}_{\alpha+1}^x - \mathbf{u}_{\alpha}^x \right) \otimes \left( \mathbf{u}_{\alpha+1}^x + \mathbf{u}_{\alpha}^x \right) \cdot \nabla_{\mathbf{x}} z_{\alpha+\frac{1}{2}} \right). \tag{1.42}$$



The sum of terms (a.3) produces

$$\sum_{\alpha=1}^{N-1} \frac{(\mathbf{u}_{\alpha+1}^x - \mathbf{u}_{\alpha}^x)^2}{h_{\alpha+\frac{1}{2}}} \sqrt{1 + |\nabla_{\mathbf{x}} z_{\alpha+\frac{1}{2}}|^2}$$

which also are dissipative terms. Finally, for the term (a.2) $_{\alpha}$  is easy to verify the following identity:

$$\nabla (h_{\alpha} \nabla \cdot \mathbf{u}) \cdot \mathbf{u} = \nabla \cdot (h_{\alpha} \mathbf{u} \nabla \cdot \mathbf{u}) - h_{\alpha} (\nabla \cdot \mathbf{u})^2.$$

Therefore, all the terms (a) in (1.39) are controlled. Next, for the term (b) we trivially have

$$\sum_{\alpha=1}^N (b)_{\alpha} = \frac{g \cos \theta}{2} \sum_{\alpha=1}^N (h_{\alpha} \partial_t h - h \partial_t h_{\alpha}) = \frac{g \cos \theta}{2} (h \partial_t h - h \partial_t h) = 0.$$

Moreover, by using that  $G_{\frac{1}{2}} = G_{N+\frac{1}{2}} = 0$  (there is no transfer with the bottom and the atmosphere, respectively), we have that

$$\sum_{\alpha=1}^N (c)_{\alpha} = 0.$$

Finally, by collecting all the resulting terms, and taking into account that the boundary condition at the bottom and free surface are usually dissipative terms, the proof is completed.  $\square$

**Remark 1.** Note that it is not possible to reproduce this proof for the model (1.28). The key point is the combination of terms (1.40) and (1.41) to give (1.42). For this step is essential the fact of having the term with the trace operator,  $Tr(\nabla_{\mathbf{x}} \mathbf{u}^x) \mathcal{L}_2$ , instead of the one with the gradient  $(\nabla_{\mathbf{x}} \mathbf{u}^x)'$  in the definition of viscous terms at the interfaces (1.34). The corresponding terms for the model (1.28) cannot be controlled, and consequently they are responsible of not having an energy balance in that case.



# A $\mu(I)$ rheology multilayer shallow model for dry granular flows\*

\*The results of this chapter have been published in the paper: E.D. Fernández-Nieto, J. Garres-Díaz, A. Mangeney, & G. Narbona-Reina, A multilayer shallow model for dry granular flows with the  $\mu(I)$  rheology: Application to granular collapse on erodible beds, *Journal of Fluid Mechanics*, 798 (2016), pp. 643–681.

## 2.1 Introduction

In this chapter we present a multilayer shallow model for dry granular flows, which approximates the Navier-Stokes equations with the  $\mu(I)$  rheology. The derivation of the model follows Chapter 1 (see also Fernández-Nieto *et al.* [56]), thus leading to a solution of the resulting model that is a particular weak solution of the full Navier-Stokes equations with the  $\mu(I)$  rheology. The novelty with respect the previous model is twofold: firstly, the model is obtained through a dimensional analysis based on the shallow water hypothesis; secondly, the  $\mu(I)$  rheology introduces a velocity-pressure viscosity coefficient, versus the constant viscosity coefficient considered in the previous chapter. The resulting model fully satisfies a dissipative energy inequality, thus complying with a requirement for a geophysical model to achieve a solution with physical meaning.

The accuracy of the numerical model has been demonstrated by comparing the numerical solutions to: (i) the steady uniform Bagnold flow, whose analytical solution is known ([60, 107, 79]); (ii) analytical solution and laboratory experiments of granular surface flows in narrow channel, where the lateral walls have an important role in the velocity profile ([75, 77]). Finally, by comparing the numerical results with experimental data on granular collapses in Mangeney *et al.* [87], we show that the proposed multilayer model with the  $\mu(I)$  rheology qualitatively reproduces the effect of the erodible bed on granular flow dynamics and deposits. In particular, the model reflects the increase of runout distance with increasing thickness of the erodible bed, whereas the use of a

constant friction coefficient in the multilayer model leads to the opposite behaviour.

An important result is that this multilayer approach allows us to obtain the normal profiles of the downslope and normal velocities. These profiles qualitatively agree with the typical granular flow profiles during the developed flow and during the stopping phase (GDR MiDi [60]), including the presence of static and flowing zones within the granular column. In particular, the model makes it possible to reproduce the change from Bagnold-like to S-shaped velocity profiles, characteristic of flows over a rigid substrate and over a layer of static grains, respectively. As a result, this model should be applicable to a larger range of flow regimes than the depth-averaged models proposed by Capart *et al.* [32] and Edwards & Gray [49] for which velocity profiles are prescribed.

The chapter is organised as follows. Section 2.2 is devoted to presenting the  $\mu(I)$  rheology and how it is included in the model, and the appropriate boundary condition at the bottom. In Section 2.3 we present the multilayer approach to derive a 2D multilayer model for dry granular flows up to first order when considering the thin-layer asymptotic approximation. The final  $\mu(I)$  rheology multilayer shallow model is also presented in this section together with the associated energy balance. Finally, Section 2.4 is devoted to presenting the numerical results.

## 2.2 Initial system with the $\mu(I)$ rheology

In order to simplify the presentation and since the numerical tests are two-dimensional, we consider that case in the whole chapter, although the derivation of the model may be easily generalized to the full three dimensional case. Therefore, bold (regular) characters denote two (one)-dimensional variables hereafter. Again, we consider tilted coordinates (see Section 1.2). Thus, we consider a granular mass with velocity  $\mathbf{u} = (u, w) \in \mathbb{R}^2$ , and  $\nabla = (\partial_x, \partial_z)$  is the differential operator.

In this section we present the two-dimensional model considered to describe the dynamics of granular flows. In particular, the definition of the stress tensor including the  $\mu(I)$  rheology.

We consider the system (1.1), where the stress tensor is

$$\boldsymbol{\sigma} = -p\mathcal{I} + \boldsymbol{\tau},$$

with the deviatoric stress tensor  $\boldsymbol{\tau} = \eta D(\mathbf{u})$  depending on  $\eta$ , the viscosity. This viscosity coefficient must be defined according to a rheological law describing the dynamics of granular flows. As discussed in the Introduction, we consider the so-called  $\mu(I)$  rheology (see Jop *et al.* [76]) in order to take into account the non-Newtonian nature of those flows.

Hence, the viscosity coefficient is defined by

$$\eta = \frac{\mu(I)p}{\|D(\mathbf{u})\|}, \quad (2.1)$$

with  $\|D\| = \sqrt{0.5 D : D}$  the usual second invariant of a tensor  $D$ . The friction coefficient  $\mu(I)$  is written as

$$\mu(I) = \mu_s + \frac{\mu_2 - \mu_s}{I_0 + I} I,$$

where  $I_0$  and  $\mu_2 > \mu_s$  are constant parameters that are determined from experiments. Actually,  $\mu_s$  is the usual static friction coefficient (or tangent of the repose angle) and  $\mu_2$  is the dynamical friction coefficient, which is the limiting value for the friction.  $I$  is the inertial number

$$I = \frac{2d_s\|D(\mathbf{u})\|}{\sqrt{p/\rho_s}}, \quad (2.2)$$

where  $d_s$  is the particle diameter and  $\rho_s$  the particle density. The apparent flow density is then defined as

$$\rho = \varphi_s \rho_s, \quad (2.3)$$

where the solid volume fraction, denoted by  $\varphi_s$ , is assumed to be constant.

Thus, this rheology relates the effective friction  $\mu(I)$  to the inertial number  $I$ , which reflects the local state of the granular packing. In fact,  $I$  can be interpreted (see figure 6.7 in Andreotti *et al.* [2]) as

$$I = \frac{t_{micro}}{t_{macro}},$$

the ratio between the timescale of the microscopic rearrangement of granular particles ( $t_{micro}$ ) and the timescale of the macroscopic deformations ( $t_{macro}$ ). Assuming two layers of particles, the time  $t_{micro}$  represents the time needed for a grain to fall in a hole of size  $d_s$  between two grains, under a pressure  $p$ , and the time  $t_{macro}$  represents the time required for a grain to pass the grain below. Note that when the shear rate is equal to zero,  $\mu(I)$  is reduced to  $\mu_s$ . For high values of the inertial number,  $\mu(I)$  converges to  $\mu_2$ . Otherwise, if we consider a constant value of  $\mu$ , independent of  $I$ , the model is always ill-posed (see Schaeffer [106]).

The  $\mu(I)$  rheology includes a Drucker-Prager plasticity criterion, the deviatoric tensor is defined as

$$\left\{ \begin{array}{ll} \boldsymbol{\tau} = \frac{\mu(I)p}{\|D\|} D & \text{if } \|D\| \neq 0, \\ \|\boldsymbol{\tau}\| \leq \mu_s p & \text{if } \|D\| = 0. \end{array} \right.$$

Note that the  $\mu(I)$  rheology can equivalently be written as a decomposition of the deviatoric stress in a sum of a plastic term and a rate-dependent viscous term (see

Ionescu *et al.* [70]):

$$\begin{cases} \boldsymbol{\tau} = \frac{\mu_s p}{\|D\|} D + 2\tilde{\eta} D & \text{if } \|D\| \neq 0, \\ \|\boldsymbol{\tau}\| \leq \mu_s p & \text{if } \|D\| = 0; \end{cases}$$

with a viscosity defined as  $\tilde{\eta} = \frac{(\mu_2 - \mu_s)p}{\frac{I_0}{d_s} \sqrt{p/\rho_s} + 2\|D\|}$ . Here we investigate the rheology defined by a variable friction  $\mu(I)$  and a constant friction  $\mu_s$ . In [70], the authors showed that simulations of the front propagation of granular column collapses and of their deposits are very sensitive to the value of the average value of the viscosity (see their figures 8 and 13). However, replacing  $\tilde{\eta}$  by a constant viscosity equal to the averaged value of the spatio-temporal viscosity  $\tilde{\eta}$  does not significantly change the simulated dynamics and deposit. Here we compare the case where  $\mu = \mu_s$  so that  $\tilde{\eta} = 0$  with the  $\mu(I)$  rheology corresponding to typical values of the viscosity  $\eta = 1$  Pa·s for granular collapses over horizontal and inclined planes ([70]).

The model considering a viscosity defined by (2.1) presents a discontinuity when  $\|D(\mathbf{u})\| = 0$ . In order to avoid this singularity there are several ways to proceed. One of them is to apply a duality method, such as augmented Lagrangian methods (Glowinski & Tallec [63]) or the Bermúdez-Moreno algorithm (Bermúdez & Moreno [16]). Another option is to use a regularization of  $D(\mathbf{u})$ , which is cheaper computationally; however it does not give an exact solution, contrary to duality methods.

Note that with the Drucker-Prager plasticity criterion, the case when  $\|D(\mathbf{u})\| = 0$  corresponds with a static granular mass whose velocity is trivially zero, in contrast with other rheological laws (e.g. Bingham) for which we can obtain a static mass moving with constant velocity. Then, the Drucker-Prager plasticity case is well approximated by means of a regularization method, since it is equivalent to consider a quite high viscosity coefficient, which makes the granular mass to stop with velocity close to zero.

In this work, we take into consideration two kinds of regularizations of  $D(\mathbf{u})$ . First, we use the regularization proposed in Lagrée *et al.* [79], which consist of bounding the viscosity by  $\eta_M = 250\rho\sqrt{gh^3}$  Pa·s, considering instead of (2.1),

$$\eta = \frac{\mu(I)p}{\max\left(\|D(\mathbf{u})\|, \frac{\mu(I)p}{\eta_M}\right)}. \quad (2.4)$$

In this way, we obtain  $\eta = \eta_M$  if  $\|D(\mathbf{u})\|$  is close to zero. We used this regularization in the simulation of the granular flow experiments. However, as explained in Subsection 2.4.1.1, we cannot consider this regularization in some tests presented below, for which we have to take into account the regularization (see Lusso *et al.* [85], Bercovier & Engelman [13]),

$$\eta = \frac{\mu(I)p}{\sqrt{\|D(\mathbf{u})\|^2 + \delta^2}},$$

where  $\delta > 0$  is a small parameter.

Finally, as commented in Chapter 1, the no-penetration boundary condition at the bottom must be completed with an appropriate friction condition (see (1.6)), whereas for the free surface we set (1.3)-(1.4). We consider a Coulomb-type friction law involving the variable friction coefficient  $\mu(I)$ :

$$\boldsymbol{\sigma} \mathbf{n}^b - ((\boldsymbol{\sigma} \mathbf{n}^b) \cdot \mathbf{n}^b) \mathbf{n}^b = \begin{pmatrix} \mu(I)p \frac{u}{|u|} \\ 0 \end{pmatrix}, \text{ at the bottom.} \quad (2.5)$$

Note that the multilayer approach considered here can also be deduced by considering a no-slip condition, i.e.  $\mathbf{u} = \mathbf{0}$  at the bottom, which implies the no penetration condition (1.5). This will be analysed in Chapter 3 (concretely Subsection 3.2.1.2).

## 2.3 The $\mu(I)$ rheology multilayer model

In this section, we present a multilayer model designed to approximate the dynamics of granular flows. We follow Fernández-Nieto *et al.* [56], in which a multilayer approach was developed to solve the Navier-Stokes equations. In our case, the system to approximate is given by the equations (1.7) together with the boundary conditions (1.3), (1.4) and (2.5). Again, the originality of this chapter is to develop the multilayer approach together with an asymptotic approximation. The system is deduced under several specific changes involving the asymptotic approximation and the definition of the stress tensor according to the  $\mu(I)$  rheology that introduces a non-constant viscosity coefficient. The advantage of this approach is that we recover the normal profile of the downslope and normal components of the velocity.

In the first subsection we show the dimensional analysis of the equations and write the non-dimensional system in matrix form. In the second part we present the procedure to obtain the multilayer model and the model itself. We give a detailed presentation of the deduction, where we focus on the aspects of the derivation that differ from the exposed method in Chapter 1.

### 2.3.1 Dimensional analysis

In this subsection we carry out a dimensional analysis of the system (1.1)-(2.5) under the local coordinates system specified in Section 1.2. We consider a shallow domain by assuming that the ratio  $\varepsilon = H/L$  between the characteristic height  $H$  and the characteristic length  $L$  is small. We also introduce the characteristic density  $\rho_0$ . Following the scaling analysis proposed in Gray & Edwards [64], we define the dimensionless

variables, denoted with the tilde symbol ( $\tilde{\cdot}$ ), as follows:

$$\begin{aligned} (x, z, t) &= (L\tilde{x}, H\tilde{z}, (L/U)\tilde{t}), & (u, w) &= (U\tilde{u}, \varepsilon U\tilde{w}), \\ h &= H\tilde{h}, & \rho &= \rho_0\tilde{\rho}, & p &= \rho_0 U^2 \tilde{p}, \\ \eta &= \rho_0 U H \tilde{\eta}, & \eta_M &= \rho_0 U H \tilde{\eta}_M, \\ (\tau_{xx}, \tau_{xz}, \tau_{zz}) &= \rho_0 U^2 (\varepsilon \tilde{\tau}_{xx}, \tilde{\tau}_{xz}, \varepsilon \tilde{\tau}_{zz}). \end{aligned}$$

Let us also note that

$$D(\mathbf{u}) = \frac{U}{H} \frac{1}{2} \begin{pmatrix} 2\varepsilon \partial_{\tilde{x}} \tilde{u} & \partial_{\tilde{z}} \tilde{u} + \varepsilon^2 \partial_{\tilde{x}} \tilde{w} \\ \partial_{\tilde{z}} \tilde{u} + \varepsilon^2 \partial_{\tilde{x}} \tilde{w} & 2\varepsilon \partial_{\tilde{z}} \tilde{w} \end{pmatrix},$$

and the Froude number

$$Fr = \frac{U}{\sqrt{g \cos \theta H}}.$$

Then, the system of equations (1.7) can be rewritten using this change of variables as (tildes have been dropped for simplicity):

$$\begin{cases} \partial_x u + \partial_z w = 0, \\ \rho(\partial_t u + u \partial_x u + w \partial_z u) + \partial_x p = -\frac{1}{\varepsilon} \rho \frac{1}{Fr^2} \tan \theta + \varepsilon \partial_x \tau_{xx} + \frac{1}{\varepsilon} \partial_z \tau_{xz}, \\ \varepsilon^2 \rho(\partial_t w + u \partial_x w + w \partial_z w) + \partial_z p = -\rho \frac{1}{Fr^2} + \varepsilon \partial_x \tau_{xz} + \varepsilon \partial_z \tau_{zz}. \end{cases} \quad (2.6)$$

We also write the boundary and kinematic conditions using dimensionless variables. At the free surface we get

$$\partial_t h + u|_{z=b+h} \partial_x (b+h) - w|_{z=b+h} = O(\varepsilon^2); \quad p|_{z=b+h} = 0, \quad (2.7)$$

and at the bottom we obtain

$$\begin{aligned} u|_{z=b} \partial_x b &= w|_{z=b}; \\ \frac{1}{2}(\eta \partial_z u)|_{z=b} &= \left( \mu(I) p \frac{u}{|u|} \right)_{|z=b} + O(\varepsilon^2). \end{aligned} \quad (2.8)$$

As shown previously, it is convenient to write the set of equations (2.6) in matrix notation before applying the multilayer approach. First, we focus on the equations of momentum. We multiply the horizontal momentum equation by  $\varepsilon$  and the vertical one



by  $1/\varepsilon$ . This gives

$$\begin{aligned}\varepsilon\rho(\partial_t u + u\partial_x u + w\partial_z w) + \varepsilon\partial_x p &= -\rho\frac{1}{Fr^2}\tan\theta + \varepsilon^2\partial_x\tau_{xx} + \partial_z\tau_{xz}, \\ \varepsilon\rho(\partial_t w + u\partial_x w + w\partial_z w) + \frac{1}{\varepsilon}\partial_z p &= -\frac{1}{\varepsilon}\rho\frac{1}{Fr^2} + \partial_x\tau_{xz} + \partial_z\tau_{zz}.\end{aligned}$$

Note that the stress tensor can be written:

$$\boldsymbol{\tau}_\varepsilon = \eta D_\varepsilon(\mathbf{u}) \quad \text{with} \quad D_\varepsilon(\mathbf{u}) := \frac{1}{2} \begin{pmatrix} 2\varepsilon^2\partial_x u & \partial_z u + \varepsilon^2\partial_x w \\ \partial_z u + \varepsilon^2\partial_x w & 2\partial_z w \end{pmatrix}. \quad (2.9)$$

We introduce the notation:

$$\mathbf{f} = \left( \frac{\tan\theta}{Fr^2}, \frac{1}{\varepsilon Fr^2} \right)' \quad \text{and} \quad \mathcal{E} = \begin{pmatrix} \varepsilon & 0 \\ 0 & 1/\varepsilon \end{pmatrix}.$$

Now we can write the momentum equations as follows

$$\varepsilon\rho\partial_t \mathbf{u} + \varepsilon\rho\nabla \cdot (\mathbf{u} \otimes \mathbf{u}) + \nabla \cdot (p\mathcal{E}) = -\rho\mathbf{f} + \nabla \cdot (\eta D_\varepsilon(\mathbf{u})),$$

and we obtain the system (2.6) in matrix notation:

$$\begin{cases} \nabla \cdot \mathbf{u} = 0, \\ \rho\partial_t \mathbf{u} + \rho\nabla \cdot (\mathbf{u} \otimes \mathbf{u}) - \frac{1}{\varepsilon}\nabla \cdot \boldsymbol{\sigma} = -\frac{1}{\varepsilon}\rho\mathbf{f}, \end{cases} \quad (2.10)$$

where the stress tensor is rewritten as  $\boldsymbol{\sigma} = -p\mathcal{E} + \boldsymbol{\tau}_\varepsilon$ , with  $\boldsymbol{\tau}_\varepsilon$  given by (2.9).

### 2.3.2 A multilayer approach

We apply the multilayer approach to the system (2.7)-(2.10). Note that the structure of the system (2.10) looks like that of Navier-Stokes equations (1.1) and then the whole procedure developed in Subsection 1.3 can be followed. In the next lines we describe the main points of the derivation in which this model differs from the one presented in Chapter 1.

We look for a particular weak solution  $(\mathbf{u}, p, \rho)$  of (2.10) such that it is a usual weak solution in each layer  $\Omega_\alpha(t)$ , and it satisfies the normal flux jump condition for the mass and momentum equations at the interfaces between the internal layers.

We take a particular family of velocity functions  $\mathbf{u}_\alpha$  on layer  $\alpha$ , with horizontal and vertical components  $u_\alpha$  and  $w_\alpha$  respectively, and structure (1.11)-(1.13). There are two

main differences with the derivation in Subsection 1.3: first, the  $\mu(I)$  rheology produces a non-constant viscosity coefficient, which implies an additional difficulty in order to develop the momentum balances at the interfaces. Second, the system to be solved is an asymptotic approximation of the Navier-Stokes equations, which helps to resolve the previous difficulty since we look for a first-order approximation in  $\varepsilon$ .

As a consequence of the asymptotic analysis, we directly get a hydrostatic pressure at first order in  $\varepsilon$ , in contrast to Chapter 1 where it is assumed. From the vertical momentum equation in (2.6) we get:

$$\partial_z p_\alpha = -\rho \frac{1}{Fr^2} + \mathcal{O}(\varepsilon).$$

By using the continuity of the dynamic pressure, we deduce at first order that

$$p_\alpha(z) = \frac{\rho}{Fr^2}(b + h - z). \quad (2.11)$$

Regarding the normal flux jump condition for the mass equation, it coincides with the one in previous case. Thus, we recall that the expression for the mass transference term is

$$G_{\alpha+\frac{1}{2}} = \partial_t z_{\alpha+\frac{1}{2}} + \frac{u_\alpha + u_{\alpha+1}}{2} \partial_x z_{\alpha+\frac{1}{2}} - w_{\alpha+\frac{1}{2}}, \quad \text{where} \quad w_{\alpha+\frac{1}{2}} = \frac{w_{\alpha+\frac{1}{2}}^+ + w_{\alpha+\frac{1}{2}}^-}{2}, \quad (2.12)$$

and making use of last equation together with the incompressibility condition, the vertical velocity is defined by (1.16)-(1.17).

On the other hand, the non-dimensional momentum jump conditions at the interface  $\Gamma_{\alpha+\frac{1}{2}}$  read

$$\left[ (\rho \mathbf{u}; \rho \mathbf{u} \otimes \mathbf{u} - \frac{1}{\varepsilon} \boldsymbol{\sigma}) \right]_{\alpha+\frac{1}{2}} \mathbf{n}_{t,\alpha+\frac{1}{2}} = 0.$$

Following the calculations in previous chapter, the previous condition leads to

$$\frac{1}{\varepsilon} [\boldsymbol{\sigma}]_{\alpha+\frac{1}{2}} \mathbf{n}_{\alpha+\frac{1}{2}} = \frac{\rho G_{\alpha+\frac{1}{2}}}{\sqrt{1 + \left| \partial_x z_{\alpha+\frac{1}{2}} \right|^2}} [\mathbf{u}]_{\alpha+\frac{1}{2}},$$

where the total stress tensor is

$$\boldsymbol{\sigma}_{\alpha+\frac{1}{2}}^\pm = -p_{\alpha+\frac{1}{2}} \boldsymbol{\mathcal{E}} + \boldsymbol{\tau}_{\varepsilon,\alpha+\frac{1}{2}}^\pm, \quad \text{for } \alpha = 1, \dots, N-1.$$

Then, we obtain the condition

$$\boldsymbol{\tau}_{\varepsilon,\alpha+\frac{1}{2}}^\pm \mathbf{n}_{\alpha+\frac{1}{2}} = \tilde{\boldsymbol{\tau}}_{\varepsilon,\alpha+\frac{1}{2}} \mathbf{n}_{\alpha+\frac{1}{2}} \pm \frac{1}{2} \frac{\varepsilon \rho G_{\alpha+\frac{1}{2}}}{\sqrt{1 + \left| \partial_x z_{\alpha+\frac{1}{2}} \right|^2}} [\mathbf{u}]_{\mathcal{G}_{\alpha+\frac{1}{2}}(t)}, \quad (2.13)$$

where  $\tilde{\boldsymbol{\tau}}_{\varepsilon, \alpha + \frac{1}{2}}$  is an approximation of  $(\eta D_\varepsilon(\mathbf{u}_\alpha))|_{\Gamma_{\alpha + \frac{1}{2}}}$ , defined by

$$\tilde{\boldsymbol{\tau}}_{\varepsilon, \alpha + \frac{1}{2}} = \eta_{\alpha + \frac{1}{2}} \tilde{D}_{\varepsilon, \alpha + \frac{1}{2}} = \frac{1}{2} \eta_{\alpha + \frac{1}{2}} \begin{pmatrix} 2\varepsilon^2 \partial_x \left( \frac{u_{\alpha + \frac{1}{2}}^+ + u_{\alpha + \frac{1}{2}}^-}{2} \right) & \tilde{D}_{\varepsilon, \alpha + \frac{1}{2}}^{xz} \\ \left( \tilde{D}_{\varepsilon, \alpha + \frac{1}{2}}^{xz} \right)' & 2\mathcal{U}_{\mathcal{Z}, \alpha + \frac{1}{2}}^V \end{pmatrix}. \quad (2.14)$$

Here,

$$\tilde{D}_{\varepsilon, \alpha + \frac{1}{2}}^{xz} = \varepsilon^2 \partial_x \left( \frac{w_{\alpha + \frac{1}{2}}^+ + w_{\alpha + \frac{1}{2}}^-}{2} \right) + \mathcal{U}_{\mathcal{Z}, \alpha + \frac{1}{2}}^H,$$

where  $\mathcal{U}_{\mathcal{Z}, \alpha + \frac{1}{2}} = (\mathcal{U}_{\mathcal{Z}, \alpha + \frac{1}{2}}^H, \mathcal{U}_{\mathcal{Z}, \alpha + \frac{1}{2}}^V)$  is defined as in (1.21) to approximate the derivatives in  $z$ . In this case, the non-dimensional form of  $\mathcal{U}_{\mathcal{Z}, \alpha + \frac{1}{2}}^H$  (1.22) reads

$$\mathcal{U}_{\mathcal{Z}, \alpha + \frac{1}{2}}^H = \frac{u_{\alpha+1} - u_\alpha}{h_{\alpha + \frac{1}{2}}} \sqrt{1 + \varepsilon \left| \partial_x z_{\alpha + \frac{1}{2}} \right|^2} + \varepsilon^2 \partial_x \left( \frac{u_\alpha + u_{\alpha+1}}{2} \right) \partial_x z_{\alpha + \frac{1}{2}},$$

therefore we consider the first order approximation

$$\mathcal{U}_{\mathcal{Z}, \alpha + \frac{1}{2}}^H = \frac{u_{\alpha+1} - u_\alpha}{h_{\alpha + \frac{1}{2}}}, \quad \text{for } \alpha = 1, \dots, N-1.$$

Moreover,

$$\mathcal{U}_{\mathcal{Z}, \frac{1}{2}}^H = \frac{u_1}{h_1},$$

according to the friction condition at the bottom (see Subsection 3.2.1.2 for details).

Let us remark that the previous expression of the tensor  $\tilde{\boldsymbol{\tau}}_{\varepsilon, \alpha + \frac{1}{2}}$  in (2.14) has the same structure as the original case in Chapter 1 (also in [56]), except for the viscosity that now is not constant because it is defined by the  $\mu(I)$  rheology in (2.4). Then, we must give an approximation of the viscosity at the interface up to first order in  $\varepsilon$ , which we denoted by  $\eta_{\alpha + \frac{1}{2}}$ . We have considered the following first-order approximation of  $\|D(\mathbf{u})\|$  at  $z = z_{\alpha + \frac{1}{2}}$ ,

$$\|D(\mathbf{u})\|_{\alpha + \frac{1}{2}} \approx \frac{1}{2} \left| \mathcal{U}_{\mathcal{Z}, \alpha + \frac{1}{2}}^H \right|. \quad (2.15)$$

Then, it reads

$$\eta_{\alpha + \frac{1}{2}} = \eta_{\alpha + \frac{1}{2}}(\mathcal{U}_{\mathcal{Z}, \alpha + \frac{1}{2}}^H) = \frac{\mu(I_{\alpha + \frac{1}{2}}) p_{\alpha + \frac{1}{2}}}{\max \left( \frac{1}{2} \left| \mathcal{U}_{\mathcal{Z}, \alpha + \frac{1}{2}}^H \right|, \frac{\mu(I_{\alpha + \frac{1}{2}}) p_{\alpha + \frac{1}{2}}}{\eta_M} \right)}, \quad (2.16)$$

with

$$p_{\alpha + \frac{1}{2}} = \frac{\rho}{Fr^2} \sum_{\beta=\alpha+1}^N h_\beta, \quad I_{\alpha + \frac{1}{2}} = \frac{d_s \left| \mathcal{U}_{\mathcal{Z}, \alpha + \frac{1}{2}}^H \right|}{\sqrt{p_{\alpha + \frac{1}{2}} / \rho_s}}, \quad \text{for } \alpha = 0, \dots, N-1. \quad (2.17)$$

Note that  $\eta_{N+1/2} = 0$ , because we suppose that the atmospheric pressure is zero.

### 2.3.3 Derivation of the final model with $\mu(I)$ viscosity

The derivation of the final model is totally analogous to the development in Subsection 1.4. We consider the weak formulation of (2.10) in  $\Omega_\alpha(t)$  for  $\alpha = 1, \dots, N$

$$\left\{ \begin{array}{l} 0 = \int_{\Omega_\alpha(t)} (\nabla \cdot \mathbf{u}_\alpha) \varphi \, d\Omega, \\ -\frac{1}{\varepsilon} \int_{\Omega_\alpha(t)} \rho \mathbf{g} \cdot \mathbf{v} \, d\Omega = \int_{\Omega_\alpha(t)} \rho \partial_t \mathbf{u}_\alpha \cdot \mathbf{v} \, d\Omega + \int_{\Omega_\alpha(t)} \rho (\mathbf{u}_\alpha \cdot \nabla \mathbf{u}_\alpha) \cdot \mathbf{v} \, d\Omega + \\ + \frac{1}{\varepsilon} \int_{\Omega_\alpha(t)} (\nabla \cdot (\mathcal{E} p_\alpha)) \cdot \mathbf{v} \, d\Omega - \frac{1}{\varepsilon} \int_{\Omega_\alpha(t)} (\nabla \cdot (\boldsymbol{\tau}_{\varepsilon, \alpha})) \cdot \mathbf{v} \, d\Omega, \end{array} \right. \quad (2.18)$$

for all  $\varphi \in L^2(\Omega_\alpha(t))$  and for all  $\mathbf{v} \in H^1(\Omega_\alpha(t))^2$ , where  $\mathbf{u}_\alpha \in L^2(0, T; H^1(\Omega_\alpha(t))^2)$ ,  $\partial_t \mathbf{u}_\alpha \in L^2(0, T; L^2(\Omega_\alpha(t))^2)$  and  $p_\alpha \in L^2(0, T; L^2(\Omega_\alpha(t)))$ .

From one hand, the mass equation is obtained as for system (1.23), then the mass conservation law for each layer is

$$\partial_t h_\alpha + \partial_x (h_\alpha u_\alpha) = G_{\alpha+\frac{1}{2}} - G_{\alpha-\frac{1}{2}}, \quad \alpha = 1, \dots, N \quad (2.19)$$

where  $G_{N+1/2}$  and  $G_{1/2}$  are given data.

From the other hand, for a weak solution  $\mathbf{u}$  and for all  $\alpha = 1, \dots, N$ , the horizontal momentum equation reads:

$$\begin{aligned} -\frac{1}{\varepsilon} \int_{\Omega_\alpha(t)} \rho \mathbf{g} \cdot (v, 0) \, d\Omega &= \int_{\Omega_\alpha(t)} \rho \partial_t (u_\alpha, \varepsilon w_\alpha) \cdot (v, 0) \, d\Omega + \\ + \int_{\Omega_\alpha(t)} \rho \left( (u_\alpha, \varepsilon w_\alpha) \cdot \nabla (u_\alpha, w_\alpha) \right) \cdot (v, 0) \, d\Omega - \\ - \frac{1}{\varepsilon} \int_{\Omega_\alpha(t)} (p_\alpha \mathcal{E}) : \nabla (v, 0) \, d\Omega + \frac{1}{\varepsilon} \int_{\Omega_\alpha(t)} \boldsymbol{\tau}_{\varepsilon, \alpha} : \nabla (v, 0) \, d\Omega + \\ + \frac{1}{\varepsilon} \int_{\Gamma_{\alpha+\frac{1}{2}}(t)} \left( \left( -p_{\alpha+\frac{1}{2}} \mathcal{E} + \boldsymbol{\tau}_{\varepsilon, \alpha+\frac{1}{2}}^- \right) \mathbf{n}_{\alpha+\frac{1}{2}} \right) \cdot (v, 0) \, d\Gamma - \\ - \frac{1}{\varepsilon} \int_{\Gamma_{\alpha-\frac{1}{2}}(t)} \left( \left( -p_{\alpha-\frac{1}{2}} \mathcal{E} + \boldsymbol{\tau}_{\varepsilon, \alpha-\frac{1}{2}}^+ \right) \mathbf{n}_{\alpha-\frac{1}{2}} \right) \cdot (v, 0) \, d\Gamma. \end{aligned} \quad (2.20)$$

Now each term of this equation is developed accounting that  $\partial_z u_\alpha = \partial_z v = \mathbf{v}|_{\partial I_F(t)} = 0$ . The only terms that differ from those in Subsection 1.3.3 are those affected by the stress tensor. So we specify the development just for them. The rest of the terms in (2.20) follow the same pattern as previously.

We prove that the term corresponding with the horizontal diffusion is a second-order term:

$$\frac{1}{\varepsilon} \int_{\Omega_\alpha(t)} \tau_{\varepsilon,\alpha}^{xx} \partial_x v \, d\Omega = -\frac{1}{\varepsilon} \int_{I_F(t)} \partial_x \left( \int_{z_{\alpha-1/2}}^{z_{\alpha+1/2}} \tau_{\varepsilon,\alpha}^{xx} \, dz \right) v \, dx.$$

Because  $\partial_z u_\alpha = 0$ , we obtain that  $\|D_\varepsilon(\mathbf{u}_\alpha)\|$  is independent of  $z$  up to order  $\varepsilon$ , since

$$D_\varepsilon(\mathbf{u}_\alpha) = \begin{pmatrix} \varepsilon^2 \partial_x u_\alpha & 0 \\ 0 & \partial_z w \end{pmatrix}.$$

Then, we get

$$\frac{1}{\varepsilon} \int_{z_{\alpha-1/2}}^{z_{\alpha+1/2}} \tau_{\varepsilon,\alpha}^{xx} \, dz = \frac{1}{\varepsilon} \int_{z_{\alpha-1/2}}^{z_{\alpha+1/2}} \varepsilon^2 \eta \partial_x u_\alpha \, dz = O(\varepsilon).$$

Therefore, we can neglect this term since we are interested in the first-order model. Thus, the momentum equation reads

$$\begin{aligned} & \rho h_\alpha \partial_t u_\alpha + \rho h_\alpha u_\alpha \partial_x u_\alpha + \frac{\rho}{Fr^2} h_\alpha \partial_x (b+h) + \rho \frac{1}{\varepsilon} h_\alpha \frac{\tan \theta}{Fr^2} + \\ & + \frac{1}{\varepsilon} \left( \tau_{\varepsilon,\alpha+1/2}^{xx,-} \partial_x z_{\alpha+1/2} - \tau_{\varepsilon,\alpha+1/2}^{xz,-} \right) - \frac{1}{\varepsilon} \left( \tau_{\varepsilon,\alpha-1/2}^{xx,+} \partial_x z_{\alpha-1/2} - \tau_{\varepsilon,\alpha-1/2}^{xz,+} \right) = 0, \end{aligned}$$

for each layer  $\alpha = 1, \dots, N$ . Analogously to Subsection 1.3.3, we can write the terms that appears at the interfaces by using (2.13):

$$\tau_{\varepsilon,\alpha+1/2}^{xx,-} \partial_x z_{\alpha+1/2} - \tau_{\varepsilon,\alpha+1/2}^{xz,-} = \tilde{\tau}_{\varepsilon,\alpha+1/2}^{xx} \partial_x z_{\alpha+1/2} - \tilde{\tau}_{\varepsilon,\alpha+1/2}^{xz} - \frac{\varepsilon}{2} \rho G_{\alpha+1/2} (u_{\alpha+1} - u_\alpha),$$

and

$$\tau_{\varepsilon,\alpha-1/2}^{xx,+} \partial_x z_{\alpha-1/2} - \tau_{\varepsilon,\alpha-1/2}^{xz,+} = \tilde{\tau}_{\varepsilon,\alpha-1/2}^{xx} \partial_x z_{\alpha-1/2} - \tilde{\tau}_{\varepsilon,\alpha-1/2}^{xz} + \frac{\varepsilon}{2} \rho G_{\alpha-1/2} (u_\alpha - u_{\alpha-1}).$$

Therefore, the momentum equation is rewritten as

$$\begin{aligned} & \rho h_\alpha \partial_t u_\alpha + \rho h_\alpha u_\alpha \partial_x u_\alpha + \frac{\rho}{Fr^2} h_\alpha \partial_x (b+h) + \rho \frac{1}{\varepsilon} h_\alpha \frac{\tan \theta}{Fr^2} + \\ & + \frac{1}{\varepsilon} \left( \tilde{\tau}_{\varepsilon,\alpha+1/2}^{xx} \partial_x z_{\alpha+1/2} - \tilde{\tau}_{\varepsilon,\alpha+1/2}^{xz} \right) - \frac{1}{\varepsilon} \left( \tilde{\tau}_{\varepsilon,\alpha-1/2}^{xx} \partial_x z_{\alpha-1/2} - \tilde{\tau}_{\varepsilon,\alpha-1/2}^{xz} \right) = \\ & = \frac{1}{2} \rho G_{\alpha+1/2} (u_{\alpha+1} - u_\alpha) + \frac{1}{2} \rho G_{\alpha-1/2} (u_\alpha - u_{\alpha-1}). \end{aligned}$$

In this case, the non-dimensional term  $K_{\alpha+\frac{1}{2}}$  (1.27) reads,

$$\begin{aligned} K_{\alpha+\frac{1}{2}} &= \frac{1}{\varepsilon} \left( \tilde{\tau}_{\varepsilon, \alpha+\frac{1}{2}}^{xx} \partial_x z_{\alpha+\frac{1}{2}} - \tilde{\tau}_{\varepsilon, \alpha+\frac{1}{2}}^{xz} \right) = \frac{1}{\varepsilon} \left[ \tilde{\boldsymbol{\tau}}_{\varepsilon, \alpha+\frac{1}{2}} \mathbf{n}_{\alpha+\frac{1}{2}} \sqrt{1 + \left( \partial_x z_{\alpha+\frac{1}{2}} \right)^2} \right]_H = \\ &= \frac{1}{\varepsilon} \left[ \eta \tilde{D}_{\varepsilon, \alpha+\frac{1}{2}} \mathbf{n}_{\alpha+\frac{1}{2}} \right]_H \sqrt{1 + \left( \partial_x z_{\alpha+\frac{1}{2}} \right)^2} = \varepsilon \eta_{\alpha+\frac{1}{2}} \partial_x \left( \frac{u_{\alpha+\frac{1}{2}}^+ + u_{\alpha+\frac{1}{2}}^-}{2} \right) \partial_x z_{\alpha+\frac{1}{2}} - \\ &-\frac{\varepsilon}{2} \eta_{\alpha+\frac{1}{2}} \left( \partial_x \left( \frac{w_{\alpha+\frac{1}{2}}^+ + w_{\alpha+\frac{1}{2}}^-}{2} \right) \right)' - \frac{1}{2\varepsilon} \eta_{\alpha+\frac{1}{2}} \mathcal{U}_{Z, \alpha+\frac{1}{2}}^H. \end{aligned}$$

Thus, we get

$$K_{\alpha+\frac{1}{2}} = -\frac{1}{2\varepsilon} \eta_{\alpha+\frac{1}{2}} \mathcal{U}_{Z, \alpha+\frac{1}{2}}^H + \mathcal{O}(\varepsilon), \quad (2.21)$$

where  $\eta_{\alpha+\frac{1}{2}}$  is defined by (2.16)-(2.17).

By combining the previous equation with (2.19) we get the momentum equation up to order  $\varepsilon$ ,

$$\begin{aligned} \rho \partial_t (h_\alpha u_\alpha) + \rho \partial_x (h_\alpha u_\alpha^2) + \frac{\rho}{Fr^2} h_\alpha \partial_x (b+h) + \rho \frac{1}{\varepsilon} h_\alpha \frac{\tan \theta}{Fr^2} &= \\ = K_{\alpha-\frac{1}{2}} - K_{\alpha+\frac{1}{2}} + \frac{1}{2} \rho G_{\alpha+\frac{1}{2}} (u_{\alpha+1} + u_\alpha) - \frac{1}{2} \rho G_{\alpha-\frac{1}{2}} (u_\alpha + u_{\alpha-1}), \end{aligned} \quad (2.22)$$

for  $\alpha = 1, \dots, N$ .

Next, we must impose the friction condition at the bottom ( $\Gamma_{\alpha-\frac{1}{2}}$  with  $\alpha = 1$ ). We can translate (2.8) into the notation of the multilayer approach, giving

$$w|_{\Gamma_{\frac{1}{2}}} = 0; \quad \frac{1}{2\varepsilon} \eta_{\frac{1}{2}} \mathcal{U}_{Z, \frac{1}{2}}^H = \frac{\mu(I_{\frac{1}{2}})}{\varepsilon} p_{\frac{1}{2}} \frac{u_{\frac{1}{2}}^+}{|u_{\frac{1}{2}}^+|}.$$

Therefore to impose the friction condition, we should change definition (2.21) of  $K_{\frac{1}{2}}$ , taking into account that  $u_{\frac{1}{2}}^+ = u_1$ . Then we obtain

$$K_{\frac{1}{2}} = -\frac{1}{2\varepsilon} \eta_{\frac{1}{2}} \mathcal{U}_{Z, \frac{1}{2}}^H = -\frac{\mu(I_{\frac{1}{2}})}{\varepsilon} p_{\frac{1}{2}} \frac{u_1}{|u_1|}.$$

The last step is to come back to the original variables taking into account the assumptions described in Subsection 2.3.1.

### 2.3.4 Final model

The final model reads, for  $\alpha = 1, \dots, N$ ,

$$\begin{cases} l_\alpha \left( \partial_t h + \partial_x (h u_\alpha) \right) = G_{\alpha+\frac{1}{2}} - G_{\alpha-\frac{1}{2}}, \\ l_\alpha \left( \rho \partial_t (h u_\alpha) + \rho \partial_x (h u_\alpha^2) + \rho g \cos \theta h \partial_x (b + \tilde{b} + h) \right) = \\ = K_{\alpha-\frac{1}{2}} - K_{\alpha+\frac{1}{2}} + \frac{1}{2} \rho G_{\alpha+\frac{1}{2}} (u_{\alpha+1} + u_\alpha) - \frac{1}{2} \rho G_{\alpha-\frac{1}{2}} (u_\alpha + u_{\alpha-1}) \end{cases} \quad (2.23)$$

where  $G_{\alpha+\frac{1}{2}}$  are given in (2.12),

$$K_{\alpha+\frac{1}{2}} = -\frac{1}{2} \eta_{\alpha+\frac{1}{2}} (\mathcal{U}_{Z, \alpha+\frac{1}{2}}^H) \mathcal{U}_{Z, \alpha+\frac{1}{2}}^H \quad \text{and} \quad K_{\frac{1}{2}} = -\mu(I_{\frac{1}{2}}) \rho g \cos \theta h \frac{u_1}{|u_1|}, \quad (2.24)$$

for  $\eta_{\alpha+\frac{1}{2}}$  defined in (2.16)-(2.17).

As in Chapter 1, the proposed model can be rewritten with  $N+1$  equations and unknowns: the total height ( $h$ ) and the discharge of each layer ( $q_\alpha = h u_\alpha$ , for  $\alpha = 1, \dots, N$ ). By introducing the coefficients  $\xi_{\alpha, \gamma}$  defined by (1.31), the system (2.23)-(2.24) is rewritten as

$$\begin{cases} \partial_t h + \partial_x \left( \sum_{\beta=1}^N l_\beta q_\beta \right) = 0, \\ \partial_t q_\alpha + \partial_x \left( \frac{q_\alpha^2}{h} + g \cos \theta \frac{h^2}{2} \right) + g \cos \theta h \partial_x z_b + \\ + \sum_{\gamma=1}^N \frac{1}{2h l_\alpha} \left( (q_\alpha + q_{\alpha-1}) \xi_{\alpha-1, \gamma} - (q_{\alpha+1} + q_\alpha) \xi_{\alpha, \gamma} \right) \partial_x q_\gamma = \\ = \frac{1}{\rho l_\alpha} \left( K_{\alpha-\frac{1}{2}} - K_{\alpha+\frac{1}{2}} \right) \quad \alpha = 1, \dots, N, \end{cases}$$

where we recall that  $z_b = b + \tilde{b}$ .

Moreover, we can see that this model satisfies a dissipative energy inequality. Denoting the energy of the layer  $\alpha = 1, \dots, N$  for the system (2.23)-(2.24) by

$$E_\alpha = h_\alpha \left( \frac{|u_\alpha|^2}{2} + g \cos \theta \left( z_b + \frac{h}{2} \right) \right),$$

the following dissipative energy inequality is satisfied:

$$\begin{aligned} & \rho \partial_t \left( \sum_{\alpha=1}^N E_\alpha \right) + \rho \partial_x \left[ \sum_{\alpha=1}^N u_\alpha \left( E_\alpha + \rho g \cos \theta h_\alpha \frac{h}{2} \right) \right] \leq \\ & \leq -\rho g \cos \theta h |u_1| \mu(I) - \sum_{\alpha=1}^{N-1} \frac{\eta_{\alpha+\frac{1}{2}}}{2} \frac{(u_{\alpha+1} - u_\alpha)^2}{h_{\alpha+\frac{1}{2}}}. \end{aligned}$$

The proof of previous inequality follows directly from the calculations developed in Chapter 1 for the case of constant viscosity, taking into account that  $K_{\alpha+\frac{1}{2}}$  is defined by (2.24) and the horizontal diffusion term does not appear.

Finally, note that if we consider a no-slip condition to deduce the model instead of the Coulomb friction condition (2.5), the only difference that appears in the multilayer approach is the definition of  $K_{\frac{1}{2}}$ . It must be defined according to that boundary condition (see Subsection 3.2.1.2 for details).

## 2.4 Numerical tests

The numerical approximation is performed in 2D (downslope and normal directions). It will be explained in detail in Chapter 3. Summarising, we rewrite the model as a non-conservative hyperbolic system with source terms as in [56]. Then a splitting procedure is considered. First, we set aside the term that appears at the internal interfaces and a standard path-conservative finite volume method is applied. The second step is to solve the contribution of the term at the internal interfaces. In this step, a semi-implicit scheme is employed, taking into account the regularization of  $\|D(\mathbf{u}_\alpha)\|$  mentioned in Subsection 2.2 in order to avoid the singularity when  $\|D(\mathbf{u}_\alpha)\|$  vanishes.

In order to validate the Multilayer Shallow Model (denoted MSM hereafter) with the  $\mu(I)$  rheology, we compare it to (i) 2D steady and transient uniform flows over inclined surfaces with and without the effect of sidewall friction (analytical solutions and experimental data for deep and surface flows), (ii) laboratory experiments of highly transient and non-uniform granular flows over inclined planes covered by an erodible bed, in which case the shape of the velocity profiles strongly changes with time and space.

### 2.4.1 Granular surface flows in a channel

In this subsection we deal with several Bagnold flows. First, we consider a uniform Bagnold flow without taking into account the effect of the lateral wall friction. Then, we show that our multilayer model is able to capture the velocity profiles for flows in a



narrow channel when sidewall friction is introduced. In that case we compare with the analytical solution and laboratory experiments. Note that Bagnold flows satisfy, at the free surface

$$p|_{z=H} = 0 \quad \text{and} \quad \|D(\mathbf{u})\|_{|z=H} = \frac{1}{2} |\partial_z u|_{|z=H} = 0.$$

Therefore, we cannot use the regularization (2.4) since its denominator vanishes at the free surface. In this case we use the regularization

$$\eta = \frac{\mu(I)p}{\sqrt{\|D(\mathbf{u})\|^2 + \delta^2}},$$

where  $\delta > 0$  is a small parameter (see Bercovier & Engelman [13]).

#### 2.4.1.1 Steady uniform Bagnold flow: analytical solution

Let us first compare the model with the analytical solution for a uniform flow over an inclined plane of slope  $\theta$  and thickness  $H > 0$ , i.e. a Bagnold flow (see [60], [107] or [79]). This solution is obtained by imposing zero pressure and zero shear stress at the free surface and a no-slip condition at the bottom (Coulomb friction can be easily changed by no-slip condition in the  $\mu(I)$  rheology multilayer model, see Subsection 3.2.1.2).

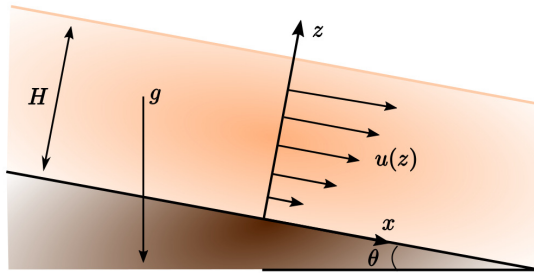


Figure 2.1: Sketch of the analytical solution.

By denoting  $u$  and  $w$  the downslope and normal velocities,  $p$  the pressure and  $\tau$  the shear stress and by taking the rheological parameters defined in Subsection 2.2, the steady uniform Bagnold flow is described by

$$\left\{ \begin{array}{l}
u(z) = \frac{2}{3d_s} I_0 \left( \frac{\tan \theta - \mu_s}{\mu_2 - \tan \theta} \right) \sqrt{\varphi_s g \cos \theta} \left( H^{3/2} - (H - z)^{3/2} \right), \\
u(z=0) = 0, \quad w = 0, \\
p(z) = \rho g \cos \theta (H - z), \\
\tau(z) = \mu(I)p = \rho g \sin \theta (H - z), \\
p(z=H) = 0, \quad \tau(z=H) = 0, \\
\mu(I) = \tan(\theta),
\end{array} \right. \quad \text{for } z \in (0, H). \quad (2.25)$$

For the numerical simulation, as in the analytical solution, we consider a uniform flow with constant thickness  $H = 1$  m and velocity  $u = w = 0$  m·s<sup>-1</sup> at the initial time  $t = 0$  s. The boundary conditions at the free surface and at the bottom have been set as in (2.25). At the right and left boundaries, we use open boundary conditions.

We choose the rheological parameters  $I_0 = 0.279$  and  $\mu_s = 0.38 \approx \tan(20.8^\circ)$ ,  $\mu_2 = 0.62 \approx \tan(31.8^\circ)$  and the particle diameter  $d_s = 4$  cm with solid volume fraction  $\varphi_s = 0.62$ . The slope angle is taken as  $\theta = 0.43$  rad  $\approx 24.64^\circ$ . Figure 2.2 shows the good agreement between the simulated and exact solutions for the profiles of the velocity, pressure, shear stress,  $\mu(I)$  and  $\|D(u)\|$ . It also shows the downslope velocity at the free surface as a function of the slope angle. Note that for slopes smaller than  $\arctan(\mu_s)$ , the surface velocity is close to zero (it is not equal to zero, because of the regularization method), namely  $u(z=H) \sim 10^{-5}$ , so that the mass is almost at rest.

These results are computed using 50 layers in the MSM. Note that we use a slope in the well-posed region described in Barker *et al.* [12] for the full  $\mu(I)$  rheology, which is smaller than the well-posed region for the depth-averaged  $\mu(I)$  rheology (well-posed for  $\delta_s = 20.8^\circ \leq \theta < \delta_2 = 31.8^\circ$  in the case of depth-averaged  $\mu(I)$  rheology). If we use a slope close enough to  $\delta_2$  the system becomes unstable because of the ill-posedness of the full  $\mu(I)$  rheology in this region.

Figure 2.3 shows the computing time required to simulate 50 seconds (on a laptop with Intel®Core™ i7-4500U and 8 GB of RAM) and the relative error between the computed velocity and the exact solution using a different number of layers and 30 nodes in the  $x$ -direction. In table 2.1 we show that second-order accuracy is reached in norms  $L^1$  and  $L^2$ , while in norm  $L^\infty$  the order is over 1.5. This behaviour in norm  $L^\infty$  is due to the boundary conditions at the free surface, where the analytical solution satisfies that  $\partial_z u = 0$ .

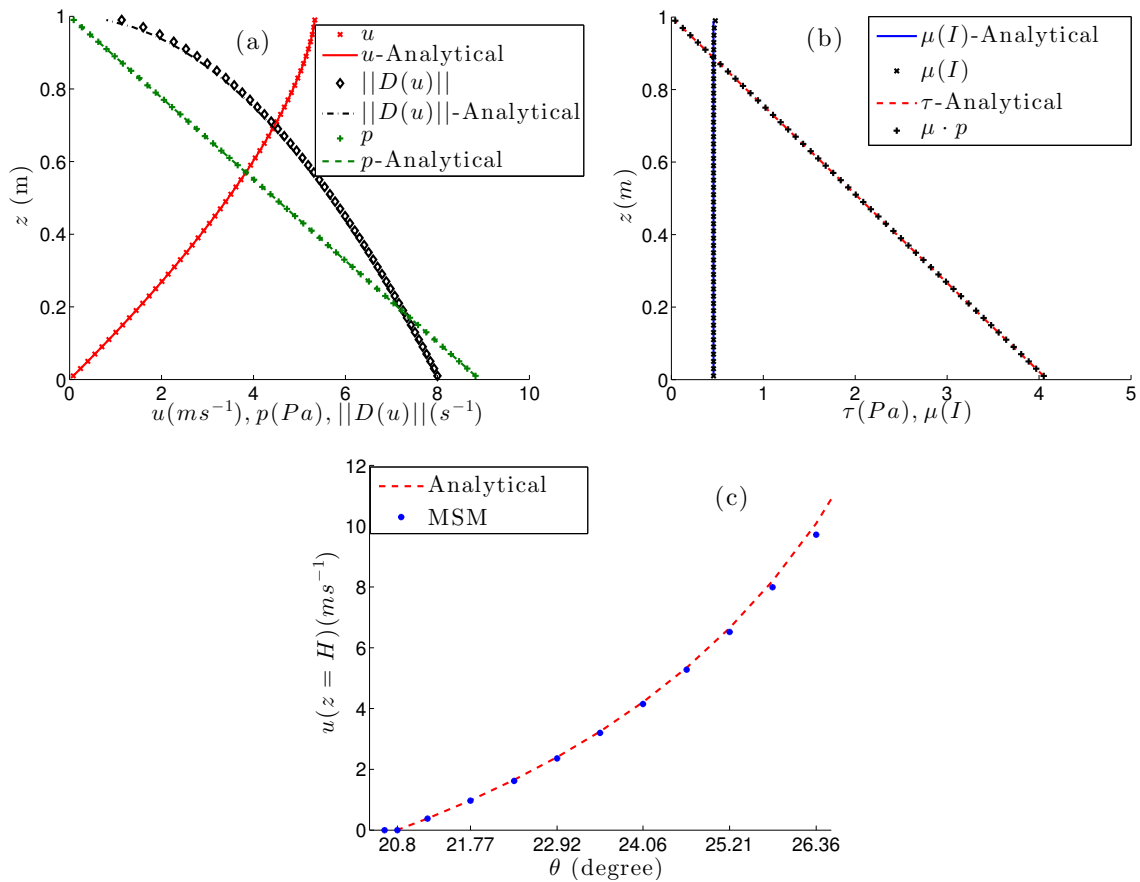


**Figure 2.2:** Comparison between the analytical solution (dashed and solid lines) and the simulations obtained using the MSM with the  $\mu(I)$  rheology (symbols). (a) Analytical and simulated downslope horizontal velocity  $u$ , pressure  $p$  and strain rate  $\|D(\mathbf{u})\|$ ; (b) Analytical and simulated shear stress and friction coefficient  $\mu(I)$ ; (c) Comparison between the simulated (symbols) and the exact (dashed line) horizontal velocity at the free surface as a function of the slope angle.

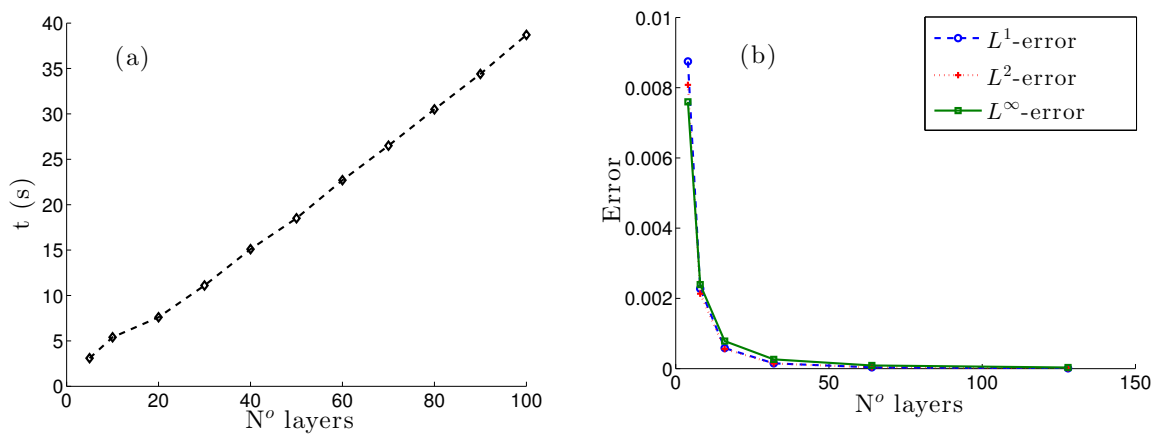


**Figure 2.3:** (a) Computing time as a function of the number of layers in the MSM and (b) relative error between the computed and exact velocity for simulations over a slope of  $\theta = 24.64^\circ$ .

$N(\Delta z = 1/N)$	$L^1$ - Error	$L^1$ - Order	$L^2$ - Error	$L^2$ - Order	$L^\infty$ - Error	$L^\infty$ - Order
4	$8.74 \times 10^{-3}$	–	$8.08 \times 10^{-3}$	–	$7.59 \times 10^{-3}$	–
8	$2.27 \times 10^{-3}$	1.84	$2.13 \times 10^{-3}$	1.92	$2.39 \times 10^{-3}$	1.66
16	$5.84 \times 10^{-4}$	1.96	$5.58 \times 10^{-4}$	1.93	$7.84 \times 10^{-4}$	1.61
32	$1.48 \times 10^{-4}$	1.97	$1.45 \times 10^{-4}$	1.941	$2.62 \times 10^{-4}$	1.57
64	$3.76 \times 10^{-5}$	1.982	$3.76 \times 10^{-5}$	1.948	$8.94 \times 10^{-5}$	1.55
128	$9.48 \times 10^{-6}$	1.988	$9.73 \times 10^{-6}$	1.95	$3.08 \times 10^{-5}$	1.53

Table 2.1: Order of the error for the velocity of the Bagnold flow.

### 2.4.1.2 2D steady uniform flow in a channel: sidewalls effect on the velocity profile

The relevance of the lateral wall friction when a granular material flows in a channel has been proved by Jop *et al.* [75] (see also Baker *et al.* [10]). Under the hypothesis of a steady uniform flow and neglecting the variations in the transverse direction, they propose to model this effect with a modified  $\mu(I)$  rheology by adding an extra term, which defines an effective friction term

$$\mu(I) = \mu_s + \frac{\mu_2 - \mu_s}{I_0 + I} I + \mu_w \frac{H - z}{W}, \quad (2.26)$$

where  $W$  is the channel width,  $\mu_w$  is the constant coefficient of friction with the side walls and  $H$  the thickness of the flow. Note that this extra term (last term) increases when we get closer to the bottom from the free surface. In addition, for a channel slope  $\theta$  with respect to the horizontal axis, the analytical expression for the velocity profile reads (see appendix B in Jop *et al.* [75]):

$$u(z) = 2 \frac{I_0 \sqrt{\varphi_s g \cos \theta}}{d_s} \left[ \frac{1}{3} (H - z)^{3/2} - \frac{1}{3} (H - h^*)^{3/2} - \frac{\mu_2 - \mu_s}{\mu_w} W \left( (H - z)^{1/2} - (H - h^*)^{1/2} \right) + \sqrt{h_2} \frac{\mu_2 - \mu_s}{\mu_w} W \left( \arctan \sqrt{\frac{H - z}{h_2}} - \arctan \sqrt{\frac{H - h^*}{h_2}} \right) \right],$$

where

$$h^* = H - \frac{\tan \theta - \mu_s}{\mu_w} W, \quad h_2 = \frac{\mu_2 - \tan \theta}{\mu_w} W.$$

Note that we can integrate the last equation and the discharge is obtained as a function of the slope  $\theta$ . In these experiments, Jop *et al.* [75] fixed the discharge and computed the velocity profile for different widths. We choose the same material and rheological properties and perform these experiments. The grain diameter is  $d_s = 0.53$  mm and the volume fraction is  $\varphi_s = 0.6$ . The rheological parameters are  $\mu_s = \tan(20.9^\circ)$ ,  $\mu_2 = \tan(32.76^\circ)$

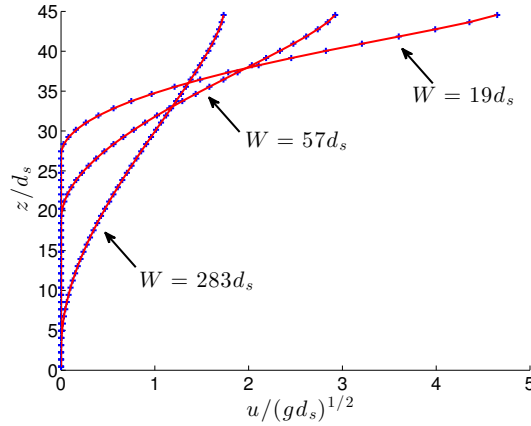


Figure 2.4: Comparison between the analytical solution (solid lines) and the simulations obtained using the MSM with the  $\mu(I)$  rheology (symbols) for the velocity profile for  $Q^* = 31.5$ , and different widths:  $W = 19d_s$ ,  $W = 57d_s$  and  $W = 283d_s$ .

$N$ ( $\Delta z = 1/N$ )	$L^1$ -Error	$L^1$ -Order	$L^2$ -Error	$L^2$ -Order	$L^\infty$ -Error	$L^\infty$ -Order
4	$1.72 \times 10^{-2}$	–	$1.41 \times 10^{-2}$	–	$1.14 \times 10^{-2}$	–
8	$4.71 \times 10^{-3}$	1.87	$5.24 \times 10^{-3}$	1.43	$6.61 \times 10^{-3}$	0.78
16	$1.33 \times 10^{-3}$	1.82	$1.21 \times 10^{-3}$	2.11	$1.42 \times 10^{-3}$	2.21
32	$2.65 \times 10^{-4}$	2.32	$3.50 \times 10^{-4}$	1.79	$7.23 \times 10^{-4}$	0.97
64	$7.46 \times 10^{-5}$	1.83	$1.00 \times 10^{-4}$	1.80	$2.56 \times 10^{-4}$	1.49
128	$1.80 \times 10^{-5}$	2.05	$2.58 \times 10^{-5}$	1.95	$8.80 \times 10^{-5}$	1.54

Table 2.2: Order of the error for the velocity of the Bagnold flow with lateral walls friction. Case  $W = 283d_s$ .

and  $I_0 = 0.279$ . The friction coefficient with the sidewalls is  $\mu_w = \tan(10.4^\circ)$ . We set the thickness of the flow  $H = 45d_s$ , the dimensionless discharge  $Q^* = 31.5$  and different widths of the channel are considered ( $W = 19d_s, 57d_s, 283d_s$ ).

Figure 2.4 shows the exact agreement between the analytical solution and the simulations for the velocity profile. In this case we consider 50 layers to obtain the solution. In table 2.2 we present the errors and accuracy order of the method for  $W = 283d_s$ . We obtain similar results to those presented in the previous subsection.

### 2.4.1.3 Laboratory experiments: transient velocity profiles

We compare our model with the experiments and simulations presented in Jop *et al.* [77] where granular material is flowing within a narrow channel of width  $W = 19d_s \approx 1$  cm. The grain diameter is  $d_s = 0.53$  mm, the volume fraction is  $\varphi_s = 0.6$  and the rheological parameters are  $\mu_s = \tan(20.9^\circ)$ ,  $\mu_2 = \tan(32.76^\circ)$  and  $I_0 = 0.279$ . The friction with the wall is modelled as in the precedent test, following (2.26). In this case, the authors set

the friction coefficient with the sidewalls as  $\mu_w = \tan(13.1^\circ)$ .

For the simulations, we impose zero velocity at the initial time and the material flows because of the gravitational force. We use 50 layers in the MSM. Figure 2.5 shows the comparison between the results in [77] and the simulation using the MSM  $\mu(I)$  rheology model for the transient velocity profiles and its final state in two configurations. As is concluded in [77], the agreement for the transient velocity profiles is better for high slopes and less accurate for low inclinations. In the case of high inclination angles our model results are similar to their simulations (see figure 2.5b), and are slightly better in the other cases (see figure 2.5a).

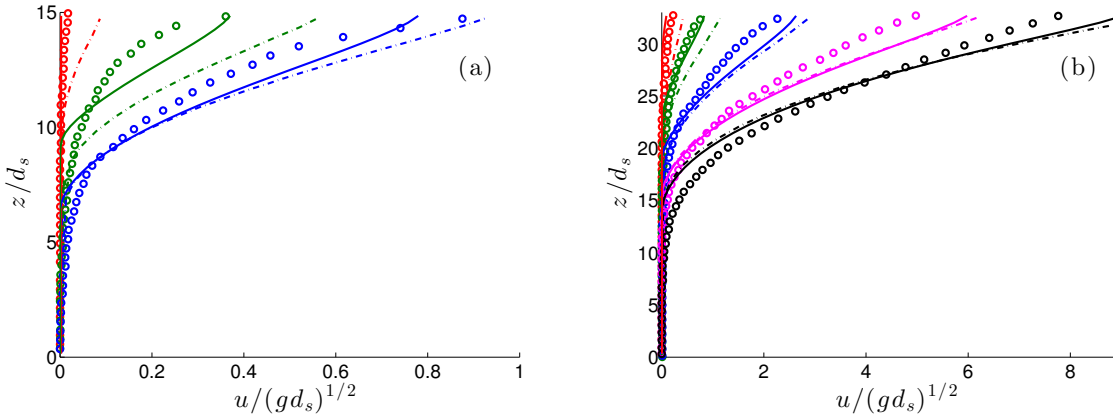


Figure 2.5: Comparison between the laboratory experiments (symbols) and simulations (dash-dotted lines) in [77], and simulations using the MSM with the  $\mu(I)$  rheology (solid lines) for the transient velocity profiles for two different slopes  $\theta$ , and times  $t^* = t/\sqrt{d_s/g}$ : (a)  $\theta = 26.1^\circ$ ,  $t^* = 1.2, 15.1, 166.1$ ; (b)  $\theta = 32.15^\circ$ ,  $t^* = 2.3, 7.5, 24.2, 77.8, 175$ .

## 2.4.2 Granular collapse experiments

We will now use the MSM to simulate the laboratory experiments performed in Mangeney *et al.* [87]. The objectives are: to evaluate if (i) the model with the  $\mu(I)$  rheology gives a reasonable approximation of the flow dynamics and deposits of highly transient and non-uniform granular flows, (ii) it recovers the strong change in the shape of the velocity profiles with time and space, (iii) it reproduces the increase in runout distance observed for increasing thickness of the erodible bed above a critical slope angle  $\theta_c \in [12^\circ, 16^\circ]$  and (iv) the multilayer approach improves the results compared to the classical depth-averaged Saint-Venant model (i.e. monolayer model).

In Subsection 2.4.2.1 we also introduce a modification in the calculation of the friction coefficient  $\mu(I)$ . In particular, we take into account second-order terms to approximate  $\|D(\mathbf{u})\|$ . As shown below, this correction provides better results in some test cases.

### 2.4.2.1 Improvement of the approximation of the $\mu(I)$ coefficient

The advantage of the multilayer models is that we obtain a variable profile of the downslope velocity, in contrast with the prescribed profile of the monolayer model. It makes it possible to obtain a better approximation of  $\|D(\mathbf{u})\|$  (see equation (2.15)). As a consequence, this improves the approximation of the inertial number  $I$  (see equations (2.2) and (2.17)), which is a key number in the variable friction coefficient  $\mu(I)$ .

As the main advantage of the multilayer model is the improvement of the approximation of  $\|D(\mathbf{u})\|$ , we present two approximations that can be made with the multilayer model. First, let us recall that a first-order approximation corresponds to the definition (2.15). This approximation considers only the leading-order term, i.e.  $\|D(\mathbf{u})\|_{\alpha+\frac{1}{2}} \approx \frac{1}{2} \left| \partial_z u_{\alpha+\frac{1}{2}} \right| = \frac{1}{2} \left| \mathcal{U}_{z, \alpha+\frac{1}{2}}^H \right|$ . Note that in dimensionless form, we have

$$\|D(\mathbf{u})\| = \frac{1}{2} \sqrt{(\partial_z u)^2 + 4\varepsilon^2 (\partial_x u)^2 + 2\varepsilon^2 \partial_x w \partial_z u + \varepsilon^4 (\partial_x w)^2}. \quad (2.27)$$

We can improve the approximation of  $\|D(\mathbf{u})\|$  at the interfaces  $z = z_{\alpha+\frac{1}{2}}$  by considering the approximation taking into account second-order terms in the previous equation. For the numerical tests, we consider the following approximation  $\|D(\mathbf{u})\|$  at the interfaces,

$$\|D(\mathbf{u})\|_{\alpha+\frac{1}{2}} \approx \frac{1}{2} \sqrt{\left| \mathcal{U}_{z, \alpha+\frac{1}{2}}^H \right|^2 + (\partial_x (u_{\alpha+1} + u_\alpha))^2}. \quad (2.28)$$

Note that this definition corresponds to an approximation of

$$\|D(\mathbf{u})\| \approx \frac{1}{2} \sqrt{(\partial_z u)^2 + 4 (\partial_x u)^2}$$

at  $z = z_{\alpha+\frac{1}{2}}$ . Nevertheless, in (2.27), the term  $2\partial_z u \partial_x w$  is not taken into account although it is of the same order as  $4(\partial_x u)^2$ . This is because when an approximation of this term is added, we obtain results that are very similar to those obtained when considering (2.28). Furthermore adding this term implies an additional computational cost since pre-calculated vertical velocities are required. Note that (2.28) is a second-order correction while we have developed a first-order model that neglects other second-order terms. This correction, however, highlights the importance of second-order terms in granular collapses over erodible beds, even if it is a partial correction.

The effect of this second-order approximation on the results is discussed below in subsections 2.4.2.3 and 2.4.2.4. In particular, we observe an improvement of the results compared to the original first-order approximation of  $\|D(\mathbf{u})\|$ .

### 2.4.2.2 Experimental and test data

In the laboratory experiments performed in Mangeney *et al.* [87], subspherical glass beads of diameter  $d_s = 0.7$  mm were used. The particle density  $\rho_s = 2500$  kg m<sup>-3</sup>

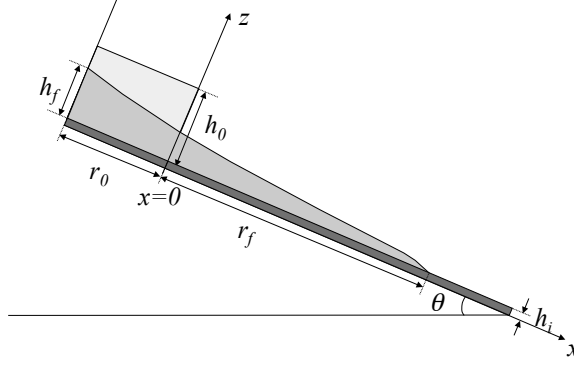


Figure 2.6: Sketch of the initial and final state of the granular collapse. A granular column with a thickness  $h_0 = 14$  cm and a length  $r_0 = 20$  cm is released on an inclined plane of slope  $\theta$ . The plane is covered by an erodible bed of thickness  $h_i$  made of the same material. When the flow stops, the maximum final thickness is  $h_f$  and its final extent  $r_f$ .

and volume fraction  $\varphi_s = 0.62$  were estimated, leading to an apparent flow density  $\rho = \varphi_s \rho_s = 1550$  kg m<sup>-3</sup>.

The variable  $r_f$  denotes the runout distance, i.e. the length of the deposit measured from the position of the front of the released material at the initial time located at  $x = 0$  m,  $t_f$  denotes the flow time from  $t = 0$  s to the time when the material stops and  $h_f$  denotes the maximum final thickness of the deposit (see figure 2.6).

In order to use the  $\mu(I)$  rheology, the rheological parameters ( $\mu_s$ ,  $\mu_2$  and  $I_0$ ) must be defined. We consider the data proposed in Ionescu *et al.* [70]. The minimum and maximum friction angles are  $\mu_s = \tan(20.9^\circ)$  and  $\mu_2 = \tan(32.76^\circ)$ , according to the measurements made in the experiments presented in Pouliquen & Forterre [100] and Jop *et al.* [75]. These parameters can be obtained by fitting the curve  $h_{stop}(\theta)$ , where  $h_{stop}$  is the thickness of the deposit lying on the slope when the supply is stopped after steady uniform flow (see Pouliquen [99] for more details). Nevertheless, in [70] the value of  $\mu_s$  and  $\mu_2$  are incremented, in order to consider the effect of lateral wall friction. Let us remember that lateral wall friction is modelled in Jop *et al.* [75] as an additional friction term  $\mu_w(h - z)/W$ , where  $\mu_w = \tan(10.4^\circ)$  is the coefficient of friction in the side walls. Moreover, the thickness of the flowing layer (see Mangeney *et al.* [87]) is approximately 0.05 m and the width of the channel  $W = 10$  cm. Therefore, the additional friction term is approximately 0.1. As a result, in Ionescu *et al.* [70] the authors propose to consider  $\mu_s = \tan(25.5^\circ) \approx \tan(20.9^\circ) + 0.1$  and  $\mu_2 = \tan(36.5^\circ) \approx \tan(32.76^\circ) + 0.1$ . Moreover, we set  $I_0 = 0.279$  (see Jop *et al.* [76]).

That might be a coarse way to introduce the wall friction effect, owing that the multilayer model is able to approximate the term  $\mu_w(h - z)/W$  in each layer. However, introducing the friction term  $\mu_w(h - z)/W$  does not give good results in this granular









Models/Data	Acronyms	Line style
Experimental data	Lab	
Multilayer Shallow Model	$\mu(I)$ - MSM	
MSM with the correction (2.28)	$\mu(I)$ - C - MSM	
Monolayer Model	$\mu(I)$ - monolayer	
MSM with const. friction coef.	$\mu_s$ - MSM	
Monolayer Model with const. friction coef.	$\mu_s$ - monolayer	

Table 2.3: Summary of notation of the different models and colors-symbols

collapse test. Actually it seems that there is not enough friction at the initial times to well capture the S-shaped profile. Note that the numerical simulations with the proposed hydrostatic multilayer approach cannot be accurate at short times because the dominant effect is the non-hydrostatic pressure. At short times the flowing layer can be overestimated, and, consequently, the effect of the lateral wall friction is not properly taken into account. These comparisons only make sense at the latter stage of the flow. We plot the results for intermediate times in order to illustrate this discussion (see figure 2.14).

This experiment has been simulated for different slopes  $\theta$  and thicknesses  $h_i$  of the erodible bed:  $\theta = 16^\circ$  and  $h_i = 1.4, 2.5, 5$  mm,  $\theta = 19^\circ$  and  $h_i = 1.5, 2.7, 5.3$  mm,  $\theta = 22^\circ$  and  $h_i = 1.82, 3.38, 4.6$  mm, and  $\theta = 23.7^\circ$  and  $h_i = 1.5, 2.5, 5$  mm. Note that the model does not take into account the effect of removing the gate during the initial instants even though it has a non-negligible impact on the flow dynamics as shown in Ionescu *et al.* [70]. For instance, when the gate is taken into account, even with no friction along it, the flow is substantially slowed down; however, the deposit is almost unchanged. All the simulations are performed using 20 layers.

We compare hereafter (i) the constant and variable friction rheologies and (ii) the monolayer and multilayer approaches. In table 2.3, we summarize the notation and symbols used for the different models. MSM is the notation for multilayer models. Note that the monolayer model with a constant friction coefficient (denoted  $\mu_s$ -monolayer model) corresponds to the Savage-Hutter classical model when  $K_{act/pas} = 1$ . This model is widely used in the literature, e.g. [65], [88]. Note also that the monolayer model with a variable friction coefficient (denoted  $\mu(I)$ -monolayer model) corresponds to the one proposed by Pouliquen [99], which has been recently used by Mangeney-Castelnau *et al.* [89] and Mangeney *et al.* [86]. This model also coincides with the one proposed in Gray & Edwards [64] by dropping second-order terms, that is, viscous terms.

### 2.4.2.3 Deposit profiles

Let us compare the deposits simulated with the  $\mu(I)$  rheology and with a constant friction coefficient  $\mu_s$  for different slopes  $\theta$  and erodible bed thicknesses  $h_i$ . Figure 2.7 shows that the deposit calculated with the variable friction coefficient  $\mu(I)$  is closer to the experimental deposit than the one calculated with a constant friction coefficient  $\mu_s$ . The runout distance with the constant coefficient  $\mu_s$  is always too long except for  $\theta = 19^\circ$  and  $h_i = 5.3$  mm (see figure 2.7d). To properly reproduce the runout distance with a constant friction coefficient, we need to increase its value. For example, with a slope  $\theta = 16^\circ$  and an erodible bed thickness  $h_i = 2.5$  mm (figure 2.7a), we need to use the value  $\mu_s = \tan(27.3^\circ)$  to produce the runout observed in the laboratory experiments. That means an increment of 0.039 in the  $\mu_s$  value. These results are consistent with the simulations of Ionescu *et al.* [70], showing that the runout is strongly overestimated when the viscosity tends to zero (i.e. when  $\mu$  tends to  $\mu_s$ ).

Figure 2.8 shows, for a slope  $\theta = 22^\circ$  and  $h_i = 1.82$  mm, the final deposit obtained using the constant or variable friction coefficients for multilayer and monolayer models. The difference between the multilayer and monolayer models is stronger when using the  $\mu(I)$  rheology. For instance, the multilayer approach changes the full deposit profiles for the  $\mu(I)$  rheology, while it only changes the front position for  $\mu_s$ . The multilayer approach makes it possible to obtain a deposit shape which is very close to the experiments with the  $\mu(I)$  rheology. More generally, the shape of the deposit is closer to the observations with  $\mu(I)$ -MSM than with  $\mu_s$ -MSM.

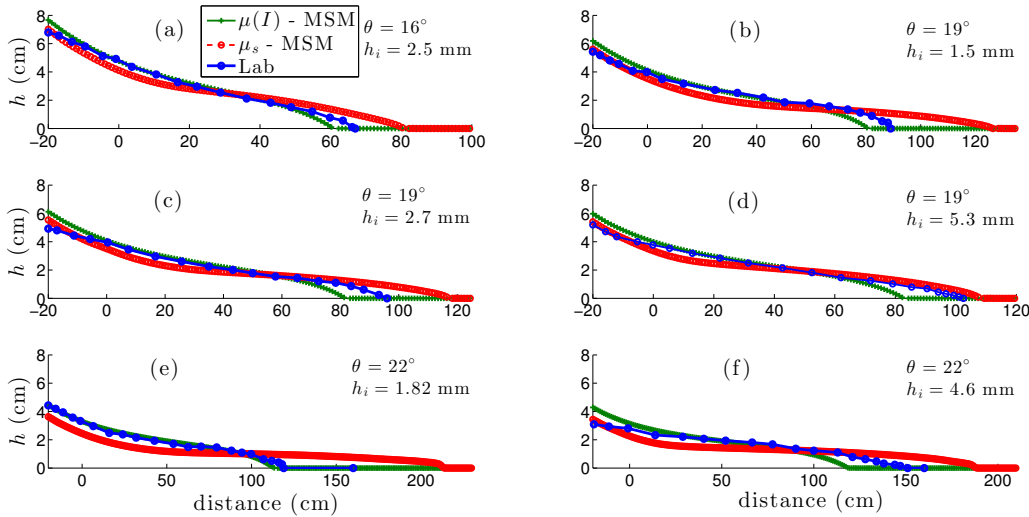


Figure 2.7: Deposit obtained in the experiments (solid-circle blue line), with the  $\mu_s$ -MSM (dotted-circle red line) and with the  $\mu(I)$ -MSM (solid-cross green line), for different slopes  $\theta$  and erodible bed thicknesses  $h_i$ .

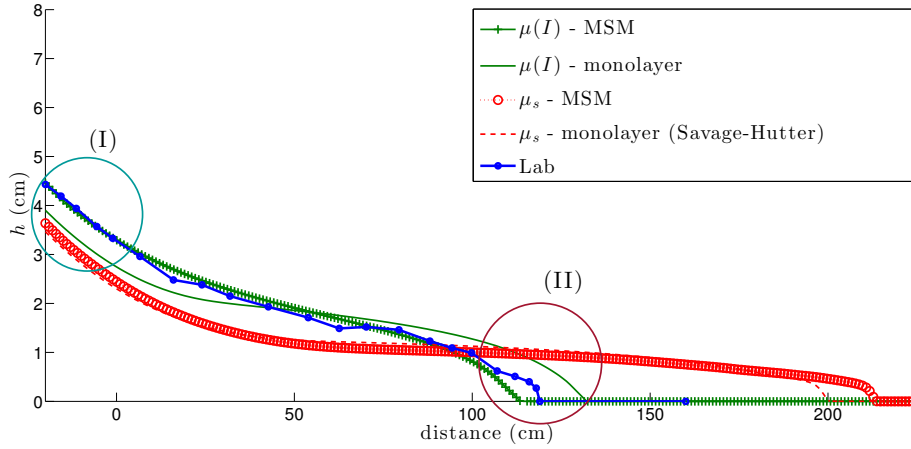


Figure 2.8: Deposit obtained in the experiments (solid-circle blue line), with the  $\mu_s$ -MSM (dotted-circle red line), the  $\mu(I)$ -MSM (solid-cross green line), the  $\mu_s$ -monolayer model (dashed red line) and with the  $\mu(I)$ -monolayer model (solid green line) for a slope  $\theta = 22^\circ$  and an erodible bed thickness  $h_i = 1.82$  mm. Circled sections indicates specific location for data shown in figure 2.9.

#### 2.4.2.4 Effect of the erodible bed

Figure 2.9 shows two zooms, one near the maximum thickness of the deposit (zone of circle (I) in figure 2.8), and one near the front (zone of circle (II) in figure 2.8), for  $\theta = 22^\circ$  and different values of  $h_i$ . With the  $\mu(I)$ -MSM, the runout distance  $r_f$  increases as the thickness of the erodible bed  $h_i$  increases (figure 2.9a(II)) as observed in laboratory experiments. On the contrary, with the  $\mu_s$ -MSM (figure 2.9b(II)), the runout distance  $r_f$  decreases with increasing  $h_i$ . Note that in both cases the maximum final thickness  $h_f$  decreases with increasing  $h_i$  as it occurs in the experiments (figure 2.9a(I),b(I)).

Figure 2.10 shows that the decrease in runout distance with increasing  $h_i$  for constant friction  $\mu_s$  is observed for all slopes, e.g.  $\theta = 0^\circ, 10^\circ, 16^\circ, 19^\circ, 22^\circ$ , and  $23.7^\circ$ . For the constant friction coefficient case, the  $\mu_s$ -MSM and  $\mu_s$ -monolayer models follow the same trend. Note that this non-physical decrease in runout distance with increasing  $h_i$  has been demonstrated analytically in [50] for the monolayer model. Moreover, laboratory experiments show that when the thickness of the erodible bed increases, for slopes  $\theta \geq \theta_c$ , where  $\theta_c \in [12^\circ, 16^\circ]$  is a critical slope, the runout distance  $r_f$  and the stopping time  $t_f$  both increase while the maximum final thickness  $h_f$  decreases. Note that there is no pattern concerning the runout when the thickness  $h_i$  is increased for slopes  $\theta < \theta_c$  ( $\theta = 0^\circ, 10^\circ$ ) in the laboratory experiments.

Figure 2.11 shows that the increase of runout distance observed in the experiments for increasing  $h_i$  is qualitatively well reproduced with the  $\mu(I)$ -MSM. With the  $\mu(I)$ -MSM, the runout increase with  $h_i$  is actually larger for higher slopes, as observed experimentally: at  $\theta = 16^\circ$ , the runout distance is almost unaffected by the thickness of the erodible bed while it increases by 26.9% at  $\theta = 22^\circ$  when the thickness of the erodible bed increase

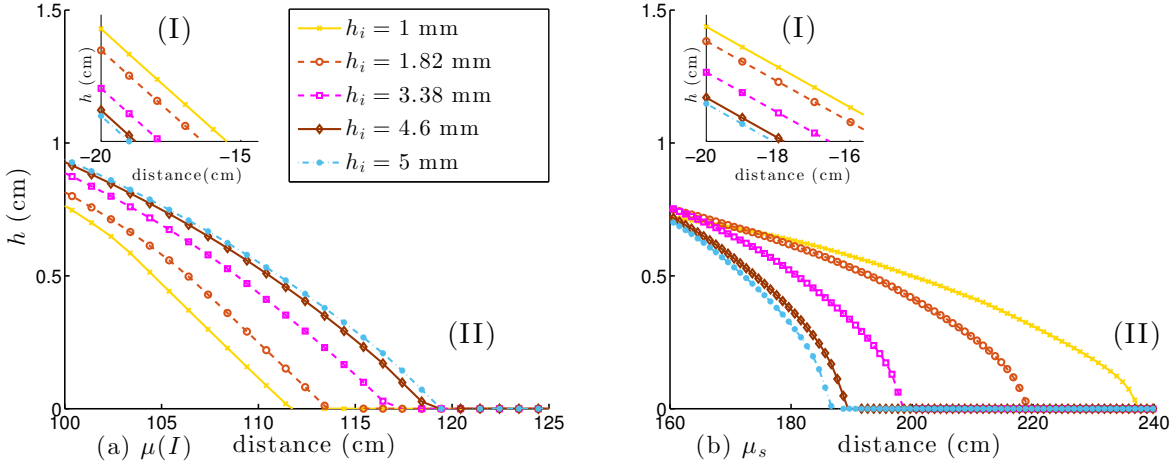


Figure 2.9: Influence of the thickness of the erodible bed on the runout distance  $r_f$  and on the maximum final thickness  $h_f$  (inset graphs) with the  $\mu(I)$ -MSM (left hand side) and with the  $\mu_s$ -MSM (right hand side), for a slope  $\theta = 22^\circ$ , in zones marked with circle in figure 2.8.

from 1.82 mm to 4.6 mm. Note that in the  $\mu(I)$ -MSM, the increase of the runout distance appears on slopes  $\theta > 16^\circ$ , higher than  $\theta_c$  in the experiments. Actually, it appears starting with the slope  $\theta = 18^\circ$ . When using the  $\mu(I)$ -monolayer model, the runout distance is higher than for the  $\mu(I)$ -MSM whatever the slope and thickness of the erodible bed. Based on the values of the runout distance in these cases, it is hard to discriminate which of the monolayer or multilayer models is closer to the experiments. However, in the  $\mu(I)$ -monolayer model, the runout distance at  $\theta = 16^\circ$  and  $19^\circ$  decreases when  $h_i$  increases, contrary to the experimental data. For  $\theta = 22^\circ$  and  $\theta = 23.7^\circ$ , the monolayer and multilayer  $\mu(I)$  models reproduce qualitatively the increase in runout with  $h_i$ . Note that for  $\theta = 0^\circ, 10^\circ$  ( $\theta < \theta_c$ ), the  $\mu(I)$  models predict a very slight decrease in the runout distance.

The  $\mu(I)$ -MSM is the model corresponding to the multilayer approach with the  $\mu(I)$  rheology when  $\|D(\mathbf{u})\|$  is approximated by the main term in (2.27), and  $\mu(I)$ -C-MSM when  $\|D(\mathbf{u})\|$  is approximated by the correction (2.28). Figure 2.11 shows that the correction of  $\|D(\mathbf{u})\|$  corresponding to  $\mu(I)$ -C-MSM improves the simulation of both the runout extent and the influence of the erodible bed. They both increase the runout when  $h_i$  increases, although the effect of erosion is still much smaller than in the experiments.

For example, for  $\theta = 19^\circ$ , when  $h_i$  varies from 1.5 mm to 5.3 mm, the experimental runout increases by 15.1%. On the contrary, for the monolayer model the runout decreases by 1.1%. For the  $\mu(I)$ -MSM the runout increases by 2.5%, and for the  $\mu(I)$ -C-MSM it increases by 6.8%. For  $\theta = 22^\circ$ , when  $h_i$  varies from 1.82 mm to 4.6 mm, the experimental runout increases by 26.9%. It increases by 2.2%, 4.4% and 8.6% for the monolayer model, the  $\mu(I)$ -MSM and the  $\mu(I)$ -C-MSM, respectively.

Note that with the  $\mu(I)$ -C-MSM the critical slope above which the runout increases

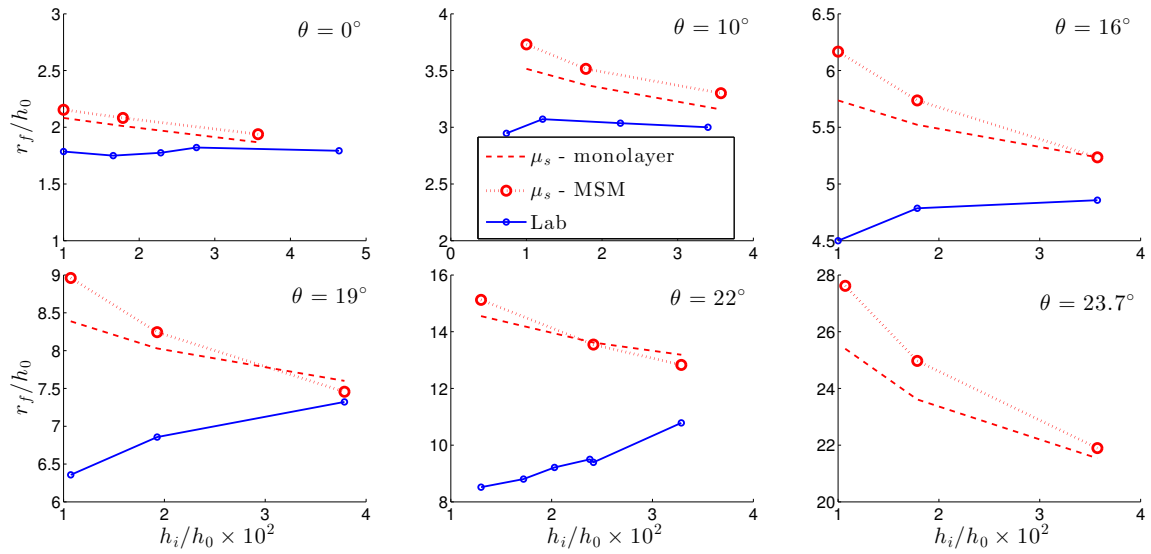


**Figure 2.10:** Influence of the thickness  $h_i$  of the erodible bed on the final runout  $r_f$  for slopes  $\theta = 0^\circ, 10^\circ, 16^\circ, 19^\circ, 22^\circ, 23.7^\circ$  observed in the experiments of [87] (solid-circle blue line) and obtained with different simulations using the  $\mu_s$ -MSM, with 20 layers (dotted-circle red line) and the  $\mu_s$ -monolayer model, i.e. the Savage-Hutter model (dashed red line). There is no laboratory data for  $\theta = 23.7^\circ$ . Normalization is made using  $h_0 = 14$  cm.

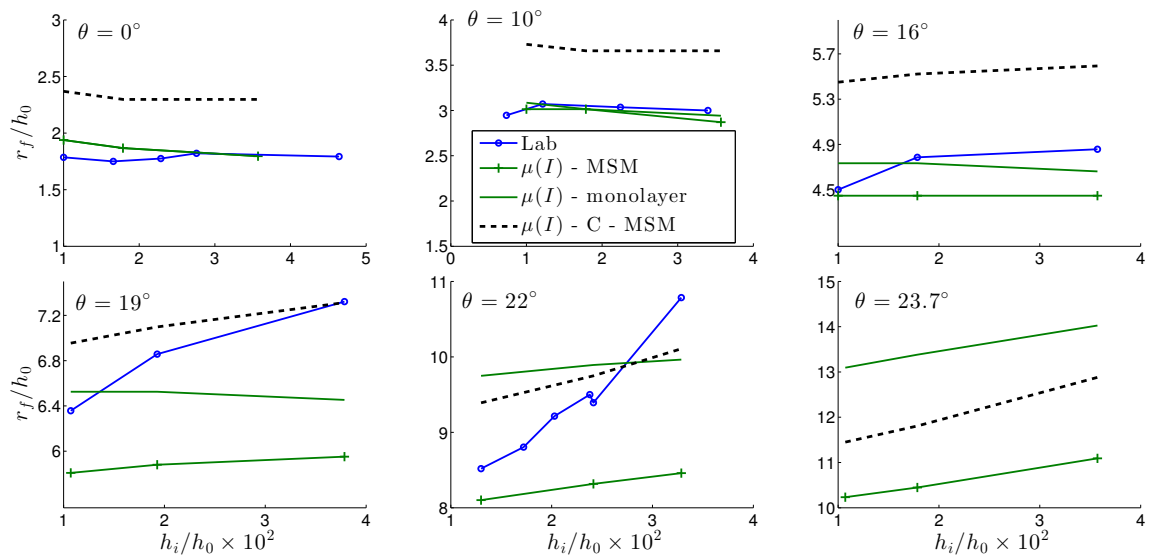


**Figure 2.11:** Influence of the thickness  $h_i$  of the erodible bed on the final runout  $r_f$  for slopes  $\theta = 16^\circ, 19^\circ, 22^\circ, 23.7^\circ$  observed in the experiments of [87] (solid-circle blue line) and obtained with different simulations using the  $\mu(I)$ -MSM, with 20 layers (solid-cross green line) and with the  $\mu(I)$ -monolayer model (solid green line) and with the  $\mu(I)$ -C-MSM (dashed black line). There is no laboratory data for  $\theta = 23.7^\circ$ . Normalization is made using  $h_0 = 14$  cm.

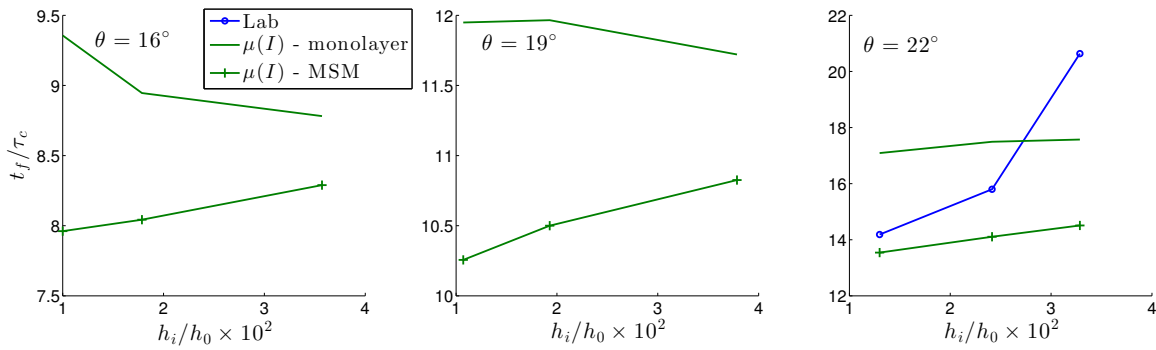


Figure 2.12: Influence of the thickness  $h_i$  of the erodible bed on the final time  $t_f$  for slopes  $\theta = 16^\circ$ ,  $19^\circ$  and  $22^\circ$  by using the  $\mu(I)$ -MSM with 20 layers (solid-cross green line), the  $\mu(I)$ -monolayer model (solid green line) and the values observed in the experiments of [87] for slope  $\theta = 22^\circ$  (solid-circle blue line). Normalization is made using  $\tau_c = \sqrt{h_0/(g \cos \theta)}$  and  $h_0 = 14$  cm.

with the thickness of the erodible bed is  $\theta \geq 16^\circ$ , which is closer to the value observed in the experiments than the critical slope predicted by the model without the second-order correction. This suggests that the extension of this shallow model up to the second order could be an important contribution.

As a conclusion, the increase of the runout distance with increasing thickness of the erodible bed is only reproduced when using the MSM with the  $\mu(I)$  rheology ( $\mu(I)$ -MSM or  $\mu(I)$ -C-MSM), although this increase is significantly underestimated. Nevertheless, this is the first time that a model has been able to reproduce this effect to our knowledge.

In figure 2.12, the final time (time at which the front stops) is plotted as a function of the thickness of the erodible bed for  $\theta = 16^\circ$ ,  $\theta = 19^\circ$  and  $\theta = 22^\circ$ . Moreover, for  $\theta = 22^\circ$ , we also plot the experimental data. Experimental data show that the final time increases when the thickness of the erodible bed increases. We can see that this is true for all the values of  $\theta$  for the multilayer method. However, we observe that it is only true for the highest value,  $\theta = 22^\circ$ , in the case of the monolayer model, whereas the final time decreases when the erodible bed increases for  $\theta = 16^\circ$  and  $\theta = 19^\circ$ .

### 2.4.2.5 Flow dynamics and velocity profiles

Figures 2.13 and 2.14 show the time evolution of the granular column thickness for a slope  $\theta = 22^\circ$  and an erodible bed of thickness  $h_i = 1.82$  mm for  $\mu_s$  and  $\mu(I)$ , respectively, for both the monolayer and multilayer models. As observed for the deposit, the difference between the thickness profiles simulated with the multilayer and the monolayer model is stronger for  $\mu(I)$  than for  $\mu_s$ . The  $\mu(I)$ -MSM makes it possible to increase the maximum thickness of the flow and decrease the thickness of the front. In particular it changes the shape of the front. This is an important result as the shape of the front may be an indicator of the flow rheology ([98, 74]).

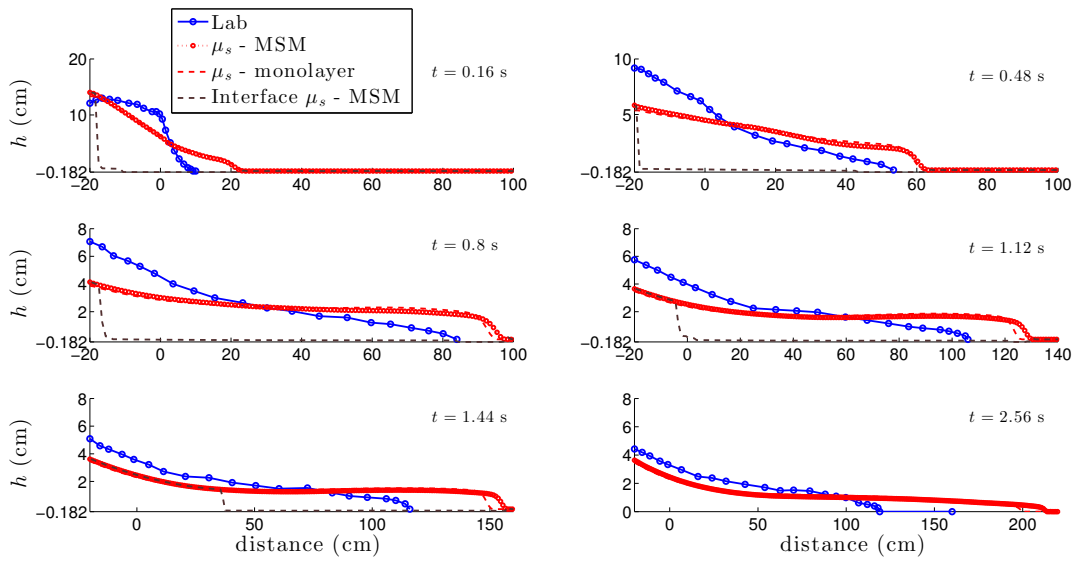


Figure 2.13: Thickness of the granular mass at different times in the experiments (solid-circle blue line), with the  $\mu_s$ -MSM with 20 layers (dotted-circle red line), with the  $\mu_s$ -monolayer model (Savage-Hutter model, dashed red line) and the flow/non-flow interface (dashed-brown line), for the slope  $\theta = 22^\circ$  and erodible bed thickness  $h_i = 1.82$  mm.

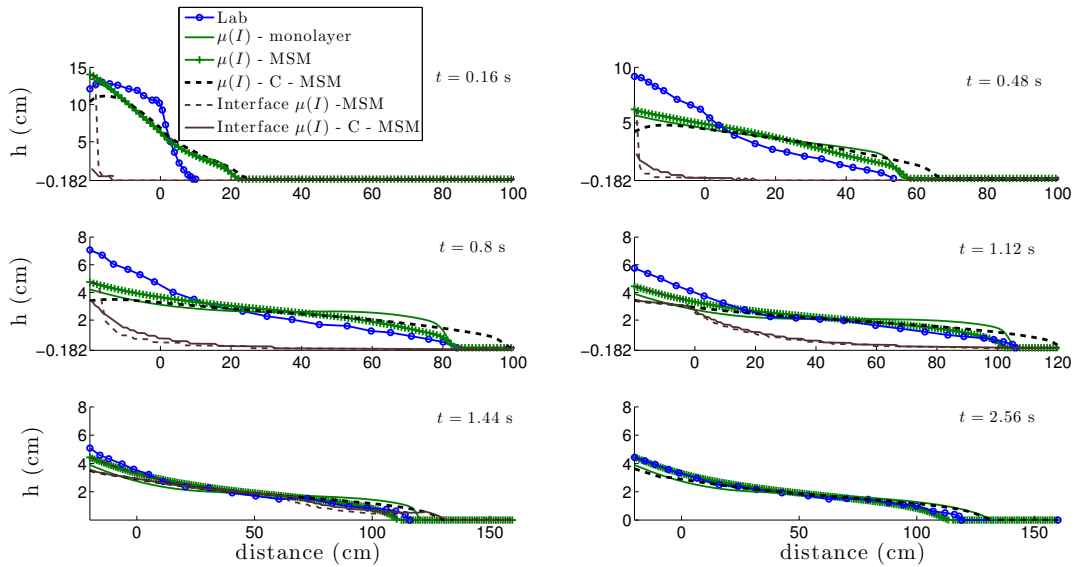


Figure 2.14: Thickness of the granular mass at different times in the experiments (solid-circle blue line), with the  $\mu(I)$ -MSM using 20 layers (solid-cross green line), with the  $\mu(I)$ -monolayer model (solid green line), with the  $\mu(I)$ -C-MSM (dashed black line), and the flow/non-flow interface with both multilayer models (dashed-brown/solid-brown lines) for the slope  $\theta = 22^\circ$  and erodible bed thickness  $h_i = 1.82$  mm.

When a constant coefficient  $\mu_s$  is used, very similar profiles are obtained with the  $\mu_s$ -MSM and  $\mu_s$ -monolayer model (Savage-Hutter model). As a result, the multilayer approach does not significantly improve the results when a constant friction coefficient

is used. Note that during the initial instants, the simulated mass spreads faster than in the experiments. This is partly due to the role of initial gate removal that is not taken into account here. However, this effect does not explain the strong difference between the simulation and experiments (see [70] for more details). The hydrostatic assumption may also be responsible for this overestimation of the spreading velocity (see e.g. [88]). In these figures we also show the flow/no-flow interfaces computed with the multilayer models  $\mu_s$  - MSM,  $\mu(I)$  - MSM and  $\mu(I)$  - C - MSM, by considering a threshold velocity of  $0.001 \text{ m/s}$  to compute these interfaces. We see in figure 2.13 that the flow/no-flow interface has a step-like shape for  $\mu_s$  - MSM while it has a smoother shape for  $\mu(I)$  - MSM (see figure 2.14) in better qualitative agreement with laboratory experiments and numerical modelling solving the full Navier-Stokes equations (i.e. figures 9 and 18 of [70]). The flow/no-flow interface in the uppermost part even seems to be improved when using  $\mu(I)$  - C - MSM. For  $\mu(I)$  - MSM and  $\mu(I)$  - C - MSM, the lower layers stop before the upper layers as observed experimentally. Note that in figures 2.13 and 2.14 we do not see the flow/no-flow interface at the final time because the material has already stopped. As was shown in Subsection 2.4.1.1, the wall friction effect is crucial to determine the position of the flow/no-flow interface. Because in this test we do not consider the exact definition of the wall friction term, as in [70], the flow/no-flow interface should not be very well captured.

Figure 2.15 shows that the second-order correction in  $\mu(I)$ -C-MSM leads to simulated deposits that are generally closer to the experimental observations than those calculated

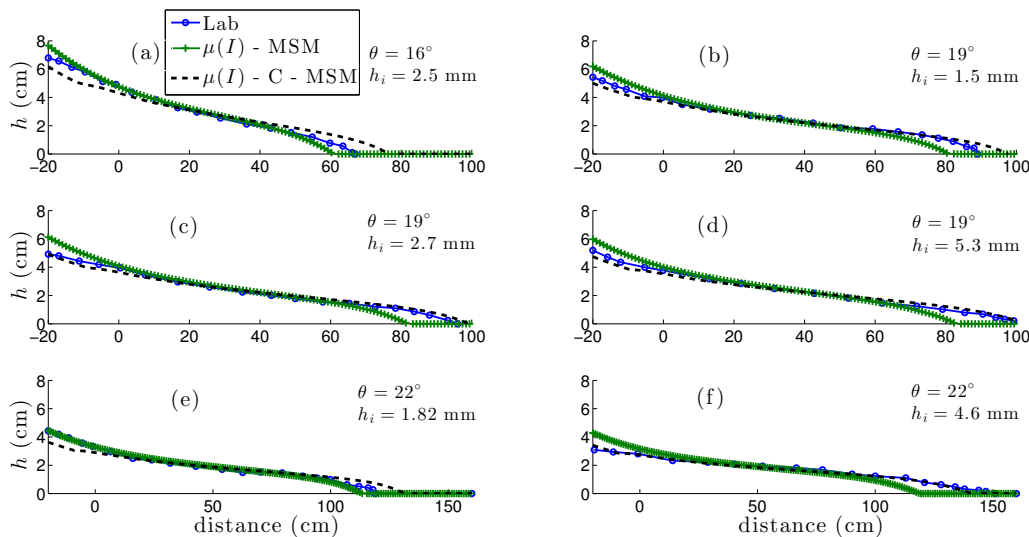


Figure 2.15: Simulated deposits at different slopes  $\theta$  and erodible bed thicknesses  $h_i$  with the  $\mu(I)$ -C-MSM (dashed black line) and the  $\mu(I)$ -MSM (solid-cross green line). The deposits observed in the experiments is represented by solid-circle blue lines.



with  $\mu(I)$ -MSM. In particular, the deposits at  $\theta = 19^\circ$  and  $\theta = 22^\circ$  with  $h_i = 4.6$  mm are very well reproduced (figure 2.15b,c,d,f). However, in some cases,  $\mu(I)$ -MSM gives better results than  $\mu(I)$ -C-MSM, for example for  $\theta = 22^\circ$  with  $h_i = 1.82$  mm. This is true for the overall dynamics as illustrated in figure 2.14 that shows the time change of the granular column thickness. We can see that with  $\mu(I)$ -C-MSM, the avalanche is faster and the runout is overestimated and very similar to the runout obtained with the  $\mu(I)$  monolayer model. As other second-order terms than those included in the  $\mu(I)$ -C-MSM model are neglected, it is not easy to draw a firm conclusion on the improvement of results when using second-order terms.

The multilayer approach makes it possible to obtain a normal profile of the downslope velocity. Figures 2.16 and 2.17 show the normal profiles of the downslope velocity obtained at different times until the mass stops, for two different configurations of slopes and erodible beds. In order to obtain a more accurate profile, 40 layers are used in the  $\mu(I)$ -MSM. The different kind of profiles observed in figures 2.16 and 2.17 are in good qualitative agreement with typical velocity profiles of granular flows GDR MiDi [60] (see also Lusso *et al.* [84, 85]), from Bagnold-like to S-shaped profiles. This shows the ability of the model to recover velocity profiles in a wide range of regimes.

Finally, let us compare the averaged velocity obtained with the  $\mu(I)$ -monolayer model to the average of the velocities over all the layers in the  $\mu(I)$ -MSM. In figure 2.16, for the green profile (respectively red and magenta profiles), the velocity in the monolayer model is 1.01 m/s (respectively 0.02 and 0.14 m/s) and it is 0.95 m/s in the multilayer model (respectively 0.03 and 0.05 m/s). Note that we obtain similar values for the first

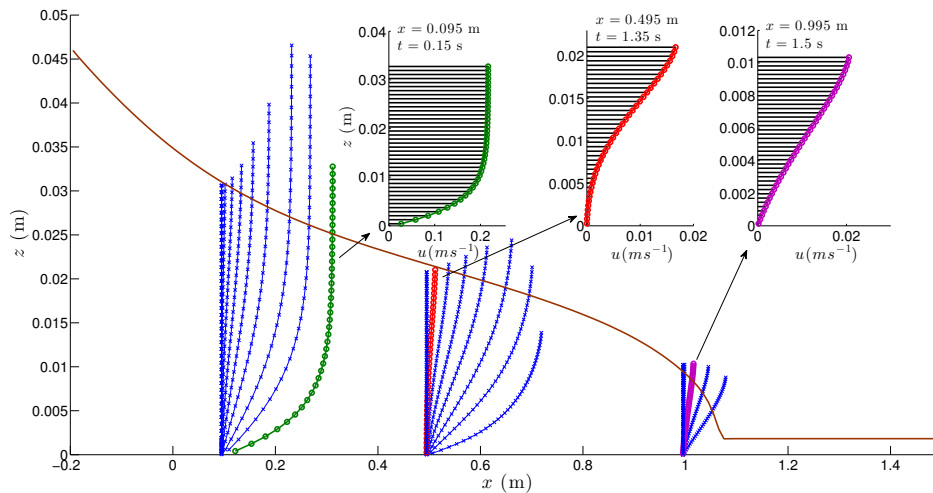


Figure 2.16: Normal profiles of the downslope velocity obtained with the  $\mu(I)$ -MSM (40 layers) for  $\theta = 22^\circ$  and  $h_i = 1.82$  mm during granular collapse at different positions ( $x = 0.095, 0.495, 0.995$  m). For these positions, we represent the velocity profiles for different times, taken every 0.15 s (blue lines). The first selected profile (green) shows a profile at the beginning of the flow and the second (red) and third (magenta) profiles were measured during the stopping stage. The final deposit is represented by the solid brown line.

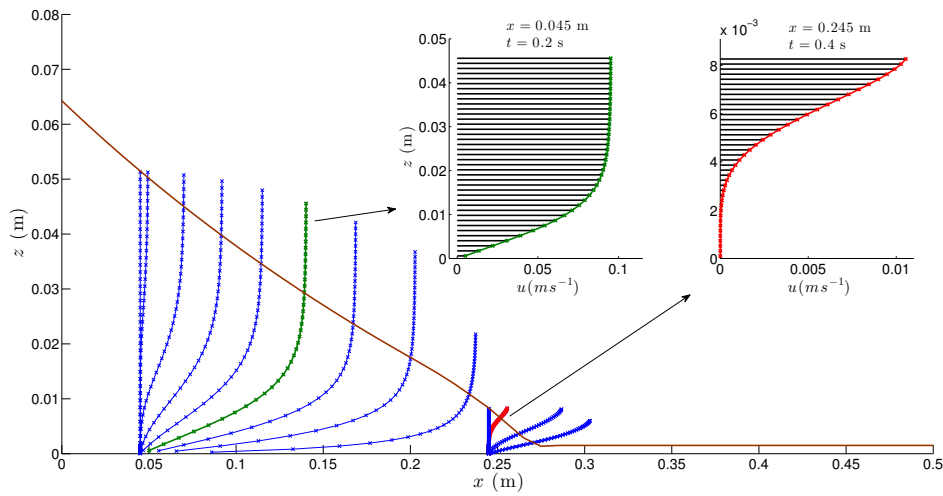


Figure 2.17: Normal profiles of the downslope velocity obtained with the  $\mu(I)$ -MSM (40 layers) for  $\theta = 0^\circ$  and  $h_i = 1.5 \text{ mm}$  during granular collapse at different positions ( $x = 0.045, 0.245 \text{ m}$ ) and times taken every  $0.05 \text{ s}$ .

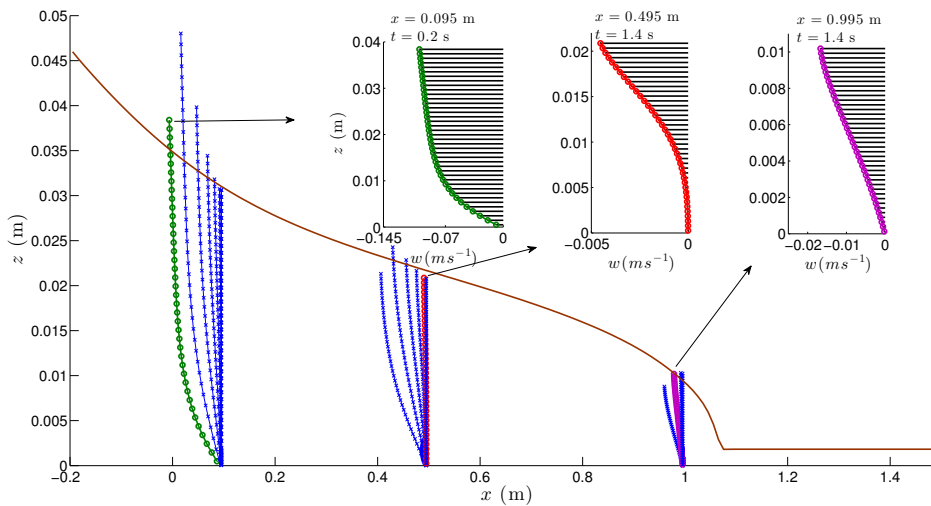


Figure 2.18: Normal profiles of the normal velocity obtained with the  $\mu(I)$ -MSM (40 layers) for  $\theta = 22^\circ$  and  $h_i = 1.82 \text{ mm}$  during granular collapse at different positions ( $x = 0.095, 0.495, 0.995 \text{ m}$ ) and times taken every  $0.2 \text{ s}$ .

and second profiles. For the third profile, the averaged velocities strongly differ. Actually, at this position and time, the velocity profile corresponds to the stopping phase for the multilayer model but not for the monolayer model. As a result, the velocity obtained in the multilayer model is lower than that obtained in the monolayer model. Figure 2.18 shows the normal profile of normal velocity for the same configuration as figure 2.16. Note that the normal velocities are always negative and that their absolute values are greater in the upper layers.



# Well-balanced multilayer discretization and side walls friction\*

\*The results in this chapter have been published in the paper: E.D. Fernández-Nieto, J. Garres-Díaz, A. Mangeney, & G. Narbona-Reina, 2D granular flows with the  $\mu(I)$  rheology and side walls friction: a well-balanced multilayer discretization, *Journal of Computational Physics*, 356 (2018), pp. 192–219.

## 3.1 Introduction

This chapter provides two main contributions. Firstly, we introduce a 2D-model for granular flows with the  $\mu(I)$  rheology in confined channels, which takes into account side walls effect with a Coulomb-type boundary condition. This model follows from a dimensional analysis of Navier-Stokes equations, the hypothesis of a one-dimensional flow, i.e. no transversal velocity ( $v = 0$ ), and the integration along the transversal direction of the channel. We also show that this model matches the one proposed in Jop *et al.* [75] under some specific assumptions, which, in particular, are satisfied for uniform flows.

Based on academic tests, we evaluate the influence of the width of the channel on the normal profiles of the downslope velocity thanks to the multilayer approach that is intrinsically able to describe changes from Bagnold to S-shaped (and vice versa) velocity profiles. This is not possible for the models proposed by Gray & Edwards [64], Edwards & Gray [49] and Baker *et al.* [10] because of the prescribed Bagnold profile neither for the model proposed by Capart *et al.* [32], which only deals with S-shaped profiles. In particular we are able to calculate what is the minimum channel width for which the granular mass flows over its all thickness, the minimum width for which a Bagnold profile is obtained instead of a S-shaped profile and the minimum width required to obtain a velocity profile independent of the channel width. This analysis may be helpful when designing and analysing laboratory experiments.

The second contribution of this chapter is the multilayer discretization for the proposed model. We present a numerical scheme with an appropriate treatment of the rheological terms in order to obtain a well-balanced scheme. To this aim, we combine a particular hydrostatic reconstruction taking into account the friction term (see Bouchut [25]) and a specific treatment of wet/dry fronts for the elliptic part of the multilayer system. This numerical approximation is also used in the previous chapter.

We present several tests with dry areas. Our simulations show that important differences in the final deposit are obtained whether the side walls friction term is approached by a multilayer or by a single-layer model. In particular, the single-layer model reproduces steady solutions with no physical meaning. Actually, the numerical scheme preserves those solutions with second order accuracy. Therefore, the side walls friction must not be included using single-layer models.

Finally, we compare the numerical results with experimental data on granular collapses. A strength of the model is the capability of computing the time evolution of the flow/no-flow interface. In particular, it reproduces the effect of erosion for granular flows over initially static material lying on the bed for uniform flows. This is possible when using a variable friction coefficient  $\mu(I)$ .

The chapter is organised as follows. Section 3.2 is devoted to the derivation of the 2D-model with the new approach to account for the side walls friction. In this section we also present the multilayer discretization of the proposed model, namely the discretization of the side walls friction term. In Section 3.3 we propose the numerical scheme for the multilayer system. Finally, the numerical tests are in Section 3.4.

## 3.2 A 2D-model including lateral walls friction

Let us consider the three-dimensional velocity  $\mathbf{u} = (u, v, w) \in \mathbb{R}^3$ , as in Chapter 1, and the total stress tensor  $\boldsymbol{\sigma} = -p\boldsymbol{\mathcal{I}} + \boldsymbol{\tau}$ , where  $\boldsymbol{\mathcal{I}}$  is the 3D identity tensor and  $\boldsymbol{\tau}$  the deviatoric stress tensor given by  $\boldsymbol{\tau} = \eta D(\mathbf{u})$ . Following Section 2.2, we consider the viscosity defined by the  $\mu(I)$  rheology

$$\eta = \frac{\mu(I)p}{\sqrt{\|D(\mathbf{u})\|^2 + \delta^2}}. \quad (3.1)$$

Let us also consider tilted coordinates  $(x, y, z) \in [x_a, x_b] \times [-W/2, W/2] \times \mathbb{R}$ , with a constant slope  $\theta$ . Here,  $W$  denotes the channel width, and the channel length is  $x_b - x_a$ , see figure 3.1. In Chapter 2 we have shown that the multilayer shallow model with the  $\mu(I)$  rheology is able to reproduce typical velocity profiles of granular flows in the presence of lateral walls. In order to approximate lateral wall friction there, we followed Jop *et al.* [75] where the flow is assumed to be one-dimensional and uniform in the downslope direction  $x$ . In that case, side wall friction is introduced by adding a second

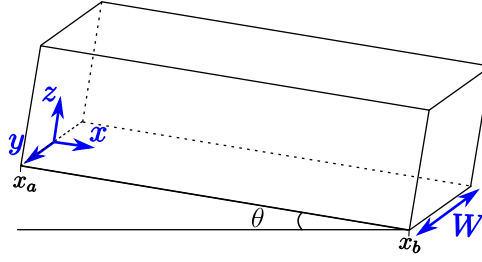


Figure 3.1: Sketch of the rectangular domain

term in the definition of the  $\mu(I)$  law:

$$\widetilde{\mu(I)} = \mu(I) + \mu_w \frac{z_b + h - z}{W}, \quad (3.2)$$

where  $\mu_w$  is the constant friction coefficient at the lateral walls, and  $z_b + h$  is the level of the free surface (see Subsection 2.4.1.2). The coefficient  $\mu_w$  is usually different and lower than the coefficient used to model friction at the bottom (see e.g. [10, 32, 70, 91, 76, 77]). Let us look for a one-dimensional model for non-uniform flow in the  $x$ -direction that takes into account the friction with the lateral walls.

The three-dimensional Navier-Stokes system (1.7) can be written as

$$\begin{cases} \partial_x u + \partial_y v + \partial_z w = 0, \\ \rho(\partial_t u + u \partial_x u + v \partial_y u + w \partial_z u) + \partial_x p = -\rho g \sin \theta + \partial_x \tau^{xx} + \partial_y \tau^{xy} + \partial_z \tau^{xz}, \\ \rho(\partial_t v + u \partial_x v + v \partial_y v + w \partial_z v) + \partial_y p = \partial_x \tau^{yx} + \partial_y \tau^{yy} + \partial_z \tau^{yz}, \\ \rho(\partial_t w + u \partial_x w + v \partial_y w + w \partial_z w) + \partial_z p = -\rho g \cos \theta + \partial_x \tau^{zx} + \partial_y \tau^{zy} + \partial_z \tau^{zz}, \end{cases} \quad (3.3)$$

At the free surface, we set the usual kinematic condition and we assume that the pressure vanishes. At the bottom, either the no-slip condition or Coulomb type friction can be considered. Moreover, we consider a Coulomb type friction at the lateral boundaries, described as follows (see Martin *et al.* [91]):

$$\boldsymbol{\sigma} \mathbf{n}^w - ((\boldsymbol{\sigma} \mathbf{n}^w) \cdot \mathbf{n}^w) \mathbf{n}^w = \left( -\mu_w p \frac{u}{|u|}, 0, 0 \right)', \quad (3.4)$$

being  $\mathbf{n}^w = (0, \pm 1, 0)'$  the normal vector at  $y = \pm W/2$ , respectively.

To derive a multilayer shallow model from dimensional analysis (see Fernández-Nieto *et al.* [54]), we assume that the aspect ratio between the characteristic height ( $H$ ) and length ( $L$ ),

$$\varepsilon = \frac{H}{L},$$

is small. Note that the influence of the lateral walls on the friction coefficient (3.2) is measured by the term  $\mu_w(z_b + h - z)/W$ . The dimension of this term is  $H/L_y$ , where  $L_y$  is the characteristic width of the channel. Therefore, the lateral walls have a higher influence on the flow when the characteristic width ( $L_y$ ) of the channel is small in comparison with its characteristic height ( $H$ ). We would like to study the influence of this scale into the system, then, in order to take it into account in the model we perform a dimensional analysis by also introducing the parameter

$$\lambda = \frac{H}{L_y}.$$

Notice that the higher the value of  $\lambda$ , the more important the lateral friction becomes. Denoting the dimensionless variables with the tilde symbol ( $\tilde{\cdot}$ ), we define

$$(x, y, z, t) = (L\tilde{x}, L_y\tilde{y}, H\tilde{z}, (L/U)\tilde{t}), \quad W = L_y\tilde{W},$$

$$(u, v, w) = (U\tilde{u}, \frac{\varepsilon}{\lambda}U\tilde{v}, \varepsilon U\tilde{w}),$$

$$h = H\tilde{h}, \quad \rho = \rho_0\tilde{\rho},$$

$$p = \rho_0 U^2 \tilde{p}, \quad \eta = \rho_0 U H \tilde{\eta}, \quad \eta_M = \rho_0 U H \tilde{\eta}_M,$$

$$(\tau^{xx}, \tau^{xy}, \tau^{yy}, \tau^{xz}, \tau^{yz}, \tau^{zz}) = \rho_0 U^2 (\varepsilon \tilde{\tau}^{xx}, \tilde{\tau}^{xy}, \varepsilon \tilde{\tau}^{yy}, \tilde{\tau}^{xz}, \varepsilon \tilde{\tau}^{yz}, \varepsilon \tilde{\tau}^{zz}). \quad (3.5)$$

with  $\rho_0$  the characteristic density. Note that since

$$D(\mathbf{u}) = \frac{U}{H} \frac{1}{2} \begin{pmatrix} 2\varepsilon \partial_{\tilde{x}} \tilde{u} & \lambda \partial_{\tilde{y}} \tilde{u} + \frac{\varepsilon^2}{\lambda} \partial_{\tilde{x}} \tilde{v} & \partial_{\tilde{z}} \tilde{u} + \varepsilon^2 \partial_{\tilde{x}} \tilde{w} \\ \lambda \partial_{\tilde{y}} \tilde{u} + \frac{\varepsilon^2}{\lambda} \partial_{\tilde{x}} \tilde{v} & 2\varepsilon \partial_{\tilde{y}} \tilde{v} & \varepsilon \lambda \partial_{\tilde{y}} \tilde{w} + \frac{\varepsilon}{\lambda} \partial_{\tilde{z}} \tilde{v} \\ \partial_{\tilde{z}} \tilde{u} + \varepsilon^2 \partial_{\tilde{x}} \tilde{w} & \varepsilon \lambda \partial_{\tilde{y}} \tilde{w} + \frac{\varepsilon}{\lambda} \partial_{\tilde{z}} \tilde{v} & 2\varepsilon \partial_{\tilde{z}} \tilde{w} \end{pmatrix},$$

we obtain by (3.5)

$$\tilde{\tau}^{xx} = \tilde{\eta} \partial_{\tilde{x}} \tilde{u}, \quad \tilde{\tau}^{xy} = \frac{\tilde{\eta}}{2} \left( \lambda \partial_{\tilde{y}} \tilde{u} + \frac{\varepsilon^2}{\lambda} \partial_{\tilde{x}} \tilde{v} \right), \quad \tilde{\tau}^{xz} = \frac{\tilde{\eta}}{2} (\partial_{\tilde{z}} \tilde{u} + \varepsilon^2 \partial_{\tilde{x}} \tilde{w}),$$

$$\tilde{\tau}^{yy} = \tilde{\eta} \partial_{\tilde{y}} \tilde{v}, \quad \tilde{\tau}^{yz} = \frac{\tilde{\eta}}{2} \left( \lambda \partial_{\tilde{y}} \tilde{w} + \frac{1}{\lambda} \partial_{\tilde{z}} \tilde{v} \right), \quad \tilde{\tau}^{zz} = \tilde{\eta} \partial_{\tilde{z}} \tilde{w}.$$

Then, the system of equations (3.3) can be rewritten using the non-dimensional variables



as (tildes have been dropped for simplicity):

$$\begin{cases} \partial_x u + \partial_y v + \partial_z w = 0, \\ \rho(\partial_t u + u\partial_x u + v\partial_y u + w\partial_z u) + \partial_x p = -\frac{1}{\varepsilon}\rho\frac{1}{Fr^2}\tan\theta + \varepsilon\partial_x\tau^{xx} + \frac{\lambda}{\varepsilon}\partial_y\tau^{xy} + \frac{1}{\varepsilon}\partial_z\tau^{xz}, \\ \rho(\partial_t v + u\partial_x v + v\partial_y v + w\partial_z v) + \frac{\lambda^2}{\varepsilon^2}\partial_y p = \frac{\lambda}{\varepsilon}\partial_x\tau^{yx} + \frac{\lambda^2}{\varepsilon}\partial_y\tau^{yy} + \frac{\lambda}{\varepsilon}\partial_z\tau^{yz}, \\ \rho\varepsilon^2(\partial_t w + u\partial_x w + v\partial_y w + w\partial_z w) + \partial_z p = -\rho\frac{1}{Fr^2} + \varepsilon\partial_x\tau^{zx} + \varepsilon\lambda\partial_y\tau^{zy} + \varepsilon\partial_z\tau^{zz}, \end{cases} \quad (3.6)$$

where  $Fr$  denotes the Froude number,

$$Fr = \frac{U}{\sqrt{gH\cos\theta}}.$$

We now assume that the flow is one dimensional (i.e.  $v = 0$ ) and keeping all the terms involving  $\lambda$ , the previous system reads

$$\begin{cases} \partial_x u + \partial_z w = 0, \\ \rho(\partial_t u + u\partial_x u + w\partial_z u) + \partial_x p = -\frac{1}{\varepsilon}\rho\frac{1}{Fr^2}\tan\theta + \frac{\lambda^2}{2\varepsilon}\partial_y(\eta\partial_y u) + \frac{1}{2\varepsilon}\partial_z(\eta\partial_z u) + \mathcal{O}(\varepsilon), \\ \partial_y p = \mathcal{O}(\varepsilon), \\ \partial_z p = -\rho\frac{1}{Fr^2} + \frac{\varepsilon\lambda^2}{2}\partial_y(\eta\partial_y w) + \mathcal{O}(\varepsilon). \end{cases} \quad (3.7)$$

Note that the term

$$\frac{\lambda^2}{2\varepsilon}\partial_y(\eta\partial_y u) \quad (3.8)$$

is of the main order  $1/\varepsilon$  and collects the lateral friction effect on the momentum equation. Lateral walls friction has then a high influence on the flow, both on the norm of the maximum velocity and on its normal velocity profile.

Moreover, this is the term that allows us to introduce the lateral Coulomb friction in the model, by integrating in the horizontal transversal direction. To this aim, we define

$$\bar{u} = \frac{1}{W}\int_{-W/2}^{W/2} u dy, \quad \bar{w} = \frac{1}{W}\int_{-W/2}^{W/2} w dy, \quad \bar{p} = \frac{1}{W}\int_{-W/2}^{W/2} p dy, \quad \bar{\eta} = \frac{1}{W}\int_{-W/2}^{W/2} \eta dy.$$

We also assume that the perturbation with respect to the transversal averages are small, therefore we can approximate  $\overline{fg}$  by  $\bar{f}\bar{g}$ , for any two variables  $f, g$ . By integrating

system (3.7) with respect to the transversal direction between  $-W/2$  and  $W/2$  we obtain

$$\begin{cases} \partial_x \bar{u} + \partial_z \bar{w} = 0, \\ \rho(\partial_t \bar{u} + \bar{u} \partial_x \bar{u} + \bar{w} \partial_z \bar{u}) + \partial_x \bar{p} = -\frac{1}{\varepsilon} \rho \frac{1}{Fr^2} \tan \theta + \frac{1}{\varepsilon} \partial_z \left( \bar{\eta} \frac{\partial_z \bar{u}}{2} \right) + \frac{\lambda^2}{W \varepsilon} (\eta \partial_y u)_{|_{W/2}} + \mathcal{O}(\varepsilon), \\ p_{|_{W/2}} = p_{|_{-W/2}} + \mathcal{O}(\varepsilon), \\ \partial_z \bar{p} = -\rho \frac{1}{Fr^2} + \frac{\varepsilon \lambda^2}{2W} \left( (\eta \partial_y w)_{|_{W/2}} - (\eta \partial_y w)_{|_{-W/2}} \right) + \mathcal{O}(\varepsilon). \end{cases}$$

In the previous equation we have supposed a symmetric profile of  $\eta \partial_y u$ , i.e., we assume that  $\eta \partial_y u_{|_{-W/2}} = -\eta \partial_y u_{|_{W/2}}$ . Moreover, from lateral friction condition (3.4) it follows that

$$\lambda \left( \frac{\eta}{2} \partial_y u \right)_{|_{W/2}} = -\mu_w p_{|_{W/2}} \left( \frac{u}{|u|} \right)_{|_{W/2}} \quad \text{and} \quad (\eta \partial_y w)_{|_{W/2}} = (\eta \partial_y w)_{|_{-W/2}} = 0. \quad (3.9)$$

Note that thanks to the second equality of previous equation we obtain hydrostatic pressure  $\bar{p}$ . Since we study the case of a uniform flow along the  $y$ -direction, we consider  $p_{|_{W/2}} = \bar{p}$ . In addition, we also suppose that the sign of the velocity at the lateral walls coincides with the sign of the averaged velocity  $\bar{u}$ , as usual in averaged models.

Therefore, to obtain the final model, we neglect terms of order  $\varepsilon$ , leading to the first order model approximation

$$\begin{cases} \partial_x \bar{u} + \partial_z \bar{w} = 0, \\ \rho(\partial_t \bar{u} + \bar{u} \partial_x \bar{u} + \bar{w} \partial_z \bar{u}) + \partial_x \bar{p} = -\frac{1}{\varepsilon} \rho \frac{1}{Fr^2} \tan \theta + \frac{1}{\varepsilon} \partial_z \left( \bar{\eta} \frac{\partial_z \bar{u}}{2} \right) - \frac{2\lambda}{W \varepsilon} \mu_w \bar{p} \frac{\bar{u}}{|\bar{u}|}, \\ \partial_z \bar{p} = -\rho \frac{1}{Fr^2}. \end{cases} \quad (3.10)$$

Going back to the dimensional variables, we get

$$\begin{cases} \partial_x \bar{u} + \partial_z \bar{w} = 0, \\ \rho(\partial_t \bar{u} + \bar{u} \partial_x \bar{u} + \bar{w} \partial_z \bar{u}) + \partial_x \bar{p} = -\rho g \sin \theta + \partial_z \left( \bar{\eta} \frac{\partial_z \bar{u}}{2} \right) - \frac{2}{W} \mu_w \bar{p} \frac{\bar{u}}{|\bar{u}|}, \\ \partial_z \bar{p} = -\rho g \cos \theta. \end{cases} \quad (3.11)$$

Hereafter bars are dropped by simplicity. We can find some similarities to previous models presented in the literature. In order to make the comparison we must take into account that terms of order  $\varepsilon$  have been neglected to obtain the proposed model (3.11). Thus, since  $\|D(\mathbf{u})\| = |\partial_z u|/2 + \mathcal{O}(\varepsilon)$ , we obtain that model (3.11) matches the one introduced in Martin *et al.* [91] for hydrostatic pressure and neglecting also here terms in  $\varepsilon$ .

In addition, if the horizontal velocity satisfies that  $\text{sign}(u) = \text{sign}(\partial_z u)$ , which is usually the case, then it also coincides with the model proposed in Jop *et al.* [75]. In that work the lateral friction effect is defined for uniform flows, by adding an extra term to the definition of  $\mu(I)$  (equation (3.2)). Let us see that in fact it is equivalent up to first order in  $\varepsilon$  to model (3.11), for flows satisfying  $\text{sign}(u) = \text{sign}(\partial_z u)$  and not only for uniform flows.

We use (3.1) with  $\delta = 0$  and the previous approximation of  $\|D(\mathbf{u})\| = |\partial_z u|/2 + \mathcal{O}(\varepsilon)$ , then the viscous term in (3.11) neglecting terms of order  $\varepsilon$  reads

$$\partial_z \left( \frac{\mu(I) p(z)}{|\partial_z u|} \partial_z u \right) - \frac{2}{W} \mu_w p(z) \frac{u}{|u|}. \quad (3.12)$$

Since we have a hydrostatic pressure,  $p(z) = \rho g (z_b + h - z)$ , the second term in the previous equation can be rewritten as

$$\begin{aligned} -\frac{2}{W} \mu_w \rho g \cos \theta (z_b + h - z) \text{sign}(u) &= \partial_z \left( \frac{1}{W} \mu_w \rho g \cos \theta (z_b + h - z)^2 \text{sign}(u) \right) = \\ &= \partial_z \left( \mu_w \frac{z_b + h - z}{W} p(z) \text{sign}(u) \right). \end{aligned}$$

Therefore (3.12) yields

$$\partial_z \left( \mu(I) p(z) \text{sign}(\partial_z u) + \mu_w \frac{z_b + h - z}{W} p(z) \text{sign}(u) \right).$$

Now, if  $\text{sign}(\partial_z u) = \text{sign}(u)$ , we obtain

$$\partial_z \left( \left( \mu(I) + \mu_w \frac{z_b + h - z}{W} \right) p(z) \text{sign}(\partial_z u) \right) = \partial_z \left( \widetilde{\mu(I)} p(z) \text{sign}(\partial_z u) \right), \quad (3.13)$$

which is the viscous term resulting of considering the modified friction coefficient proposed in Jop *et al.* [75]. Then, we obtain that in this case the model (3.11) matches the one proposed in [75].

Note also that the term on the right hand side of equation (3.13) is an approximation at order  $\varepsilon$  of  $\text{div}(\widetilde{\mu(I)} p \frac{D(u)}{\|D(u)\|})$ . For example, these terms are equal in the case of a uniform flow. However,  $\text{div}(\widetilde{\mu(I)} p \frac{D(u)}{\|D(u)\|})$  cannot be rewritten as

$$\text{div}(\mu(I) p \frac{D(u)}{\|D(u)\|}) - \frac{2}{W} \mu_w p(z) \frac{u}{|u|},$$

which is the term that appears in the full model (see Ionescu *et al.* [70]). As a result, using  $\widetilde{\mu(I)}$  to describe side walls friction is not correct in general in the full 3D model. It can be justified if we consider a model at first order in  $\varepsilon$ , with hydrostatic pressure, and  $\text{sign}(\partial_z u) = \text{sign}(u)$ .

In the next subsection we present a multilayer discretization of the model (3.11).

### 3.2.1 A multilayer discretization

In this section we briefly describe the multilayer approach for the system (3.11). This is fully analogous to the previous chapters, except for the side walls friction term. Then, reader can follow the whole procedure developed in subsections 2.3.2 and 2.3.3, and here we focus on the approximation of the new term in (3.11).

Let us recall the approximation of the viscosity  $\eta_{\alpha+\frac{1}{2}}$  up to first order. We consider as before  $\|D(\mathbf{u})\| = |\partial_z u|/2 + \mathcal{O}(\varepsilon)$ , so the approximation at  $z = z_{\alpha+\frac{1}{2}}$  is given by

$$\|D(\mathbf{u})\|_{\alpha+\frac{1}{2}} \approx \frac{1}{2} \left| \mathcal{U}_{\mathcal{Z},\alpha+\frac{1}{2}}^H \right|, \quad (3.14)$$

where

$$\mathcal{U}_{\mathcal{Z},\alpha+\frac{1}{2}}^H = \frac{u_{\alpha+1} - u_\alpha}{h_{\alpha+\frac{1}{2}}}, \quad \text{for } \alpha = 1, \dots, N-1, \quad (3.15)$$

with  $h_{\alpha+\frac{1}{2}}$  the distance between the midpoints of layers  $\alpha$  and  $\alpha+1$ . Therefore, the viscosity coefficient at the interface  $\Gamma_{\alpha+\frac{1}{2}}$  reads

$$\eta_{\alpha+\frac{1}{2}} = \eta_{\alpha+\frac{1}{2}}(\mathcal{U}_{\mathcal{Z},\alpha+\frac{1}{2}}^H) = \frac{\mu(I_{\alpha+\frac{1}{2}})p_{\alpha+\frac{1}{2}}}{\sqrt{\left| \mathcal{U}_{\mathcal{Z},\alpha+\frac{1}{2}}^H \right|^2 / 4 + \delta^2}}, \quad (3.16)$$

for  $\alpha = 0, \dots, N-1$ , and  $\eta_{N+1/2} = 0$  since we fix the atmospheric pressure,  $p_S = 0$ . In (3.16) the pressure is assumed hydrostatic, then

$$p_{\alpha+\frac{1}{2}} = \rho g \cos\theta \sum_{\beta=\alpha+1}^N h_\beta, \quad I_{\alpha+\frac{1}{2}} = \frac{d_s \left| \mathcal{U}_{\mathcal{Z},\alpha+\frac{1}{2}}^H \right|}{\sqrt{p_{\alpha+\frac{1}{2}}/\rho_s}} = \frac{d_s |u_{\alpha+1} - u_\alpha|}{h_{\alpha+\frac{1}{2}} \sqrt{\varphi_s g \cos\theta \sum_{\beta=\alpha+1}^N h_\beta}}, \quad (3.17)$$

for  $\alpha = 0, \dots, N-1$ . The definition of the viscosity at the bottom  $\eta_{1/2}$  is particularly interesting. It will depend on the considered boundary condition, either no-slip or a Coulomb type friction. Also  $\mathcal{U}_{\mathcal{Z},\frac{1}{2}}^H$  must be defined by that boundary condition. This will be discussed later.

#### 3.2.1.1 Final model

Following the procedure presented in Chapter 2, the final  $\mu(I)$  rheology multilayer model at first order in  $\varepsilon$ , including the lateral wall friction, reads, for  $\alpha = 1, \dots, N$ ,

$$\begin{cases} l_\alpha \left( \partial_t h + \partial_x (h u_\alpha) \right) = G_{\alpha+\frac{1}{2}} - G_{\alpha-\frac{1}{2}}, \\ l_\alpha \left( \rho \partial_t (h u_\alpha) + \rho \partial_x (h u_\alpha^2) + \rho g \cos\theta h \partial_x (z_b + h) \right) = K_{\alpha-\frac{1}{2}} - K_{\alpha+\frac{1}{2}} + \\ \quad + \frac{1}{2} \rho G_{\alpha+\frac{1}{2}} (u_{\alpha+1} + u_\alpha) - \frac{1}{2} \rho G_{\alpha-\frac{1}{2}} (u_\alpha + u_{\alpha-1}) + M_{\alpha,W}, \end{cases} \quad (3.18)$$

where we recall that the bottom topography had been defined through the functions

$$z_b = b + \tilde{b}; \quad \tilde{b} = -x \tan \theta,$$

and  $G_{\alpha+\frac{1}{2}}$  is the mass transference (2.12) between the layers  $\alpha$  and  $\alpha + 1$ . Once more, the vertical velocity is the piecewise linear function defined by (1.16)-(1.17). Finally, the viscous term  $K_{\alpha+\frac{1}{2}}$  is

$$K_{\alpha+\frac{1}{2}} = -\frac{1}{2}\eta_{\alpha+\frac{1}{2}}(\mathcal{U}_{\tilde{z},\alpha+\frac{1}{2}}^H)\mathcal{U}_{\tilde{z},\alpha+\frac{1}{2}}^H, \quad \alpha = 1, \dots, N-1 \quad (3.19)$$

as in previous chapter, for  $\eta_{\alpha+\frac{1}{2}}$  defined in (3.16)-(3.17). The terms  $K_{\frac{1}{2}}$  and  $K_{N+\frac{1}{2}}$  are defined by the boundary conditions at the bottom and the free surface, respectively (see Section 3.2.1.2).

The side walls friction is taken into account through the term  $M_{\alpha,W}$ . Following the multilayer procedure we obtain that

$$\begin{aligned} M_{\alpha,W} &= -\int_{z_{\alpha-1/2}}^{z_{\alpha+1/2}} \frac{2}{W}\mu_w \frac{u_\alpha}{|u_\alpha|} \rho g \cos \theta (z_b + h - z) dz = \\ &= \frac{2}{W}\mu_w \frac{u_\alpha}{|u_\alpha|} \rho g \cos \theta \left. \frac{(z_b + h - z)^2}{2} \right]_{z_{\alpha-1/2}}^{z_{\alpha+1/2}}. \end{aligned}$$

After some algebra we get

$$\left. \frac{(z_b + h - z)^2}{2} \right]_{z_{\alpha-1/2}}^{z_{\alpha+1/2}} = -h_\alpha \left( \sum_{\beta=\alpha+1}^N h_\beta + \frac{h_\alpha}{2} \right) = -h_\alpha \left( z_b + h - \left( z_b + \sum_{\beta=1}^{\alpha-1} h_\beta + \frac{h_\alpha}{2} \right) \right).$$

Therefore, denoting  $p_\alpha = \rho g \cos \theta \left( z_b + h - \left( z_b + \sum_{\beta=1}^{\alpha-1} h_\beta + \frac{h_\alpha}{2} \right) \right)$ , the pressure in the midpoint of layer  $\alpha$ , the lateral walls friction term is written

$$M_{\alpha,W} = -l_\alpha h \frac{2}{W}\mu_w p_\alpha \frac{u_\alpha}{|u_\alpha|}. \quad (3.20)$$

As in previous chapters, model (3.18) can be written as a system with  $N + 1$  equations and unknowns: the total height and the discharge of each layer, i.e.,  $(h, q_1, \dots, q_N)$ . By

defining (1.31) the auxiliary coefficients  $\xi_{\alpha,\gamma}$  the system (3.18)-(3.20) is rewritten as

$$\left\{ \begin{array}{l} \partial_t h + \partial_x \left( \sum_{\beta=1}^N l_\beta q_\beta \right) = 0, \\ \partial_t q_\alpha + \partial_x \left( \frac{q_\alpha^2}{h} + g \cos \theta \frac{h^2}{2} \right) + g \cos \theta h \partial_x z_b + \\ + \sum_{\gamma=1}^N \frac{1}{2hl_\alpha} \left( (q_\alpha + q_{\alpha-1}) \xi_{\alpha-1,\gamma} - (q_{\alpha+1} + q_\alpha) \xi_{\alpha,\gamma} \right) \partial_x q_\gamma = \\ = \frac{1}{\rho l_\alpha} \left( K_{\alpha-\frac{1}{2}} - K_{\alpha+\frac{1}{2}} + M_{\alpha,W} \right) \quad \alpha = 1, \dots, N. \end{array} \right. \quad (3.21)$$

### 3.2.1.2 Boundary conditions

The boundary condition at the free surface is simply defined by taking into account that the atmospheric pressure is neglected ( $p_S = 0$ ), therefore  $K_{N+\frac{1}{2}} = 0$ . The term  $K_{1/2}$  is

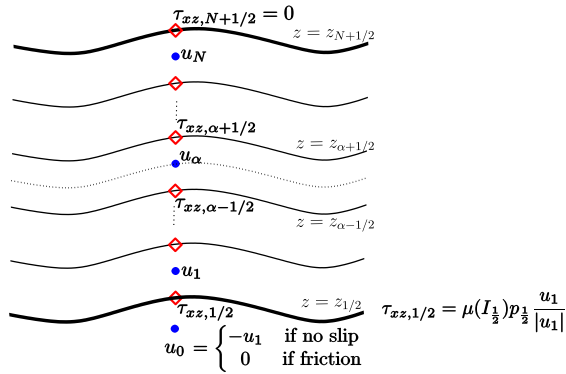


Figure 3.2: Sketch of the placing of the variables in the multilayer domain

defined by the boundary condition at the bottom. A difficult task is to strongly impose the no-slip or Coulomb type friction boundary condition at the bottom in multilayer models. A good way to impose strongly the no slip condition at the bottom would be to calculate the velocities at the vertical interfaces  $\Gamma_{\alpha+1/2}$ . On the contrary, multilayer models calculate averaged velocities within the layer, which in turn is a second order approximation of the velocity at the middle of the layer (see figure 3.2). As an example, in the first layer we have  $u_1 = u(h_1/2) + \mathcal{O}(h_1^2)$ . As a result, we can only impose the boundary conditions in a weak sense and the no slip condition is not exactly achieved, as it can be observed when looking in details the numerical results (see Section 3.4.1). Furthermore, we can not impose strongly a Coulomb type boundary condition since the

unknowns of the system are the velocities and not the stresses, contrary to Augmented Lagrangian method (see Ionescu *et al.* [70]), for example.

Let us propose simple ways to weakly impose no-slip and Coulomb type boundary condition. The key point is to approximate  $\partial_z u$  at the bottom. The value of  $\mathcal{U}_{\mathcal{Z}, \frac{1}{2}}^H$  as an approximation of  $\partial_z u$  at the bottom  $z = z_{1/2}$  depends on the velocity in the first layer  $u_1$ . In general we assume the following approximation,  $\mathcal{U}_{\mathcal{Z}, \frac{1}{2}}^H = \frac{u_1 - u_0}{h_1}$  where  $u_0$  represents the velocity in a fictitious layer under the bottom level.

If we consider a Coulomb friction law, the stress tensor must satisfy the condition

$$\boldsymbol{\sigma} \mathbf{n}^b - ((\boldsymbol{\sigma} \mathbf{n}^b) \cdot \mathbf{n}^b) \mathbf{n}^b = \left( \mu(I_{\frac{1}{2}}) p_{\frac{1}{2}} \frac{u_1}{|u_1|}, 0 \right)', \quad (3.22)$$

where  $\mathbf{n}^b$  is the downward unit normal vector to the bottom. We can consider either a friction law with a constant parameter ( $\mu(I_{\frac{1}{2}}) = \mu_s$ ) as in Martin *et al.* [91], or given by the expression of the  $\mu(I)$  rheology. In this case, we consider the approximation of  $\partial_z u$  at the bottom considering that the velocity  $u_0 = 0$ ,

$$\mathcal{U}_{\mathcal{Z}, \frac{1}{2}}^H = \frac{u_1}{h_1}.$$

This makes it possible to obtain a non-zero velocity at the bottom.

Then, the term  $K_{\frac{1}{2}}$  is given by condition (3.22),

$$K_{\frac{1}{2}} = -\rho g h \cos\theta \mu(I_{\frac{1}{2}}) \frac{u_1}{|u_1|}, \quad \text{where} \quad I_{\frac{1}{2}} = \frac{d_s |u_1/h_1|}{\sqrt{\varphi_s g h \cos\theta}}. \quad (3.23)$$

If no-slip condition is considered then we must change the approximation  $\mathcal{U}_{\mathcal{Z}, \frac{1}{2}}^H$  because now the velocity must vanish at  $z = z_{1/2}$ , so we introduce  $u_0 = -u_1$ . Hence we consider the approximation

$$\mathcal{U}_{\mathcal{Z}, \frac{1}{2}}^H = \frac{2u_1}{h_1}.$$

Then  $K_{1/2}$  is given by

$$K_{\frac{1}{2}} = -\rho g h \cos\theta \mu(I_{\frac{1}{2}}) \frac{u_1}{|u_1|}, \quad \text{where} \quad I_{\frac{1}{2}} = \frac{d_s |2u_1/h_1|}{\sqrt{\varphi_s g h \cos\theta}}. \quad (3.24)$$

As a conclusion, the viscous term at the bottom ( $K_{1/2}$ ) defined from a no-slip condition only differs from the one when considering a Coulomb friction law in the inertial number:

$$I_{\frac{1}{2}, \text{No slip}} = 2 I_{\frac{1}{2}, \text{Coulomb}}. \quad (3.25)$$

In the next section we detail the numerical discretization of the proposed multilayer system (3.21).

### 3.3 Numerical approximation

In the literature, multilayer systems have been discretized by combining a usual finite volume method with a splitting procedure [3, 5, 7, 8, 9, 56]. Thus, authors usually separate the viscous terms, which are treated with a semi-implicit scheme. We follow this structure in a particular way. One of the main contribution in Chapter 2 is to introduce a multilayer system with non-constant viscosity. Nevertheless, its numerical approximation was not explained. To our knowledge it's the first time that a numerical scheme for a multilayer system with non-constant viscosity is exposed. These rheological terms add new difficulties, namely when looking for a well-balanced scheme. Here we consider a hydrostatic reconstruction in a finite volume method in order to ensure the well-balanced property.

Firstly, we can write the system (3.21) in matrix notation as

$$\partial_t \mathbf{w} + \partial_x \mathbf{F}(\mathbf{w}) + \mathbf{S}(\mathbf{w}) \partial_x z_b + \mathbf{B}(\mathbf{w}) \partial_x \mathbf{w} = \mathbf{E}(\mathbf{w}) \quad (3.26)$$

where  $\mathbf{w} = (h, q_1, q_2, \dots, q_N)' \in \Omega \subset \mathbb{R}^{N+1}$  is the unknown vector,  $\mathbf{F}(\mathbf{w}) = (\mathbf{F}_\alpha(\mathbf{w}))_{\alpha=0,1,\dots,N}$  is a regular function from  $\mathbb{R}^{N+1}$  to  $\mathbb{R}^{N+1}$ ,  $\mathbf{B}(\mathbf{w}) = (\mathbf{B}_{\alpha,\beta}(\mathbf{w}))_{\alpha,\beta=0,1,\dots,N}$  is a regular matrix function from  $\mathbb{R}^{N+1}$  to  $\mathcal{M}_{N+1}(\mathbb{R})$ ,  $\mathbf{S}(\mathbf{w}) = (\mathbf{S}_\alpha(\mathbf{w}))_{\alpha=0,1,\dots,N}$ , and  $\mathbf{E}(\mathbf{w}) = (\mathbf{E}_\alpha(\mathbf{w}))_{\alpha=0,1,\dots,N}$  are vector functions from  $\mathbb{R}^{N+1}$  to  $\mathbb{R}^{N+1}$ .

$\mathbf{F}_\alpha(\mathbf{w})$  and  $\mathbf{S}_\alpha(\mathbf{w})$  are defined by the convective and pressure terms, respectively,

$$\mathbf{F}_\alpha(\mathbf{w}) = \begin{cases} \sum_{\beta=1}^N l_\beta q_\beta, & \text{if } \alpha = 0, \\ \frac{q_\alpha^2}{h} + g \cos \theta \frac{h^2}{2}, & \text{if } \alpha = 1, \dots, N; \end{cases} \quad \mathbf{S}_\alpha(\mathbf{w}) = \begin{cases} 0, & \text{if } \alpha = 0, \\ g \cos \theta h, & \text{if } \alpha = 1, \dots, N. \end{cases}$$

Note that the addition of convective and pressure terms can be written as

$$\partial_x \mathbf{F}(\mathbf{w}) + \mathbf{S}(\mathbf{w}) \partial_x z_b = \partial_x \mathbf{F}_c(\mathbf{w}) + \mathbf{S}(\mathbf{w}) \partial_x (z_b + h), \quad \text{with } \mathbf{F}_c(\mathbf{w}) = \mathbf{F}(\mathbf{w}) - \frac{h}{2} \mathbf{S}(\mathbf{w}).$$

Therefore,  $\mathbf{F}_c(\mathbf{w})$  contains the convective term and pressure terms are defined by  $\mathbf{S}(\mathbf{w}) \partial_x (z_b + h)$ . On the other hand,  $\mathbf{B}_{\alpha,\beta}(\mathbf{w})$  is defined in terms of the momentum transference terms,

$$\mathbf{B}_{\alpha,\beta}(\mathbf{w}) = \begin{cases} 0, & \text{if } (\alpha, \beta) \in \{0\} \times \{0, 1, \dots, N\} \cup \{1, \dots, N\} \times \{0\}, \\ \frac{1}{2hl_\alpha} (q_\alpha + q_{\alpha-1}) \xi_{\alpha-1,\beta} - \frac{1}{2hl_\alpha} (q_{\alpha+1} + q_\alpha) \xi_{\alpha,\beta}, & \text{if } \alpha, \beta = 1, \dots, N. \end{cases}$$



The viscous terms are included in the definition of  $\mathbf{E}_\alpha(\mathbf{w})$ :

$$\mathbf{E}_\alpha(\mathbf{w}) = \begin{cases} 0, & \text{if } \alpha = 0, \\ \frac{1}{\rho l_\alpha} \left( K_{\alpha-\frac{1}{2}} - K_{\alpha+\frac{1}{2}} + M_{\alpha,W} \right), & \text{if } \alpha = 1, \dots, N. \end{cases}$$

Next, we detail the two steps of the splitting procedure. In the first step we consider the hyperbolic system with the non-conservative products, corresponding to the momentum transference terms between the vertical layers. In the second step we deal with the viscous terms.

Before describing these processes, let us focus on the treatment of the bottom condition because it plays a crucial role in order to achieve the well-balanced property. The numerical discretization must solve two different difficulties related to the well-balanced property. The first one is physical, i.e., the Coulomb friction at the bottom and the walls must behave as a force which opposes the movement of the granular flow. When the total friction is greater than the sum of the other forces acting on the system, then we should obtain  $u_\alpha = 0$  for  $\alpha = 1, \dots, N$ . This effect is achieved in the second step, through the discretization of the bottom friction term  $K_{1/2}$ . The second difficulty is a numerical issue. We use a Riemann solver in order to solve the hyperbolic part of the system, which introduces numerical diffusion. This artificial diffusion must be zero in order to ensure  $\partial_t h = 0$  when the granular flow has stopped, i.e., when  $u_\alpha = 0$  for  $\alpha = 1, \dots, N$ . Next, we describe the two steps of the numerical approximation:

**Step 1:** Firstly, we do not consider viscous effects, that is,  $\mathbf{E}(\mathbf{w}) = \mathbf{0}$ . Then, we consider a finite volume solver to discretize system (3.26). Namely, we consider a HLL type method defined as follows:

$$\mathbf{w}_i^{n+1/2} = \mathbf{w}_i^n + \frac{\Delta t}{\Delta x} \left( \mathcal{F}_{c,i-1/2}^n - \mathcal{F}_{c,i+1/2}^n + \frac{1}{2} (\mathcal{B}_{i+1/2}^n + \mathcal{B}_{i-1/2}^n + \mathcal{S}_{i+1/2}^n + \mathcal{S}_{i-1/2}^n) \right), \quad (3.27)$$

with

$$\mathcal{B}_{i+1/2}^n = \frac{1}{2} (\mathbf{B}(w_{i+1}^n) + \mathbf{B}(w_i^n)) (\mathbf{w}_{i+1}^n - \mathbf{w}_i^n),$$

and

$$\mathcal{S}_{i+1/2}^n = \frac{1}{2} (\mathbf{S}(w_{i+1}^n) + \mathbf{S}(w_i^n)) (h_{i+1/2+}^n - h_{i+1/2-}^n),$$

where  $h_{i+1/2\pm}^n$  is defined by the hydrostatic reconstruction introduced in Audusse *et al.* [6]:

$$h_{i+1/2-}^n = \max(0, h_i - (\Delta Z_{i+1/2})_+); \quad (3.28)$$

$$h_{i+1/2+}^n = \max(0, h_{i+1} - (-\Delta Z_{i+1/2})_+),$$

where

$$(\Delta Z_{i+1/2})_+ = \max(0, z_{b,i+1} - z_{b,i}). \quad (3.29)$$

The numerical flux associated to the convective terms,  $\mathcal{F}_{c,i+1/2}^n$ , is

$$\mathcal{F}_{c,i+1/2}^n = \frac{1}{2} (\mathbf{F}_c(\mathbf{w}_i^n) + \mathbf{F}_c(\mathbf{w}_{i+1}^n)) - \frac{1}{2} \mathcal{D}_{i+1/2}^n,$$

where  $\mathcal{D}_{i+1/2}^n$  is the numerical diffusion of the scheme. Let us remark that this method can be seen as a path-conservative method with a second order approximation of the Roe matrix by setting the paths as segments (see Parés & Castro [95]).

Thus, in order to define the numerical diffusion, we consider the HLL extension proposed in Castro Díaz & Fernández-Nieto [35]. In this paper authors proposed a general formulation of numerical methods where the numerical viscosity matrix is defined in terms of the evaluation of a polynomial on the Roe matrix. In our case, taking into account that we use a second order approximation of Roe matrix by segments and the fact that we introduce a well-balanced correction associated to the Coulomb friction term, the numerical diffusion is defined as follows:

$$\mathcal{D}_{i+1/2} = a_0 (\widehat{\mathbf{w}}_{i+1}^n - \widehat{\mathbf{w}}_i^n) + a_1 (\mathbf{F}_c(\mathbf{w}_{i+1}^n) - \mathbf{F}_c(\mathbf{w}_i^n) + \mathcal{B}_{i+1/2}^n + \mathcal{S}_{i+1/2}^n), \quad (3.30)$$

with

$$a_0 = \frac{S_R |S_L| - S_L |S_R|}{S_R - S_L}, \quad a_1 = \frac{|S_R| - |S_L|}{S_R - S_L},$$

being  $S_L$  and  $S_R$  approximations of the minimum and maximum wave speed. In practice, to defined  $S_L$  and  $S_R$  we consider a baroclinic approximation,

$$S_L = \min \left( \sum_{\alpha=1}^N l_\alpha u_{\alpha,i}^n - \sqrt{g \cos \theta h_i^n}, \sum_{\alpha=1}^N l_\alpha u_{\alpha,i+1/2}^n - \sqrt{g \cos \theta h_{i+1/2}^n} \right),$$

$$S_R = \max \left( \sum_{\alpha=1}^N l_\alpha u_{\alpha,i+1}^n + \sqrt{g \cos \theta h_{i+1}^n}, \sum_{\alpha=1}^N l_\alpha u_{\alpha,i+1/2}^n + \sqrt{g \cos \theta h_{i+1/2}^n} \right).$$

In (3.30) we use the reconstructed states

$$\widehat{\mathbf{w}}_i^n = (\hat{h}_{i+1/2-}, q_{1,i}, \dots, q_{N,i}), \quad \widehat{\mathbf{w}}_{i+1}^n = (\hat{h}_{i+1/2+}, q_{1,i+1}, \dots, q_{N,i+1}),$$

where  $\hat{h}_{i+1/2\pm}$  is defined by (3.28) taking in this case

$$(\Delta Z_{i+1/2})_+ = \max(0, z_{b,i+1} - z_{b,i} + \Delta \mathcal{C}_{i+1/2}), \quad (3.31)$$

with  $\Delta \mathcal{C}_{i+1/2} = -f_{i+1/2} \Delta x_{i+1/2}$  defined by considering the Coulomb (or no slip) friction term. Several definitions of  $f_{i+1/2}$  can be given (see Bouchut [25]), in this work we set

$$f_{i+1/2} = -\text{proj}_{g\mu_\beta} \left( \frac{-g(h_{i+1} + z_{b,i+1} - h_i - z_{b,i})}{\Delta x} - \frac{u_{\beta,i+1/2}}{\Delta t} \right), \quad (3.32)$$

where

$$\mu_\beta = \mu_s + \frac{2}{W} \mu_w \left( \sum_{\gamma=\beta+1}^N h_\gamma + \frac{h_\beta}{2} \right)$$

being  $\beta$  the lowest layer that is moving, i.e.,  $|u_\beta| > 0$ . If all the layers are at rest then  $\beta = N$ . Moreover,

$$proj_{g\mu_\beta}(X) = \begin{cases} X & \text{if } |X| \leq g\mu_\beta; \\ g\mu_\beta \frac{X}{|X|} & \text{if } |X| > g\mu_\beta, \end{cases} \quad (3.33)$$

and  $u_{\beta,i+1/2}$  is an average state of the velocity at layer  $\beta$ . For example we can set the Roe average state

$$u_{\beta,i+1/2} = \frac{\sqrt{h_i} u_{\beta,i} + \sqrt{h_{i+1}} u_{\beta,i+1}}{\sqrt{h_i} + \sqrt{h_{i+1}}}.$$

In practice, this term is important when the granular flow is stopping. In general, upper layers are the last ones that stop in granular flows, then we can also consider  $u_{\beta,i+1/2} = u_{N,i+1/2}$ . Note that the first condition in (3.33) gives the well-balanced property by ensuring that the numerical diffusion is zero when the velocity is also zero.

**Step 2:** Now, we must add the contribution of  $\mathbf{E}(\mathbf{w})$ . With this goal, a semi-implicit discretization is considered:

$$\mathbf{w}_i^{n+1} = \mathbf{w}_i^{n+1/2} + \Delta t \mathbf{E}(\mathbf{w}_i^n, \mathbf{w}_i^{n+1}), \quad (3.34)$$

where  $\mathbf{w}_i^{n+1/2}$  is the approximation (3.27). Note that the first component of  $\mathbf{E}(\mathbf{w})$  is 0, therefore we clearly obtain  $h^{n+1} = h^{n+1/2}$ .

We get  $q_i^{n+1} = (q_1^{n+1}, \dots, q_N^{n+1})_i$  as solution of the  $N \times N$  tridiagonal system

$$q_{\alpha,i}^{n+1} = q_{\alpha,i}^{n+1/2} + \frac{\Delta t}{\rho l_\alpha} \left( \eta_{\alpha+\frac{1}{2}}(\mathbf{w}_i^n) \frac{u_{\alpha+1,i}^{n+1} - u_{\alpha,i}^{n+1}}{l_{\alpha+\frac{1}{2}} h_i^{n+1}} - \eta_{\alpha-\frac{1}{2}}(\mathbf{w}_i^n) \frac{u_{\alpha,i}^{n+1} - u_{\alpha-1,i}^{n+1}}{l_{\alpha-\frac{1}{2}} h_i^{n+1}} + M_{\alpha,W,i}^{n,n+1} \right), \quad (3.35)$$

for  $\alpha = 2, \dots, N-1$ , where  $\eta_{\alpha+\frac{1}{2}}$  is defined by (3.16). The lateral side walls friction terms approximation is

$$M_{\alpha,W,i}^{n,n+1} = -l_\alpha h_i^n \frac{2}{W} \mu_w p_{\alpha,i}^n \frac{u_{\alpha,i}^{n+1}}{\sqrt{|u_{\alpha,i}^n|^2 + \delta^2}}, \quad (3.36)$$

with

$$p_{\alpha,i}^n = \rho g \cos \theta \left( z_{b,i} + h_i^n - \left( z_{b,i} + \sum_{\beta=1}^{\alpha-1} h_{\beta,i}^n + \frac{h_{\alpha,i}^n}{2} \right) \right), \quad \text{for } \alpha = 1, \dots, N.$$

The equations for  $\alpha = 1$  and  $\alpha = N$  can be analogously obtained taking into account that  $\eta_{N+1/2} = 0$  and the definition of  $K_{1/2}$ . For the first layer we consider a regularization of (3.23)-(3.24), which can be written as follows:

$$q_{1,i}^{n+1} = q_{1,i}^{n+1/2} + \frac{\Delta t}{\rho l_1} \left( \eta_{\frac{3}{2}}(\mathbf{w}_i^n) \frac{u_{2,i}^{n+1} - u_{1,i}^{n+1}}{l_{\frac{3}{2}} h_i^{n+1}} - \frac{\rho g h_i^n \cos \theta \mu(I_{\frac{1}{2},i}^n)}{\sqrt{\left| \frac{u_{1,i}^n - u_{0,i}^n}{l_1 h_i^n} \right|^2 + \delta^2}} \frac{u_{1,i}^{n+1} - u_{0,i}^{n+1}}{l_1 h_i^{n+1}} + M_{1,W,i}^{n,n+1} \right), \quad (3.37)$$

taking into account the definition of  $I_{1/2}$  (see (3.23)-(3.25)) and  $u_0$  (see figure 3.2) depending on the bottom condition. This formulation corresponds to approximating the friction condition at the bottom with a regularization method. It is consistent with the definition of  $\eta_{1/2}$  given by (3.16). As a consequence, we cannot obtain exactly  $u = 0$  m s<sup>-1</sup> when a solution at rest is expected. Actually, for the numerical tests presented in Section 3.4 we get velocities of order  $10^{-7}$  m s<sup>-1</sup>. Let us also remark that with this formulation the friction conditions at the bottom and lateral walls are considered directly in the definition of the linear system.

For the top layer, we consider

$$q_{N,i}^{n+1} = q_{N,i}^{n+1/2} + \frac{\Delta t}{\rho l_N} \left( M_{N,W}^{n,n+1} - \eta_{N-\frac{1}{2}}(\mathbf{w}_i^n) \frac{u_{N,i}^{n+1} - u_{N-1,i}^{n+1}}{l_{N-\frac{1}{2}} h_i^{n+1}} \right). \quad (3.38)$$

Note that the symmetric matrix associated to this linear system is a strictly diagonally dominant matrix, therefore the system is well-conditioned. Finally, we use the Thomas algorithm to solve each tridiagonal system.

We consider two different hydrostatic reconstruction in the first step, which are defined by (3.28)-(3.29) and (3.28)-(3.31). In the first one we deal with the change of the topography but the friction at the bottom is not taken into account. In the second one, the friction condition is managed in order to achieve a well-balanced scheme. An important remark is that the numerical treatment of the friction condition would not be consistent if we include the friction condition in the first reconstruction. This is because in that case the friction at the bottom would be added twice in a time step.

The last consideration that we do is related with solving the linear systems. It corresponds with solving a vertical diffusion in each cell. We only solve the linear system in the cell  $I_i$  if the total height  $h_i^{n+1}$  is larger than  $\varepsilon_S$ . Otherwise, the friction law at the bottom together with the lateral walls friction are considered as in the case of a single-layer model. The friction term (bottom and side walls) is applied to the first layer and we neglect the vertical variations in those cell, i.e., we set  $q_{\alpha,i}^{n+1} = q_{1,i}^{n+1}$  for  $\alpha = 2, \dots, N$ .

Therefore, in those cells for which  $0 < h_i^{n+1} < \varepsilon_S$  (or if we consider the single-layer model  $N = 1$ ), we define

$$q_{\alpha,i}^{n+1} = \begin{cases} q_{1,i}^{n+1/2} - \Delta t \rho g \cos\theta h_i^{n+1} \mu_{1,i}^n \frac{q_{1,i}^{n+1}}{|q_{1,i}^n|}, & \text{if } |q_{1,i}^{n+1/2}| > \Delta t \sigma_{c,i}^{n,n+1} \\ 0, & \text{otherwise,} \end{cases} \quad \alpha = 1, \dots, N, \quad (3.39)$$

being  $\sigma_{c,i}^{n,n+1} = \rho g h_i^{n+1} \cos\theta \mu_{1,i}^n$ , with  $\mu_{1,i}^n = \mu(I_{\frac{1}{2},i}^n) + \frac{h_i^n}{W} \mu_w$ , where  $I_{\frac{1}{2},i}^n$  is defined by (3.23) if we consider a Coulomb friction law, or by (3.24) for a no slip condition.

## 3.4 Numerical tests

In this section we show four numerical tests in order to validate the model and the numerical scheme presented in previous sections. Firstly, in Subsection 3.4.1, we consider a uniform flow and investigate the influence of the lateral wall friction on the vertical profile of velocity. We also study the evolution of two critical values of the channel width for different bottom slopes: (i)  $W_c$  that is the first value for which all the granular mass is moving, i.e., if  $W \geq W_c$  there is no flow/no-flow interface; (ii)  $W_b$  that is the first value for which the downslope velocity along the normal direction has a Bagnold profile and not a S-shaped profile. Secondly, in Subsection 3.4.2, we perform a test focused on the well-balanced property of the scheme, combined with the treatment of the wet/dry front. Third, in Subsection 3.4.3, we show that approximating the side walls friction through a single-layer model could lead to non-physical solutions that strongly differ from those computed with a multilayer model. Finally, in Subsection 3.4.4, we compare the results obtained with our model to laboratory experiments of granular column collapse.

All the tests are computed over a reference inclined plane of angle  $\theta$  (tilted coordinates), specified for each test. As we commented in previous section, for the tests where a solution at rest is expected, we cannot obtain exactly  $u = 0 \text{ m s}^{-1}$  because of the regularization method. However, we get velocities of order  $10^{-7} \text{ m s}^{-1}$ , which can be considered as zero without meaning a loss of accuracy in the results.

### 3.4.1 Uniform flow: influence of the channel width

In this test we consider a uniform flow of granular material, whose height is  $h = 50 d_s \approx 2.65 \text{ cm}$ , which flows within a narrow channel of width  $W$  and slope  $\theta$ . The grain diameter is  $d_s = 0.53 \text{ mm}$  and the volume fraction is  $\varphi_s = 0.6$ . The rheological parameters are  $\mu_s = \tan(20.9^\circ)$ ,  $\mu_2 = \tan(32.76^\circ)$ ,  $\mu_w = \tan(13.1^\circ)$  and  $I_0 = 0.279$ , which are typical values for experiments with glass beads.

For the simulations, we impose no slip condition at the bottom and zero velocity at the initial time. The material starts to flow because of the gravitational force. We use 50 layers in the multilayer discretization and consider the regularization parameter  $\delta = 10^{-5} \text{ s}^{-1}$  in equation (3.36). The horizontal length of the domain is 1.1, which we discretize with 100 points. We let the material flow until the uniform steady state is reached, then all the results will refer to this steady state.

First, we focus on the velocity profiles in the direction normal to the slope when going from a narrow to a wider channel. Figure 3.3 shows these profiles at a slope  $\theta = 26.1^\circ$  for increasing channel widths  $W = 9 d_s, 18 d_s, \dots, 13176 d_s$ . Note that in this test the parameter  $\lambda = H/L_y$  take values in a range from  $3 \cdot 10^{-3}$  to 5.5. In particular, the influence of the channel width on the position of the flow/no-flow interface is shown. The thickness of the flowing layer increases as the width does so. Moreover,

all the granular layer flows when the thickness  $W \geq W_c = 117 d_s \approx 6.2$  cm (see figure 3.3a). Figure 3.3b shows an S-shaped velocity profile until  $W \geq W_b = 425 d_s \approx 22.5$  cm where the flow then exhibits a Bagnold profile. The critical value  $W_b$  is measured by approximating the second derivative of the downslope velocity along the normal direction. Then  $W_b$  is the first value of  $W$  for which the second derivative changes its sign. Interestingly, an asymptotic velocity profile is reached for values of  $W$  greater than 3 meters approximately ( $W = 6588 d_s$ ). Then, the velocity profile is independent of the channel width. Note that these values are related to the chosen thickness  $h = 50 d_s$  and slope angle  $\theta = 26.1^\circ$ .

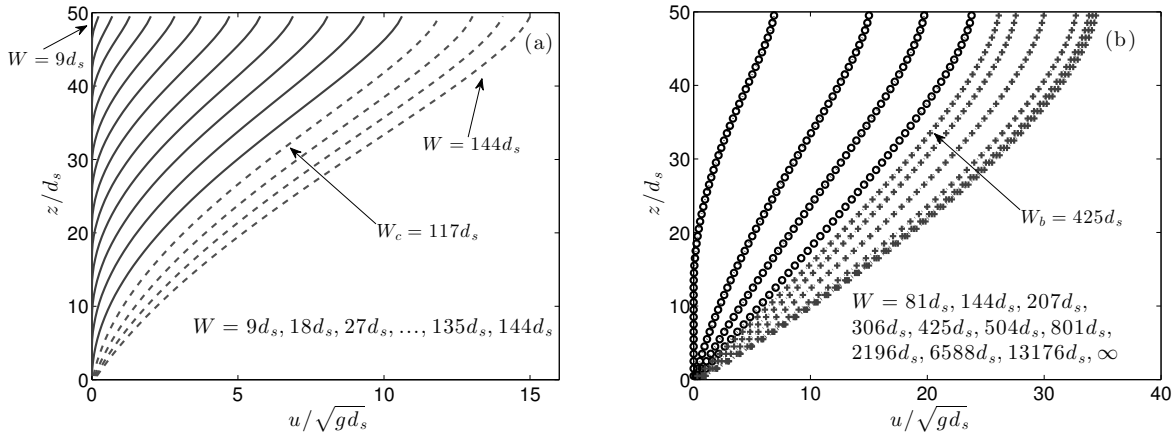


**Figure 3.3:** Normalized normal profiles of the downslope velocity ( $u$ ) on a slope  $\theta = 26.1^\circ$  and for different channel widths ( $W$ ), increasing from left to right lines. (a) Solid lines correspond to the cases when the flow/no-flow interface exists and dashed lines are the cases when the flow/no-flow interface does not exist; (b) circle-dotted lines correspond to the cases when the velocity profile is still S-shaped and cross-dotted lines are the cases when the velocity follows a Bagnold type profile.

Figure 3.4 shows the influence of the channel width on the maximum velocity (i.e. the velocity at the free surface). We can observe in this figure a nonlinear behavior of the maximum velocity in terms of the channel width. For small values of the width  $u_{max}$  scales approximately as  $(W/d_s)^{3/2}$  (see inset (a)). When the width increases the maximum velocity tends to the velocity reached when the lateral friction term is not considered (i.e.  $W = \infty$ ). For  $W_b = 425d_s \approx 22.52$  cm, the maximum velocity is still 1.3 times lower than for  $W = \infty$ .

Let us investigate how  $W_c$  (minimum width for all the granular mass to flow) and  $W_b$  (minimum width for the flow to exhibit a Bagnold profile) vary with the slope angle for a given flow thickness  $h = 50 d_s \approx 2.65$  cm (figure 3.5a).  $W_c$  and  $W_b$  are calculated by increasing the width  $W$  in steps of  $25 d_s \approx 1.33$  cm for fixed slopes  $\theta = 22^\circ, 24^\circ, 26.1^\circ, 28^\circ$  and  $30^\circ$ . For small slopes, high values of  $W$  should be reached to get fully flowing materials with Bagnold velocity profile (i.e.  $W_c \approx 35.77$  cm and  $W_b \approx 84.8$  cm at  $\theta = 22^\circ$ ). The values of  $W_c$  and  $W_b$  rapidly decrease with increasing slope angles and reach almost constant values  $W_c \approx 4$  cm and  $W_b \approx 20$  cm. For example

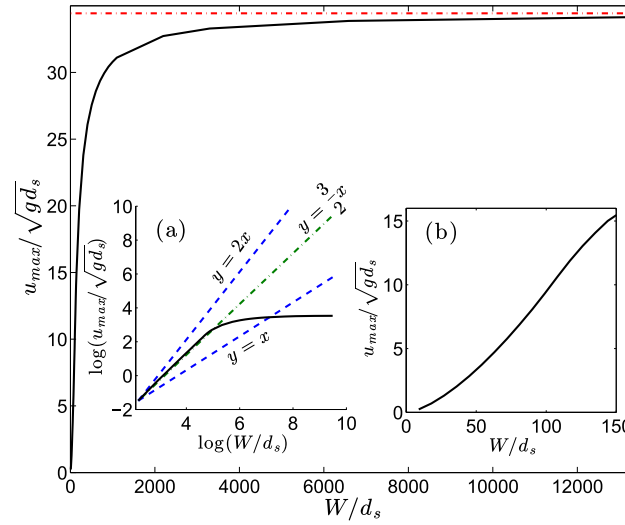


Figure 3.4: Normalized velocity (solid black lines) at the free surface as a function of the channel width  $W$ . The inner figures are (a) the logarithmic scale; (b) zoom of main figure for short widths  $W$ . Dashed-dot red line is the velocity at the free surface without side walls effect.

for a slope  $\theta = 24^\circ$ , we see that all the material flows for  $W > 9.28$  cm and that the hypothesis of Bagnold profile is valid only when  $W > 33.12$  cm. These results could help choosing the good dimensions of the channel in laboratory experiments.

Another key issue in shallow depth-averaged models is how to relate the depth-averaged velocity calculated with these models to the free surface velocity that is generally the one measured in laboratory experiments. Figure 3.5b shows the difference between the maximum velocity and the velocity averaged along the normal direction, normalized by this maximum velocity, for three different values of the width channel:  $W_0 < W_c$ ,  $W_c$  and  $W_b$  (see table 3.1). We see that this difference is huge (greater than 75 % of the maximum velocity) in the case of small widths. It is because in that case only the layers close to the free surface are moving. This difference decreases for larger widths since all the granular layer is moving. Note that for  $W = W_b$ , the difference is almost constant for all the slopes and still of about 43 % of the maximum velocity.

$\theta$ ( $^\circ$ )	$W_0$ (cm)	$W_c$ (cm)	$W_b$ (cm)
22	16	35.77	84.8
24	4	9.28	33.12
26.1	3.3	6.2	22.52
28	2.6	5.3	18.55

Table 3.1: Values of the channel width:  $W_c$  (minimum width for which all the granular layer is moving),  $W_b$  (minimum width for which the velocity follows a Bagnold profile) and  $W_0 < W_c$  as represented in figure 3.5.

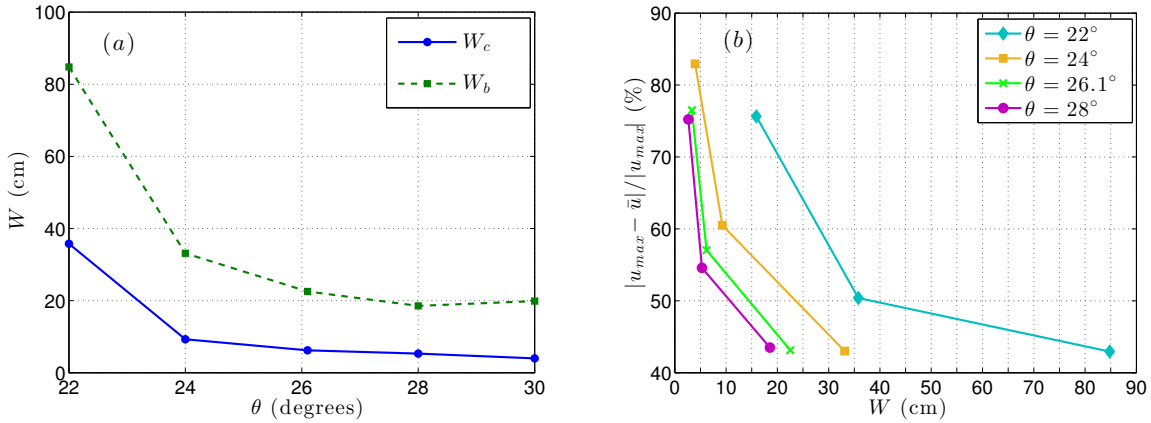


Figure 3.5: (a) Evolution of the threshold widths  $W_c$  (solid-circles blue line) and  $W_b$  (cross-dashed green line) as a function of the slope angle  $\theta$ . (b) Relative difference between the maximum and the averaged velocity for different slopes (represented by different colors) measured for widths  $W_0 < W_c$ ,  $W_c$  and  $W_b$  in table 3.1.

In these tests a no-slip condition was considered at the bottom. Figure 3.6 shows the velocity profiles with both no slip and friction condition, for a slope  $\theta = 26.1^\circ$  and three widths:  $W_c$ ,  $W_b$  and  $W \approx 7$  m for which the influence of the side walls is almost insignificant. We see that there is no difference between no-slip and basal friction conditions for the small width  $W_c$ , and a slight increase of the velocity obtained with basal friction condition for larger widths. We have also checked that the value of  $W_c$  and  $W_b$  are almost the same in both conditions, for the slope  $\theta = 26.1^\circ$ .

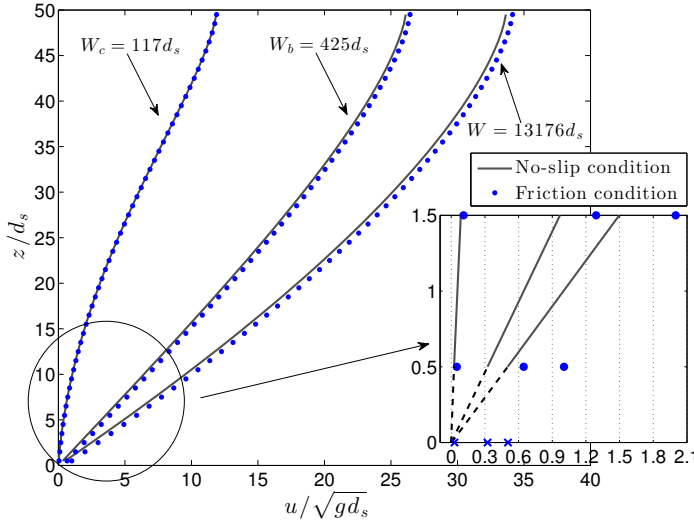


Figure 3.6: Normalized vertical profiles of the downslope velocity ( $u$ ) for different widths ( $W_c = 117 d_s$ ,  $W_b = 425 d_s$  and  $W = 13176 d_s$ ) of the channel and  $\theta = 26.1^\circ$ . Solid lines (respectively symbols) correspond to the simulations with no slip (respectively friction) condition at the bottom. Dashed black lines and blue crosses are the extrapolated velocities at the bottom.



### 3.4.2 Well-Balanced test including dry areas: granular collapse over an arbitrary bottom

In this test we consider a granular collapse over an arbitrary topography. We show that the hydrostatic reconstruction (3.28)-(3.33) is the key point making it possible to obtain the well-balanced property. By comparing the normal profiles of velocity at different times/points, we also show that our model produces results similar to the model considered in Jop *et al.* [75].

We take the grain diameter  $d_s = 0.7$  mm and the solid volume fraction  $\varphi_s = 0.62$ , leading to an apparent flow density  $\rho = 1550$  kg m<sup>-3</sup>. The friction coefficients are  $\mu_s = \tan(25.5^\circ)$ ,  $\mu_2 = \tan(36.5^\circ)$  and  $I_0 = 0.279$ . We also consider the following topography (in m) over an inclined plane with slope  $\theta = 16^\circ$  (see figure 3.7),

$$b(x) = 0.25e^{-50(x+0.5)^2} + 0.03e^{-50(x-0.75)^2}.$$

The initial condition is given by  $q = 0$  m<sup>2</sup> s<sup>-1</sup> and

$$h(x) = \begin{cases} 0.34 - b(x) & \text{if } |x| \leq 0.2; \\ 0 & \text{otherwise.} \end{cases}$$

The length of the domain is 4 m and we take 400 points for the spatial discretization. The channel width is  $W = 10$  cm and the side walls friction is included through the proposed model with the friction coefficient  $\mu_w = \tan(10.5^\circ)$ . We use 50 layers in the multilayer system. Figure 3.7 shows the evolution of the computed free surface with the multilayer model with and without the hydrostatic reconstruction. The results are shown in cartesian (left) and local (right) coordinates. We obtain similar profiles of the flowing mass in both cases at the first times. Nevertheless, when using the hydrostatic reconstruction (3.28)-(3.33) the mass stops at the final time ( $t = 1.7$  s), whereas it never stops if the hydrostatic reconstruction for the Coulomb friction is not taken into account (see figure 3.7b for longer times). The hydrostatic reconstruction (3.28)-(3.33) is thus a key ingredient of the well-balanced property of the scheme, since it allows to cancel the numerical diffusion (3.30) when the velocities are close to zero ( $u = 0$  is not exactly achieved due to the regularization method). In the following, we will always use the hydrostatic reconstruction.

In figure 3.8 we show the results with and without wall friction for the monolayer and multilayer models. More difference on the shape of the final deposit simulated with the two models is observed when wall friction is considered (left column in figure 3.8). Note that introducing this friction term in the monolayer model adds a constant extra friction over the whole granular layer whereas, in multilayer models, this terms introduces a friction starting from zero at the free surface and increasing with the flow depth. This will be deeper investigated in subSection 3.4.3.

The ability of the model to capture the different shapes of the normal profile of the downslope velocity is shown in figure 3.9. These profiles are shown at different times at

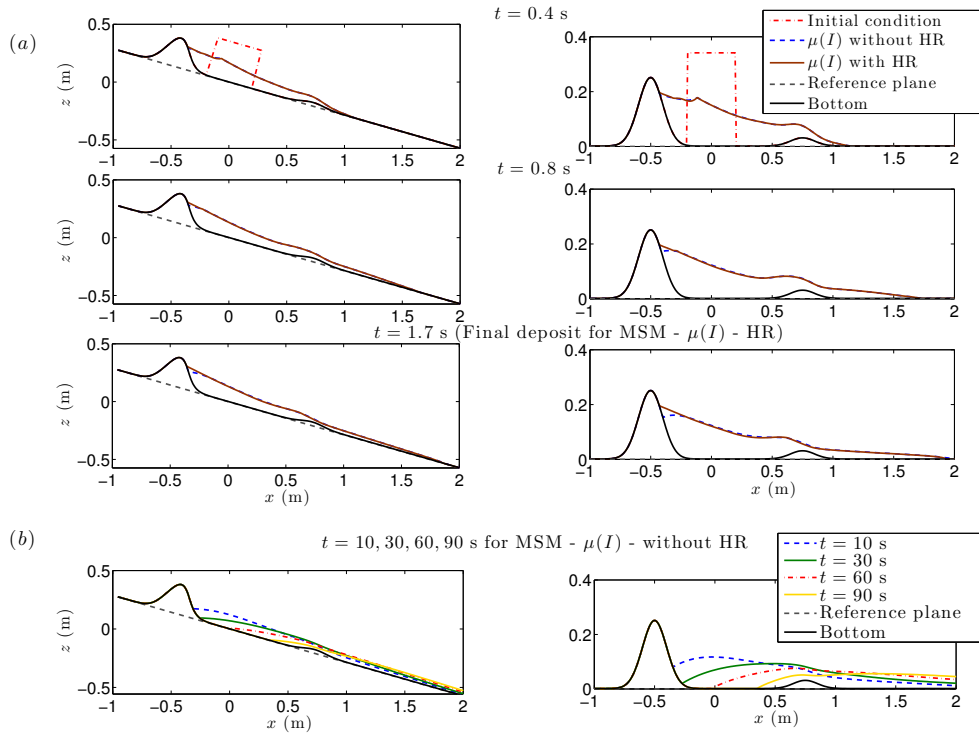


Figure 3.7: Left: representation in cartesian coordinates. Right: representation in local coordinates on the reference plane. (a) Free surface evolution during a granular collapse at different times, computed with the multilayer model, taking into account the hydrostatic reconstruction for the Coulomb friction (solid brown line) and without the hydrostatic reconstruction for the Coulomb friction (dashed blue line). (b) Free surface evolution without taking into account the hydrostatic reconstruction at larger times.

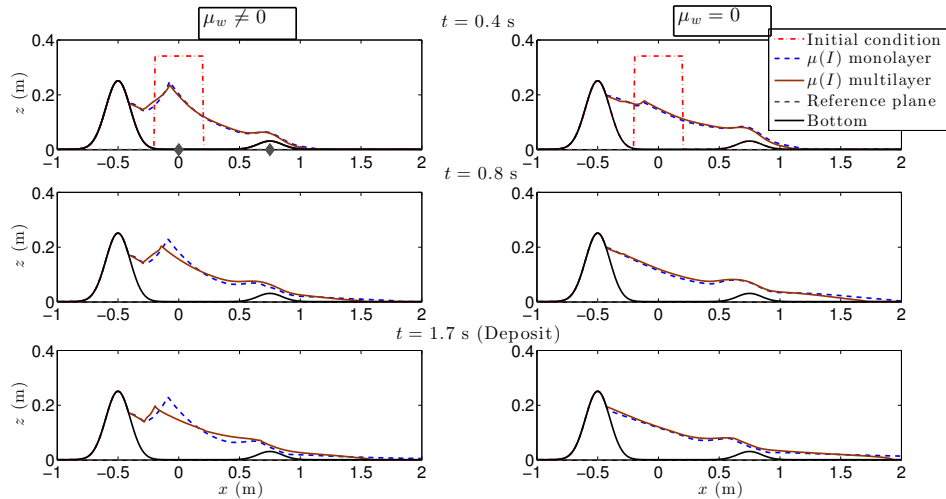


Figure 3.8: Free surface evolution in local coordinates at different times, computed with the multilayer model (solid brown line) and the monolayer model (dashed blue line), taking into account the side walls friction term (left hand side) and without this term (right hand side).

two fixed points: the center of the initial released mass ( $x = 0$  m) and the summit of the second bump of the topography ( $x = 0.75$  m). With the proposed multilayer model we can reproduce the Bagnold profile when the flow is accelerating as well as the S-shaped profiles corresponding to the stopping phase. We also show the profiles obtained when including side walls friction in the same way as in Jop *et al.* [75]. We see that the results of both models coincide. This is consistent with the remark in Section 3.2, showing that both models coincide if  $\text{sign}(u) = \text{sign}(\partial_z u)$ .

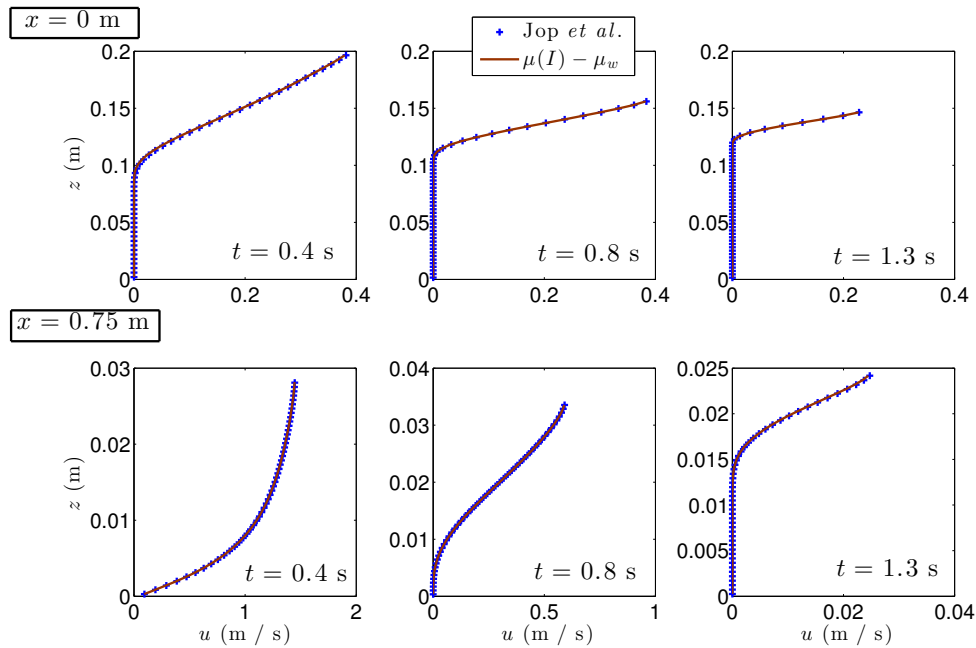


Figure 3.9: Normal profiles of downslope velocity measured at  $x = 0$  m and 0.75 m at times  $t = 0.4, 0.8, 1.3$  s. The profiles are computed with the proposed model (solid brown lines) and with the model proposed by Jop *et al.* [75] (symbols).

### 3.4.3 Solutions at rest with lateral walls friction: multilayer vs monolayer

With this test we show that an appropriate vertical discretization is essential in order to properly take into account the effect of the side walls friction.

We focus on the steady solutions of system (3.21), that is, we assume that  $u_\alpha = 0$ . For the monolayer model ( $N = 1$ ) the momentum equation in system (3.21) gives a solution at rest if the following condition is satisfied:

$$\left| \partial_x (\tilde{b} + b + h) \right| \leq \left| \mu_s + \mu_w \frac{h}{W} \right|,$$

where  $\tilde{b} = -x \tan \theta$ . Let us denote by  $\mathcal{S} = b + h$  the free surface in local coordinates. Without loss of generality let us suppose that its slope is negative and  $\theta \geq 0$ . Then, a solution at rest is defined by  $\mathcal{S}$ , solution of the following differential equation:

$$\partial_x \mathcal{S}(x) = \tan \theta - \mu_s - \frac{\mu_w}{W} (\mathcal{S}(x) - b(x)). \quad (3.40)$$

By setting the initial condition  $\mathcal{S}(x_f) = z_f$ , for some constant values  $x_f$  and  $z_f$ , the solution reads

$$\begin{aligned} \mathcal{S}(x) &= \frac{W}{\mu_w} (-\mu_s + |\tan \theta|) - \\ &- \frac{\mu_w}{W} e^{-\frac{\mu_w}{W}x} \int_x^{x_f} b(s) e^{\frac{\mu_w}{W}s} ds + \left( z_f + \frac{W}{\mu_w} (\mu_s - |\tan \theta|) \right) e^{-\frac{\mu_w}{W}(x-x_f)}. \end{aligned} \quad (3.41)$$

For the multilayer case, from the momentum equation in system (3.21) we deduce that a solution at rest is reached if

$$\left| g \cos \theta h \partial_x (\tilde{b} + b + h) \right| \leq \left| \frac{1}{\rho l_\alpha} (K_{\alpha-\frac{1}{2}} - K_{\alpha+\frac{1}{2}} + M_{\alpha,W}) \right| \quad \text{for } \alpha = 1, \dots, N.$$

From the definition of the  $K_{\alpha+1/2}$  and  $M_{\alpha,W}$ , the previous inequality reads

$$\left| \partial_x (\tilde{b} + b + h) \right| \leq \left| \mu_s + C_\alpha \mu_w \frac{h}{W} \right|,$$

where

$$C_\alpha = 2 \left( \sum_{\beta=\alpha+1}^N l_\beta + \frac{l_\alpha}{2} \right).$$

Then, the main difference between the solution at rest of a multilayer model (with  $N > 1$ ) and the monolayer model is the coefficient  $C_\alpha$  that multiplies  $\mu_w$ . For the monolayer model this coefficient is 1.

As a consequence the solution (3.41) is not a steady solution of the multilayer model. This is because the pressure varies with depth and therefore the friction is smaller for higher layers (that move) and gets bigger for lower layers (they can eventually stop). For example, assuming an odd number of vertical layers,  $N = 2n + 1$  and  $l_\alpha = 1/N$  for  $\alpha = 1, \dots, N$ , then  $C_\alpha = \frac{2}{N}(N - \alpha + \frac{1}{2})$ . The only value of  $\alpha$  that makes  $C_\alpha = 1$  is for  $\alpha = n + 1$ , that is, the middle layer. The value of  $C_\alpha$  is greater than 1 for lower layers ( $\alpha < n + 1$ ), so the friction is bigger and then the material does not move. On the contrary,  $C_\alpha < 1$  for higher layers ( $\alpha > n + 1$ ) which induces a smaller friction and the material moves. Then, in the multilayer case, the solution  $\mathcal{S}$  defined by (3.41) is not a steady solution, since the upper part of the granular mass will flow.

The solution at rest of the multilayer model converges to the solution defined by the free surface

$$\mathcal{S} = z_f + (\tan \theta - \mu_s)(x - x_f).$$

NPX	$L^1$ -Error	$L^1$ -Order	$L^2$ -Error	$L^2$ -Order	$L^\infty$ -Error	$L^\infty$ -Order
50	$7.02 \times 10^{-3}$	–	$6.47 \times 10^{-3}$	–	$9.86 \times 10^{-3}$	–
100	$2.87 \times 10^{-3}$	1.29	$2.44 \times 10^{-3}$	1.41	$2.06 \times 10^{-3}$	2.25
200	$1.82 \times 10^{-3}$	0.65	$1.55 \times 10^{-3}$	0.65	$1.26 \times 10^{-3}$	0.71
400	$1.06 \times 10^{-4}$	4.09	$1.02 \times 10^{-4}$	3.92	$2.06 \times 10^{-4}$	2.61
800	$3.08 \times 10^{-5}$	1.79	$2.67 \times 10^{-5}$	1.94	$4.65 \times 10^{-5}$	2.15
1600	$8.01 \times 10^{-6}$	1.95	$6.86 \times 10^{-6}$	1.96	$1.13 \times 10^{-5}$	2.03

Table 3.2: Errors and related order for the free surface computed with the monolayer model obtained by varying the number of points in the  $x$  direction. NPX denotes the number of points in the  $x$ -direction.

Let us perform a test showing that the analytical solution defined by (3.41) is preserved up to second order by the proposed numerical method when we consider only one layer,  $N = 1$ . On the contrary, when imposing this solution as initial condition in the multilayer model, the mass moves and the new simulated solution at rest is very different. For this test, we assume a flow with the same material and rheological properties as in the previous subsection. We consider the domain  $D = [0, 2] \times [-0.05, 0.05] \times \mathbb{R}$ , and a channel width  $W = 10$  cm. We also consider a bottom topography

$$b(x) = 0.1 e^{-100(x-0.5)^2} + 0.35 e^{-100x^2},$$

over a reference plane of angle  $\theta = 16^\circ$ . As initial condition the velocities are set to zero and the initial thickness is given by  $h = S - b$ , where  $S$  is defined by (3.41), with  $x_f = 1$  m and  $z_f = b(x_f)$ .

In this test we consider 20 layers in the multilayer model and 200 nodes in the horizontal direction. Results are shown in figure 3.10a for monolayer and multilayer solutions with side walls friction. Table 3.2 shows that the monolayer model keeps the steady solution to second order accuracy whereas the solution for the multilayer model evolves in time to a different deposit (figure 3.10a). We can observe that the slope of the final deposit obtained with the multilayer model is very close to  $(\tan(\theta) - \mu_s)$  in local coordinates, that is the slope of the solution at rest at which the multilayer model converges. The line with this slope is labeled as “Reference” in figure 3.10. Note that the slope of the computed deposit must always be lower than the slope of this reference line, given by the angle of repose of the material. Note also that the difference of runout distances predicted by the monolayer and the multilayer models is close to 50% of the extension of the initial condition.

We also show that we cannot introduce the side walls friction effect by using a monolayer model, even taking a lower friction coefficient  $\mu_w/2$ ,  $\mu_w/3$ , etc. The deposit widely differs from the solution obtained with the multilayer model in both, the shape and the runout. When the friction coefficient  $\mu_w/2$  is considered, the runout are 1.67, 2.15, 2.16 m in cases (a), (b), (c) in figure 3.10 respectively, whereas by using the multilayer model the obtained runout are 1.48, 1.76, 2.1 m respectively. Note also that

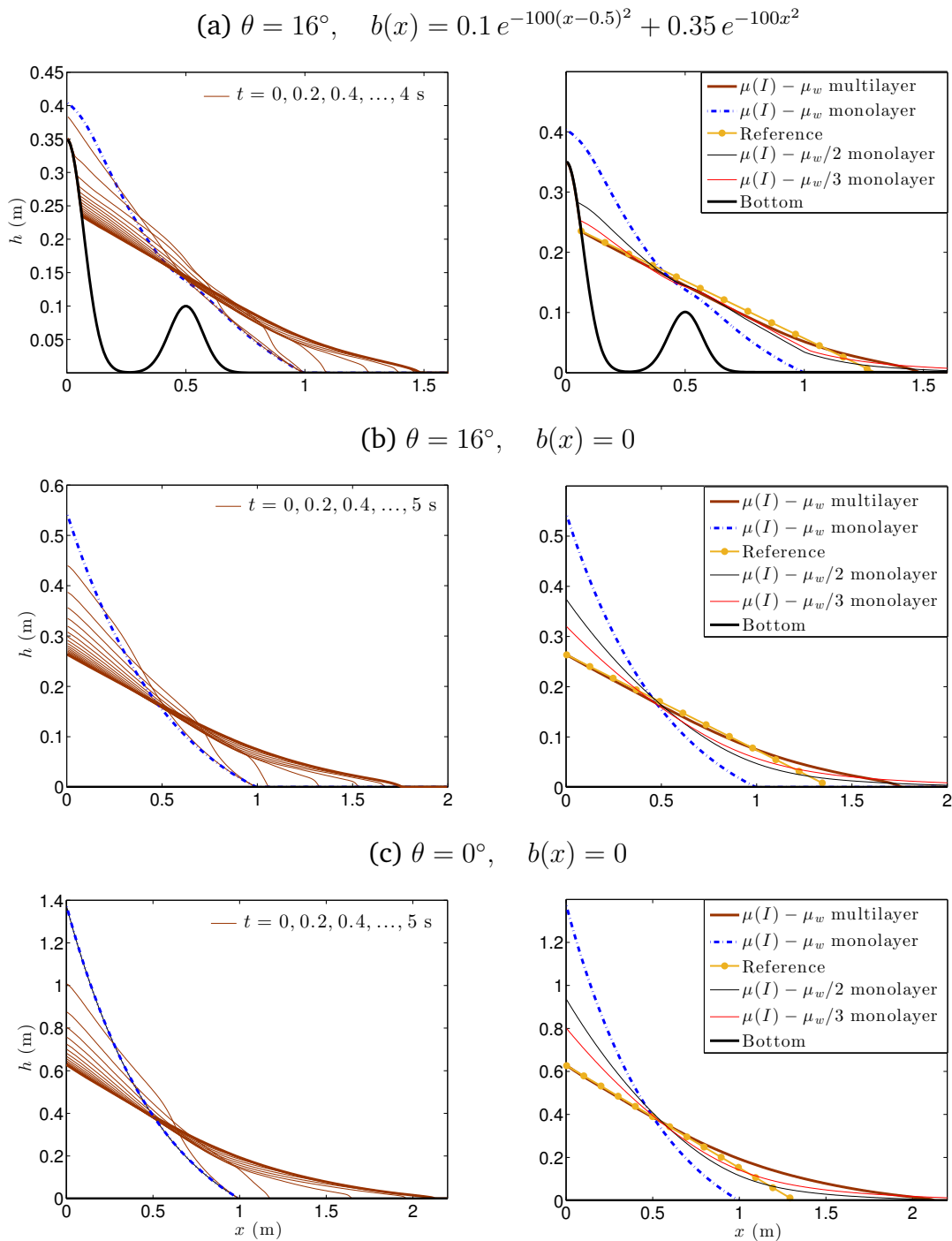


**Figure 3.10:** *Left column: evolution in time of the thickness profile for monolayer (dot-dashed blue line) and multilayer (solid brown line) models with the side walls friction term. Right column: deposit obtained with the monolayer and the multilayer models. Solid black lines (solid red lines) represent the deposit with the monolayer model taking a lower side walls friction coefficient  $\mu_w/2$  ( $\mu_w/3$ ). As a reference of theoretical solution for the multilayer model, we plot a line (point-solid gold line) whose slope is  $(\tan \theta - \mu_s)$  in local coordinates.*

despite the runout is larger, the height of the material in the initial part of the column is also bigger than the obtained in the multilayer case.

Let us also remark that the bottom topography reduces the exponential shape of the free surface profile (see the influence of  $b(x)$  in (3.41)). Therefore, the solutions with the multilayer and monolayer model are even more different in the case of flat bottom (see figures 3.10b and 3.10c). We conclude that including the side walls friction term using single-layer models is not appropriate, since they preserve non-physical solution due to the overestimation of the lateral friction term obtained because of the depth-average hypothesis.

### 3.4.4 Laboratory experiments: dam break over rigid and erodible beds

We compare here our numerical simulation with the laboratory experiments of Mangeney *et al.* [87] in the case of a rigid bed (i.e. not covered by a layer of erodible particles). This configuration was not investigated in previous chapter (also [54]) due to the difficulty to deal with dry areas ( $h = 0$ ) from a numerical point of view. When numerical models cannot handle dry areas, a thin layer of material is generally added on these dry zones. We will investigate here what is the error related to such artificial thin layer. We also study the time evolution of the flow/no-flow interface with either a variable or a constant friction coefficient.

We release a granular column of height  $h = 14$  cm and length 20 cm over an inclined plane of slope  $\theta$ , confined in a channel of  $W = 10$  cm. The granular material in the experiments is made of subspherical glass beads with the material and rheological properties described in previous Section 3.4.2. For the numerical simulation, we use 20 layers in the multilayer model.

In this test the friction with the lateral walls is modelled as in previous chapter by adding 0.1 to the friction coefficient  $\mu_s$  ([54]). As discussed in [54], hydrostatic models are not able to reproduce the first instants of the granular collapse due to the strong effect of non-hydrostatic pressure. Indeed hydrostatic models spread much faster than experiments at the beginning Mangeney-Castelnau *et al.* [88]. As a result, side walls friction is not well approximated in such models because the flowing layer is overestimated during the first instants. Despite this limitation, we compare our simulation with laboratory experiments with and without taking into account the extra friction term on the lateral walls.

Figures 3.11, 3.12 and 3.13 show the results with and without adding the side walls friction term for different slopes of the inclined plane,  $\theta = 0^\circ, 16^\circ, 19^\circ, 22^\circ$ . We see that the new term increases the effective friction, and then the approximation of the free surface improves at short times, while the runout in the final deposit decreases. The comparisons only make sense at final times as consequence of the hydrostatic assumption. As the slope  $\theta$  increases, the flow gets thinner and the downslope velocity gets higher

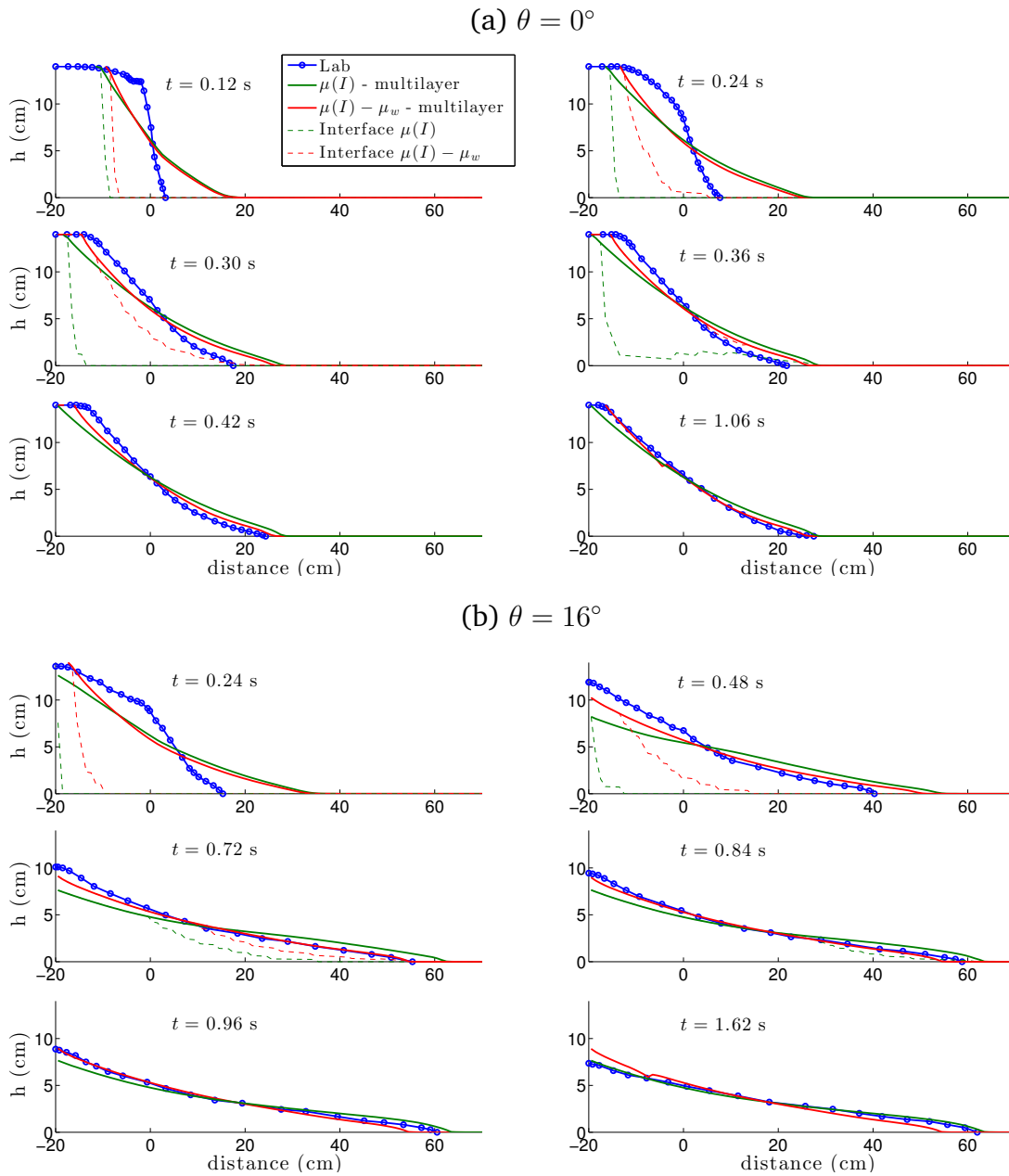


Figure 3.11: Thickness of the granular mass as a function of the position along the slope in the laboratory experiments (solid-circle blue line), with the  $\mu(I)$ -multilayer model (solid green line), and the model adding the side walls friction term ( $\mu(I) - \mu_w$ -multilayer, solid red line), for a slope (a)  $\theta = 0^\circ$ , (b)  $\theta = 16^\circ$  in the rigid bed case (without an erodible bed over the slope). Thin dashed lines are the flow/no-flow interfaces.

compared to the velocity normal to the bottom. As a result, the hydrostatic approximation (i.e. shallow flow approximation) is more correct for higher slopes. Indeed, we can see that the time evolution of the free surface is close to the one obtained with the complete visco-plastic model of Martin *et al.* [91] where non-hydrostatic pressure is taken into account (represented by gold squares in figure 3.13a). One of our objective here is to show that multilayer models can be a powerful tool to approximate the flow/no-flow



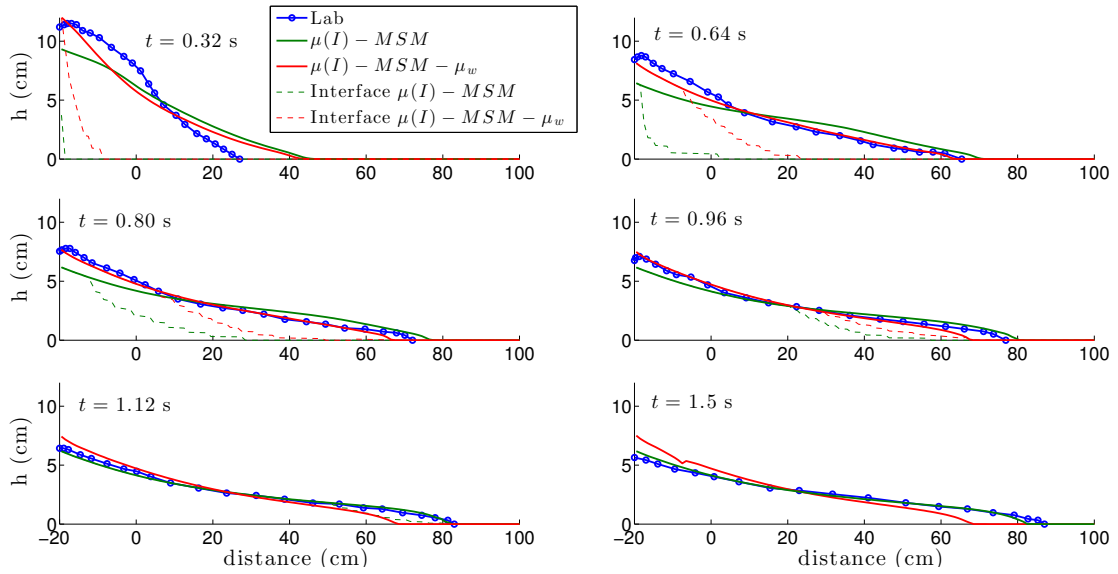


Figure 3.12: Thickness of the granular mass as a function of the position along the slope in the laboratory experiments (solid-circle blue line), with the  $\mu(I)$ -multilayer model (solid green line), and the model adding the side walls friction term ( $\mu(I) - \mu_w$ -multilayer, solid red line), for a slope  $\theta = 19^\circ$ . Thin dashed lines are the flow/no-flow interfaces.

interface position. In order to compute this interface we consider a threshold for flow, i.e. the material is assumed to flow if the velocity is higher than  $1 \text{ cm s}^{-1}$ .

Figures 3.14 and 3.15 show the distribution of the horizontal and vertical velocities, and the variable friction coefficient computed with the  $\mu(I)$  - multilayer and the  $\mu(I) - \mu_w$  - multilayer model for the slopes  $\theta = 0^\circ$  and  $\theta = 16^\circ$  at an intermediate time. We see that the absolute value of the velocities (horizontal and vertical) computed with the  $\mu(I) - \mu_w$  multilayer model is lower close to the bottom due to the fact that the new friction term is greater there. This difference is more clear in figure 3.15, corresponding to a non flat bottom. In both cases, we see that the variable friction coefficient is greater close to the front since the strain rates are also greater and the pressure is small leading to high inertial number too. Note that this friction coefficient is quite similar with both models in figures 3.14 and 3.15. In particular, this means that the difference between the velocities for the two models is due to the lateral friction term in the  $\mu(I) - \mu_w$  - multilayer model.

Dealing with a rigid bed involving wet/dry fronts is usually hard numerically. Therefore, a thin layer of material is sometimes added on the rigid bed to get rid from numerical issues while expecting to get similar result to the case of true rigid bed. To quantify the error related to this artificial layer, we simulate here the collapse over a thin layer of material of thickness  $h_i$  of a mass with initial thickness:

$$h(x, 0) = \begin{cases} 14 \text{ cm} & \text{if } x \leq 0; \\ h_i & \text{otherwise,} \end{cases} \quad \text{with } h_i = 0, 0.014, 0.14, 1.4, 4.6 \text{ mm.}$$

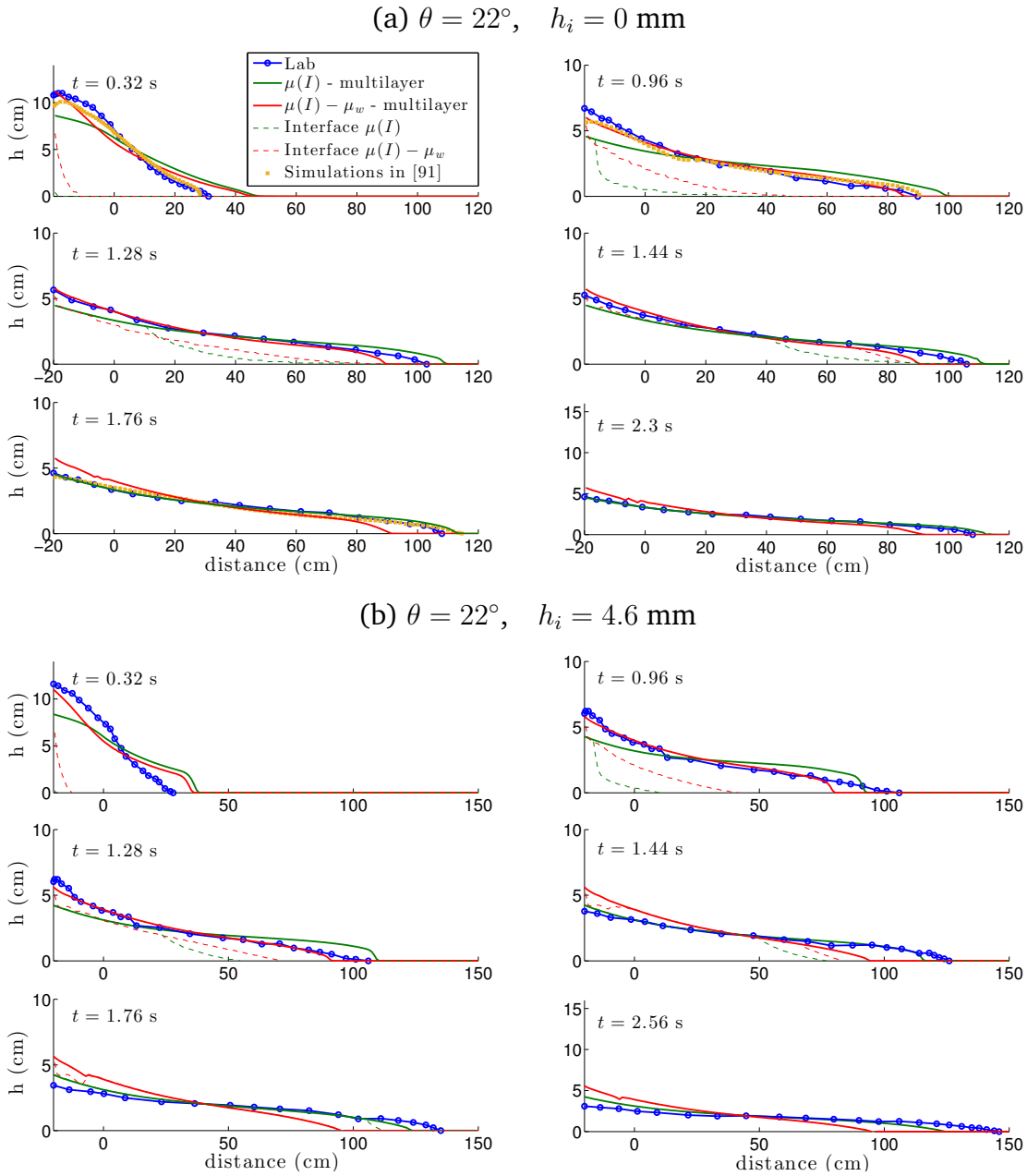


Figure 3.13: Thickness of the granular mass as a function of the position along the slope in the laboratory experiments (solid-circle blue line), with the  $\mu(I)$ -multilayer model (solid green line), and the model adding the side walls friction term ( $\mu(I) - \mu_w$ -multilayer, solid red line), for a slope  $\theta = 22^\circ$  (a) in the rigid bed case, (b) with an erodible bed  $h_i = 4.6$  mm. Thin dashed lines are the flow/no-flow interfaces and gold squares are the simulations of Martin et al. [91], corresponding to  $t = 0.32, 0.96, 1.76$  s, based on a complete visco-plastic model (i.e. without the shallow approximation).

Figure 3.16 shows the collapsing mass profiles and the deposits simulated for a slope  $\theta = 22^\circ$ . We see that, when the layer is thin enough ( $h_i = 0.014$  mm), the simulated mass profiles and deposit are similar to the case when  $h_i = 0$  (true rigid bed). Slight differences appear at  $h_i = 0.14$  mm and get stronger for larger thicknesses ( $h_i = 1.4$

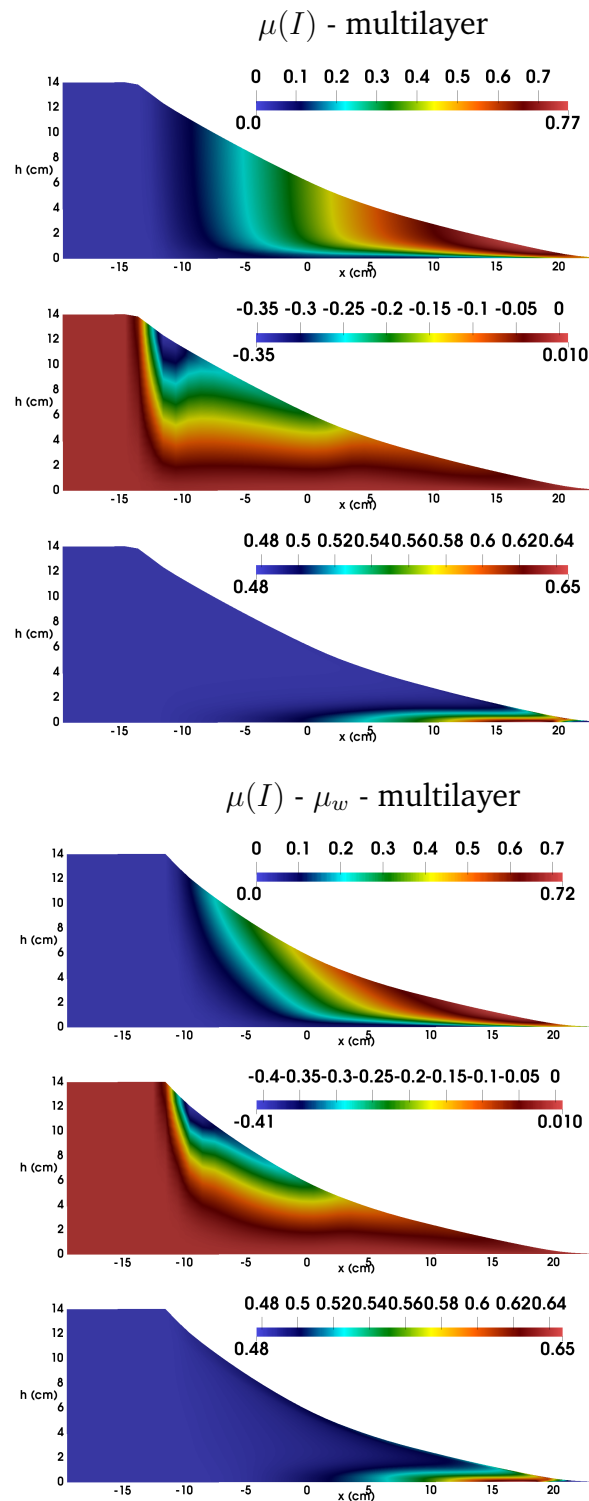


Figure 3.14: Free surface in the case  $\theta = 0^\circ$  at time  $t = 0.18$  s computed with the  $\mu(I)$ -multilayer model (left hand side) and with the  $\mu(I)$ - $\mu_w$ -multilayer (right hand side). Colors represent the distribution of horizontal velocities  $u$  (upper part), vertical velocities  $w$  (middle part) and variable coefficient of friction  $\mu(I)$  (lower part).

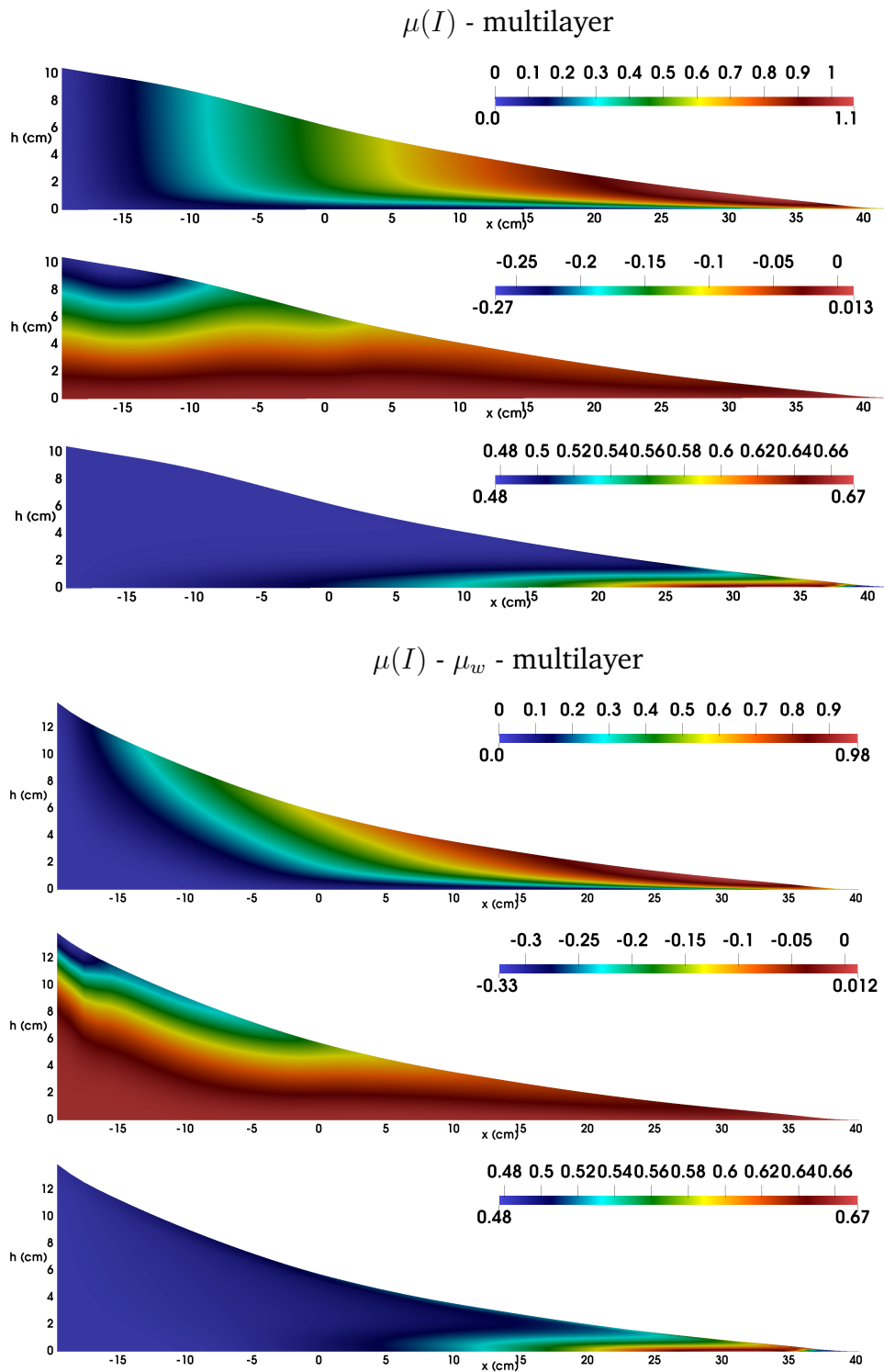


Figure 3.15: Free surface in the case  $\theta = 16^\circ$  at time  $t = 0.3$  s computed with the  $\mu(I)$ -multilayer model (left hand side) and with the  $\mu(I) - \mu_w$ -multilayer (right hand side). Colors represent the distribution of horizontal velocities  $u$  (upper part), vertical velocities  $w$  (middle part) and variable coefficient of friction  $\mu(I)$  (lower part).

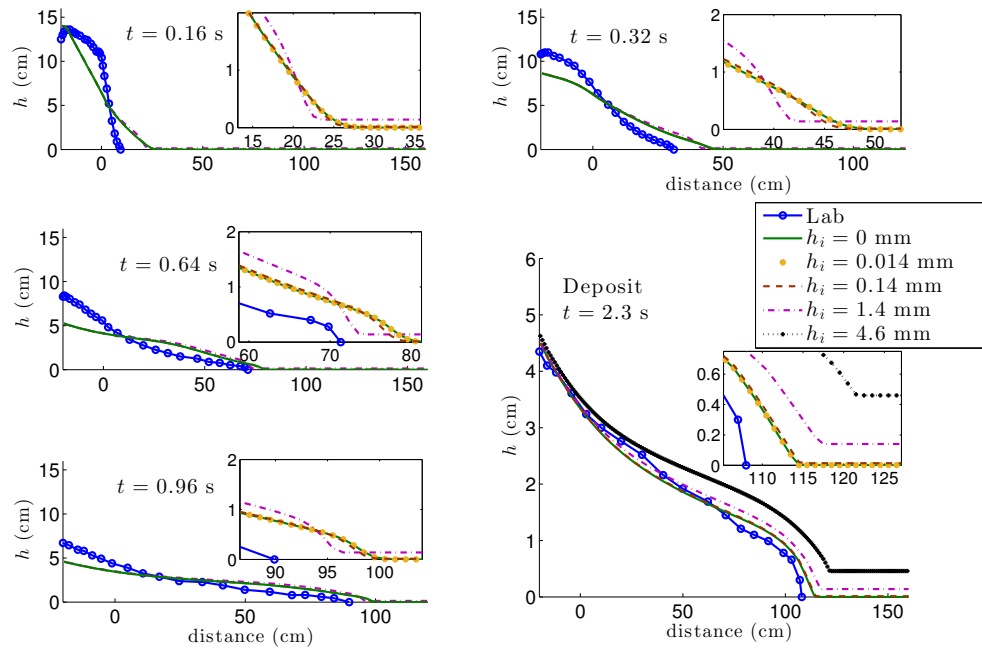


Figure 3.16: Deposit obtained in the laboratory experiments (solid-circle blue line), with the  $\mu(I)$ -multilayer model, for a slope  $\theta = 22^\circ$  at different times and for thicknesses of the thin layer  $h_i = 0.014$  mm (gold points), 0.14 mm (dashed brown line), 1.4 mm (dot-dashed magenta line) and 4.6 mm (dotted-cross black line). The solid green line is rigid bed case.

mm). In this case, we observe an increase of the runout distance and a different shape of the deposit, in particular near the front as shown in inset zooms in figure 3.16 at intermediates times.

Note that  $h_i = 0.14$  mm represents about 0.1% of the thickness of the initial granular column. As a conclusion, similar results can be obtained when a very thin layer of material is added to the rigid bed instead of having a true rigid bed. Nevertheless, the error made may be large if this layer is not thin enough.

Figure 3.17 shows the evolution of the flow/no-flow interface  $b(x, t)$  for the granular collapse over a slope  $\theta = 22^\circ$  at  $x = 20$  and  $x = 60$  cm for flow over a rigid bed (left column) and over an erodible bed of thickness  $h_i = 4.6$  mm (right column). The simulations are performed using the multilayer model (with 50 layers) with a variable friction coefficient  $\mu(I)$  or a constant coefficient  $\mu_s$ , and adding or not the side walls friction term.

When the variable friction coefficient  $\mu(I)$  is used (with and without the friction term at lateral walls) to simulate granular collapse over a rigid bed, the flow/no-flow interface goes from the bottom to the top of the granular layer until the whole thickness stops. For granular collapse over erodible bed, the flow/no-flow interface penetrates into the erodible bed very rapidly (i.e. erosion of the granular bed), stays at the bottom for a while (i.e. the whole thickness is flowing) and then goes up to the free surface. This qualitative behaviour is very similar to what is observed in experiments (see e.g.

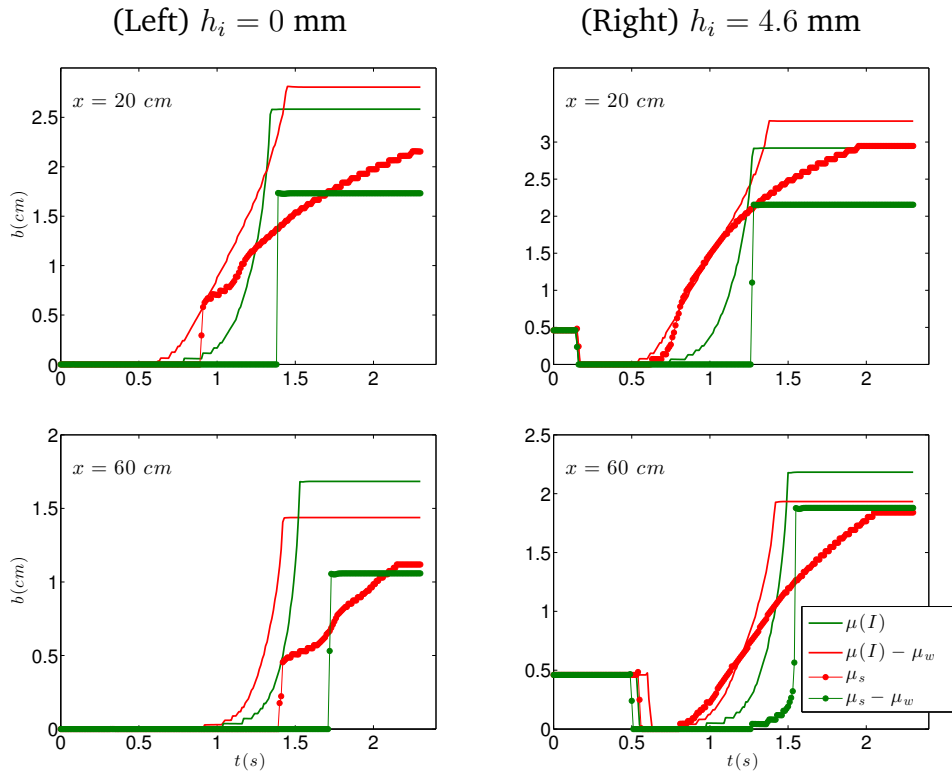


Figure 3.17: Time evolution of the flow/no-flow interface computed for the granular collapse ( $W = 10$  cm) over a slope  $\theta = 22^\circ$ , covered by a layer of thickness  $h_i = 0$  mm (left column) and  $h_i = 4.6$  mm (right column) of the same material, at  $x = 20, 60$  cm. The solid green (green symbols) lines represent the simulations by using the variable friction coefficient  $\mu(I)$  (constant coefficient  $\mu_s$ ) without adding the side walls contribution. The solid red (red symbols) lines represent the simulations with the variable friction coefficient  $\mu(I)$  (constant coefficient  $\mu_s$ ) adding the side walls friction term.

[87, 84]). Adding walls friction with the  $\mu(I)$  rheology makes the flow/no-flow interfaces go up earlier and change the shape of its time evolution up to the free surface. With a constant friction coefficient  $\mu_s$  and no wall effects for flows over a rigid bed, the mass moves all over the depth until all the granular thickness suddenly stops, contrary to what is observed experimentally. When adding walls friction, the flow/no-flow interface propagates from the bottom to the top due to increasing friction with depth. For flows over erodible bed with  $\mu_s$ , the flow/no-flow interface penetrates into the erodible layer as rapidly as with  $\mu(I)$  but then, again, goes abruptly up to the free surface. Adding walls friction in this case drastically change the flow/no-flow behaviour that get closer to the results obtained with  $\mu(I)$ .

Lusso *et al.* [84] investigated the evolution of the flow/no-flow interface  $b(t)$  through a simplified model which takes into account the variation in the direction normal to the topography but not in the downslope direction. They compare their results to what was measured experimentally in the well-developed shallow flow following granular collapse over a channel of width  $W = 20$  cm and slope  $\theta = 22^\circ$  covered by a static layer of thickness  $h_i = 5$  mm. The configuration and material properties of these

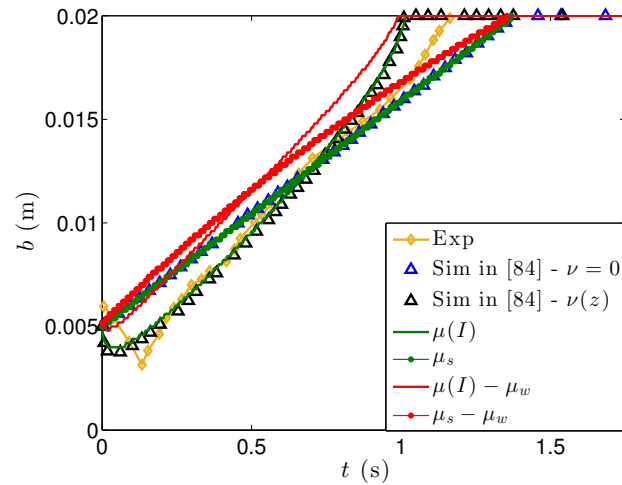


Figure 3.18: Time evolution of the flow/no-flow interface computed with the multilayer model for a uniform flow, with linear initial velocity profile, over a slope  $\theta = 22^\circ$  which is covered by a static layer of thickness  $h_i = 5$  mm. In this case the channel width is  $W = 20$  cm. The solid green (green symbols) lines represent the simulations with the variable friction coefficient  $\mu(I)$  (constant coefficient  $\mu_s$ ) without adding the side walls contribution. The solid red (red symbols) lines represent the simulations with the variable friction coefficient  $\mu(I)$  (constant coefficient  $\mu_s$ ) adding the side walls friction term. The diamonds-solid gold line is the experiments in [84] for this test.

experiments are the same as those exposed previously. They compared the position of the flow/no-flow interface at  $x = 90$  cm with analytical and numerical solution of the non depth-averaged shallow equations for uniform flow in the downslope direction. The parameter and initial condition of the test are:

$$\mu_s = \tan(26^\circ), \quad \mu_2 = \tan(28^\circ), \quad d_s = 0.7 \text{ mm}, \quad \varphi = 0.62, \quad I_0 = 0.279,$$

$$h_0 = h(t = 0, x) = 2 \text{ cm}, \quad b_0 = b(t = 0, x) = 5 \text{ mm}.$$

The linear initial profile of velocity is assumed in the moving layer ( $b_0 < z < h_0$ ):

$$u(t = 0, z) = 70 (z - b_0) \text{ m/s} \quad \text{if } z > b_0; \quad u(t = 0, z) = 0 \text{ m/s} \quad \text{if } z < b_0.$$

This test is simulated here. In order to improve the precision 100 vertical layers are used. Figure 3.18 shows the evolution of the flow/no-flow interface  $b(t)$  computed with the variable coefficient of friction  $\mu(I)$  and the constant coefficient  $\mu_s$ , including or not the side walls friction term. We see that our result without lateral wall friction agrees almost perfectly with the ones presented in Lusso *et al.* [84] (see cases  $\nu = 0$  and  $\nu = \nu(Z)$  in figure 16 in [84]). By using the friction constant coefficient the profile flow/no-flow interface evolution in time is a straight line, whereas the convex shaped profile observed in experiments is reproduced for the variable friction  $\mu(I)$ . Based on these results, Lusso *et al.* [84] suggested that for uniform flows erosion (i.e. penetration within the erodible layer) can only be obtained for a variable friction coefficient (called viscosity in their paper) and not for a constant friction coefficient  $\mu_s$ . In the case of granular collapse

presented above, erosion is also obtained with  $\mu_s$ , certainly due to the non-uniformity of the flow and in particular to downslope pressure gradients (see Section 5 in [84]).

As a conclusion, despite the fact that the approximation of the lateral walls friction is not good enough and we still need to add 0.1 to the friction coefficient, shallow multilayer models appear to be a very interesting alternative to shallow depth-averaged models by making it possible to describe changes of the velocity profiles, lateral wall effects and erosion processes with still reasonable computational cost.



# Semi-implicit time discretization with variable number of layers\*

\*The results in this chapter have been published in the paper: L. Bonaventura, E.D. Fernández-Nieto, J. Garres-Díaz, & G. Narbona-Reina, Multilayer shallow water models with locally variable number of layers and semi-implicit time discretization, *Journal of Computational Physics*, 364 (2018), pp. 209–234.

## 4.1 Introduction

The goal of this chapter is to apply the multilayer approach to the case of large scale geophysical flows. To this end, we propose two strategies acting at the same time to make multilayer models more efficient and fully competitive with their  $z$ - and  $\sigma$ -coordinates counterparts. On one hand, a novel discretization approach is proposed, in which the number of vertical layers and their distribution are allowed to change in different regions of the computational domain. On the other hand, efficient semi-implicit discretizations are applied for the first time to the discretization of the free surface gradients and the flow divergence in multilayer models, leading to a significant efficiency improvement for subcritical regimes. Notice that a semi-implicit approach for the discretization of vertical viscosity and friction terms has instead been introduced in [7, 56]. In addition, we propose a more efficient way to implement an IMEX-ARK method to discretize the multilayer system, which mimics what is done for the simpler  $\theta$ -method. As an example of the potential of the proposed techniques, applications to tidally forced flow and to a sediment transport problem are presented, where we show that the computational time required is significantly reduced and that the vertical number of layers, as well as their distribution, can be adapted to the local features of the problem.

In order to further simplify the presentation, we only introduce the discretization for an  $x - z$  vertical slice, even though both, the multilayer approach and any of the methods presented, can be generalized to the full three dimensional case. In this chapter, again

for simplicity, we have restricted our attention to constant density flows. An extension to variable density problems in the Boussinesq regime will be investigated in the future. However, as a first step, we present in a detailed description of the coupled discretization of a tracer equation. Not only it is the basis for the variable density extension, but, as shown in [66], the coupling of this equation to the discretized continuity equation is not a trivial issue and it is very important to verify compatibility conditions between the discrete continuity equation and the discrete tracer equations.

The chapter is organised as follows. In Section 4.2, the equations defining the multilayer shallow water models of interest will be reviewed. In Section 4.3, the spatial discretization is introduced in a simplified framework, showing how the number of layers can be allowed to vary over the computational domain. In Section 4.4, some semi-implicit time discretizations are introduced for the model with a variable number of layers. Results of a number of numerical experiments are reported in Section 4.5, showing the significant efficiency gains that can be achieved by combination of these two techniques.

## 4.2 Multilayer shallow water models

In this chapter we use cartesian coordinates ( $\tilde{b} = 0$  in Subsection 1.2) instead of the tilted coordinates considered in previous chapters, for simplicity. Then, we consider a multilayer subdivision of the domain as in figure 4.1. Let us recall that this subdivision

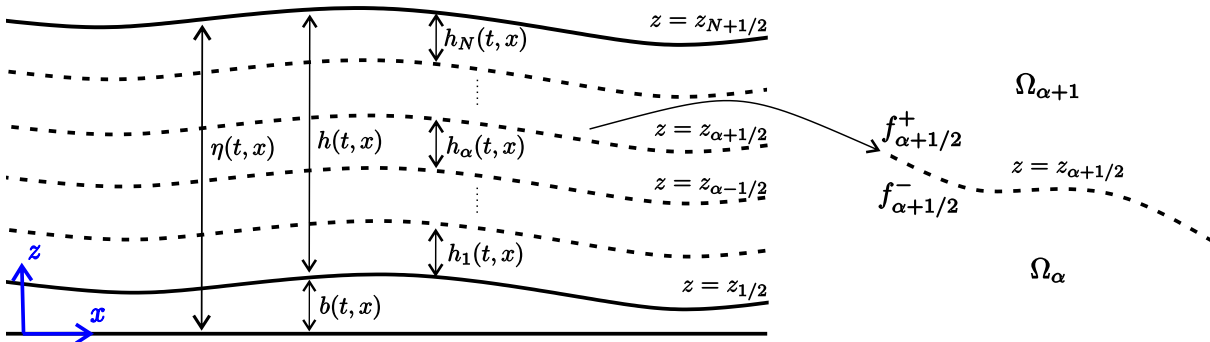


Figure 4.1: Sketch of the domain and of its subdivision in a constant number of layers.

corresponds to the vertical discretization of the domain, which, a priori, is not related to the characteristics neither of the flow nor of the domain. Note that in this chapter  $\eta$  denotes the free surface position, and not the dynamic viscosity as in previous chapters. Then, we set as customary in the literature

$$\eta = b + h. \quad (4.1)$$

Following Chapter 1 (also Fernández-Nieto *et al.* [54, 56]), the equations describing this multilayer approach can be written for  $\alpha = 1, \dots, N$  as

$$\left\{ \begin{array}{l} \partial_t h_\alpha + \partial_x (h_\alpha u_\alpha) = G_{\alpha+\frac{1}{2}} - G_{\alpha-\frac{1}{2}}, \\ \partial_t (h_\alpha u_\alpha) + \partial_x (h_\alpha u_\alpha^2) + \\ + gh_\alpha \partial_x (b+h) = K_{\alpha-\frac{1}{2}} - K_{\alpha+\frac{1}{2}} + \\ + \frac{1}{2} G_{\alpha+\frac{1}{2}} (u_{\alpha+1} + u_\alpha) - \frac{1}{2} G_{\alpha-\frac{1}{2}} (u_\alpha + u_{\alpha-1}). \end{array} \right. \quad (4.2)$$

As in previous chapters, we consider a fluid with constant density. The vertical velocity profile is obtained as in Chapter 1. Let us recall its expression, it is recovered from both the integrated incompressibility and the mass jump condition, obtaining for  $\alpha = 1, \dots, N$  and  $z \in (z_{\alpha-\frac{1}{2}}, z_{\alpha+\frac{1}{2}})$ ,

$$w_\alpha(t, x, z) = w_{\alpha-\frac{1}{2}}^+(t, x) - \left( z - z_{\alpha-\frac{1}{2}}(t, x) \right) \partial_x u_\alpha(t, x), \quad (4.3a)$$

$$w_{\alpha+\frac{1}{2}}^+(t, x) = \left( u_{\alpha+1}(t, x) - u_\alpha(t, x) \right) \partial_x z_{\alpha+\frac{1}{2}}(t, x) + w_{\alpha+\frac{1}{2}}^-(t, x), \quad (4.3b)$$

$$w_{\alpha+\frac{1}{2}}^-(t, x) = w_{\alpha-\frac{1}{2}}^+(t, x) - h_\alpha(x) \partial_x u_\alpha(t, x), \quad (4.3c)$$

where  $w_{\frac{1}{2}}^+ = u_1 \partial_x b - G_{\frac{1}{2}}$ , at the bottom. Since we are focusing in this chapter mostly on subcritical flows, there is no special reason to choose discharge rather than velocity as a model variable. Therefore, we rewrite the previous system as

$$\left\{ \begin{array}{l} \partial_t h_\alpha + \partial_x (h_\alpha u_\alpha) = G_{\alpha+\frac{1}{2}} - G_{\alpha-\frac{1}{2}}, \\ h_\alpha \partial_t u_\alpha + h_\alpha u_\alpha \partial_x u_\alpha + gh_\alpha \partial_x (b+h) = \\ = K_{\alpha-\frac{1}{2}} - K_{\alpha+\frac{1}{2}} + G_{\alpha+\frac{1}{2}} \Delta \tilde{u}_{\alpha+\frac{1}{2}} + G_{\alpha-\frac{1}{2}} \Delta \tilde{u}_{\alpha-\frac{1}{2}}, \end{array} \right. \quad (4.4)$$

where  $\Delta \tilde{u}_{\alpha+\frac{1}{2}} = (u_{\alpha+1} - u_\alpha)/2$ . From the derivation in previous chapters, it follows that

$$G_{\alpha+\frac{1}{2}} = \partial_t z_{\alpha+\frac{1}{2}} + u_{\alpha+\frac{1}{2}}^\pm \partial_x z_{\alpha+\frac{1}{2}} - w_{\alpha+\frac{1}{2}}^\pm, \quad (4.5a)$$

$$K_{\alpha+\frac{1}{2}} = -\nu_{\alpha+\frac{1}{2}} \mathcal{U}_{\alpha+\frac{1}{2}}^H, \quad (4.5b)$$

where  $\nu$  denotes the kinematic viscosity and  $\mathcal{U}_{\alpha+\frac{1}{2}}^H$  is the approximation of  $\partial_z u_\alpha$  at  $\Gamma_{\alpha+\frac{1}{2}}$ . We recall that the vertical partition of the domain is defined through the positive coefficients  $l_\alpha$ , satisfying  $h_\alpha = l_\alpha h$  and

$$\sum_{\alpha=1}^N l_\alpha = 1.$$

Note that these coefficients, whose choice is completely free, determine the thickness of the vertical layers  $h_\alpha$ . Since these are not material layers, mass can flow through them. Usually, the  $l_\alpha$  coefficients have been taken to be constants (see Chapters 1, 2, 3), while in this chapter we consider them as a function of space, as detailed in Section 4.3.

As explained in Chapter 1, the mass transfer term can be rewritten as (see (1.30))

$$G_{\alpha+\frac{1}{2}} = \sum_{\beta=1}^{\alpha} \left( \partial_x (h l_\beta u_\beta) - l_\beta \sum_{\zeta=1}^N \partial_x (l_\zeta h u_\zeta) \right). \quad (4.6)$$

As conclusion,  $G_{\alpha+\frac{1}{2}}$  is written in terms of the total height ( $h$ ) and the horizontal velocities ( $u_\alpha$ ), and the system is rewritten with  $N + 1$  equations and unknowns.

Assuming also  $\partial_t b = 0$ , system (4.4)-(4.5) is finally re-written as

$$\begin{cases} \partial_t \eta + \partial_x \left( h \sum_{\beta=1}^N l_\beta u_\beta \right) = 0, \\ \partial_t u_\alpha + u_\alpha \partial_x u_\alpha + g \partial_x \eta = \\ = \frac{K_{\alpha-\frac{1}{2}} - K_{\alpha+\frac{1}{2}}}{h_\alpha} + \frac{G_{\alpha+\frac{1}{2}} \Delta \tilde{u}_{\alpha+\frac{1}{2}} + G_{\alpha-\frac{1}{2}} \Delta \tilde{u}_{\alpha-\frac{1}{2}}}{h_\alpha}, \end{cases} \quad (4.7)$$

for  $\alpha = 1, \dots, N$ , where  $\eta$  is defined by (4.1) and denotes the free surface position.

The transport equation for a passive scalar can be coupled to the previous continuity and momentum equation (4.7), in such a way as to guarantee compatibility with the continuity equation in the sense of Gross *et al.* [66]. If  $\rho_\alpha$  denotes the average density of the passive scalar in  $\Omega_\alpha$ , it satisfies the following tracer equation:

$$\partial_t (\rho_\alpha h_\alpha) + \nabla_x \cdot (\rho_\alpha h_\alpha u_\alpha) = \rho_{\alpha+1/2} G_{\alpha+\frac{1}{2}} - \rho_{\alpha-1/2} G_{\alpha-\frac{1}{2}}, \quad (4.8)$$

where

$$\rho_{\alpha+1/2} = \frac{\rho_\alpha + \rho_{\alpha+1}}{2} + \frac{1}{2} \text{sgn}(G_{\alpha+\frac{1}{2}}) (\rho_{\alpha+1} - \rho_\alpha).$$

In principle, any appropriate turbulence and friction model can be considered to define  $K_{\alpha+\frac{1}{2}}$ ,  $\alpha = 0, \dots, N$ . Here we have employed a parabolic turbulent viscosity profile and friction coefficients derived from a logarithmic wall law:

$$\nu = \kappa \hat{u} (z - b) \left( 1 - \frac{z - b}{h} \right),$$

where  $\kappa = 0.41$  is the von Karman constant,  $\hat{u} = \sqrt{\tau_b / \rho_0}$  is the friction velocity and  $\tau_b$  denotes the shear stress. In order to approximate this turbulence model we set for

$\alpha = 1, \dots, N - 1$ :

$$K_{\alpha+\frac{1}{2}} = -\nu_{\alpha+\frac{1}{2}} \frac{u_{\alpha+1} - u_{\alpha}}{(h_{\alpha} + h_{\alpha+1})/2}, \quad \text{with } \nu_{\alpha+\frac{1}{2}} = \kappa \widehat{u}_{\alpha+\frac{1}{2}} \left( \sum_{\beta=1}^{\alpha} l_{\beta} h \right) \left( \sum_{\zeta=\alpha+1}^N l_{\zeta} \right).$$

For  $\alpha = 0$  and  $\alpha = N$ , standard quadratic models for bottom and wind stress are considered. We then set

$$K_{1/2} = -C_f |u_1| u_1, \quad K_{N+1/2} = -C_w |u_w - u_N| (u_w - u_N),$$

where  $u_w$  denotes the wind velocity and  $C_w$  the friction coefficient at the free surface. The friction coefficient  $C_f$  is defined, according to the derivation in Decoene *et al.* [46], as:

$$C_f = \kappa^2 \frac{\left(1 - \frac{\Delta z_r}{h}\right)}{\left(\ln\left(\frac{\Delta z_r}{\Delta z_0}\right)\right)^2}, \quad (4.9)$$

where  $\Delta z_0$  is the roughness length and  $\Delta z_r$  is the length scale for the bottom layer. Under the assumption that  $\Delta z_0 \ll \Delta z_r$  it can be seen that

$$\frac{u_t}{\widehat{u}} \approx \frac{1}{\kappa} \ln\left(\frac{z-b}{\Delta z_0}\right)$$

where  $u_t$  is the tangential velocity. In practice, we identify  $u_t$  with  $u_1$ , the horizontal velocity of the layer closest to the bottom, in the multilayer model. The definition of  $C_f$  given by equation (4.9) is deduced by using previous relation of the ratio between  $u_1$  and  $\widehat{u}$  (see [46]). Then, we set

$$\widehat{u}_{\alpha+\frac{1}{2}} = \frac{u_1 \kappa}{\ln\left(\sum_{\beta=1}^{\alpha} l_{\beta} h / \Delta z_0\right)},$$

in the definition of  $K_{\alpha+\frac{1}{2}}$ .

### 4.3 Spatial discretization with variable number of layers

The multilayer shallow water model (4.7) can be discretized in principle with any spatial discretization approach. For simplicity, we present the proposed discretization approach in the framework of simple finite volume/finite difference discretization on a staggered Cartesian mesh with C-grid staggering. A discussion of the advantages of this approach for large scale geophysical models can be found in Durran [48]. The C-grid staggering also has the side benefit of providing a more compact structure for the

system of equations that is obtained when a semi-implicit method is applied for time discretization. Generalization to structured and unstructured meshes can be obtained e.g. by the approaches proposed in Casulli & Catani [40] and Bonaventura & Ringler [22], Casulli & Walters [42], Casulli & Zanolli [43], respectively, but higher order methods such as those of Tumolo *et al.* [109, 110] could also be applied. It is to be remarked that the choice of a staggered mesh is by no means necessary and that the approach proposed below to handle a variable number of layers can be easily extended to colocated meshes as well.

On the other hand, the vertical number of layers employed, in the approach proposed in Fernández-Nieto *et al.* [56], is a discretization parameter whose choice depends on the desired accuracy in the approximation of the vertical structure of the flow. In order to make this type of model more flexible and more efficient, we propose to allow for a number of vertical layers that is not constant throughout the domain. This is one of the main contributions of this chapter. Our motivation is twofold: firstly, the use of this technique in order to adapt the vertical subdivision to the characteristic of the bathymetry. This is the case when both shallow and deep regions are present in the same computational domain. Secondly, in the case we are interested in a detailed vertical profile of velocity in a specific region, but not somewhere else. Then we could use multilayer only in that region, while maintaining a coarser resolution elsewhere.

The solution domain will coincide with an interval  $[0, L]$ , that is assumed to be subdivided into control volumes  $V_i = (x_{i-1/2}, x_{i+1/2})$ , with centers  $x_i = (x_{i+1/2} + x_{i-1/2})/2$ , for  $i = 1, \dots, M$ . Let us also denote  $\Delta x_i = x_{i+1/2} - x_{i-1/2}$  and  $\Delta x_{i+1/2} = x_{i+1} - x_i$ . The discrete free surface variables  $\eta_i$  are defined at the centers of the control volumes,  $x_i$ , while the discrete velocities  $u_{\alpha, i+1/2}$  are defined at the interfaces,  $x_{i+1/2}$ .

The transition between regions with different numbers of layers is assumed to take place at the center of a control volume  $V_i$ , so that one may have different  $N_{i+1/2}$  for  $i = 0, \dots, M$  and as a consequence, the discrete layer thickness coefficients  $l_{\alpha, i+1/2}$  are also defined at the half-integer locations  $i + 1/2$ . The number of layers considered at the cell center for the purpose of the discretization of the tracer equation are defined as  $N_i = \max \{N_{i-1/2}, N_{i+1/2}\}$  and the discrete layer thickness coefficients at integer locations  $l_{\alpha, i}$  are taken to be equal to those at the neighbouring half-integer location with larger number of layers. We will also assume that, whenever for some  $i + \frac{1}{2}$  one has, without loss of generality,  $N_{i-1/2} > N_{i+1/2}$ , then for any  $\beta = 1, \dots, N_{i+1/2}$  there exist

$$1 \leq \alpha_{i-1/2}^-(\beta) \leq \alpha_{i-1/2}^+(\beta) \leq N_{i-1/2} \quad \text{such that} \quad l_{\beta, i+1/2} = \sum_{\alpha=\alpha_{i-1/2}^-(\beta)}^{\alpha_{i-1/2}^+(\beta)} l_{\alpha, i-1/2}. \quad (4.10)$$

Note that the above formula means that the vertical mesh is assumed to be conforming. This allows a more straightforward implementation of the numerical approximation of horizontal advection in the velocity and in the tracer equation, which are the only

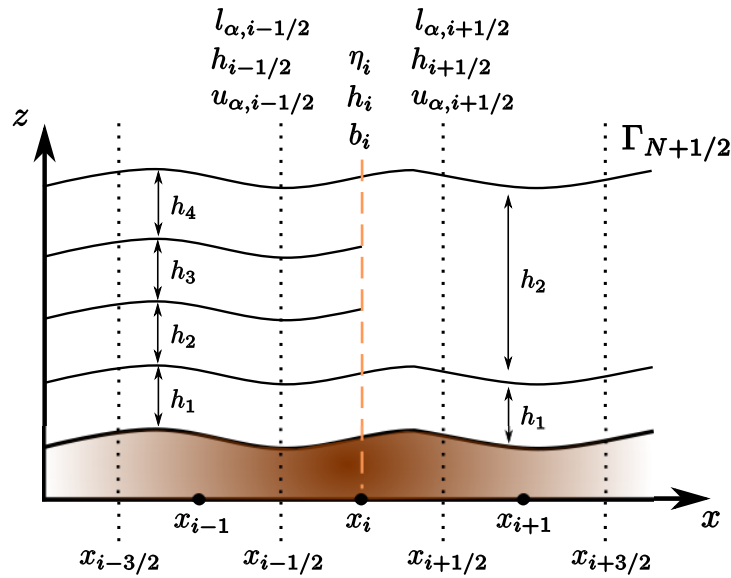


Figure 4.2: Sketch of the domain subdivision in a variable number of layers.

ones involving a horizontal stencil. Finally, again for simplicity of the implementation and without great loss of generality, it is assumed that just a single transition between cells with different number of vertical layers is possible in a 3-point stencil, that is, two consecutive transitions are not allowed. In terms of the number of layers, it means that if  $N_{i+1/2} \neq N_{i-1/2}$  one has  $N_{i-3/2} = N_{i-1/2}$  and  $N_{i+3/2} = N_{i+1/2}$ .

A sample configuration of this kind is depicted in figure 4.2. Notice that a dependence of the number of layers on time could also be introduced, in order to adapt the global maximum number of layers to the flow conditions, but this has not been done in the present implementation. Note also that the expression of the model would change in this case, namely a new term would appear in equation (4.6) where we use  $\partial_t h_\beta = l_\beta \partial_t h$ .

## 4.4 Semi-implicit time discretizations

The previous definitions yield a space discretization that can be easily coupled to any time discretization that yields a stable fully discrete space time scheme. For example, a time discretization by a third order Runge Kutta scheme has been employed as a reference in the numerical tests presented in Section 4.5. This explicit method requires a stability restriction (*CFL* condition) for the time step  $\Delta t$ , given by the well-known Courant number associated to the celerity, hereafter denoted  $C_{cel}$ . However, we will focus here on semi-implicit time discretization approaches aimed at reducing the computational cost in subcritical regime simulations. By using these semi-implicit discretizations, a less restrictive *CFL* condition is to be complied with, since the term associated to the celerity is removed. In that case, we consider the Courant number associated to the velocity,

hereafter denoted  $C_{vel}$ . We define the maximum Courant numbers as

$$C_{vel} = \max_{1 \leq i \leq M} \max_{1 \leq \alpha \leq N} \left| u_{\alpha, i+\frac{1}{2}} \right| \frac{\Delta t}{\Delta x_i}; \quad (4.11a)$$

$$C_{cel} = \max_{1 \leq i \leq M} \max_{1 \leq \alpha \leq N} \left( \left| u_{\alpha, i+\frac{1}{2}} \right| + \sqrt{g h_i} \right) \frac{\Delta t}{\Delta x_i}. \quad (4.11b)$$

With the goal of reducing the computational cost, it is immediate to notice that the formal structure of system (4.7) is entirely analogous to that of the three dimensional hydrostatic system considered in Casulli & Cheng [41], Casulli & Cattani [40], so that we can build semi-implicit time discretizations along the same lines, i.e. by treating implicitly the velocity in the continuity equation and the free surface gradient in the momentum equation. It should be stressed that our aim is not to propose new or optimal time discretizations, but rather to show that some semi-implicit approaches, which have been widely applied to model coastal flows and other environmental flows for standard vertical discretizations or for one layer models, can also be naturally extended to multilayer approaches, even when the number of layers changes in space. For this purpose, firstly we focus on a more conventional time discretization based on the off-centered trapezoidal rule (or  $\theta$ -method, see e.g. Lambert [80]). Secondly, we present a alternative approach based on a potentially more accurate (and equally robust) Implicit-Explicit Additive Runge Kutta method (IMEX-ARK). Other second and third order semi-implicit methods that could be employed are described e.g. in Boscarino *et al.* [24]. Notice also that, in the semi-implicit methods that are more standard for these applications, simplifications are usually introduced in the standard time discretization methods employed, that amount to linearizing in time at each time step. This is done in order to avoid solving a large nonlinear system at each time step, which would increase significantly the computational cost. Even though this entails a potential loss of accuracy, we have employed these simplifications here, consistently with our goal of coupling multilayer approaches to widely used semi-implicit techniques for environmental flows.

**Remark 2.** Notice that, in general, time discretizations do not guarantee positivity without additional CFL-like restrictions, see the discussion and literature review in Bonaventura & Rocca [20]. On the other hand, for the semi-implicit approaches considered in this chapter, the CFL restrictions based on the flow velocity that are required by the explicit part of the scheme are usually sufficient to guarantee positivity. In particular, following Gross *et al.* [66], the positivity of the  $\theta$ -method can be proved under the condition

$$c_{i+1/2}^+ + c_{i-1/2}^- \leq 1,$$

where  $c^+$  ( $c^-$ ) denotes the positive (negative) part

$$\begin{aligned} c^+ &= \max(0, c); \\ c^- &= \max(0, -c), \end{aligned} \quad \text{and} \quad c_{i+1/2} = \frac{\Delta t}{\Delta x_{i+1/2}} \sum_{\alpha=1}^{N_{i+1/2}} l_{\alpha, i+1/2} u_{\alpha, i+1/2}^{n+\theta},$$

with  $u^{n+\theta} = \theta u^{n+1} + (1 - \theta)u^n$ . A similar condition can be derived for the IMEX-ARK2.



#### 4.4.1 A $\theta$ -method time discretization

Following Casulli & Cattani [40], we first consider a semi-implicit discretization based on the  $\theta$ -method, which can be defined for a generic ODE system  $y' = f(y, t)$  as

$$\mathbf{y}_{n+1} = \mathbf{y}_n + \Delta t [\theta \mathbf{f}(\mathbf{y}_{n+1}, t_{n+1}) + (1 - \theta) \mathbf{f}(\mathbf{y}_n, t_n)],$$

where  $\Delta t$  denotes the time step and  $\theta \in [0, 1]$  is a implicitness parameter. If  $\theta \geq 1/2$  the method is unconditionally stable and the numerical diffusion introduced by the method increases when increasing  $\theta$ . For  $\theta = 1/2$  the second order Crank-Nicolson method is obtained. In practical applications,  $\theta$  is usually chosen just slightly larger than  $1/2$ , in order to allow for some damping of the fastest linear modes and nonlinear effects. We then proceed to describe the time discretization of system (4.7) based on the  $\theta$ -method.

For control volume  $i$ , the continuity equation in (4.7) is then discretized as

$$\begin{aligned} \eta_i^{n+1} + \theta \frac{\Delta t}{\Delta x_i} \left( \sum_{\beta=1}^{N_{i+\frac{1}{2}}} l_{\beta, i+\frac{1}{2}} h_{i+\frac{1}{2}}^n u_{\beta, i+\frac{1}{2}}^{n+1} - \sum_{\beta=1}^{N_{i-\frac{1}{2}}} l_{\beta, i-\frac{1}{2}} h_{i-\frac{1}{2}}^n u_{\beta, i-\frac{1}{2}}^{n+1} \right) &= \eta_i^n - \\ - (1 - \theta) \frac{\Delta t}{\Delta x_i} \left( \sum_{\beta=1}^{N_{i+\frac{1}{2}}} l_{\beta, i+\frac{1}{2}} h_{i+\frac{1}{2}}^n u_{\beta, i+\frac{1}{2}}^n - \sum_{\beta=1}^{N_{i-\frac{1}{2}}} l_{\beta, i-\frac{1}{2}} h_{i-\frac{1}{2}}^n u_{\beta, i-\frac{1}{2}}^n \right). \end{aligned} \quad (4.12)$$

It can be noticed that the dependency on  $h$  has been frozen at time level  $n$  in order to avoid solving a nonlinear system at each timestep. As shown in [40, 109], this does not degrade the accuracy of the method, even in the case of a full second order discretization is employed. In addition, as suggested in Gross *et al.* [66], the value of  $h_{i+\frac{1}{2}}$  is taken to be that of the control volume located upwind of the volume edge. For nodes  $i + \frac{1}{2}$ , the momentum equations for  $\alpha = 2, \dots, N_{i+\frac{1}{2}} - 1$  in (4.7) are then discretized as

$$\begin{aligned} u_{\alpha, i+\frac{1}{2}}^{n+1} + g\theta \frac{\Delta t}{\Delta x_{i+\frac{1}{2}}} (\eta_{i+1}^{n+1} - \eta_i^{n+1}) - \\ - \frac{\Delta t \theta}{l_{\alpha, i+\frac{1}{2}} h_{i+\frac{1}{2}}^n} \left( \nu_{\alpha+\frac{1}{2}, i+\frac{1}{2}}^n \frac{u_{\alpha+1, i+\frac{1}{2}}^{n+1} - u_{\alpha, i+\frac{1}{2}}^{n+1}}{l_{\alpha+\frac{1}{2}, i+\frac{1}{2}} h_{i+\frac{1}{2}}^n} - \nu_{\alpha-\frac{1}{2}, i+\frac{1}{2}}^n \frac{u_{\alpha, i+\frac{1}{2}}^{n+1} - u_{\alpha-1, i+\frac{1}{2}}^{n+1}}{l_{\alpha-\frac{1}{2}, i+\frac{1}{2}} h_{i+\frac{1}{2}}^n} \right) &= \\ = u_{\alpha, i+\frac{1}{2}}^n + \Delta t \mathcal{A}_{\alpha, i+\frac{1}{2}}^{u, n} - g(1 - \theta) \frac{\Delta t}{\Delta x_{i+\frac{1}{2}}} (\eta_{i+1}^n - \eta_i^n) + \\ + \frac{\Delta t (1 - \theta)}{l_{\alpha, i+\frac{1}{2}} h_{i+\frac{1}{2}}^n} \left( \nu_{\alpha+\frac{1}{2}, i+\frac{1}{2}}^n \frac{u_{\alpha+1, i+\frac{1}{2}}^n - u_{\alpha, i+\frac{1}{2}}^n}{l_{\alpha+\frac{1}{2}, i+\frac{1}{2}} h_{i+\frac{1}{2}}^n} - \nu_{\alpha-\frac{1}{2}, i+\frac{1}{2}}^n \frac{u_{\alpha, i+\frac{1}{2}}^n - u_{\alpha-1, i+\frac{1}{2}}^n}{l_{\alpha-\frac{1}{2}, i+\frac{1}{2}} h_{i+\frac{1}{2}}^n} \right) + \\ + \frac{\Delta t}{\Delta x_{i+\frac{1}{2}} l_{\alpha, i+\frac{1}{2}} h_{i+\frac{1}{2}}^n} \left( \Delta \tilde{u}_{\alpha+\frac{1}{2}, i+\frac{1}{2}}^n \mathcal{G}_{\alpha+\frac{1}{2}, i+\frac{1}{2}}^n + \Delta \tilde{u}_{\alpha-\frac{1}{2}, i+\frac{1}{2}}^n \mathcal{G}_{\alpha-\frac{1}{2}, i+\frac{1}{2}}^n \right), \end{aligned} \quad (4.13)$$

where  $\Delta \tilde{u}_{\alpha+\frac{1}{2}, i+\frac{1}{2}}^n = (u_{\alpha+1, i+\frac{1}{2}}^n - u_{\alpha, i+\frac{1}{2}}^n)/2$ ,  $\mathcal{G}_{\alpha+\frac{1}{2}, i+\frac{1}{2}}^n / \Delta x_{i+\frac{1}{2}}$  denotes a discretization of the mass transfer term and  $\mathcal{A}_{\alpha, i+\frac{1}{2}}^{u, n}$  denotes some spatial discretization of the velocity

advection term. In the present implementation, we employ the following upstream based second order finite difference approximation:

$$\left(u_\alpha \partial_x u_\alpha\right)\Big|_{i+1/2} = u_{\alpha,i+1/2} \partial_x u_\alpha \Big|_{i+1/2}$$

with

$$\partial_x u_\alpha \Big|_{i+1/2} = \begin{cases} \frac{u_{\alpha,i-\frac{3}{2}} - 4u_{\alpha,i-\frac{1}{2}} + 3u_{\alpha,i+\frac{1}{2}}}{2\Delta x_{i+\frac{1}{2}}} & \text{if } u_{\alpha,i+\frac{1}{2}} > 0, \\ -\frac{u_{\alpha,i+\frac{5}{2}} - 4u_{\alpha,i+\frac{3}{2}} + 3u_{\alpha,i+\frac{1}{2}}}{2\Delta x_{i+\frac{1}{2}}} & \text{if } u_{\alpha,i+\frac{1}{2}} < 0. \end{cases}$$

It is important to remark that, if the  $\theta$ -scheme is also applied to the advection and mass transfer terms, we would obtain a fully implicit method, for which we would have to solve a global nonlinear problem. This entails a much larger computational cost and is usually avoided in the most numerical models for this kind of applications. Notice that, to define this advection term, velocity values from different layers may have to be employed, if some of the neighbouring volumes has a number of layers different from that at  $i + \frac{1}{2}$ . For example, assuming again without loss of generality  $N_{i-\frac{1}{2}} > N_{i+\frac{1}{2}}$  and  $u_{\beta,i+\frac{1}{2}}^n > 0$  and using the notation in (4.10), values

$$u_{\beta,i-\frac{1}{2}}^* = \frac{1}{l_{\beta,i+\frac{1}{2}}} \sum_{\alpha=\alpha_{i-\frac{1}{2}}^-(\beta)}^{\alpha_{i-\frac{1}{2}}^+(\beta)} l_{\alpha,i-\frac{1}{2}} u_{\alpha,i-\frac{1}{2}}^n,$$

which are the averaged velocities computed with the velocities of the involved layers, will be used to compute the approximation of the velocity gradient at  $x_{i+\frac{1}{2}}$ . Clearly, this may result in a local loss of accuracy, but the numerical results reported show that this has limited impact on the overall accuracy of the proposed method.

The discretization of the mass transfer term is defined as

$$\mathcal{G}_{\alpha+\frac{1}{2},i+\frac{1}{2}} = \sum_{\beta=1}^{\alpha} l_{\beta,i+\frac{1}{2}} \left( \left( hu_\beta - \sum_{\zeta=1}^N l_\zeta hu_\zeta \right) \Big|_{i+1} - \left( hu_\beta - \sum_{\zeta=1}^N l_\zeta hu_\zeta \right) \Big|_i \right),$$

where  $\left( hu_\beta - \sum_{\zeta=1}^N l_\zeta hu_\zeta \right) \Big|_i$  denotes the upwind value depending on the averaged velocity  $u_{\beta,i} = (u_{\beta,i-\frac{1}{2}} + u_{\beta,i+\frac{1}{2}})/2$ , i.e.,

$$\left( hu_\beta - \sum_{\zeta=1}^N l_\zeta hu_\zeta \right) \Big|_i = \begin{cases} h_{i-\frac{1}{2}} u_{\beta,i-\frac{1}{2}} - \sum_{\zeta=1}^N l_{\zeta,i-\frac{1}{2}} h_{i-\frac{1}{2}} u_{\zeta,i-\frac{1}{2}} & \text{if } u_{\beta,i} > 0, \\ h_{i+\frac{1}{2}} u_{\beta,i+\frac{1}{2}} - \sum_{\zeta=1}^N l_{\zeta,i+\frac{1}{2}} h_{i+\frac{1}{2}} u_{\zeta,i+\frac{1}{2}} & \text{if } u_{\beta,i} < 0. \end{cases}$$

Here we have used the fact that  $l_\beta$  is a piecewise constant function where the transitions between regions with a different number of layers are located in the center of a control volume. Therefore  $l_{\beta,i+1/2}$  is constant in  $(x_i, x_{i+1})$ . For the tracer equation, this term appears at the center of the control volume, in contrast with the case of the momentum equation, so that we set instead

$$\begin{aligned} G_{\alpha+\frac{1}{2},i} &= \frac{1}{\Delta x_i} \sum_{\beta=1}^{\alpha} \left( l_{\beta,i+\frac{1}{2}} h_{i+\frac{1}{2}} u_{\beta,i+\frac{1}{2}} - l_{\beta,i-\frac{1}{2}} h_{i-\frac{1}{2}} u_{\beta,i-\frac{1}{2}} - \right. \\ &\quad \left. - l_{\beta,i} \sum_{\zeta=1}^{N_i} \left( l_{\zeta,i+\frac{1}{2}} h_{i+\frac{1}{2}} u_{\zeta,i+\frac{1}{2}} - l_{\zeta,i-\frac{1}{2}} h_{i-\frac{1}{2}} u_{\zeta,i-\frac{1}{2}} \right) \right). \end{aligned} \quad (4.14)$$

The above formulas are to be modified appropriately for cells in which  $N_{i-\frac{1}{2}} \neq N_{i+\frac{1}{2}}$ , by summing all the contributions on the cell boundary with more layers that correspond to a given term  $l_{\beta,i\pm\frac{1}{2}} h_{i\pm\frac{1}{2}} u_{\beta,i\pm\frac{1}{2}}^n$  on the cell boundary with fewer layers, according to the definitions in the previous section.

**Remark 3.** *The time discretization of the mass transfer terms could be easily turned into an implicit one, by taking instead*

$$\begin{aligned} &u_{\alpha,i+\frac{1}{2}}^{n+1} + g\theta \frac{\Delta t}{\Delta x_{i+\frac{1}{2}}} (\eta_{i+1}^{n+1} - \eta_i^{n+1}) - \\ & - \frac{\Delta t\theta}{l_{\alpha,i+\frac{1}{2}} h_{i+\frac{1}{2}}^n} \left( \zeta_{\alpha+\frac{1}{2},i+\frac{1}{2}}^n \left( u_{\alpha+1,i+\frac{1}{2}}^{n+1} - u_{\alpha,i+\frac{1}{2}}^{n+1} \right) - \delta_{\alpha-\frac{1}{2},i+\frac{1}{2}}^n \left( u_{\alpha,i+\frac{1}{2}}^{n+1} - u_{\alpha-1,i+\frac{1}{2}}^{n+1} \right) \right) = \\ &= u_{\alpha,i+\frac{1}{2}}^n + \Delta t \mathcal{A}_{\alpha,i+\frac{1}{2}}^{u,n} - g(1-\theta) \frac{\Delta t}{\Delta x_{i+\frac{1}{2}}} (\eta_{i+1}^n - \eta_i^n) + \\ & + \frac{\Delta t(1-\theta)}{l_{\alpha,i+\frac{1}{2}} h_{i+\frac{1}{2}}^n} \left( \zeta_{\alpha+\frac{1}{2},i+\frac{1}{2}}^n \left( u_{\alpha+1,i+\frac{1}{2}}^n - u_{\alpha,i+\frac{1}{2}}^n \right) - \delta_{\alpha-\frac{1}{2},i+\frac{1}{2}}^n \left( u_{\alpha,i+\frac{1}{2}}^n - u_{\alpha-1,i+\frac{1}{2}}^n \right) \right), \end{aligned}$$

where now

$$\zeta_{\alpha+\frac{1}{2},i+\frac{1}{2}}^n = \frac{\nu_{\alpha+\frac{1}{2},i+\frac{1}{2}}^n}{l_{\alpha+\frac{1}{2},i+\frac{1}{2}} h_{i+\frac{1}{2}}^n} + \frac{\mathcal{G}_{\alpha+\frac{1}{2},i+\frac{1}{2}}^n}{2\Delta x_{i+\frac{1}{2}}} \quad \delta_{\alpha-\frac{1}{2},i+\frac{1}{2}}^n = \frac{\nu_{\alpha-\frac{1}{2},i+\frac{1}{2}}^n}{l_{\alpha-\frac{1}{2},i+\frac{1}{2}} h_{i+\frac{1}{2}}^n} - \frac{\mathcal{G}_{\alpha-\frac{1}{2},i+\frac{1}{2}}^n}{2\Delta x_{i+\frac{1}{2}}}.$$

This approach might be helpful to relax stability restrictions if large values of  $\mathcal{G}_{\alpha+\frac{1}{2},i+\frac{1}{2}}^n$  arise. In the implementation employed to obtain the numerical results of Section 4.5, however, only the discretization (4.13) was applied so far.

At the bottom ( $\alpha = 1$ ) and at the free surface ( $\alpha = N_{i+\frac{1}{2}}$ ) layers, the viscous terms are modified by the friction and drag terms at  $\Gamma_{1/2}$  and  $\Gamma_{N_{i+\frac{1}{2}}+1/2}$ , respectively. We have then

$$\begin{aligned}
& u_{1,i+\frac{1}{2}}^{n+1} + g\theta \frac{\Delta t}{\Delta x_{i+\frac{1}{2}}} (\eta_{i+1}^{n+1} - \eta_i^{n+1}) - \\
& - \frac{\Delta t\theta}{l_{1,i+\frac{1}{2}} h_{i+\frac{1}{2}}^n} \left( \nu_{1+\frac{1}{2},i+\frac{1}{2}}^n \frac{u_{2,i+\frac{1}{2}}^{n+1} - u_{1,i+\frac{1}{2}}^{n+1}}{l_{1+\frac{1}{2},i+\frac{1}{2}} h_{i+\frac{1}{2}}^n} - C_{f,i+\frac{1}{2}}^n |u_{1,i+\frac{1}{2}}^n| u_{1,i+\frac{1}{2}}^{n+1} \right) = \\
& = u_{1,i+\frac{1}{2}}^n + \Delta t \mathcal{A}_{1,i+\frac{1}{2}}^{u,n} - g(1-\theta) \frac{\Delta t}{\Delta x_{i+\frac{1}{2}}} (\eta_{i+1}^n - \eta_i^n) + \\
& + \frac{\Delta t}{\Delta x_{i+\frac{1}{2}} l_{1,i+\frac{1}{2}} h_{i+\frac{1}{2}}^n} \Delta \tilde{u}_{\frac{3}{2},i+\frac{1}{2}}^n \mathcal{G}_{\frac{3}{2},i+\frac{1}{2}}^n + \\
& + \frac{\Delta t(1-\theta)}{l_{1,i+\frac{1}{2}} h_{i+\frac{1}{2}}^n} \left( \nu_{1+\frac{1}{2},i+\frac{1}{2}}^n \frac{u_{2,i+\frac{1}{2}}^n - u_{1,i+\frac{1}{2}}^n}{l_{1+\frac{1}{2},i+\frac{1}{2}} h_{i+\frac{1}{2}}^n} - C_{f,i+\frac{1}{2}}^n |u_{1,i+\frac{1}{2}}^n| u_{1,i+\frac{1}{2}}^n \right), \tag{4.15}
\end{aligned}$$

and

$$\begin{aligned}
& u_{N_{i+\frac{1}{2}},i+\frac{1}{2}}^{n+1} + g\theta \frac{\Delta t}{\Delta x_{i+\frac{1}{2}}} (\eta_{i+1}^{n+1} - \eta_i^{n+1}) + \frac{\Delta t\theta}{l_{N_{i+\frac{1}{2}},i+\frac{1}{2}} h_{i+\frac{1}{2}}^n} \widetilde{C}_{w,i+\frac{1}{2}}^n u_{N_{i+\frac{1}{2}},i+\frac{1}{2}}^{n+1} + \\
& + \frac{\Delta t\theta}{l_{N_{i+\frac{1}{2}},i+\frac{1}{2}} h_{i+\frac{1}{2}}^n} \left( \nu_{N_{i+\frac{1}{2}},i+\frac{1}{2}}^n \frac{u_{N_{i+\frac{1}{2}},i+\frac{1}{2}}^{n+1} - u_{N_{i+\frac{1}{2}},i+\frac{1}{2}}^{n+1}}{l_{N_{i+\frac{1}{2}},i+\frac{1}{2}} h_{i+\frac{1}{2}}^n} \right) = \\
& = u_{N_{i+\frac{1}{2}},i+\frac{1}{2}}^n + \Delta t \mathcal{A}_{N_{i+\frac{1}{2}},i+\frac{1}{2}}^{u,n} - g(1-\theta) \frac{\Delta t}{\Delta x_{i+\frac{1}{2}}} (\eta_{i+1}^n - \eta_i^n) + \\
& + \frac{\Delta t \widetilde{C}_{w,i+\frac{1}{2}}^n}{l_{N_{i+\frac{1}{2}},i+\frac{1}{2}} h_{i+\frac{1}{2}}^n} \left( \theta u_{w,i+\frac{1}{2}}^{n+1} + (1-\theta) \left( u_{w,i+\frac{1}{2}}^n - u_{N_{i+\frac{1}{2}},i+\frac{1}{2}}^n \right) \right) - \\
& - \frac{(1-\theta)\Delta t}{l_{N_{i+\frac{1}{2}},i+\frac{1}{2}} h_{i+\frac{1}{2}}^n} \nu_{N_{i+\frac{1}{2}},i+\frac{1}{2}}^n \frac{u_{N_{i+\frac{1}{2}},i+\frac{1}{2}}^n - u_{N_{i+\frac{1}{2}},i+\frac{1}{2}}^n}{l_{N_{i+\frac{1}{2}},i+\frac{1}{2}} h_{i+\frac{1}{2}}^n} + \\
& + \frac{\Delta t}{\Delta x_{i+\frac{1}{2}} l_{N_{i+\frac{1}{2}},i+\frac{1}{2}} h_{i+\frac{1}{2}}^n} \Delta \tilde{u}_{N_{i+\frac{1}{2}},i+\frac{1}{2}}^n \mathcal{G}_{N_{i+\frac{1}{2}},i+\frac{1}{2}}^n. \tag{4.16}
\end{aligned}$$

Notice that, in previous equation, we define  $\widetilde{C}_w^n = C_w |u_{w,i+\frac{1}{2}}^n - u_{N_{i+\frac{1}{2}},i+\frac{1}{2}}^n|$ .

Replacing the expressions for the velocities at time step  $n + 1$  into the continuity equation yields a linear system whose unknowns are the values of the free surface  $\eta_i^{n+1}$ . This can be done rewriting the discrete momentum equations in matrix notation as in [40], after rescaling both sides of the equations by  $l_{\alpha,i+\frac{1}{2}} h_{i+\frac{1}{2}}^n$ . We denote by  $\mathbf{F}_{i+\frac{1}{2}}^n$  the collection of all the explicit terms and by  $\mathbf{A}_{i+\frac{1}{2}}^n$  the matrix resulting from the discretization of the vertical diffusion terms. Since it is a tridiagonal, positive definite, diagonally

dominant matrix, it is an M-matrix and its inverse matrix exists and is also an M-matrix (see e.g. Herman & Plemmons [15]). We also define

$$\mathbf{U}_{i+\frac{1}{2}} = \begin{pmatrix} u_{1,i+\frac{1}{2}} \\ \vdots \\ u_{\alpha,i+\frac{1}{2}} \\ \vdots \\ u_{N_{i+\frac{1}{2}},i+\frac{1}{2}} \end{pmatrix}; \quad \mathbf{H}_{i+\frac{1}{2}} = \begin{pmatrix} l_{1,i+\frac{1}{2}} h_{i+\frac{1}{2}} \\ \vdots \\ l_{\alpha,i+\frac{1}{2}} h_{i+\frac{1}{2}} \\ \vdots \\ l_{N_{i+\frac{1}{2}},i+\frac{1}{2}} h_{i+\frac{1}{2}} \end{pmatrix}.$$

As a result, one can reformulate equations (4.13), (4.15) and (4.16) as

$$\begin{aligned} \mathbf{U}_{i+\frac{1}{2}}^{n+1} &= \left( \mathbf{A}_{i+\frac{1}{2}}^n \right)^{-1} \mathbf{F}_{i+\frac{1}{2}}^n - \\ &\quad - g\theta \frac{\Delta t}{\Delta x_{i+\frac{1}{2}}} (\eta_{i+1}^{n+1} - \eta_i^{n+1}) \left( \mathbf{A}_{i+\frac{1}{2}}^n \right)^{-1} \mathbf{H}_{i+\frac{1}{2}}^n. \end{aligned} \quad (4.17)$$

The discrete continuity equation is rewritten in this matrix notation as

$$\begin{aligned} \eta_i^{n+1} &= \eta_i^n - \theta \frac{\Delta t}{\Delta x_i} \left( (\mathbf{H}_{i+\frac{1}{2}}^n)^T \mathbf{U}_{i+\frac{1}{2}}^{n+1} - (\mathbf{H}_{i-\frac{1}{2}}^n)^T \mathbf{U}_{i-\frac{1}{2}}^{n+1} \right) - \\ &\quad - (1 - \theta) \frac{\Delta t}{\Delta x_i} \left( (\mathbf{H}_{i+\frac{1}{2}}^n)^T \mathbf{U}_{i+\frac{1}{2}}^n - (\mathbf{H}_{i-\frac{1}{2}}^n)^T \mathbf{U}_{i-\frac{1}{2}}^n \right). \end{aligned}$$

Substituting formally equation (4.17) in the continuity equation yields the tridiagonal system

$$\begin{aligned} \eta_i^{n+1} &- g\theta^2 \frac{\Delta t^2}{\Delta x_i} \left( [\mathbf{H}^T \mathbf{A}^{-1} \mathbf{H}]_{i+\frac{1}{2}}^n \frac{\eta_{i+1}^{n+1} - \eta_i^{n+1}}{\Delta x_{i+\frac{1}{2}}} - \right. \\ &\quad \left. - [\mathbf{H}^T \mathbf{A}^{-1} \mathbf{H}]_{i-\frac{1}{2}}^n \frac{\eta_i^{n+1} - \eta_{i-1}^{n+1}}{\Delta x_{i-\frac{1}{2}}} \right) = \\ &= \eta_i^n - \theta \frac{\Delta t}{\Delta x_i} \left( [\mathbf{H}^T \mathbf{A}^{-1} \mathbf{F}]_{i+\frac{1}{2}}^n - [\mathbf{H}^T \mathbf{A}^{-1} \mathbf{F}]_{i-\frac{1}{2}}^n \right) - \\ &\quad - (1 - \theta) \frac{\Delta t}{\Delta x_i} \left( (\mathbf{H}_{i+\frac{1}{2}}^n)^T \mathbf{U}_{i+\frac{1}{2}}^n - (\mathbf{H}_{i-\frac{1}{2}}^n)^T \mathbf{U}_{i-\frac{1}{2}}^n \right). \end{aligned}$$

The new values of the free surface  $\eta_i^{n+1}$  are computed by solving this system, and the values  $h_i$  are updated to time  $t^{n+1}$  using the definition of  $\eta$  (4.1). The values  $\eta_i^{n+1}$  are then replaced in (4.17) to obtain  $u_{\alpha,i+\frac{1}{2}}^{n+1}$ .

Finally, the evolution equation for  $\rho_\alpha$  is discretized as

$$\begin{aligned} l_{\alpha,i} h_i^{n+1} \rho_{\alpha,i}^{n+1} &= l_{\alpha,i} h_i^n \rho_{\alpha,i}^n - \\ &\quad - \frac{\Delta t}{\Delta x_i} \left( l_{\alpha,i+\frac{1}{2}} h_{i+\frac{1}{2}}^n \rho_{\alpha,i+\frac{1}{2}}^n u_{\alpha,i+\frac{1}{2}}^{n+\theta} - l_{\alpha,i-\frac{1}{2}} h_{i-\frac{1}{2}}^n \rho_{\alpha,i-\frac{1}{2}}^n u_{\alpha,i-\frac{1}{2}}^{n+\theta} \right) + \\ &\quad + \Delta t \left( \rho_{\alpha+\frac{1}{2},i}^n G_{\alpha+\frac{1}{2},i}^n - \rho_{\alpha-\frac{1}{2},i}^n G_{\alpha-\frac{1}{2},i}^n \right), \end{aligned} \quad (4.18)$$

where  $u_\alpha^{n+\theta} = \theta u_\alpha^{n+1} + (1 - \theta)u_\alpha^n$ . The values  $\rho_{\alpha,i\pm\frac{1}{2}}^n, \rho_{\alpha\pm\frac{1}{2},i}^n$  can be defined by appropriate numerical fluxes. Also the discretization of the tracer equation could be easily turned into an implicit one in the vertical if required for stability reasons, by setting

$$\begin{aligned} l_{\alpha,i} h_i^{n+1} \rho_{\alpha,i}^{n+1} - \theta \Delta t \left( \rho_{\alpha+\frac{1}{2},i}^{n+1} G_{\alpha+\frac{1}{2},i}^n - \rho_{\alpha-\frac{1}{2},i}^{n+1} G_{\alpha-\frac{1}{2},i}^n \right) &= l_{\alpha,i} h_i^n \rho_{\alpha,i}^n - \\ - \frac{\Delta t}{\Delta x_i} \left( l_{\alpha,i+\frac{1}{2}} h_{i+\frac{1}{2}}^n \rho_{\alpha,i+\frac{1}{2}}^n u_{\alpha,i+\frac{1}{2}}^{n+\theta} - l_{\alpha,i-\frac{1}{2}} h_{i-\frac{1}{2}}^n \rho_{\alpha,i-\frac{1}{2}}^n u_{\alpha,i-\frac{1}{2}}^{n+\theta} \right) &+ \\ + (1 - \theta) \Delta t \left( \rho_{\alpha+\frac{1}{2},i}^n G_{\alpha+\frac{1}{2},i}^n - \rho_{\alpha-\frac{1}{2},i}^n G_{\alpha-\frac{1}{2},i}^n \right). \end{aligned} \quad (4.19)$$

Notice that, as in formula (4.14), the previous definitions have to be modified appropriately for cells in which  $N_{i-\frac{1}{2}} \neq N_{i+\frac{1}{2}}$ , by summing all the contributions on the cell boundary with more layers that correspond to a given term  $l_{\alpha,i\pm\frac{1}{2}} h_{i\pm\frac{1}{2}}^n \rho_{\alpha,i\pm\frac{1}{2}}^n u_{\alpha,i\pm\frac{1}{2}}^{n+\theta}$  on the cell boundary with fewer layers, according to the definitions in the previous sections.

It is also important to remark that, if  $\rho_{\alpha,i}^{n+1} = \rho_{\alpha,i}^n = 1$  is assumed in either (4.18), (4.19), as long as a consistent flux is employed for the definition of  $\rho_{\alpha,i\pm\frac{1}{2}}^n, \rho_{\alpha\pm\frac{1}{2},i}^n$ , discretizations of the first equation in (4.2) are obtained, which then summed over the whole set of layers  $\alpha = 1, \dots, N_i$  yield exactly formula (4.12). This implies that complete consistency with the discretization of the continuity equation is guaranteed. The importance of this property for the numerical approximation of free surface problems has been discussed extensively in Gross *et al.* [66].

#### 4.4.2 A more accurate IMEX-ARK discretization

A more accurate time discretization can be achieved employing an IMplicit EXplicit (IMEX) Additive Runge Kutta method (ARK) Kennedy & Carpenter [78]. These techniques address the discretization of ODE systems that can be written as  $\mathbf{y}' = \mathbf{f}_s(\mathbf{y}, t) + \mathbf{f}_{ns}(\mathbf{y}, t)$ , where the  $s$  and  $ns$  subscripts denote the stiff and non-stiff components of the system, respectively. In the case of system (4.7), the non-stiff term would include the momentum advection and mass exchange terms, while the stiff term would include free surface gradients and vertical viscosity terms. Concretely, we have  $\mathbf{f}_k = (\mathbf{f}_k^0, \mathbf{f}_k^1, \dots, \mathbf{f}_k^N)'$ , for  $k = s, ns$ , where

$$\begin{aligned} \mathbf{f}_s^0 &= -\frac{1}{\Delta x_i} \sum_{\beta=1}^N \left( l_{\beta,i+\frac{1}{2}} h_{i+\frac{1}{2}} u_{\beta,i+\frac{1}{2}} - l_{\beta,i-\frac{1}{2}} h_{i-\frac{1}{2}} u_{\beta,i-\frac{1}{2}} \right); \\ \mathbf{f}_s^\alpha &= -\frac{1}{\Delta x_{i+\frac{1}{2}}} l_{\alpha,i+\frac{1}{2}} h_{i+\frac{1}{2}} g (\eta_{i+1} - \eta_i) + \\ &+ \left( \nu_{\alpha+\frac{1}{2},i+\frac{1}{2}} \frac{u_{\alpha+1,i+\frac{1}{2}} - u_{\alpha,i+\frac{1}{2}}}{l_{\alpha+\frac{1}{2},i+\frac{1}{2}} h_{i+\frac{1}{2}}} - \nu_{\alpha-\frac{1}{2},i+\frac{1}{2}} \frac{u_{\alpha,i+\frac{1}{2}} - u_{\alpha-1,i+\frac{1}{2}}}{l_{\alpha-\frac{1}{2},i+\frac{1}{2}} h_{i+\frac{1}{2}}} \right), \end{aligned}$$

and

$$\mathbf{f}_{ns}^0 = 0;$$

$$\mathbf{f}_{ns}^\alpha = l_{\alpha, i+\frac{1}{2}} h_{i+\frac{1}{2}} \mathcal{A}_{\alpha, i+\frac{1}{2}}^u + \frac{1}{\Delta x_{i+\frac{1}{2}}} \left( \Delta \tilde{u}_{\alpha+\frac{1}{2}, i+\frac{1}{2}} \mathcal{G}_{\alpha+\frac{1}{2}, i+\frac{1}{2}} + \Delta \tilde{u}_{\alpha-\frac{1}{2}, i+\frac{1}{2}} \mathcal{G}_{\alpha-\frac{1}{2}, i+\frac{1}{2}} \right),$$

for  $\alpha = 1, \dots, N$ .

A generic  $s$ -stage IMEX-ARK method can be defined as follows. If  $l_{\max}$  is the number of intermediate states of the method, then for  $l = 1, \dots, l_{\max}$ :

$$\mathbf{u}^{(l)} = \mathbf{u}^n + \Delta t \sum_{m=1}^{l-1} \left( a_{lm} \mathbf{f}_{ns}(\mathbf{u}^{(m)}, t + c_m \Delta t) + \tilde{a}_{lm} \mathbf{f}_s(\mathbf{u}^{(m)}, t + c_m \Delta t) \right) + \Delta t \tilde{a}_{ll} \mathbf{f}_s(\mathbf{u}^{(l)}, t + c_l \Delta t). \quad (4.20)$$

Finally,  $u^{n+1}$  is computed:

$$\mathbf{u}^{n+1} = \mathbf{u}^n + \Delta t \sum_{l=1}^{l_{\max}} b_l (\mathbf{f}_{ns}(\mathbf{u}^{(l)}, t + c_l \Delta t) + \mathbf{f}_s(\mathbf{u}^{(l)}, t + c_l \Delta t)).$$

Coefficients  $a_{lm}$ ,  $\tilde{a}_{lm}$ ,  $c_l$  and  $b_l$  are determined so that the method is consistent of a given order. In addition to the order conditions specific to each sub-method, the coefficients should respect coupling conditions. Here we use the IMEX method proposed in Giraldo *et al.* [62], whose coefficients are presented in the Butcher tableaux. The method is composed of an implicit method that is  $L$ -stable, since it coincides with the TR-BDF2 scheme described in Hosea & Shampine [69] and of an explicit method that is stable under a standard CFL restriction, based however, due to the IMEX approach, on the velocity of the flow rather than on the celerity. See tables 4.1 and 4.2 for the explicit and implicit method, respectively. The coefficients of the explicit method were proposed in [62], while the implicit method, also employed in the same paper, coincides indeed with the TR-BDF2 method proposed in [11, 69] and applied to the shallow water and Euler equations in Tumolo & Bonaventura [109].

0	0	0	0	$c_l$	$a_{lm}$
$2 \mp \sqrt{2}$	$2 \mp \sqrt{2}$	$(3 + 2\sqrt{2})/6$	$(3 + 2\sqrt{2})/6$	$1 \mp \frac{1}{\sqrt{2}}$	$b_l$
1	$1 - (3 + 2\sqrt{2})/6$	$\pm \frac{1}{2\sqrt{2}}$	$\pm \frac{1}{2\sqrt{2}}$	$1 \mp \frac{1}{\sqrt{2}}$	

Table 4.1: Butcher tableaux of the explicit ARK2 method

While a straightforward application of (4.20) is certainly possible, we will outline here a more efficient way to implement this method to the discretization of equations

0	0			
$2 \mp \sqrt{2}$	$1 \mp \frac{1}{\sqrt{2}}$	$1 \mp \frac{1}{\sqrt{2}}$		
1	$\pm \frac{1}{2\sqrt{2}}$	$\pm \frac{1}{2\sqrt{2}}$	$1 \mp \frac{1}{2\sqrt{2}}$	$c_l$
	$\pm \frac{1}{2\sqrt{2}}$	$\pm \frac{1}{2\sqrt{2}}$	$1 \mp \frac{1}{\sqrt{2}}$	$\tilde{a}_{lm}$
				$b_l$

Table 4.2: Butcher tableaux of the implicit ARK2 method

(4.7), that mimics what done above for the simpler  $\theta$ -method. For the first stage, we define  $\eta_i^{n,1} = \eta_i^n$ ,  $u_{\alpha,i+\frac{1}{2}}^{n,1} = u_{\alpha,i+\frac{1}{2}}^n$  and  $\rho_{\alpha,i}^{n,1} = \rho_{\alpha,i}^n$ , respectively. For the second stage, we get for the continuity equation

$$\begin{aligned} \eta_i^{n,2} + \tilde{a}_{22} \frac{\Delta t}{\Delta x_i} \left( \sum_{\beta=1}^{N_{i+\frac{1}{2}}} l_{\beta,i+\frac{1}{2}} h_{i+\frac{1}{2}}^n u_{\beta,i+\frac{1}{2}}^{n,2} - \sum_{\beta=1}^{N_{i-\frac{1}{2}}} l_{\beta,i-\frac{1}{2}} h_{i-\frac{1}{2}}^n u_{\beta,i-\frac{1}{2}}^{n,2} \right) = \\ = \eta_i^n - \tilde{a}_{21} \frac{\Delta t}{\Delta x_i} \left( \sum_{\beta=1}^{N_{i+\frac{1}{2}}} l_{\beta,i+\frac{1}{2}} h_{i+\frac{1}{2}}^n u_{\beta,i+\frac{1}{2}}^{n,1} - \sum_{\beta=1}^{N_{i-\frac{1}{2}}} l_{\beta,i-\frac{1}{2}} h_{i-\frac{1}{2}}^n u_{\beta,i-\frac{1}{2}}^{n,1} \right) \end{aligned}$$

and for the momentum equations

$$\begin{aligned} u_{\alpha,i+\frac{1}{2}}^{n,2} + g \tilde{a}_{22} \frac{\Delta t}{\Delta x_{i+\frac{1}{2}}} (\eta_{i+1}^{n,2} - \eta_i^{n,2}) - \\ - \frac{\Delta t \tilde{a}_{22}}{l_{\alpha,i+\frac{1}{2}} h_{i+\frac{1}{2}}^n} \left( \nu_{\alpha+\frac{1}{2},i+\frac{1}{2}}^n \frac{u_{\alpha+1,i+\frac{1}{2}}^{n,2} - u_{\alpha,i+\frac{1}{2}}^{n,2}}{l_{\alpha+\frac{1}{2}} h_{i+\frac{1}{2}}^n} - \nu_{\alpha-\frac{1}{2},i+\frac{1}{2}}^n \frac{u_{\alpha,i+\frac{1}{2}}^{n,2} - u_{\alpha-1,i+\frac{1}{2}}^{n,2}}{l_{\alpha-\frac{1}{2}} h_{i+\frac{1}{2}}^n} \right) = \\ = u_{\alpha,i+\frac{1}{2}}^n + \Delta t a_{21} \mathcal{F}_{\alpha,i+\frac{1}{2}}^{n,1} + \Delta t \tilde{a}_{21} \mathcal{I}_{\alpha,i+\frac{1}{2}}^{n,1} \end{aligned}$$

for  $\alpha = 1, \dots, N$ , with the appropriate corrections for the top and bottom layers, respectively. Here we define

$$\mathcal{F}_{\alpha,i+\frac{1}{2}}^{n,j} = \mathcal{A}_{\alpha,i+\frac{1}{2}}^{u,n,j} + \frac{1}{\Delta x_{i+\frac{1}{2}} l_{\alpha,i+\frac{1}{2}} h_{i+\frac{1}{2}}^n} \left( \Delta \tilde{u}_{\alpha+\frac{1}{2},i+\frac{1}{2}}^{n,j} \mathcal{G}_{\alpha+\frac{1}{2},i+\frac{1}{2}}^{n,j} + \Delta \tilde{u}_{\alpha-\frac{1}{2},i+\frac{1}{2}}^{n,j} \mathcal{G}_{\alpha-\frac{1}{2},i+\frac{1}{2}}^{n,j} \right)$$

and

$$\begin{aligned} \mathcal{I}_{\alpha,i+\frac{1}{2}}^{n,j} = -\frac{g}{\Delta x_{i+\frac{1}{2}}} (\eta_{i+1}^{n,j} - \eta_i^{n,j}) + \\ + \frac{1}{l_{\alpha,i+\frac{1}{2}} h_{i+\frac{1}{2}}^n} \left( \nu_{\alpha+\frac{1}{2},i+\frac{1}{2}}^n \frac{u_{\alpha+1,i+\frac{1}{2}}^{n,j} - u_{\alpha,i+\frac{1}{2}}^{n,j}}{l_{\alpha+\frac{1}{2}} h_{i+\frac{1}{2}}^n} - \nu_{\alpha-\frac{1}{2},i+\frac{1}{2}}^n \frac{u_{\alpha,i+\frac{1}{2}}^{n,j} - u_{\alpha-1,i+\frac{1}{2}}^{n,j}}{l_{\alpha-\frac{1}{2}} h_{i+\frac{1}{2}}^n} \right), \end{aligned}$$

and all the other symbols have the same interpretation as in the presentation of the  $\theta$ -method. It can be noticed that, again, the dependency on  $h$  has been frozen at time



level  $n$  in order to avoid solving a nonlinear system at each timestep. As shown in [18, 40, 109], this does not degrade the accuracy of the method. Also the dependency on time of the vertical viscosity is frozen at time level  $n$ . The same will be done for both kinds of coefficients also in the third stage of the method. As in the previous discussion, the above discrete equations can be rewritten in vector notation as

$$\mathbf{U}_{i+\frac{1}{2}}^{n,2} = \left(\mathbf{A}_{i+\frac{1}{2}}^n\right)^{-1} \mathbf{F}_{i+\frac{1}{2}}^{n,1} - g \tilde{a}_{22} \frac{\Delta t}{\Delta x_{i+\frac{1}{2}}} (\eta_{i+1}^{n,2} - \eta_i^{n,2}) \left(\mathbf{A}_{i+\frac{1}{2}}^n\right)^{-1} \mathbf{H}_{i+\frac{1}{2}}^n, \quad (4.21)$$

where now  $\mathbf{F}_{i+\frac{1}{2}}^1$  has components given by

$$l_{\alpha,i+\frac{1}{2}} h_{i+\frac{1}{2}}^n \left( u_{\alpha,i+\frac{1}{2}}^n + \Delta t a_{21} \mathcal{F}_{\alpha,i+\frac{1}{2}}^{n,1} + \Delta t \tilde{a}_{21} \mathcal{I}_{\alpha,i+\frac{1}{2}}^{n,1} \right).$$

The discrete continuity equation is rewritten in this matrix notation as

$$\begin{aligned} \eta_i^{n,2} &= \eta_i^{n,2} - \tilde{a}_{22} \frac{\Delta t}{\Delta x_i} \left( (\mathbf{H}_{i+\frac{1}{2}}^n)^T \mathbf{U}_{i+\frac{1}{2}}^{n,2} - (\mathbf{H}_{i-\frac{1}{2}}^n)^T \mathbf{U}_{i-\frac{1}{2}}^{n,2} \right) - \\ &- \tilde{a}_{21} \frac{\Delta t}{\Delta x_i} \left( (\mathbf{H}_{i+\frac{1}{2}}^n)^T \mathbf{U}_{i+\frac{1}{2}}^n - (\mathbf{H}_{i-\frac{1}{2}}^n)^T \mathbf{U}_{i-\frac{1}{2}}^n \right). \end{aligned}$$

Substituting formally equation (4.21) in the momentum equation yields the tridiagonal system

$$\begin{aligned} \eta_i^{n,2} - g \tilde{a}_{22} \frac{\Delta t^2}{\Delta x_i} \left( [\mathbf{H}^T \mathbf{A}^{-1} \mathbf{H}]_{i+\frac{1}{2}}^n \frac{\eta_{i+1}^{n,2} - \eta_i^{n,2}}{\Delta x_{i+\frac{1}{2}}} - [\mathbf{H}^T \mathbf{A}^{-1} \mathbf{H}]_{i-\frac{1}{2}}^n \frac{\eta_i^{n,2} - \eta_{i-1}^{n,2}}{\Delta x_{i-\frac{1}{2}}} \right) &= \\ = \eta_i^n - \tilde{a}_{22} \frac{\Delta t}{\Delta x_i} \left( [\mathbf{H}^T \mathbf{A}^{-1} \mathbf{F}^1]_{i+\frac{1}{2}}^n - [\mathbf{H}^T \mathbf{A}^{-1} \mathbf{F}^1]_{i-\frac{1}{2}}^n \right) - \\ - \tilde{a}_{21} \frac{\Delta t}{\Delta x_i} \left( (\mathbf{H}_{i+\frac{1}{2}}^n)^T \mathbf{U}_{i+\frac{1}{2}}^n - (\mathbf{H}_{i-\frac{1}{2}}^n)^T \mathbf{U}_{i-\frac{1}{2}}^n \right). \end{aligned}$$

The new values of the free surface  $\eta_i^{n,2}$  are computed by solving this system and they are replaced in (4.21) to find  $u_{\alpha,i+\frac{1}{2}}^{n,2}$ . The evolution equation for  $\rho_\alpha$  is then discretized as

$$\begin{aligned} l_{\alpha,i} h_i^{n,2} \rho_{\alpha,i}^{n,2} &= l_{\alpha,i} h_i^n \rho_{\alpha,i}^{n,1} - \\ &- \frac{\Delta t}{\Delta x_i} \left( l_{\alpha,i+\frac{1}{2}} h_{i+\frac{1}{2}}^n \rho_{\alpha,i+\frac{1}{2}}^{n,1} u_{\alpha,i+\frac{1}{2}}^{*,2} - l_{\alpha,i-\frac{1}{2}} h_{i-\frac{1}{2}}^n \rho_{\alpha,i-\frac{1}{2}}^{n,1} u_{\alpha,i-\frac{1}{2}}^{*,2} \right) + \\ &+ a_{21} \Delta t \left( \rho_{\alpha+\frac{1}{2},i}^{n,1} G_{\alpha+\frac{1}{2},i}^{n,1} - \rho_{\alpha-\frac{1}{2},i}^{n,1} G_{\alpha-\frac{1}{2},i}^{n,1} \right), \end{aligned}$$

where now  $u_{\alpha}^{*,2} = \tilde{a}_{22} u_{\alpha}^{n,2} + \tilde{a}_{21} u_{\alpha}^{n,1}$ .

The last stage of the IMEX-ARK2 method can then be written in vector notation as

$$\begin{aligned} \mathbf{U}_{i+\frac{1}{2}}^{n,3} &= \left(\mathbf{A}_{i+\frac{1}{2}}^n\right)^{-1} \mathbf{F}_{i+\frac{1}{2}}^{n,2} - \\ &- g \tilde{a}_{33} \frac{\Delta t}{\Delta x_{i+\frac{1}{2}}} (\eta_{i+1}^{n,3} - \eta_i^{n,3}) \left(\mathbf{A}_{i+\frac{1}{2}}^n\right)^{-1} \mathbf{H}_{i+\frac{1}{2}}^n, \end{aligned} \quad (4.22)$$

where now  $\mathbf{F}_{i+\frac{1}{2}}^{n,2}$  has components given by

$$l_{\alpha,i+\frac{1}{2}} h_{i+\frac{1}{2}}^n \left( u_{\alpha,i+\frac{1}{2}}^n + \Delta t a_{31} \mathcal{F}_{\alpha,i+\frac{1}{2}}^{n,1} + \Delta t a_{32} \mathcal{F}_{\alpha,i+\frac{1}{2}}^{n,2} + \Delta t \tilde{a}_{31} \mathcal{I}_{\alpha,i+\frac{1}{2}}^{n,1} + \Delta t \tilde{a}_{32} \mathcal{I}_{\alpha,i+\frac{1}{2}}^{n,2} \right).$$

The discrete continuity equation is rewritten in this matrix notation as

$$\begin{aligned} \eta_i^{n,3} &= \eta_i^{n,3} - \tilde{a}_{33} \frac{\Delta t}{\Delta x_i} \left( (\mathbf{H}_{i+\frac{1}{2}}^n)^T \mathbf{U}_{i+\frac{1}{2}}^{n,3} - (\mathbf{H}_{i-\frac{1}{2}}^n)^T \mathbf{U}_{i-\frac{1}{2}}^{n,3} \right) - \\ &- \tilde{a}_{31} \frac{\Delta t}{\Delta x_i} \left( (\mathbf{H}_{i+\frac{1}{2}}^n)^T \mathbf{U}_{i+\frac{1}{2}}^1 - (\mathbf{H}_{i-\frac{1}{2}}^n)^T \mathbf{U}_{i-\frac{1}{2}}^1 \right) - \\ &- \tilde{a}_{32} \frac{\Delta t}{\Delta x_i} \left( (\mathbf{H}_{i+\frac{1}{2}}^n)^T \mathbf{U}_{i+\frac{1}{2}}^2 - (\mathbf{H}_{i-\frac{1}{2}}^n)^T \mathbf{U}_{i-\frac{1}{2}}^2 \right). \end{aligned}$$

As a result, substitution of (4.22) into the third stage of the continuity equation yields the tridiagonal system

$$\eta_i^{n,3} - g \tilde{a}_{33}^2 \frac{\Delta t^2}{\Delta x_i} \left( [\mathbf{H}^T \mathbf{A}^{-1} \mathbf{H}]_{i+\frac{1}{2}}^n \frac{\eta_{i+1}^{n,3} - \eta_i^{n,3}}{\Delta x_{i+\frac{1}{2}}} - [\mathbf{H}^T \mathbf{A}^{-1} \mathbf{H}]_{i-\frac{1}{2}}^n \frac{\eta_i^{n,3} - \eta_{i-1}^{n,3}}{\Delta x_{i-\frac{1}{2}}} \right) = \mathcal{E}_i,$$

where now all the explicit terms have been collected in  $\mathcal{E}_i$ . The new values of the free surface  $\eta_i^{n,3}$  are computed by solving this system and they are replaced in (4.22) to find  $u_{\alpha,i+\frac{1}{2}}^{n,3}$ . The tracer density is then updated as

$$\begin{aligned} l_{\alpha,i} h_i^{n,3} \rho_{\alpha,i}^{n,3} &= l_{\alpha,i} h_i^{n,2} \rho_{\alpha,i}^{n,2} - \\ &- \frac{\Delta t}{\Delta x_i} \left( l_{\alpha,i+\frac{1}{2}} h_{i+\frac{1}{2}}^n \rho_{\alpha,i+\frac{1}{2}}^n u_{\alpha,i+\frac{1}{2}}^{*,3} - l_{\alpha,i-\frac{1}{2}} h_{i-\frac{1}{2}}^n \rho_{\alpha,i-\frac{1}{2}}^n u_{\alpha,i-\frac{1}{2}}^{*,3} \right) + \\ &+ a_{32} \Delta t \left( \rho_{\alpha+\frac{1}{2},i}^{n,2} G_{\alpha+\frac{1}{2},i}^{n,2} - \rho_{\alpha-\frac{1}{2},i}^{n,1} G_{\alpha-\frac{1}{2},i}^{n,2} \right) - \\ &- \frac{\Delta t}{\Delta x_i} \left( l_{\alpha,i+\frac{1}{2}} h_{i+\frac{1}{2}}^n \rho_{\alpha,i+\frac{1}{2}}^n u_{\alpha,i+\frac{1}{2}}^{*,2} - l_{\alpha,i-\frac{1}{2}} h_{i-\frac{1}{2}}^n \rho_{\alpha,i-\frac{1}{2}}^n u_{\alpha,i-\frac{1}{2}}^{*,2} \right) + \\ &+ a_{31} \Delta t \left( \rho_{\alpha+\frac{1}{2},i}^{n,1} G_{\alpha+\frac{1}{2},i}^{n,1} - \rho_{\alpha-\frac{1}{2},i}^{n,1} G_{\alpha-\frac{1}{2},i}^{n,1} \right), \end{aligned}$$

where now  $u_{\alpha}^{*,3} = \tilde{a}_{32} u_{\alpha}^{n,3} + \tilde{a}_{31} u_{\alpha}^{n,2}$ .

The final assembly of the solution at time level  $n+1$  has then the form

$$\begin{aligned} \eta_i^{n+1} &= \eta_i^n - \\ &- \frac{\Delta t}{\Delta x_i} \sum_{j=1}^3 \tilde{b}_j \left( \sum_{\beta=1}^{N_{i+\frac{1}{2}}} l_{\beta,i+\frac{1}{2}} h_{i+\frac{1}{2}}^n u_{\beta,i+\frac{1}{2}}^{n,j} - \sum_{\beta=1}^{N_{i-\frac{1}{2}}} l_{\beta,i-\frac{1}{2}} h_{i-\frac{1}{2}}^n u_{\beta,i-\frac{1}{2}}^{n,j} \right) \end{aligned} \quad (4.23)$$

for the continuity equation, and

$$u_{\alpha,i+\frac{1}{2}}^{n+1} = u_{\alpha,i+\frac{1}{2}}^n + \Delta t \sum_{j=1}^3 \left( \tilde{b}_j \mathcal{I}_{\alpha,i+\frac{1}{2}}^{n,j} + b_j \mathcal{F}_{\alpha,i+\frac{1}{2}}^{n,j} \right) \quad (4.24)$$

for the momentum equations for  $\alpha = 1, \dots, N_{i+\frac{1}{2}}$ , with the appropriate corrections for the top and bottom layers, respectively, and

$$\begin{aligned} l_{\alpha,i} h_i^{n+1} \rho_{\alpha,i}^{n+1} &= l_{\alpha,i} h_i^n \rho_{\alpha,i}^n - \\ &- \frac{\Delta t}{\Delta x_i} \sum_{j=1}^3 b_j \left( l_{\alpha,i+\frac{1}{2}} h_{i+\frac{1}{2}}^n \rho_{\alpha,i+\frac{1}{2}}^{n,j} u_{\alpha,i+\frac{1}{2}}^{n,j} - l_{\alpha,i-\frac{1}{2}} h_{i-\frac{1}{2}}^n \rho_{\alpha,i-\frac{1}{2}}^{n,j} u_{\alpha,i-\frac{1}{2}}^{n,j} \right) + \\ &+ \Delta t \sum_{j=1}^3 b_j \left( \rho_{\alpha+\frac{1}{2},i}^{n,j} G_{\alpha+\frac{1}{2},i}^{n,j} - \rho_{\alpha-\frac{1}{2},i}^{n,j} G_{\alpha-\frac{1}{2},i}^{n,j} \right). \end{aligned} \quad (4.25)$$

Notice that, also in this case, consistency with the discrete continuity equation in the sense of Gross *et al.* [66] is guaranteed and an implicit treatment of the vertical advection term would be feasible with the same procedure outlined above for the  $\theta$ -method. Furthermore, the two linear systems that must be solved for each time step have identical structure and matrices that only differ by a constant factor, thanks to the freezing of their coefficients at time level  $n$ . This implies that, recomputing their entries does not entail a major overhead. It was shown in Tumolo & Bonaventura [109] that, while apparently more costly than the simpler  $\theta$ -method, this procedure leads indeed to an increase in efficiency by significantly increasing the accuracy that can be achieved with a given time step.

## 4.5 Numerical results

In this section, we describe the results of several numerical experiments that were performed in order to investigate the accuracy and efficiency of the proposed methods. In particular, the potential loss of accuracy when reducing the number of vertical layers is investigated in each test, as well as the reduction of the number of degrees of freedom of the system achieved by simplifying the vertical discretization in certain areas of the domain.

Regarding the use of a variable number of layers, the presented tests are related with the motivations explained in Section 4.3. In Sections 4.5.1 and 4.5.2 we look for an accurate approximation of the vertical profile of velocity in a specific region only. In particular, we study the extreme case in which the multilayer configuration is completely removed in a half of the domain. A more complex application for this motivation is shown in Section 4.5.4, for a sediment transport problem. The objective of adapting the vertical discretization to a domain with complex bathymetry is investigated in Section

**4.5.3.** In that test, we deal with a shallow region at the beginning of the domain and we simplify the vertical discretization there, whereas the full multilayer approach is kept elsewhere. In all these tests we show that this configuration is indeed effective, that is, there is no significant loss of accuracy in the regions in which a higher vertical resolution is maintained.

In order to evaluate the accuracy of the semi-implicit schemes, we compute the relative errors between the computed solution and a reference solution. We denote by  $Err_\eta[l_2]$  and  $Err_\eta[l_\infty]$  the relative error for the free surface when considering the usual  $l_2$  and  $l_\infty$  norm, respectively. For the velocity we define

$$Err_u[l_2] = \left( \frac{\sum_{\alpha=1}^N \sum_{i=1}^M |u_{\alpha,i+\frac{1}{2}} - u_{\alpha,i+\frac{1}{2}}^{ref}|^2 \Delta x_i h_{\alpha,i}}{\sum_{\alpha=1}^N \sum_{i=1}^M |u_{\alpha,i+\frac{1}{2}}^{ref}|^2 \Delta x_i h_{\alpha,i}} \right)^{1/2}; \quad (4.26a)$$

$$Err_u[l_\infty] = \frac{\max_\alpha \max_i |u_{\alpha,i+\frac{1}{2}} - u_{\alpha,i+\frac{1}{2}}^{ref}|}{\max_\alpha \max_i |u_{\alpha,i+\frac{1}{2}}^{ref}|}, \quad (4.26b)$$

where  $u^{ref}$  denotes the reference solution. We consider as a reference solution the one computed by using an explicit third order Runge Kutta method with a maximum value for the celerity Courant number of 0.1. Therefore, for the explicit scheme the Courant number is fixed and we consider an adaptive time step  $\Delta t = \min_{1 \leq i \leq M} (\Delta x_i / \lambda_i) C_{cel}$ , where  $\lambda_i$  is an upper bound on the eigenvalues of the multilayer system. Following [93], we deduce the following bound of the associated eigenvalues of the multilayer system (4.7) :

$$\lambda_i = |\bar{u}_i| + \sqrt{gh_i + 2 \sum_{\alpha=1}^N (\bar{u}_i - u_{\alpha,i})^2}, \quad \text{with} \quad \bar{u}_i = \sum_{\alpha=1}^N l_{\alpha,i} u_{\alpha,i}.$$

In practice, since we only consider subcritical regimes, it is sufficient to consider the approximation  $\lambda_i = |\bar{u}_i| + \sqrt{g \bar{h}_i}$ .

In all these tests, we use the viscosity defined by the chosen turbulence model in Section 4.2, and 10 layers in the multilayer code, unless specified different.

### 4.5.1 Free oscillations in a closed basin

We consider here a subcritical flow in a closed domain of length  $L = 10$  km. The bottom topography is given by the Gaussian function

$$b(x) = 4 e^{-(x-x_0)^2/\sigma^2},$$

where  $x_0 = 5$  km and  $\sigma = 0.1 L$  (see figure 4.3). At the initial time the flow is at rest and we take as initial free surface profile  $\eta(0, x) = 10 + ax$  m, where  $a$  is chosen so that the water height is  $h = 10$  m at  $x = 0$  and  $h = 11$  m at  $x = 10$  km. We simulate the resulting

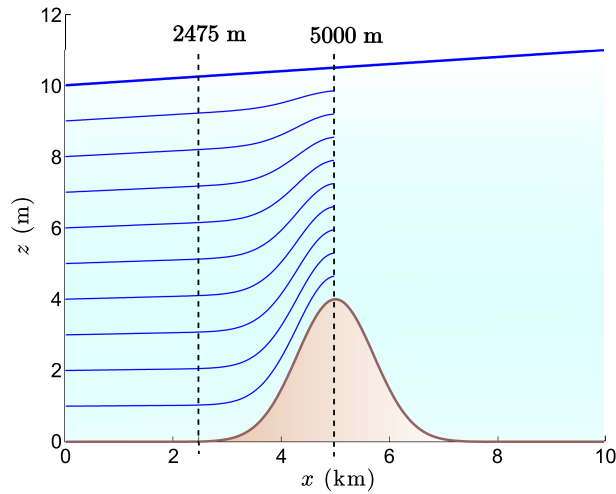


Figure 4.3: Sketch of the multilayer configuration with the variable number of layers for the free oscillations test.

oscillations until  $t = 10800$  s (3 h). All the simulations are performed by using a uniform space discretization step  $\Delta x = 50$  m. The friction coefficient  $C_f$  is defined by (4.9) with  $\Delta z_r = h_1$  ( $h_1 = l_1 h$ ),  $\Delta z_0 = 3.3 \times 10^{-5}$  and  $\kappa = 0.41$ . The wind drag is defined by the coefficient value  $C_w = 1.2 \times 10^{-6}$  and we set a constant wind velocity  $u_w = -1$  m/s.

In figure 4.4 we show free surface profiles at different times until the final time, as computed with the semi implicit methods described in Section 4.4. The  $\theta$ -method and the IMEX-ARK2 are very close to the reference solution. However, the IMEX-ARK2 captures the shape of the free surface slightly better than the  $\theta$ -method when considering the same time step. By using the implicitness parameter  $\theta = 0.55$  and the IMEX-ARK2 with  $\Delta t = 12.5$  or 25 s, we get a difference in the free surface of approximately 3 cm at the final time. In table 4.3 we report the corresponding relative errors and the maximum Courant number achieved by (4.26)-(4.11), at time  $t = 10000$  s. We see that the IMEX-ARK2 method slightly improves the results with respect to the  $\theta$ -method.

SI-method	$\Delta t$ (s)	$C_{vel}$	$C_{cel}$	$Err_\eta [l_2/l_\infty]$ ( $\times 10^{-3}$ )	$Err_u [l_2/l_\infty]$ ( $\times 10^{-1}$ )
$\theta = 0.55$	12.5	0.18	2.62	1.6/3.2	0.9/1.5
IMEX-ARK2	12.5	0.18	2.62	0.6/2.0	0.4/0.6
$\theta = 0.55$	25	0.34	5.24	2.6/5.4	1.3/1.7
IMEX-ARK2	25	0.34	5.24	0.9/2.2	1.2/1.7
$\theta = 0.52$	50	0.7	10.48	3.1/6.3	1.6/1.5
$\theta = 0.55$	50	0.68	10.47	3.9/7.7	2.2/2.0
IMEX-ARK2	50	0.69	10.48	2.4/5.2	1.4/1.7

Table 4.3: Relative errors and Courant numbers achieved by using semi-implicit methods in the free oscillations test at  $t = 10000$  s.

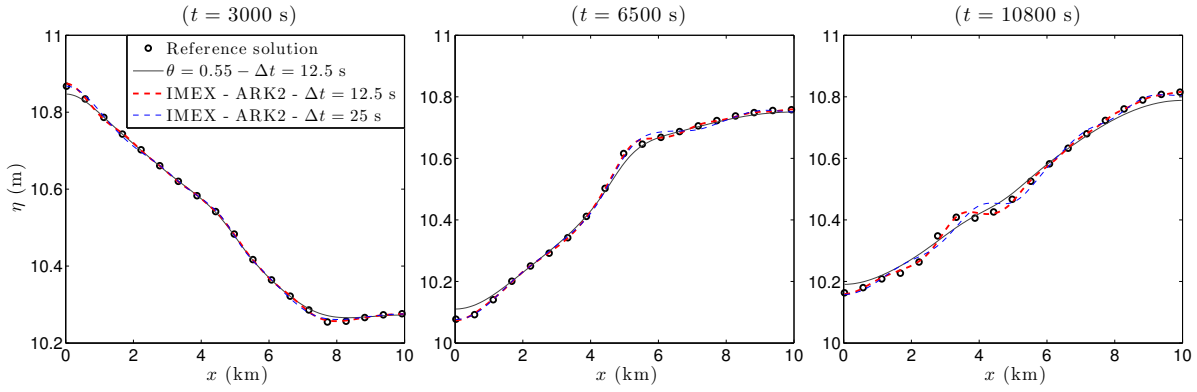


Figure 4.4: Free surface profile at different times by using the semi-implicit methods (color lines) and the reference solution (black circles) computed with the explicit scheme in the free oscillations test.

Even though it is hard to make a rigorous efficiency comparison in the framework of our preliminary implementation, for the subcritical regime the semi-implicit methods turn out to be more efficient than the explicit one. Actually, the computational time required to get the 3 hours of simulation (on a Mac Mini with Intel®Core™ i7-4578U and 16 GB of RAM) is approximately 12 s for the explicit scheme using the Courant number  $C_{cel} = 0.9$  (103 s for the reference solution), while it is approximately 1.64 s (3.83 s) for the  $\theta$ -method (IMEX-ARK2) with  $\Delta t = 12.5$  s. This time is 0.82 s (1.92 s) with  $\Delta t = 25$  s and 0.4 s (0.97 s) when considering the time step  $\Delta t = 50$  s.

We then compare results obtained with a fixed and variable number of vertical layers. Figure 4.5 shows the absolute error for the free surface by using the  $\theta$ -method with  $\theta = 0.55$  and  $\Delta t = 25$  s, as computed using either  $N = 10$  layers throughout the domain or considering (see figure 4.3)

$$N = \begin{cases} 10 & \text{if } x \leq 5000, \\ 1 & \text{otherwise.} \end{cases} \quad (4.27)$$

Similar results are obtained if the time step is  $\Delta t = 12.5$  s. We see that usually the difference between the constant and variable layer cases computed by the semi-implicit method is of the order of 0.1% of the solution values (absolute error 1 cm), while the number of degrees of freedom of the multilayer system is significantly reduced (from 2210 to 1310).

Moreover, figure 4.6 shows the vertical profiles of horizontal velocity at the point  $x = 2475$  m (see figure 4.3), as computed by the semi-implicit method with a constant and variable number of layers (see (4.27)) and with the reference Runge-Kutta method for constant number of layers 1, 2 and 5, respectively. The advantage of using a variable number of layers is apparent. We see that a good approximation of the velocity profiles is obtained even when removing the multilayer configuration in a half of the domain. Actually, these vertical profiles are more accurate than the ones obtained by using 1 and 2 layers in the whole domain. As a conclusion, the vertical effects, which are induced by

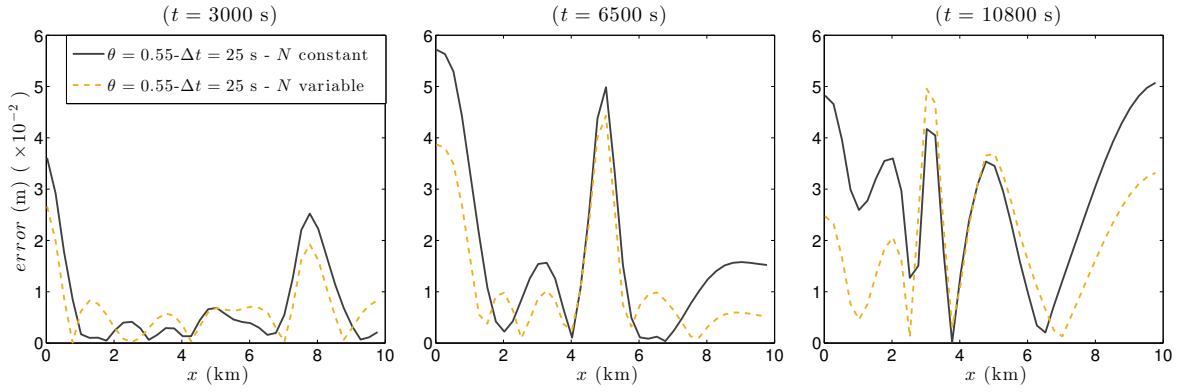


Figure 4.5: Absolute errors for the free surface at different times in the free oscillations test, obtained with the  $\theta$ -method ( $\theta = 0.55$  and  $\Delta t = 25$  s) with either 10 layers in the whole domain (solid black line) or a single layer in the first half of the domain only (dashed yellow line).

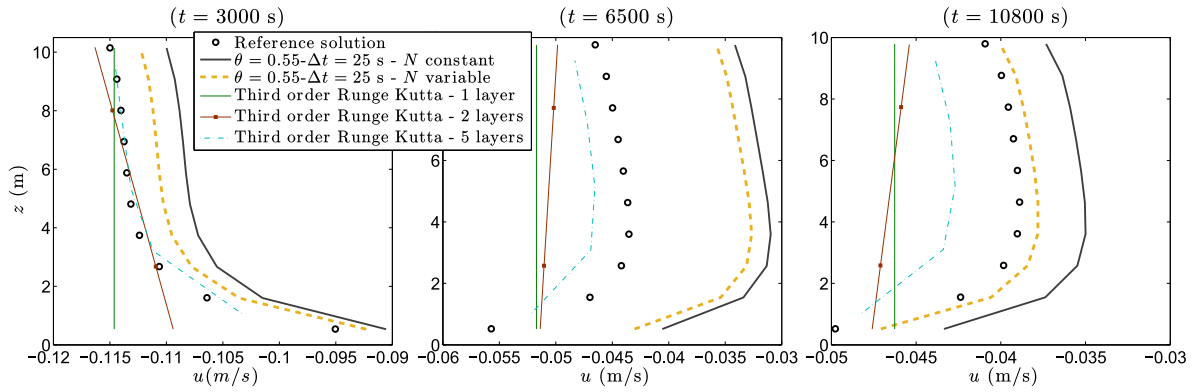


Figure 4.6: Vertical profiles of horizontal velocity in the free oscillations test, obtained with the reference solution (black circles), and the  $\theta$ -method ( $\theta = 0.55$  and  $\Delta t = 25$  s) with either 10 layers in the whole domain (solid black line) or a single layer in the first half of the domain only (dashed yellow line), and with the third order Runge-Kutta method with constant number of layers 1, 2 and 5. Profiles are taken at the point  $x = 2475$  m and times  $t = 3000, 6500, 10800$  s.

both the turbulence viscosity and the friction at the bottom and increased by the obstacle, are relevant enough to consider a multilayer approach for this test.

#### 4.5.2 Steady subcritical flow over a peak with friction

The proposed semi-implicit schemes are exactly well-balanced for water at rest solutions. Indeed, if  $u_\alpha^n = 0$  for  $\alpha = 1, \dots, N$  is imposed in the equations of Section 4.4,  $\eta_i^{n+1} = \eta_i^n$  and  $u_{\alpha, i+\frac{1}{2}}^{n+1} = 0, \forall n \geq 0, \forall \alpha, \forall i$  results. In this test, we consider a steady flow in the subcritical regime, as done for example in Rosatti *et al.* [102]. The length of the domain is  $L = 50$  m, and the bottom bathymetry is given by the function

$$b(x) = 0.05 - 0.001x + \begin{cases} 2 \cos^2\left(\frac{\pi x}{10}\right), & \text{if } |x| < 5; \\ 0 & \text{otherwise.} \end{cases} \quad (4.28)$$

SI-method	$\Delta t$ (s)	$C_{vel}$	$C_{cel}$	$Err_\eta [l_2/l_\infty]$ ( $\times 10^{-6}$ )	$Err_u [l_2/l_\infty]$ ( $\times 10^{-5}$ )
$\theta = 0.55$	0.11	0.71	3.58	1.58/1.8	1.84/7.11
$\theta = 0.7$	0.11	0.70	3.58	1.58/1.8	1.84/7.11
IMEX-ARK2	0.11	0.72	3.5	1.58/1.8	1.84/7.11

Table 4.4: Relative errors and Courant numbers achieved by using semi-implicit methods in the steady subcritical flow test.

The initial conditions are given by  $\eta(0, x) = 5$  m and  $q(0, x) = 4.42 \text{ m}^2 \text{ s}^{-1}$  and subcritical boundary conditions are considered, (see e.g. [102]). The same values of discharge and free surface are used for the upstream condition  $q(t, -25)$ , and the downstream one  $\eta(t, L)$ . We take a uniform space discretization step  $\Delta x = 0.25$  m and the same values for the turbulent viscosity and bottom friction as in the previous test, while the wind stress is not taken into account in this case.

In figure 4.7 we see the free surface at the steady state, as computed with the semi-implicit  $\theta$ -method and IMEX-ARK2, along with the reference solution. In table 4.4 we show the relative errors and the maximum Courant numbers achieved. The results computed with the semi-implicit methods are identical in this steady state case. Figure 4.8 shows the absolute difference on the free surface by using a semi-implicit method with either a constant number of layers or considering

$$N = \begin{cases} 10 & \text{if } x > -10, \\ 1 & \text{otherwise.} \end{cases} \quad (4.29)$$

The order of this difference is  $10^{-4}$ , with larger values where only one layer is employed. We also show the vertical profiles of horizontal velocity at three different points  $x =$

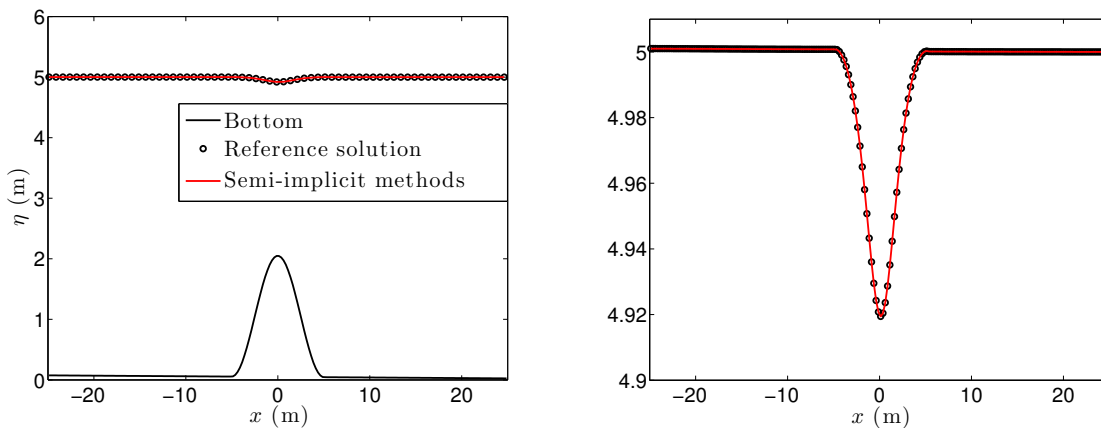


Figure 4.7: Free surface profile at steady state, as computed in the steady subcritical flow test by the semi-implicit methods (solid red line) and reference solution (black circles) computed with the explicit scheme. The inset figure is a zoom of the free surface profile.



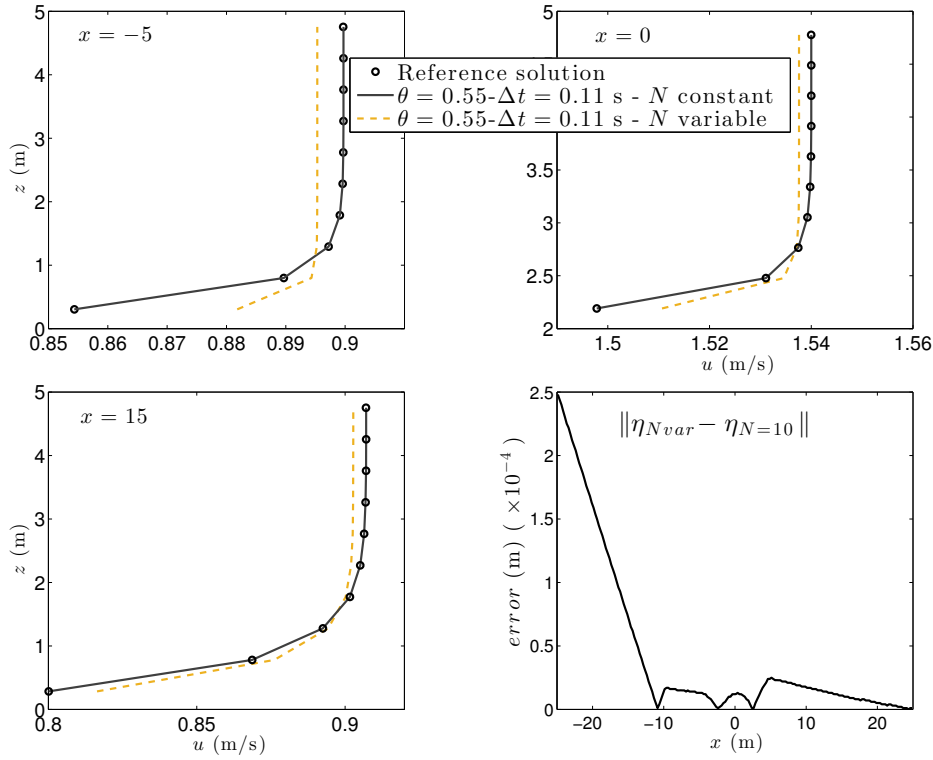


Figure 4.8: Vertical profiles of horizontal velocity in the steady subcritical flow test, obtained with the reference solution (black circles), and the  $\theta$ -method ( $\theta = 0.55$ ) with either 10 layers in the whole domain (solid black line) or a single layer in the first half of the domain only (dashed yellow line). Profiles are taken at steady state at the points  $x = -5, 0, 15$  m. The solid black line denotes the absolute difference between the free surface computed with 10 layers in the whole domain or a single layer in the first half of the domain only.

$-5, 0, 15$  m. These results show that we can reduce the number of degrees of freedom of our system from 2210 to 1661, without a significant loss of accuracy where the multilayer configuration is kept.

### 4.5.3 Tidal forcing over variable bathymetry

In this test we try to simulate a more realistic situation for coastal flow simulations. We consider a domain of length  $L = 25$  km. The bottom bathymetry is taken as in figure 4.9, such that the bathymetry is much shallower in one part of the computational domain than in the other. We define

$$b(x) = z_0 - z_1 \tanh(\lambda(x - x_0)) + 70 e^{-(x-x_1)^2/\sigma^2},$$

with  $z_0 = -z_1 = 44$ ,  $x_0 = 7500$ ,  $x_1 = 16000$ ,  $\lambda = -1/3000$  and  $\sigma = 2000$ . We consider water at rest and constant free surface  $\eta(0, x) = 100$  m at initial time. Subcritical boundary conditions are imposed, namely the upstream condition is  $q(t, -5000) = 1 \text{ m}^2 \text{ s}^{-1}$ , and the tidal downstream condition is  $\eta(t, L) = 100 + 3 \sin(\omega t)$  m, where  $\omega = 2\pi/43200$ . We simulate three 12-hours periods of tide, i.e., 36 hours. The friction

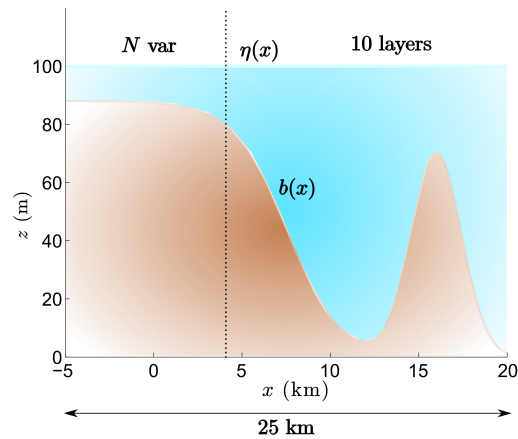


Figure 4.9: Sketch of the bottom topography.

parameters are taken as in previous tests with the exception of  $\Delta z_0 = 3.3 \times 10^{-3}$ , which increases the bottom friction in order to obtain a more complex velocity field. In this case, a wind stress is included with a wind velocity of  $1 \text{ m s}^{-1}$ . As in previous tests, we use 10 vertical layers in the multilayer system and a uniform space discretization step  $\Delta x = 50 \text{ m}$ .

Figure 4.10 shows the obtained velocity field, where we can see some recirculations. Moreover, regarding the deepest area we realise that the upper and lower velocities have opposite direction.

Figure 4.11 shows the free surface position at different times. We see that both the

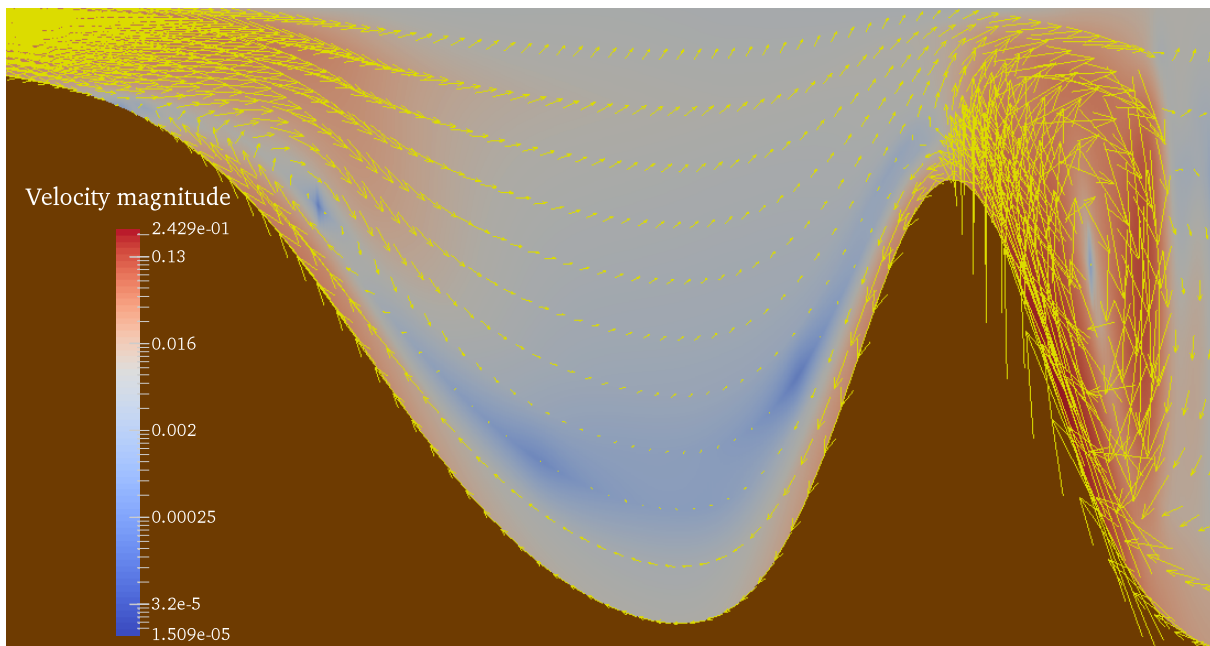


Figure 4.10: Vector map of the whole velocity field  $\mathbf{u} = (u, w)$  at time  $t = 33 \text{ h}$ . Colors represent the magnitude of the velocity in logarithmic scale.

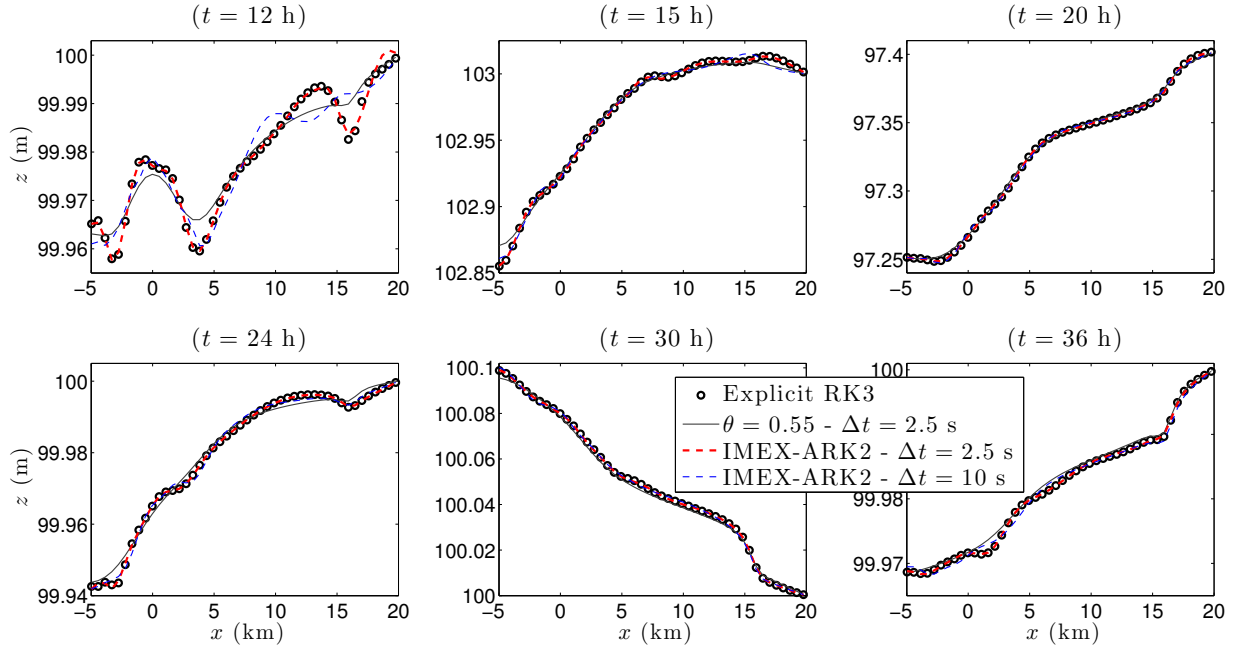


Figure 4.11: Free surface profile at different times by using the semi-implicit methods (color lines) and the reference solution (black circles) computed with the explicit scheme in the tidal forcing test.

$\theta$ -method and the IMEX-ARK2 method are close of the reference solution. As in the free oscillation test, the IMEX-ARK2 approximates better the shape of the free surface. In particular, looking at table 4.5, where we report the relative errors at final time ( $t = 36$  h), we see that this method notably improves the results of the  $\theta$ -method. Note also that, in this typical coastal subcritical regime, large values of the Courant number can be achieved, the maximum value being  $C_{cel} = 34.8$ , without sensibly degrading the accuracy of the results.

In table 4.6 we report the computational times and speed-up achieved. With the explicit code about 16 minutes of computation are required (2.5 hours for the reference solution), while the semi-implicit methods can reduce this time to seconds. Note also that the IMEX-ARK2 is sensibly more efficient than the  $\theta$ -method in this case, since it is about 2.3 times more expensive than the  $\theta$ -method, whereas the errors decrease by a much bigger factor.

We also investigate the influence of simplifying the vertical discretization in the shallowest part of the domain (see figure 4.9). We consider three different configurations, which we denote hereinafter as (NVAR1)-(NVAR3). Firstly, we totally remove the vertical discretization by considering a single layer in the first part of the domain:

$$N = \begin{cases} 1, & l_1 = 1, & \text{if } x \leq 4000; \\ 10, & l_i = 1/10, i = 1, \dots, N, & \text{otherwise.} \end{cases} \quad (\text{NVAR1})$$

Secondly, we keep a thin layer close to the bottom in order to improve the approximation

SI-method	$\Delta t$ (s)	$C_{vel}$	$C_{cel}$	$Err_\eta [l_2/l_\infty]$ ( $\times 10^{-5}$ )	$Err_u [l_2/l_\infty]$ ( $\times 10^{-2}$ )
$\theta = 0.55$	2.5	0.03	1.6	0.77/2.08	0.55/1.01
IMEX-ARK2	2.5	0.03	1.6	0.10/0.26	0.05/0.06
$\theta = 0.55$	5	0.05	3.2	1.32/2.95	0.89/1.35
IMEX-ARK2	5	0.05	3.2	0.24/0.75	0.16/0.19
$\theta = 0.55$	10	0.1	6.3	2.41/4.45	1.51/1.86
IMEX-ARK2	10	0.1	6.3	0.69/1.42	0.32/0.65
$\theta = 0.55$	25	0.24	15.8	5.34/8.36	3.08/3.53
IMEX-ARK2	25	0.25	15.8	1.02/2.31	0.44/0.90
$\theta = 0.55$	55	0.52	34.8	10.2/14.7	5.26/5.81
IMEX-ARK2	55	0.55	34.8	1.43/3.29	0.67/0.89

Table 4.5: Relative errors and Courant numbers achieved by using semi-implicit methods at  $t = 36$  h in the tidal forcing test.

Method	$\Delta t$ (s)	$C_{cel}$	Comput. time (s)	Speed-up
Runge-Kutta 3	-	0.1 (ref. sol.)	9040 (150.6 m)	-
Runge-Kutta 3	-	0.88	1014 (16.9 m)	1
$\theta = 0.55$	2.5	1.6	230 (3.8 m)	4.4
IMEX-ARK2	2.5	1.6	544 (9.1 m)	1.9
$\theta = 0.55$	5	3.2	116 (1.9 m)	8.7
IMEX-ARK2	5	3.2	271 (4.5 m)	3.74
$\theta = 0.55$	10	6.3	58	17.5
IMEX-ARK2	10	6.3	136 (2.3 m)	7.5
$\theta = 0.55$	25	15.8	23	44.1
IMEX-ARK2	25	15.8	54	18.7
$\theta = 0.55$	55	34.8	10	101.4
IMEX-ARK2	55	34.8	24	42.3

Table 4.6: Computational times and speed-up in the tidal forcing test case for the simulation up to  $t = 36$  h.

of the friction term:

$$N = \begin{cases} 2, & l_1 = 0.1, l_2 = 0.9, & \text{if } x \leq 4000; \\ 10, & l_i = 1/10, i = 1, \dots, N, & \text{otherwise.} \end{cases} \quad (\text{NVAR2})$$

Finally, we improve again the vertical discretization close to the bottom by adding another thin layer:

$$N = \begin{cases} 3, & l_1 = l_2 = 0.1, l_3 = 0.8, & \text{if } x \leq 4000; \\ 10, & l_i = 1/10, i = 1, \dots, N, & \text{otherwise.} \end{cases} \quad (\text{NVAR3})$$

In this way, the number of degrees of freedom of the multilayer system is reduced from 5510 to 3890 (NVAR1), 4070 (NVAR2), or 4250 (NVAR3). Note that configurations

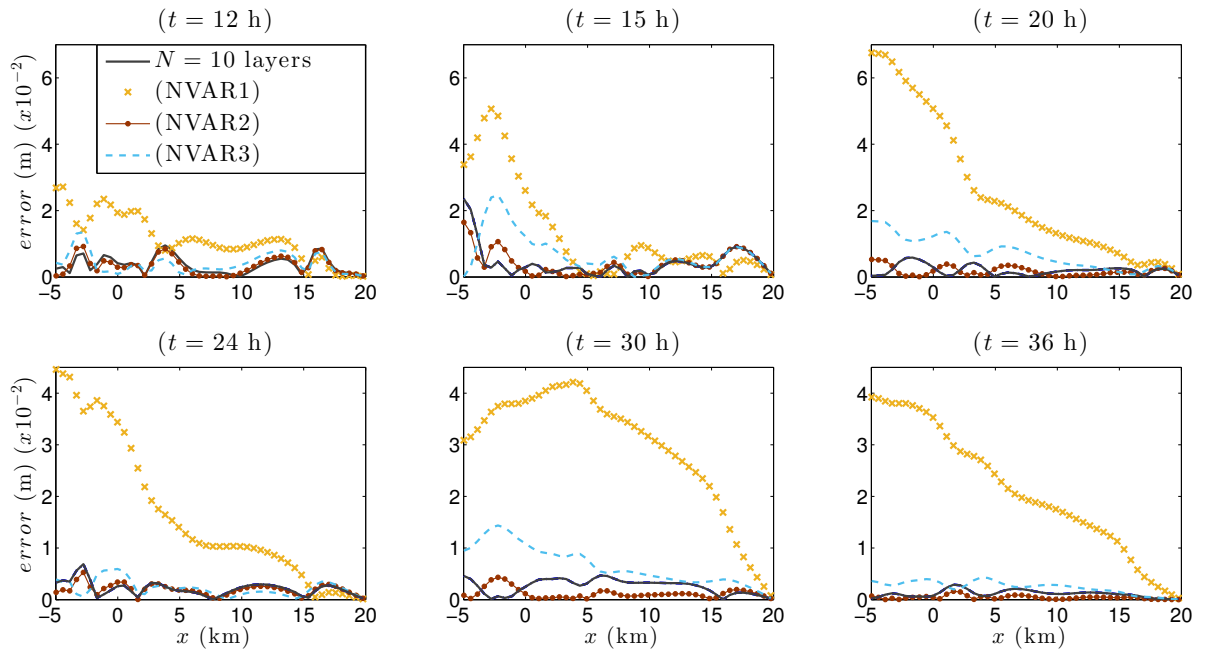


Figure 4.12: Absolute errors for the free surface at different times obtained in the tidal forcing test with the  $\theta$ -method ( $\theta = 0.55$  and  $\Delta t = 5$  s) with either 10 layers in the whole domain (solid black line) or configurations (NVAR1)-(NVAR3) in the first part of the domain.

(NVAR2) and (NVAR3) employ a non-uniform distribution of the vertical layers. Figure 4.12 shows the absolute errors with the  $\theta$ -method with  $\Delta t = 5$  s ( $C_{cel} = 3.2$ ) using 10 layers in the whole domain and with configurations (NVAR1)-(NVAR3). We see that the simplest configuration (NVAR1) leads to the largest error. However, by using configurations (NVAR2) and (NVAR3) these errors are much more similar to the case in which a constant number of layer is employed in the whole domain. As expected, the smallest error is achieved with the configuration (NVAR3). Figure 4.13 shows the vertical profile of horizontal velocity at point  $x = 16025$  m (the top of the peak) at different times. The conclusions are similar, i.e., the differences are larger with configuration (NVAR1), whereas (NVAR2) and (NVAR3) give accurate approximations of the vertical profile obtained with a constant number of layers.

#### 4.5.4 An application to sediment transport problems

In order to emphasize the usefulness of the proposed method and the potential advantages of its application to more realistic problems, we consider the extension of equations (4.7) to the movable bed case. For simplicity, we work with a decoupled, essentially monophase model, according to the classification in Garegnani *et al.* [58], [59], which is appropriate in the limit of small sediment concentration. Quantity  $b$  in (4.7) is then assumed to be dependent on time and an Exner equation for the bed evolution is also

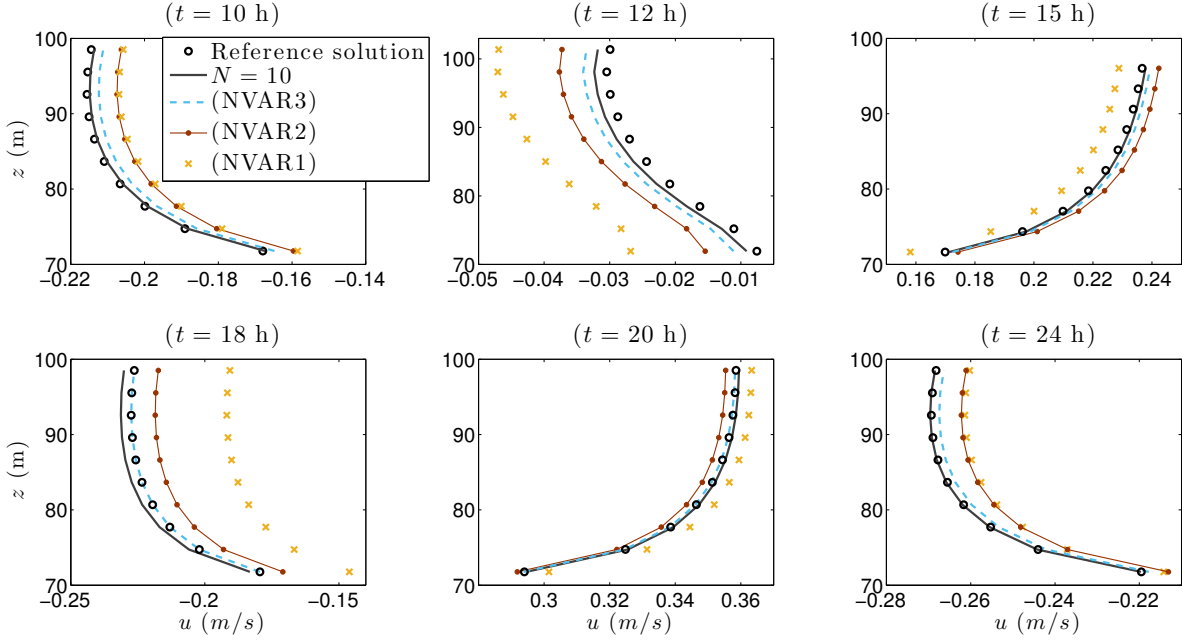


Figure 4.13: Vertical profiles of horizontal velocity obtained in the tidal forcing test with the reference solution (black circles), and the  $\theta$ -method ( $\theta = 0.55$  and  $\Delta t = 5$  s) with either 10 layers in the whole domain (solid black line) or configurations (NVAR1)-(NVAR3) in the first part of the domain. Profiles are taken at the point  $x = 16025$  m and times  $t = 12, 15, 20, 24, 30, 36$  h.

considered

$$\frac{\partial b}{\partial t} + \xi \frac{\partial Q_b}{\partial x} = 0, \quad (4.30)$$

where  $\xi = 1/(1 - \psi_0)$  with  $\psi_0$  the porosity of the sediment bed, and the solid transport discharge is defined by an appropriate formula, see e.g. Castro Díaz *et al.* [36]. Here we consider a simple definition of the solid transport discharge given by the Grass equation

$$Q_b = A_g |u|^2 u,$$

where  $A_g$  ( $\text{s}^2/\text{m}$ )  $\in (0, 1)$  is an experimental constant depending on the grain diameter and the kinematic viscosity. For control volume  $i$ , equation (4.30) is easily discretized along the lines of Section 4.4. For the  $\theta$ -method, the discrete equation reads

$$\begin{aligned} b_i^{n+1} = b_i^n &+ \theta \xi A_g \frac{\Delta t}{\Delta x} \left( |u_{1,i-\frac{1}{2}}^{n+1}|^2 u_{1,i-\frac{1}{2}}^{n+1} - |u_{1,i+\frac{1}{2}}^{n+1}|^2 u_{1,i+\frac{1}{2}}^{n+1} \right) + \\ &+ (1 - \theta) \xi A_g \frac{\Delta t}{\Delta x} \left( |u_{1,i-\frac{1}{2}}^n|^2 u_{1,i-\frac{1}{2}}^n - |u_{1,i+\frac{1}{2}}^n|^2 u_{1,i+\frac{1}{2}}^n \right). \end{aligned} \quad (4.31)$$

On the other hand, the IMEX-ARK2 discretization of equation (4.30) consists of a simple updating of the values of the movable bed, since the values  $u_\alpha^{n,j}$  are known when  $b^{n,j}$  is computed. For the first stage we have  $b_i^{n,1} = b_i^n$ . Next,  $b_i^{n,2}$  and  $b_i^{n,3}$  are computed

by the formula

$$b_i^{n,j} = b_i^n + \xi A_g \frac{\Delta t}{\Delta x} \sum_{k=1}^j \tilde{a}_{jk} \left( |u_{1,i-\frac{1}{2}}^{n,k}|^2 u_{1,i-\frac{1}{2}}^{n,k} - |u_{1,i+\frac{1}{2}}^{n,k}|^2 u_{1,i+\frac{1}{2}}^{n,k} \right).$$

Finally, the solution at time  $n + 1$  is

$$b_i^{n+1} = b_i^n + \xi A_g \frac{\Delta t}{\Delta x} \sum_{j=1}^3 \tilde{b}_j \left( |u_{1,i-\frac{1}{2}}^{n,j}|^2 u_{1,i-\frac{1}{2}}^{n,j} - |u_{1,i+\frac{1}{2}}^{n,j}|^2 u_{1,i+\frac{1}{2}}^{n,j} \right).$$

We consider a simple test in which a parabolic dune is displaced by the flow (see [36]). The computational domain has length 1000 m and 150 nodes are used in the spatial discretization. We set the constant  $A_g$  in the Grass formula to 0.001 and we take the porosity value  $\psi_0 = 0.4$ . We consider viscosity effects with the same parameters as in the previous tests, disregarding wind stress. Subcritical boundary conditions are imposed, namely the upstream condition is  $q(t, 0) = q(0, 0)$  and the downstream one is  $\eta(t, L) = 15$  m. The initial condition for the bottom profile is given by

$$b(0, x) = \begin{cases} 0.1 + \sin^2 \left( \frac{\pi(x - 300)}{200} \right) & \text{if } 300 \leq x \leq 500; \\ 0.1 & \text{otherwise,} \end{cases} \quad (4.32)$$

and the initial height is  $h(0, x) = 15 - b(0, x)$ . For the discharge, we take into account the vertical structure of the flow in order to have a single dune moving along the domain. With this purpose, we run a first simulation of the movement of the dune (4.32), where the initial discharge is  $q_i = 15 \text{ m}^2 \text{ s}^{-1}$ , for  $i = 1, \dots, N$ , until it reaches a steady structure at the outlet. These values of the discharge are used as initial and upstream boundary condition in the final simulation. If a constant discharge were used, this would sweep along the sediment in the initial part of the domain and create another dune within the computational domain. While this is physically correct, we prefer in this test to study a simpler configuration.

We use 10 layers in the multilayer code and simulate until  $t = 691200$  s (8 days). Figure 4.14 shows the evolution of the dune and figure 4.15 shows zooms of evolution of the free surface and of the movable bed, as computed with either the explicit third order Runge-Kutta or the semi-implicit ( $\theta$ -method and IMEX-ARK2). The results are essentially indistinguishable. This is confirmed looking at table 4.7, where we report the relative errors and the Courant number achieved. We see that there are not significant differences between the semi-implicit methods, due to the fact that the flow is essentially a steady one and the bed evolution is very slow.

As remarked before, a rigorous comparison of the efficiency of the proposed methods is not possible in our preliminary implementation. However, a preliminary assessment is reported in Table 4.8, showing the computational time and the speed-up obtained for the simulation of 192 hours (8 days). For the reference solution with the explicit

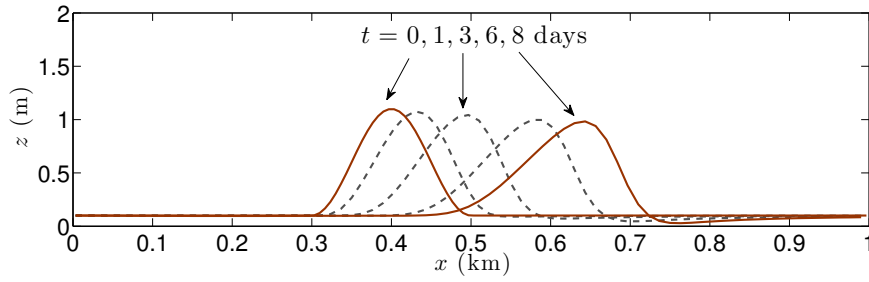


Figure 4.14: Profile of the dune at different times in the sediment transport test case, including the initial condition and the final position.

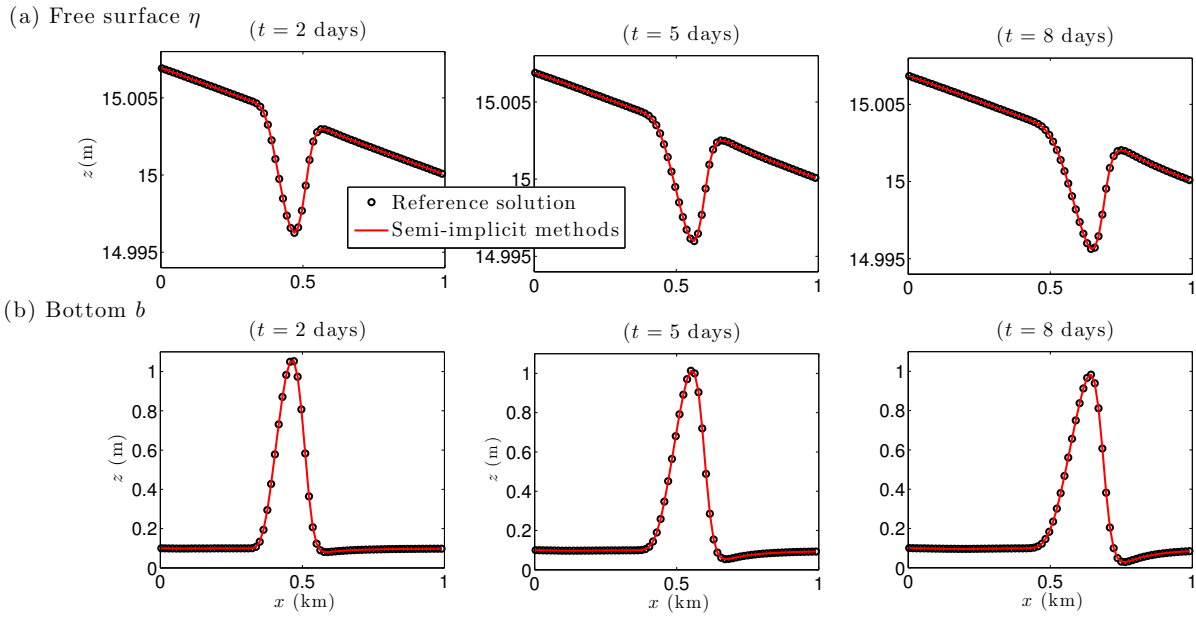


Figure 4.15: Free surface and bottom profile at different times in the sediment transport test case, as computed by the semi-implicit methods (solid red line) and by the reference explicit scheme (black circles).

SI-method	$\Delta t$ (s)	$C_{vel}$	$C_{cel}$	$Err_{\eta}$ [ $l_2/l_{\infty}$ ] ( $\times 10^{-7}$ )	$Err_u$ [ $l_2/l_{\infty}$ ] ( $\times 10^{-6}$ )	$Err_b$ [ $l_2/l_{\infty}$ ] ( $\times 10^{-5}$ )
$\theta = 0.55$	1	0.17	1.98	1.4/5.35	0.29/1.41	1.09/1.52
IMEX-ARK2	1	0.16	1.97	1.29/5.39	0.27/1.41	1.03/1.40
$\theta = 0.55$	2	0.34	3.94	1.69/6.13	0.55/2.90	2.25/3.13
$\theta = 0.6$	2	0.34	3.94	1.69/6.13	0.55/2.90	2.25/3.13
IMEX-ARK2	2	0.33	3.93	1.68/6.47	0.50/2.33	2.11/2.87

Table 4.7: Relative errors and Courant numbers achieved in the sediment transport test case by semi-implicit methods at  $t = 192$  hours (eight days).

scheme approximately 13 hours are necessary (78 minutes with maximum  $C_{cel}$ ), whereas 8 minutes (respectively, 19 minutes) are needed with the  $\theta$ -method and IMEX-ARK2



Method	$\Delta t$ (s)	$C_{cel}$	Comput. time (s)	Speed-up
Runge-Kutta 3	-	0.1 (ref. sol.)	45978 (12.7 h)	-
Runge-Kutta 3	-	0.99	4700 (78.33 m)	1
$\theta$ -method	1	1.98	1048 (17.5 m)	4.5
IMEX-ARK2	1	1.97	2368 (39.4 m)	1.99
$\theta$ -method	2	3.94	509 (8.5 m)	9.2
IMEX-ARK2	2	3.93	1164 (19.4 m)	4.04

Table 4.8: Computational times and speed-up in the sediment transport test case for the simulation up to  $t = 192$  h (eight days).

method when considering a time step  $\Delta t = 2$  s. This gives a speed up of 9 (4 for the IMEX-ARK2). Even taking a small time step ( $\Delta t = 1$  s) the computational time required is notably reduced to 17 min (39 min for the IMEX).

Finally, we can further reduce the computational time by reducing locally the number of layers employed. In this test, the vertical structure cannot be completely removed without causing a major loss of accuracy, since the dynamics of the movable bed depends on the velocity of the layer closest to the bottom. For this reason, we consider the following configuration (see also figure 4.16):

$$N = \begin{cases} 10, & l_i = 1/10, i = 1, \dots, N, & \text{if } 200 \leq x \leq 700; \\ 6, & l_i = 1/10, i = 1, \dots, 5; l_6 = 0.5, & \text{otherwise.} \end{cases} \quad (4.33)$$

Note that, in this way, both a variable number of vertical layers and a non-uniform distribution of these layers are tested. Figure 4.17 shows the absolute differences on the free surface and on the movable bed profiles at different times when we use either a constant number of layers ( $N = 10$ ) or the configuration (4.33). The difference between

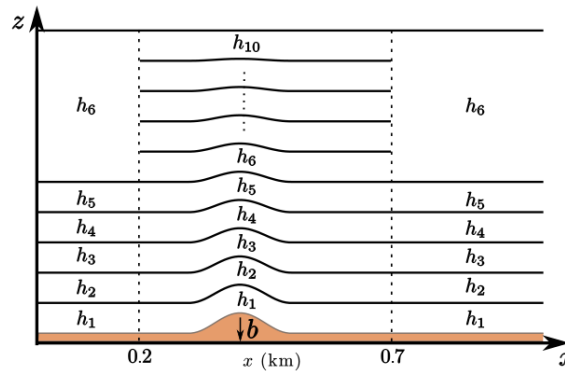


Figure 4.16: Sketch of the multilayer configuration with the variable number of layers for the sediment transport test case.

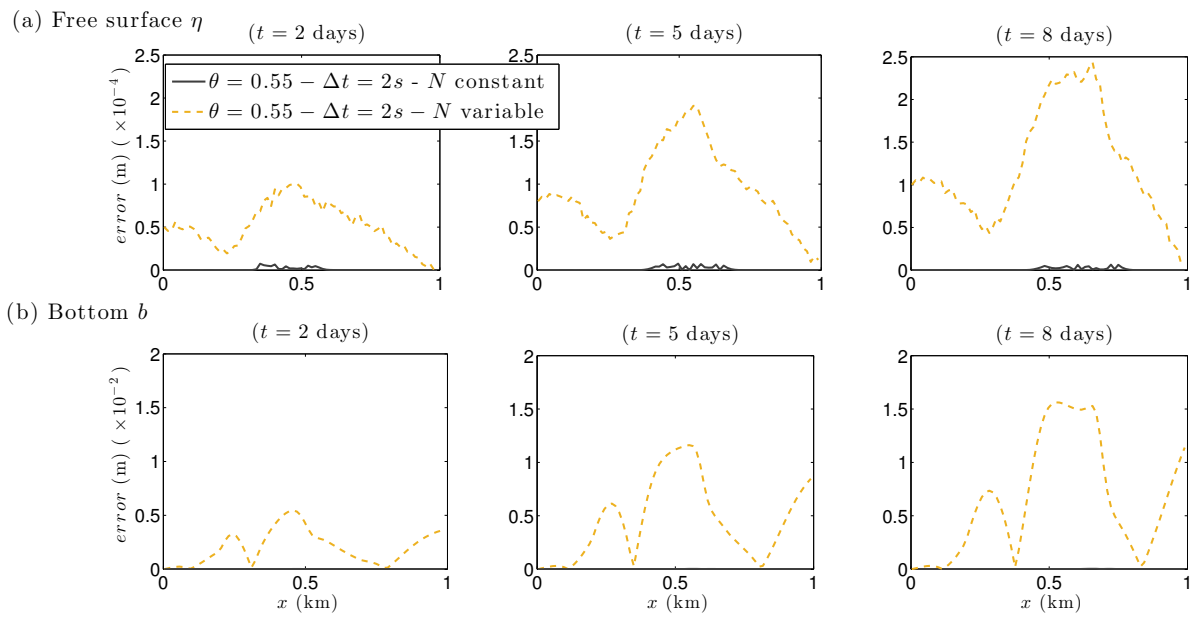


Figure 4.17: Absolute differences for the free surface ( $\eta$ ) and bottom ( $b$ ) at different times in the sediment transport test case, by using the  $\theta$ -method ( $\theta = 0.55$  and  $\Delta t = 2$  s). We compare the results with 10 layers in the whole domain (solid black line) with those obtained with the variable number of layers (see (4.33), dashed yellow line).

both configurations for the bottom is lower than the 2% of its thickness, whereas the number of degrees of freedom of the problem is reduced from 1660 to 1352.

---

## Bibliography

- [1] A. J. ADCROFT, C. N. HILL AND J. C. MARSHALL, *Representation of topography by shaved cells in a height coordinate ocean model*, Monthly Weather Review, 125 (1997), pp. 2293–2315.
- [2] B. ANDREOTTI, Y. FORTERRE AND O. POULIQUEN, *Granular Media: Between Fluid and Solid*, Cambridge University Press, 2013.
- [3] E. AUDUSSE, *A multilayer Saint-Venant model: derivation and numerical validation*, Discrete and Continuous Dynamical Systems Series B, 5 (2005), pp. 189–214.
- [4] E. AUDUSSE, F. BENKHALDOUN, J. SAINTE-MARIE AND M. SEAID, *Multilayer saint-venant equations over movable beds*, Discrete and Continuous Dynamical Systems - Series B, 15 (2011), pp. 917–934.
- [5] E. AUDUSSE, F. BENKHALDOUN, S. SARI, M. SEAID AND P. TASSI, *A fast finite volume solver for multi-layered shallow water flows with mass exchange*, Journal of Computational Physics, 272 (2014), pp. 23–45.
- [6] E. AUDUSSE, F. BOUCHUT, M. BRISTEAU, R. KLEIN AND B. PERTHAME, *A fast and stable well-balanced scheme with hydrostatic reconstruction for shallow water flows*, SIAM Journal on Scientific Computing, 25 (2004), pp. 2050–2065.
- [7] E. AUDUSSE, M. BRISTEAU, B. PERTHAME AND J. SAINTE-MARIE, *A multilayer Saint-Venant system with mass exchanges for shallow water flows. derivation and numerical validation*, ESAIM: Mathematical Modelling and Numerical Analysis, 45 (2011), pp. 169–200.
- [8] E. AUDUSSE, M.-O. BRISTEAU AND A. DECOENE, *Numerical simulations of 3D free surface flows by a multilayer Saint-Venant model*, International Journal for Numerical Methods in Fluids, 56 (2008), pp. 331–350.

- [9] E. AUDUSSE, M.-O. BRISTEAU, M. PELANTI AND J. SAINTE-MARIE, *Approximation of the hydrostatic Navier-Stokes system for density stratified flows by a multilayer model: kinetic interpretation and numerical solution*, Journal of Computational Physics, 230 (2011), pp. 3453–3478.
- [10] J. L. BAKER, T. BARKER AND J. M. N. T. GRAY, *A two-dimensional depth-averaged  $\mu(I)$ -rheology for dense granular avalanches*, Journal of Fluid Mechanics, 787 (2016), pp. 367–395.
- [11] R. E. BANK, W. M. COUGHRAN, W. FICHTNER, E. H. GROSSE, D. J. ROSE AND R. K. SMITH, *Transient Simulation of Silicon Devices and Circuits*, IEEE Transactions on Electron Devices, 32 (1985), pp. 1992–2007.
- [12] T. BARKER, D. G. SCHAEFFER, P. BOHORQUEZ AND J. M. N. T. GRAY, *Well-posed and ill-posed behaviour of the  $\mu(I)$ -rheology for granular flow*, Journal of Fluid Mechanics, 779 (2015), pp. 794–818.
- [13] M. BERCOVIER AND M. ENGELMAN, *A finite-element method for incompressible non-Newtonian flows*, Journal of Computational Physics, 36 (1980), pp. 313–326.
- [14] C. BERGER, B. W. MCARDELL AND F. SCHLUNEGGER, *Direct measurement of channel erosion by debris flows, illgraben, switzerland*, Journal of Geophysical Research: Earth Surface, 116 (2011). F01002.
- [15] A. BERMAN AND R. PLEMMONS, *Nonnegative Matrices in the Mathematical Sciences*, Society for Industrial and Applied Mathematics, 1994.
- [16] A. BERMÚDEZ AND C. MORENO, *Duality methods for solving variational inequalities*, Computers & Mathematics with Applications, 7 (1981), pp. 43–58.
- [17] R. BLECK AND D. BOUDRA, *Wind-driven spin-up in eddy-resolving ocean models formulated in isopycnic and isobaric coordinates*, Journal of Geophysical Research (Oceans), 91 (1986), pp. 7611–7621.
- [18] L. BOITTIN, *Assessment of numerical methods for uncertainty quantification in river hydraulics modelling*, Master’s thesis, Politecnico di Milano, 2015.
- [19] L. BONAVENTURA, *A semi-implicit, semi-lagrangian scheme using the height coordinate for a nonhydrostatic and fully elastic model of atmospheric flows*, Journal of Computational Physics, 158 (2000), pp. 186–213.
- [20] L. BONAVENTURA AND A. DELLA ROCCA, *Unconditionally strong stability preserving extensions of the TR-BDF2 method.*, Journal of Scientific Computing, 70 (2017), pp. 859–895.
- [21] L. BONAVENTURA, R. REDLER AND R. BUDICH, *Earth System Modelling 2: Algorithms, Code Infrastructure and Optimisation*, Springer Verlag, New York, 2012.

- 
- [22] L. BONAVENTURA AND T. RINGLER, *Analysis of discrete shallow water models on geodesic Delaunay grids with C-type staggering*, Monthly Weather Review, 133 (2005), pp. 2351–2373.
- [23] L. BONAVENTURA, E. D. FERNÁNDEZ-NIETO, J. GARRES-DÍAZ AND G. NARBONA-REINA, *Multilayer shallow water models with locally variable number of layers and semi-implicit time discretization*, Journal of Computational Physics, 364 (2018), pp. 209 – 234.
- [24] S. BOSCARINO, F. FILBET AND G. RUSSO, *High order semi-implicit schemes for time dependent partial differential equations*, Journal of Scientific Computing, 68 (2016), pp. 975–1001.
- [25] F. BOUCHUT, *Nonlinear Stability of Finite Volume Methods for Hyperbolic Conservation Laws: And Well-Balanced Schemes for Sources*, Springer Science & Business Media, 2004.
- [26] F. BOUCHUT, E. D. FERNÁNDEZ-NIETO, A. MANGENEY AND G. NARBONA-REINA, *A two-phase shallow debris flow model with energy balance*, ESAIM: M2AN, 49 (2015), pp. 101–140.
- [27] F. BOUCHUT, I. IONESCU AND A. MANGENEY, *An analytic approach for the evolution of the static-flowing interface in viscoplastic granular flows*, Communications in Mathematical Sciences, 14 (2016), pp. 2101–2126.
- [28] F. BOUCHUT, A. MANGENEY-CASTELNAU, B. PERTHAME AND J.-P. VILOTTE, *A new model of Saint Venant and Savage–Hutter type for gravity driven shallow water flows*, Comptes Rendus Mathématique, 336 (2003), pp. 531–536.
- [29] F. BOUCHUT AND M. WESTDICKENBERG, *Gravity driven shallow water models for arbitrary topography*, Communications in Mathematical Sciences, 2 (2004), pp. 359–389.
- [30] M.-O. BRISTEAU, B. DI MARTINO, C. GUICHARD AND J. SAINTE-MARIE, *Layer-averaged Euler and Navier-Stokes equations*, Communications in Mathematical Sciences, 15 (2015), pp. 1221–1246.
- [31] K. BRYAN, *A numerical method for the study of the circulation of the world ocean*, Journal of Computational Physics, 4 (1969), pp. 347–376.
- [32] H. CAPART, C.-Y. HUNG AND C. P. STARK, *Depth-integrated equations for entraining granular flows in narrow channels*, Journal of Fluid Mechanics, 765 (2015).
- [33] M. J. CASTRO, A. M. FERREIRO FERREIRO, J. A. GARCÍA-RODRÍGUEZ, J. M. GONZÁLEZ-VIDA, J. MACÍAS, C. PARÉS AND M. E. VÁZQUEZ-CENDÓN, *The numerical treatment of wet/dry fronts in shallow flows: application to one-layer and*

- two-layer systems*, *Mathematical and Computer Modelling*, 42 (2005), pp. 419–439.
- [34] M. J. CASTRO, J. M. GONZÁLEZ-VIDA AND C. PARÉS, *Numerical treatment of wet/dry fronts in shallow flows with a modified roe scheme*, *Mathematical Models and Methods in Applied Sciences*, 16 (2006), pp. 897–931.
- [35] M. J. CASTRO DÍAZ AND E. D. FERNÁNDEZ-NIETO, *A class of computationally fast first order finite volume solvers: PVM methods*, *SIAM Journal on Scientific Computing*, 34 (2012), pp. A2173–A2196.
- [36] M. J. CASTRO DÍAZ, E. D. FERNÁNDEZ-NIETO AND A. M. FERREIRO, *Sediment transport models in Shallow Water equations and numerical approach by high order finite volume methods*, *Computers & Fluids*, 37 (2008), pp. 299–316.
- [37] M. J. CASTRO DÍAZ, A. PARDO AND C. PARÉS, *Well-balanced numerical schemes based on a generalized hydrostatic reconstruction technique*, *Mathematical Models and Methods in Applied Sciences*, 17 (2007), p. 2055–2113.
- [38] V. CASULLI, *Semi-implicit finite difference methods for the two-dimensional shallow water equations*, *Journal of Computational Physics*, 86 (1990), pp. 56–74.
- [39] V. CASULLI, *Numerical simulation of three-dimensional free surface flow in isopycnal coordinates*, *International Journal of Numerical Methods in Fluids*, 25 (1997), pp. 645–658.
- [40] V. CASULLI AND E. CATTANI, *Stability, accuracy and efficiency of a semi-implicit method for three-dimensional shallow water flow*, *Computers & Mathematics with Applications*, 27 (1994), pp. 99–112.
- [41] V. CASULLI AND R. T. CHENG, *Semi-implicit finite difference methods for three-dimensional shallow water flow*, *International Journal for Numerical Methods in Fluids*, 15 (1992), pp. 629–648.
- [42] V. CASULLI AND R. A. WALTERS, *An unstructured grid, three-dimensional model based on the shallow water equations*, *International Journal of Numerical Methods in Fluids*, 32 (2000), pp. 331–348.
- [43] V. CASULLI AND P. ZANOLLI, *Semi-implicit numerical modelling of non-hydrostatic free-surface flows for environmental problems*, *Mathematical and Computer Modelling*, 36 (2002), pp. 1131–1149.
- [44] S. J. CONWAY, A. DECAULNE, M. R. BALME, J. B. MURRAY AND M. C. TOWNER, *A new approach to estimating hazard posed by debris flows in the westfjords of iceland*, *Geomorphology*, 114 (2010), pp. 556–572.

- [45] T. DAVIES, M. J. P. CULLEN, A. J. MALCOLM, M. H. MAWSON, A. STANIFORTH, A. A. WHITE AND N. WOOD, *A new dynamical core for the Met Office's global and regional modelling of the atmosphere*, Quarterly Journal of the Royal Meteorological Society, 131 (2005), pp. 1759–1782.
- [46] A. DECOENE, L. BONAVENTURA, E. MIGLIO AND F. SALERI, *Asymptotic derivation of the section-averaged shallow water equations for natural river hydraulics*, Mathematical Models and Methods in Applied Sciences, 19 (2009), pp. 387–417.
- [47] R. DELANNAY, A. VALANCE, A. MANGENEY, O. ROCHE AND P. RICHARD, *Granular and particle-laden flows: from laboratory experiments to field observations*, Journal of Physics D: Applied Physics, 50 (2017), p. 053001.
- [48] D. R. DURRAN, *Numerical methods for wave equations in geophysical fluid dynamics*, Springer Science & Business Media, 2013.
- [49] A. N. EDWARDS AND J. M. N. T. GRAY, *Erosion-deposition waves in shallow granular free-surface flows*, Journal of Fluid Mechanics, 762 (2015), pp. 35–67.
- [50] G. FACCANONI AND A. MANGENEY, *Exact solution for granular flows*, International Journal for Numerical and Analytical Methods in Geomechanics, 37 (2013), pp. 1408–1433.
- [51] M. FARIN, A. MANGENEY AND O. ROCHE, *Fundamental changes of granular flow dynamics, deposition, and erosion processes at high slope angles: Insights from laboratory experiments*, Journal of Geophysical Research: Earth Surface, 119 (2014), pp. 504–532.
- [52] P. FAVREAU, A. MANGENEY, A. LUCAS, G. CROSTA AND F. BOUCHUT, *Numerical modeling of landquakes*, Geophysical Research Letters, 37 (2010), pp. n/a–n/a. L15305.
- [53] E. D. FERNÁNDEZ-NIETO, F. BOUCHUT, D. BRESCH, M. J. CASTRO DÍAZ AND A. MANGENEY, *A new Savage-Hutter type model for submarine avalanches and generated tsunami*, Journal of Computational Physics, 227 (2008), pp. 7720–7754.
- [54] E. D. FERNÁNDEZ-NIETO, J. GARRES-DÍAZ, A. MANGENEY AND G. NARBONAREINA, *A multilayer shallow model for dry granular flows with the  $\mu(I)$  rheology: Application to granular collapse on erodible beds*, Journal of Fluid Mechanics, 798 (2016), pp. 643–681.
- [55] E. D. FERNÁNDEZ-NIETO, J. GARRES-DÍAZ, A. MANGENEY AND G. NARBONAREINA, *2D granular flows with the  $\mu(I)$  rheology and side walls friction: a well-balanced multilayer discretization*, Journal of Computational Physics, 356 (2018), pp. 192–219.

- [56] E. D. FERNÁNDEZ-NIETO, E. H. KONÉ AND T. CHACÓN REBOLLO, *A Multilayer Method for the Hydrostatic Navier-Stokes Equations: A Particular Weak Solution*, *Journal of Scientific Computing*, 60 (2014), pp. 408–437.
- [57] E. D. FERNÁNDEZ-NIETO, T. MORALES DE LUNA, G. NARBONA-REINA AND J. D. ZABSONRÉ, *Formal deduction of the Saint-Venant–Exner model including arbitrarily sloping sediment beds and associated energy*, *ESAIM: M2AN*, 51 (2017), pp. 115–145.
- [58] G. GAREGNANI, G. ROSATTI AND L. BONAVENTURA, *Free surface flows over mobile bed: mathematical analysis and numerical modeling of coupled and decoupled approaches*, *Communications in Applied and Industrial Mathematics*, 1 (2011).
- [59] G. GAREGNANI, G. ROSATTI AND L. BONAVENTURA, *On the range of validity of the Exner-based models for mobile-bed river flow simulations*, *Journal of Hydraulic Research*, 51 (2013), pp. 380–391.
- [60] GDR MIDI, *On dense granular flows*, *The European Physical Journal E*, 14 (2004), pp. 341–365.
- [61] J.-F. GERBEAU AND B. PERTHAME, *Derivation of viscous saint-venant system for laminar shallow water; numerical validation*, *Discrete and Continuous Dynamical Systems - Series B*, 1 (2001), pp. 89–102.
- [62] F. X. GIRALDO, J. F. KELLY AND E. M. CONSTANTINESCU, *Implicit-explicit formulations of a three-dimensional nonhydrostatic unified model of the atmosphere (NUMA)*, *SIAM Journal on Scientific Computing*, 35 (2013).
- [63] R. GLOWINSKI AND P. L. TALLEC, *Augmented Lagrangian and operator-splitting methods in nonlinear mechanics*, *SIAM Studies in Applied Mathematics*, 9 (1989).
- [64] J. M. N. T. GRAY AND A. N. EDWARDS, *A depth-averaged  $\mu(I)$ -rheology for shallow granular free-surface flows*, *Journal of Fluid Mechanics*, 755 (2014), pp. 503–534.
- [65] J. M. N. T. GRAY, Y.-C. TAI AND S. NOELLE, *Shock waves, dead zones and particle-free regions in rapid granular free-surface flows*, *Journal of Fluid Mechanics*, 491 (2003), pp. 161–181.
- [66] E. S. GROSS, L. BONAVENTURA AND G. ROSATTI, *Consistency with continuity in conservative advection schemes for free-surface models*, *International Journal of Numerical Methods in Fluids*, 38 (2002), pp. 307–327.
- [67] D. HAIDVOGEL, J. WILKIN AND R. YOUNG, *A semi-spectral primitive equation ocean circulation model using sigma and orthogonal curvilinear coordinates*, *Journal of Computational Physics*, 94 (1991), pp. 151–185.



- [68] R. L. HANEY, *On the pressure gradient force over steep topography in sigma coordinate ocean models*, *Journal of Physical Oceanography*, 21 (1991), pp. 610–619.
- [69] M. E. HOSEA AND L. F. SHAMPINE, *Analysis and implementation of TR-BDF2*, *Applied Numerical Mathematics*, 20 (1996), pp. 21–37.
- [70] I. R. IONESCU, A. MANGENEY, F. BOUCHUT AND R. ROCHE, *Viscoplastic modeling of granular column collapse with pressure-dependent rheology*, *Journal of Non-Newtonian Fluid Mechanics*, 219 (2015), pp. 1–18.
- [71] R. M. IVERSON AND R. P. DENLINGER, *Flow of variably fluidized granular masses across three-dimensional terrain: 1. coulomb mixture theory*, *Journal of Geophysical Research: Solid Earth*, 106 (2001), pp. 537–552.
- [72] R. M. IVERSON, M. E. REID, M. LOGAN, R. G. LAHUSEN, J. W. GODT AND J. P. GRISWOLD, *Positive feedback and momentum growth during debris-flow entrainment of wet bed sediment*, *Nature Geoscience*, 4 (2011), pp. 116–121.
- [73] R. M. IVERSON, *The physics of debris flows*, *Reviews of Geophysics*, 35 (1997), pp. 245–296.
- [74] D. E. JESSOP, K. KELFOUN, P. LABAZUY, A. MANGENEY, O. ROCHE, J.-L. TILLIER, M. TROUILLET AND G. THIBAUT, *LiDAR derived morphology of the 1993 Lascar pyroclastic flow deposits, and implication for flow dynamics and rheology*, *Journal of Volcanology and Geothermal Research*, 245-246 (2012), pp. 81–97.
- [75] P. JOP, Y. FORTERRE AND O. POULIQUEN, *Crucial role of sidewalls in granular surface flows: consequences for the rheology*, *Journal of Fluid Mechanics*, 541 (2005), pp. 167–192.
- [76] P. JOP, Y. FORTERRE AND O. POULIQUEN, *A constitutive law for dense granular flows*, *Nature*, 441 (2006), pp. 727–730.
- [77] P. JOP, Y. FORTERRE AND O. POULIQUEN, *Initiation of granular surface flows in a narrow channel*, *Physics of Fluids (1994-present)*, 19 (2007), p. 088102.
- [78] C. A. KENNEDY AND M. H. CARPENTER, *Additive Runge-Kutta schemes for convection-diffusion-reaction equations*, *Applied Numerical Mathematics*, 44 (2003), pp. 139–181.
- [79] P.-Y. LAGRÉE, L. STARON AND S. POPINET, *The granular column collapse as a continuum: validity of a two-dimensional Navier-Stokes with a  $\mu(I)$ -rheology*, *Journal of Fluid Mechanics*, 686 (2011), pp. 378–408.
- [80] J. LAMBERT, *Numerical methods for ordinary differential systems*, Wiley, 1991.

- [81] R. J. LEVEQUE, *Finite-Volume Methods for Hyperbolic Problems*, Cambridge University Press, 2002.
- [82] A. LUCAS AND A. MANGENEY, *Mobility and topographic effects for large Valles Marineris landslides on Mars*, *Geophysical Research Letters*, 34 (2007), pp. n/a–n/a. L10201.
- [83] A. LUCAS, A. MANGENEY AND J. P. AMPUERO, *Frictional velocity-weakening in landslides on earth and on other planetary bodies*, *Nature Communications*, 5 (2014).
- [84] C. LUSSO, F. BOUCHUT, A. ERN AND A. MANGENEY, *A free interface model for static/flowing dynamics in thin-layer flows of granular materials with yield: Simple shear simulations and comparison with experiments*, *Applied Sciences*, 7 (2017).
- [85] C. LUSSO, A. ERN, F. BOUCHUT, A. MANGENEY, M. FARIN AND O. ROCHE, *Two-dimensional simulation by regularization of free surface viscoplastic flows with Drucker-Prager yield stress and application to granular collapse*, *Journal of Computational Physics*, 333 (2017), pp. 387–408.
- [86] A. MANGENEY, F. BOUCHUT, N. THOMAS, J. P. VILOTTE AND M. O. BRISTEAU, *Numerical modeling of self-channeling granular flows and of their levee-channel deposits*, *Journal of Geophysical Research: Earth Surface*, 112 (2007), pp. n/a–n/a. F02017.
- [87] A. MANGENEY, O. ROCHE, O. HUNGR, N. MANGOLD, G. FACCANONI AND A. LUCAS, *Erosion and mobility in granular collapse over sloping beds*, *Journal of Geophysical Research: Earth Surface* (2003–2012), 115 (2010).
- [88] A. MANGENEY-CASTELNAU, F. BOUCHUT, J. P. VILOTTE, E. LAJEUNESSE, A. AUBERTIN AND M. PIRULLI, *On the use of Saint Venant equations to simulate the spreading of a granular mass*, *Journal of Geophysical Research: Solid Earth*, 110 (2005), pp. n/a–n/a. B09103.
- [89] A. MANGENEY-CASTELNAU, J.-P. VILOTTE, M. O. BRISTEAU, B. PERTHAME, F. BOUCHUT, C. SIMEONI AND S. YERNENI, *Numerical modeling of avalanches based on Saint Venant equations using a kinetic scheme*, *Journal of Geophysical Research: Solid Earth*, 108 (2003), pp. n/a–n/a. 2527.
- [90] N. MANGOLD, A. MANGENEY, V. MIGEON, V. ANSAN, A. LUCAS, D. BARATOUX AND F. BOUCHUT, *Sinuuous gullies on mars: Frequency, distribution, and implications for flow properties*, *Journal of Geophysical Research: Planets*, 115 (2010), pp. n/a–n/a. E11001.

- 
- [91] N. MARTIN, I. R. IONESCU, A. MANGENEY, F. BOUCHUT AND M. FARIN, *Continuum viscoplastic simulation of a granular column collapse on large slopes:  $\mu(I)$  rheology and lateral wall effects*, *Physics of Fluids*, 29 (2017), p. 013301.
- [92] S. MCDUGALL AND O. HUNGR, *A model for the analysis of rapid landslide motion across three-dimensional terrain*, *Canadian Geotechnical Journal*, 41 (2004), pp. 1084–1097.
- [93] R. W. D. NICKALLS, *95.60 a new bound for polynomials when all the roots are real*, *The Mathematical Gazette*, 95 (2011), pp. 520–526.
- [94] C. PARÉS, *Numerical methods for nonconservative hyperbolic systems: a theoretical framework*, *SIAM Journal on Numerical Analysis*, 44 (2006), pp. 300–321.
- [95] C. PARÉS AND M. CASTRO, *On the well-balance property of roe’s method for non-conservative hyperbolic systems. applications to shallow-water systems*, *ESAIM: mathematical modelling and numerical analysis*, 38 (2004), pp. 821–852.
- [96] M. PIRULLI AND A. MANGENEY, *Results of back-analysis of the propagation of rock avalanches as a function of the assumed rheology*, *Rock Mechanics and Rock Engineering*, 41 (2008), pp. 59–84.
- [97] E. B. PITMAN AND L. LE, *A two-fluid model for avalanche and debris flows*, *Philosophical Transactions of the Royal Society of London A: Mathematical, Physical and Engineering Sciences*, 363 (2005), pp. 1573–1601.
- [98] O. POULIQUEN, *On the shape of granular fronts down rough inclined planes*, *Physics of Fluids*, 11 (1999).
- [99] O. POULIQUEN, *Scaling laws in granular flows down rough inclined planes*, *Physics of Fluids (1994-present)*, 11 (1999), pp. 542–548.
- [100] O. POULIQUEN AND Y. FORTERRE, *Friction law for dense granular flows: application to the motion of a mass down a rough inclined plane*, *Journal of Fluid Mechanics*, 453 (2002), pp. 133–151.
- [101] A. ROBERT, *A stable numerical integration scheme for the primitive meteorological equations*, *Atmosphere-Ocean*, 19 (1981), pp. 35–46.
- [102] G. ROSATTI, L. BONAVENTURA, A. DEPONTI AND G. GAREGNANI, *An accurate and efficient semi-implicit method for section-averaged free-surface flow modelling*, *International Journal of Numerical Methods in Fluids*, 65 (2011), pp. 448–473.
- [103] A. J. C. B. DE SAINT-VENANT, *Théorie du mouvement non permanent des eaux, avec application aux crues des rivières et à l’introduction des marées dans leur lit*, *C. R. Académie des Sciences, Paris*, 73 (1871), pp. 147–154.

- [104] J. SAINTE-MARIE, *Vertically averaged models for the free surface non-hydrostatic Euler system: derivation and kinetic interpretation*, *Mathematical Models and Methods in Applied Sciences*, 21 (2011), pp. 459–490.
- [105] S. B. SAVAGE AND K. HUTTER, *The motion of a finite mass of granular material down a rough incline*, *Journal of Fluid Mechanics*, 199 (1989), pp. 177–215.
- [106] D. SCHAEFFER, *Instability in the evolution equations describing incompressible granular flow*, *Journal of Differential Equations*, 66 (1987), pp. 19–50.
- [107] L. E. SILBERT, D. ERTAŞ, G. S. GREST, T. C. HALSEY, D. LEVINE AND S. J. PLIMPTON, *Granular flow down an inclined plane: Bagnold scaling and rheology*, *Physical Review E*, 64 (2001), p. 051302.
- [108] N. TABERLET, P. RICHARD, A. VALANCE, W. LOSERT, J. M. PASINI, J. T. JENKINS AND R. DELANNAY, *Superstable granular heap in a thin channel*, *Physical Review Letters*, 91 (2003), p. 264301.
- [109] G. TUMOLO AND L. BONAVENTURA, *A semi-implicit, semi-Lagrangian, DG framework for adaptive numerical weather prediction*, *Quarterly Journal of the Royal Meteorological Society*, 141 (2015), pp. 2582–2601.
- [110] G. TUMOLO, L. BONAVENTURA AND M. RESTELLI, *A semi-implicit, semi-Lagrangian,  $p$ -adaptive discontinuous Galerkin method for the shallow water equations*, *Journal of Computational Physics*, 232 (2013), pp. 46–67.

